UNIVERSITY OF OKLAHOMA

GRADUATE COLLEGE

ESTIMATING AND MITIGATING ERRORS IN DUAL-POLARIZATION RADAR ATTENUATION CORRECTION

A DISSERTATION

SUBMITTED TO THE GRADUATE FACULTY

in partial fulfillment of the requirements for the

Degree of

DOCTOR OF PHILOSOPHY

By

RYAN MICHAEL MAY
Norman, Oklahoma
2014

ESTIMATING AND MITIGATING ERRORS IN DUAL-POLARIZATION RADAR ATTENUATION CORRECTION

A DISSERTATION APPROVED FOR THE
SCHOOL OF METEOROLOGY

BY

Dr. Michael Biggerstaff, Chair

Dr. Robert Palmer

Dr. Ming Xue

Dr. Tian-You Yu

Dr. Louis Wicker

Dr. Mark Yeary

This dissertation is dedicated to the love of my life, my wife Macie, without whose love and support this work would never have happened.

Acknowledgements

First and foremost, I want to acknowledge the support of my family and so many friends. This dissertation has been (too) long in coming, and I would not have made it to the finish line without your support.

I am grateful to my thesis advisor, Dr. Michael Biggerstaff, for all the long hours of discussion that helped to shape the scope and direction of this work. His mentorship has helped to make me a better writer and a better scientist.

I would also like to thank the members of my thesis committee, Drs. Robert Palmer, Louis Wicker, Ming Xue, Mark Yeary, and Tian-You Yu. Your advice was instrumental in helping me to chose a focused and manageable scope for my thesis work. I am also grateful for your patience in dealing with the logistical challenges that were associated with serving on my doctoral committee.

I would also like to express my thanks to Dr. Ted Mansell for performing the numerical storm simulations that served as key input to this work.

Table of Contents

List of Tables

List of Figures

Abstract

Correction for rain attenuation is an important data quality issue when using data collected by radars operating at attenuating wavelengths, specifically C and X bands. Such issues are especially important for quantitative use of the data, such as rainfall estimation, where a 3dB error in reflectivity factor can result in more than 60% error in the rainfall estimate. In this work, the errors from several different attenuation correction techniques are examined. To test the corrections, simulated time-series dual-polarization radar data are used. The basis for the simulations is the use of a discretized radar pulse, where each pulse element generates the appropriately calculated stochastic value to give realistic radar time series data. In addition to providing for a sufficient number of elements to generate statistically meaningful data, this discretized pulse model also enables the simulation of spatial sampling aspects of the radar beam, allowing for differential attenuation and phase shift across the radar beam.

These simulated data are used to quantify the performance of several rain attenuation correction algorithms: linear Φ_{DP}, ZPHI, and Self-Consistent, as well as a modified version of the Self-Consistent algorithm. Using the simulated data and respective truth fields, the performance of the algorithms is examined in detail across a variety of scattering and microphysics configurations, to study the impact of the assumptions made on the quality of algorithm performance. A wide array of radar spatial sampling strategies are also examined to identify the impacts on algorithm performance.

Chapter 1

Introduction

1.1 Motivation

Radar-based Quantitative Precipitation Estimation (QPE) has been an active area of research since the advent of radar meteorology (Marshall et al. 1947; Stout and Mueller 1968). In fact, QPE is one of the primary missions of the National Weather Services (NWS) Weather Surveillance Radar 1988-Doppler (WSR-88D) network (Crum and Alberty 1993; Klazura and Imy 1993). Traditional radar-based estimation of precipitation relies on reflectivity (Z) only, which roughly depends on the sum of the 6th power of the diameters of all scattering particles (rain drops). This results in a non-unique relation between the volume of water in the sampling volume of the radar pulse and the reflectivity estimated by the radar—the relation depends on the actual distribution of droplet sizes (Stout and Mueller 1968). Additionally, high reflectivity values are often associated with the hail cores of severe storms, resulting in severe over-estimation of rain in those areas. Non-meteorological echoes (e.g. ground clutter, insects, birds, chaff, etc.) can also cause an automatic algorithm to estimate rain when none is falling. Other problems include beam-blockage and attenuation, which causes rainfall under-estimation due to the relation between Z and absolute returned power. Similarly, calibration of the radar is also important and is a non-trivial problem (Atlas 2002).

To address these shortcomings, many radars now transmit and receive electromagnetic radiation at two orthogonal polarizations (i.e., horizontal and vertical). Since electromagnetic scattering is related to the size of the particle in the direction of wave polarization, having these two channels gives much more information about the shape and orientation of the scatterers within the volume. For instance, liquid water drops are increasingly deformed by aerodynamic stresses as their diameter increases. This effect gives them a larger radar cross section (RCS) for horizontally polarized waves than for vertically polarized. Thus, by comparing the amount of power returned in the vertical and horizontal channels, Z_{DR}, one can estimate to what extent the raindrops are deformed from spheres; this allows some inferences about the sizes of the drops to be made. Additionally, the non-spherical raindrops will result in a different effective index of refraction along the radar propagation path. This difference results in a phase shift (ϕ_{DP}) between the channels; the range derivative of this parameter, K_{DP}, can be related to rain amounts along the path (Bringi and Chandrasekar 2001). Using K_{DP} and Z_{DR}, regions with larger water drops can be differentiated from those with only small (and mostly spherical) drops. There are also applications for detecting ice crystals, hail, and non-meteorological echoes (see for example Straka et al. 2000; Jameson 1983; Giuli et al. 1991; Hubbert et al. 1993). Utilizing this increased information, dual-polarization radar data has been shown to yield an improvement in radar-based QPE. This improvement, combined with the ability to classify the radar echoes, has demonstrated sufficient gains in utility that the WSR-88D network has been upgraded with dual-polarization capabilities (Ryzhkov et al. 2005b,c; Doviak et al. 2000).

As promising as they seems, there are significant challenges remaining in using dual-polarization data for radar-based QPE. Careful calibration of the radar is still

important, and for dual polarization measurements, two separate channels need to be calibrated. Also, the meteorological range of Z_{DR} is much less than that of Z, so the relative calibration of the two channels must be an order of magnitude more precise than the absolute calibration of a single channel (Ryzhkov et al. 2005a).

1.2 Attenuation Correction

At a wavelength in S-band (nominally $10\,$cm), attenuation is small and usually neglected; however, in heavy rain, one can still see attenuation up to $0.04\,$db/km (Bringi et al. 1990). At wavelengths in C-band and X-band (nominally $5\,$cm and $3\,$cm, respectively), attenuation can be significant, up to $0.3\,$dB/km for C-band and $2\,$dB/km for X-band (Bringi et al. 1990). Therefore, data at these wavelengths must be corrected for attenuation before being used quantitatively. With only reflectivity data from a single channel available, however, trying to correct attenuation is unstable (Hitschfeld and Bordan 1954; Hildebrand 1978).

With the advent of dual-polarization radars, additional possibilities emerged for correcting attenuation of reflectivity. This also brought the new problem of correcting for *differential* attenuation. Bringi et al. (1990) laid the theoretical framework for such corrections by computing K_{DP}, attenuation (A_H), and differential attenuation (A_{DP}) at S-, C-, and X-bands for a range of gamma DSD parameters. Linear regressions through the resulting scatter of points showed promise in terms of producing linear relationships between K_{DP} and both A_H and A_{DP}, which could be used to estimate attenuation and correct for it. Aydin et al. (1989) instead proposed a correction procedure for dual-polarization data that used an empirical relationship between A_H/Z_H

and Z_{DR}. Gorgucci et al. (1996) modified this procedure to use a more straightforward formulation of A_H and A_{DP} in terms of Z_H and Z_{DR}. Gorgucci et al. (1998) performed a comparison between the methods proposed by Hildebrand (1978); Aydin et al. (1989); Bringi et al. (1990) at C-band. The corrections using only Z and Z_{DR} were found to perform much better than corrections using only K_{DP}. This is likely because K_{DP}, as the range derivative of ϕ_{DP}, is a difficult parameter to estimate robustly in all conditions (Gorgucci et al. 2000). However, the (Z_H, Z_{DR}) method relies upon having a properly calibrated radar, which is difficult to achieve and maintain (Ryzhkov et al. 2005a), especially operationally; conversely, calibration is not required to use K_{DP}.

Scarchilli et al. (1993), working at C-band, introduced a simple method based on Bringi et al. (1990) that calculates A_H and A_{DP} as linearly proportional to K_{DP}; this implies that the path integrated (differential) attenuation is linearly related to the change in ϕ_{DP} up to that point. The method then uses the corrected Z_{DR} data to estimate backscatter differential phase (δ), which can then be removed from the ϕ_{DP} data. This procedure is iterated until the differences in the ϕ_{DP} data between iterations became small.

Ryzhkov and Zrnić (1995) applied the linear $A_H - \phi_{DP}$ and $A_{DP} - \phi_{DP}$ relations as well, but took the step of using an empirical procedure to estimate the proportionality constants at S-band. These constants were estimated by looking at how a subset of the Z_H data (based on the corresponding K_{DP} values) changed as a function of the total ϕ_{DP} change; the slope of this scatter plot gave the appropriate $A_H - \phi_{DP}$. A similar procedure was performed for Z_{DR} to estimate A_{DP}. This technique was applied by Carey et al. (2000) at C-band to correct rainfall estimates in tropical convection. Carey

et al. (2000) also noted the spread in published coefficients at the time and attributed the variation to the dependence on a considerable amount of theoretical assumptions: temperature, drop size distribution (DSD), and drop shape model. The study found that an advantage of empirical estimates was its ability to find coefficients appropriate for the actual observed conditions.

Matrosov et al. (2002) extended this same approach to X-band, but slightly modified the technique so that the drop shape factor, used to calculate the coefficient of proportionality between A_H and K_{DP}, is calculated from Z_H and Z_{DR} (initially corrected with a stock shape factor). The proportionality constants between A_H or A_{DP} and K_{DP} are calculated from this shape factor. Anagnostou et al. (2006a) extended this slightly to calculate the proportionality constant between A_{DP} and K_{DP} as well. Anagnostou et al. (2006a) differs in that they find a "best" fit shape factor for the whole case, where "best" was determined based on consistency of corrected data with raindrop spectra. These methods attempt to explicitly adjust for the dependence of the relationship between attenuation and K_{DP} on the actual drop shapes.

Smyth and Illingworth (1998) proposed a scheme that used as a constraint the total path differential attenuation, estimated from the negative Z_{DR} values in a distant stratiform region; this constraint assumes that the intrinsic Z_{DR} value for such a region is 0 dB. This attenuation (A_{DP}) was distributed among all gates with sufficient K_{DP} magnitude based on the value of K_{DP} relative to the total ϕ_{DP} change. The values of K_{DP} and A_{DP} were combined to retrieve the DSD, and from there the value of A_H. Having the values of both A_H and A_{DP} at all gates, corrected fields of Z_H and Z_{DR} were then generated. While the use of a region with an intrinsic Z_{DR} of 0 dB can be robust for estimating the path integrated differential attenuation, automating

the process of identifying such regions is extremely difficult, making the technique difficult to implement operationally. Additionally, this procedure offered no solution for scenarios without a distant stratiform region to act as a constraint.

Testud et al. (2000), based on a "rain-profiling" method used for satellite-based radar rainfall retrievals, used ϕ_{DP} as a constraint for correcting Z_H for attenuation, using both ϕ_{DP} and Z_H to estimate A_H (hence being commonly referred to as the ZPHI method). The estimated A_H profile is then used to correct Z_H. Using the obtained specific attenuation, values for normalized intercept parameter (N_0) were obtained, which were combined with specific attenuation to estimate rainfall. Separate sets of power law constants were given for the horizontal and vertical polarizations, which could be used together to correct Z_{DR} for differential attenuation. Alternatively, Testud et al. (2000) also provided a relation for calculating A_{DP} from A_H and N_0. Anagnostou et al. (2004) applied this method to X-band, but the increased dependence of attenuation and K_{DP} on microphysical parameters (N_0, etc.) led to the estimation over sets of range intervals within a radial. These intervals defined regions over which N_0 was held fixed, and the procedure was iterated to find the optimal set of coefficients for the interval, increasing the stability of the correction. From these corrected data, rainfall estimates using Z_H, Z_{DR}, and K_{DP} were found to be superior to those using only Z_H at X-band.

Bringi et al. (2001) extended the ZPHI approach with a "self-consistent" methodology that dynamically estimates the constant of proportionality between K_{DP} and A_H, α. The procedure is iterative, using the radial profile of Z_H and the change in ϕ_{DP} over the radial to estimate a radial profile of A_H. This profile of A_H is integrated using α to calculate an estimated change in ϕ_{DP}. The difference between the

calculated and measured values is used to adjust α and the procedure is iterated until convergence is achieved. Because the relationship between A_{DP} and K_{DP} is not as linear at C-band, an estimate of the intrinsic Z_{DR} at a far range is used to provide a constraint on the maximum A_{DP}, similar to Smyth and Illingworth (1998). In this work, however, an empirical relationship is used to estimate an average Z_{DR} value from the corrected Z_H data. Park et al. (2005a,b) extended this method to X-band in a straightforward fashion, only updating various coefficients and empirical relations to ones appropriate for the wavelength. These updates came from a detailed evaluation of scattering simulations. Liu et al. (2006) extends the approach slightly for Z_H by using the Levenberg-Marquardt solver to improve convergence when solving for α. Liu et al. (2006) also modified the approach by running the same technique, using different coefficients, to correct Z_V data and combining corrected Z_H and Z_V to obtain corrected Z_{DR}.

Gorgucci et al. (2006) corrected for attenuation and differential attenuation using a self-consistent approach at X-band as well, but with important differences. Instead of extending ZPHI to adaptively estimate the coefficient relating A_H and ϕ_{DP}, Gorgucci et al. (2006) utilized the full self-consistency of Z_H, Z_{DR}, K_{DP}, and A_H. Again, due to the challenges of working with K_{DP}, an estimated profile of ϕ_{DP} was calculated from corrected estimates of Z_H, Z_{DR}, and A_H (combined using a power-law). Differences between the observed and calculated ϕ_{DP} profile were used to adjust a constant, which yielded a new estimate of A_H, and hence new profiles of Z_H and Z_{DR}. This procedure was iterated until the value of the constant converged; initial values were obtained from the procedure of Bringi et al. (2001). In this method, A_{DP} was estimated using the same procedure (with different coefficients), but in a separate set of

steps and convergence. Gorgucci and Baldini (2007) (working at C-band) modified this to simultaneously estimate A_H and A_{DP}, making use of the approximately linear relationship between the two variables. The unified approach was found to have reduced errors over the separated approach. The validation of the technique was based on C-band profiles reconstructed from S-band data.

Beyond these main trees of approaches, there have been several novel techniques tried, with varying degrees of success. Vulpiani et al. (2005) used an artificial neural network to approximate the non-linear relationship for calculating attenuation from Z_H and Z_{DR}. This algorithm worked iteratively, like Hitschfeld and Bordan (1954), running from the furthest range inward, constraining the total attenuation correction using ϕ_{DP}, as in Bringi et al. (2001). This approach was demonstrated to have less error than the ZPHI approach, but training the neural network makes the approach challenging from an operational implementation standpoint. Vulpiani et al. (2008) attempted to address the issue of spatial variability in the coefficients relating attenuation to radar observables by using a Bayesian classifier. The classifier, using Z_H, Z_{DR}, K_{DP}, and ρ_{HV}, identified regions as one of four classes (large drops or light, medium, or heavy rain); the results of the classification were used to select an appropriate set of coefficients for estimating A_H and A_{DP} from ϕ_{DP}. Using intrinsic values of Z_{DR} at long ranges, they demonstrated slightly reduced root mean square error in comparison with ZPHI.

Gourley et al. (2007) introduced a novel approach that advects cells between radar scans using a cross-correlation analysis. The decreases in Z_H and Z_{DR} for individual cells were matched to increases in ϕ_{DP}, which was used to retrieve the coefficients relating ϕ_{DP} to A_H and A_{DP}. The technique relied on the fact that the mean change

in intrinsic Z_H and Z_{DR} over the whole radar coverage area for several hours was approximately zero (i.e., no mean intensity changes).

A subject of much recent research are the so called "hot spot" regions, as identified by Ryzhkov and Zrnić (1995). These are regions of anomalously high attenuation caused by the presence of anomalously large scatterers (compared with the sizes normally assumed for rain drop size distributions). Tabary et al. (2009) and Borowska et al. (2011) attribute the cause of such areas to be wet ice particles, likely from melting hail. Because such regions differ greatly from the surrounding areas in terms of the size distribution of scatterers, attenuation from the areas are not properly corrected using mean profiles generated from most scattering simulations (Carey et al. 2000). Gu et al. (2011) proposed a correction method that identifies "hot spot" regions using Z_H and ρ_{HV}; after identification, these regions were corrected for attenuation using coefficients adjusted from their "background" values, as estimated in Ryzhkov and Zrnić (1995).

1.3 Simulation

Given all of the challenges and advances in radar-based QPE, one natural way to evaluate the relative quality of different methods is through simulation. Recent advances in numerical modeling have made it possible to simulate convective storms at very fine scales over a broad range of environmental conditions (e.g. Wicker and Wilhelmson 1995; Lewellen et al. 1997; Jung et al. 2010). Coupling a software radar simulator with high-resolution numerical simulations, one can generate large sets of simulated

radar data that span a wide range of radar operating characteristics. These simulated datasets can be used to provide truth data for objective evaluation of algorithms.

Many approaches have been taken previously in simulating radar data, varying in sophistication from simple time series simulation (Zrnić 1975) to moment calculation (Chandrasekar and Bringi 1987; Krajewski et al. 1993; Gosset 2004) or full simulation of radar returns from each pulse (Capsoni and DAmico 1998; Capsoni et al. 2001; Muschinski et al. 1999). Zrnić (1975) generated simulated time series radar data and Doppler spectra using an assumed Gaussian distribution of velocities within the resolution volume. Chandrasekar and Bringi (1987) looked at the variation of simulated reflectivity values as a function of raindrop size distribution parameters. Similarly, Krajewski et al. (1993) calculated values of reflectivity factor and differential reflectivity using rainfall rates from a numerical model combined with an assumed drop size distribution. Neither of these studies was concerned with Doppler velocity or the impacts of scanning strategies. Jung et al. (2010) used detailed scattering calculations to generate reflectivity, differential reflectivity, differential propagation phase, and copolar cross-correlation data from a numerical simulation. These data were used to look at the effects of different numerical model microphysics schemes. Wood and Brown (1997) evaluated the effects of WSR-88D (Crum and Alberty 1993) radar scanning strategies on the sampling of mesocyclones and tornadoes. The effects of the scanning strategy were accounted for by using an effective beamwidth for the radar, which was used to scan an analytic vortex with a uniform reflectivity field. Gosset (2004) used analytic fields to calculate dual-polarization moments in order to analyze the effect of non-uniform beam-filling on moment estimates. As mentioned previously, Zahiri et al. (2008) calculated polarimetric radar data from 1 km numerical simulation output

interpolated onto a polar grid; these simulated data included error by adding normally distributed noise terms. Berne and Uijlenhoet (2005) simulated reflectivity data using a sophisticated statistical model. Using stochastic, auto-regressive range-profiles of rain distribution parameters, they examined errors in the attenuation correction method of Hitschfeld and Bordan (1954), as applied to satellite data. Beyond the sophisticated statistical model, however, the radar simulation was simplistic, and did not include any beam-weighting or azimuthal gradients.

Capsoni and DAmico (1998) simulated the pulse-to-pulse time series of radar data by combining the simulated returns from individual representative hydrometeors within a radar volume (Monte Carlo Sampling). This work was extended to generate polarimetric signatures by Capsoni et al. (2001). Due to the computational requirements of this approach, the radar data were generated for only a single range gate only, and thus many aspects of the scanning radar were not simulated. A similar approach was presented by Cheong et al. (2008) for general use in generating simulated radar signals (IQ data) at a single polarization from the output of numerical storm models. Muschinski et al. (1999) used a different scheme for simulating time series data for a wind profiler from a large eddy simulation. It relied on using a fixed grid of scattering centers which return appropriate phase shifts; when combined with a random initial phase, this procedure yielded realistic radar signals.

The work presented herein describes a radar simulator designed to simulate the returns from a scanning Doppler radar on a pulse-to-pulse basis, based on the radar configuration and scanning strategy used. This work extends that of May et al. (2007), which demonstrated that the simulator is capable of simulating several radar data

characteristics including: range resolution, azimuthal over- and under-sampling, non-standard (anomalous) propagation, Rayleigh attenuation, antenna sidelobes, velocity aliasing, and range aliasing. Starting with output from a high-resolution numerical simulation, the simulator generates both time-series and volume-averaged moments for H and V polarizations in the linear basis. Time series data are generated using the method demonstrated by Muschinski et al. (1999). This approach is combined with that of Galati (1995) to add appropriate correlation between the horizontal and vertical channels. These polarimetric capabilities will be demonstrated for a variety of wavelengths and scattering models.

1.4 Application

In developing methods for attenuation correction and radar-based QPE, validation is a frequent challenge. Many validation methods rely on simple simulation, such as generating X-band profiles from S-band data. These have the benefit of removing some DSD variability, but rely upon many assumptions about scattering processes in order to relate radar observables at one band to those at another. For attenuation correction, another method is to compare co-located radars, with one operating at a non-attenuating wavelength, such as S-band (Anagnostou et al. 2006b; Snyder et al. 2010). This requires careful calibration of two radars and has errors due to slightly different locations, different observation paths, as well as differences in the intrinsic values due to resonance regime effects. Another validation approach, especially for QPE, is to compare point measurements of rain from gauges (or full DSD measurements from disdrometers) to radar data, but this approach has problems due to the inherent

difference in scale between point measurements and the volume averaging involved in remote sensing. Additionally, at longer ranges from the radar, the remotely sensed data can be more than a km above the point measurement, introducing significant variance into the comparison.

Many of these previous shortcomings in validation can be addressed using a sophisticated radar simulation, such as that described previously. In this work, errors inherent in attenuation correction at multiple wavelengths (C- and X-band) are quantified and analyzed to identify specific sources of these errors. In the process, several different techniques will be evaluated; of particular interest are the effects of temperature and non-uniform beam-filling, including down-range impacts of differential attenuation across the radar beam. Because the simulation includes full propagation effects as well as a discretized radar pulse that can be filled with a heterogeneous field, the effects of non-uniform beam-filling are also taken into account. Also, because the simulator contains all relevant truth data, calculating errors in retrieved attenuation profiles is straightforward. Since the simulation is stochastic in nature, simulated data replicate the variability seen in real data, including the effects of low signal to noise ratio; this implies that error estimates will reflect those of real world data.

Chapter 2

Radar Simulator

2.1 Design

Since the performance and accuracy of the simulation of radar data is critical to the validity of the work that will follow, a large section of this work is dedicated to a detailed description of the radar simulator used, which is an extension of the work done by May et al. (2007). The extensions can be summarized as:

- Inclusion of new scattering models for polarimetric variables
- Extension for model input which includes two-moment microphysics schemes
- Expansion to enable the generation of time series data in additional to simple volume average-based moments
- Generation of additional diagnostic fields to help identify regions where the pulse is non-uniformly filled.

The flow of the program is as follows (with the details covered in subsequent sections):

- Read configuration
- Calculate radar variables from model input fields
- As the radar scans:

- Interpolate model fields to discretized radar resolution volume
- Generate a sample from the pulse
- As appropriate, generate a radial of data from the samples

2.1.1 Simulator configuration and input

The behavior of the radar simulator is controlled by specifying radar characteristics and scanning strategy (Table 2.1). Note that the antenna beamwidth, gain, and wavelength are treated independently to allow for simulation of antennas with different classes of performance. The actual form of the antenna pattern is fixed based on the analytic function discussed later. It should also be noted that the polarization of the radar is fixed to simultaneous horizontal and vertical transmission. This is an implementation detail rather than a limitation, as adding transmit polarization flexibility would be straightforward. The minimum detectable signal is used as a threshold for the calculated moments and also as a noise power value for the time series simulation. The pulse repetition time and pulse length are given independently, but in reality they are usually constrained by the duty cycle of the transmitter. Enforcement of a duty cycle is up to the user when creating the configuration. The antenna pointing angles can be specified for either full or sector plan-position indicator (PPI) scans, or range-height indicator (RHI) scans. The simulator allows for overlapped sampling in both azimuth (or elevation for RHI scans) and in range. In addition to the radar configuration parameters, the drop shape model, canting angle distribution width (for T-matrix), and scattering model can be specified at runtime. This simplifies the evaluation of the impacts of the use of these different models.

Radar Parameters	Scanning Parameters	Simulation Parameters
Location	PRT	Input simulation
Antenna beamwidth	Pulse length	Scattering model
Antenna gain and sidelobes	Antenna rotation rate	Drop shape model
Wavelength	Pulses per radial	Canting distribution width
Transmit power	Radar gate spacing	PRNG seed
Range to first gate	Scan fixed angle	
Minimum detectable signal	Start and end angles	

Table 2.1: Simulator control parameters.

The input data to the radar simulator are three-dimensional gridded fields that describe the state of the atmosphere. Wind components and the appropriate variables describing the hydrometeor content (depending on the microphysics scheme used) are required fields. Water vapor, temperature, and pressure are also needed for calculating the atmospheric index of refraction, which is used for determining the propagation path of the radar beam. Temperature is also used in determining the dielectric constant for the hydrometeors.

2.1.2 Calculation of Radar Variables

2.1.2.1 Scattering

The simulator supports several different scattering assumptions: Rayleigh, Rayleigh-Gans, Mie, and T-matrix (Mishchenko et al. 1996; Bringi and Chandrasekar 2001; Doviak and Zrnić 1993; Waterman 1971). For Rayleigh-Gans and T-matrix scattering,

there are options to use either spheres or oblate spheroids as the assumed shape for hydrometeors. It should be noted that using sphere as the shape for T-matrix or Rayleigh-Gans scattering produces identical results to Mie and Rayleigh, respectively. When using oblate spheroids for raindrops, by default the axis ratio (r) for the spheroids is calculated using the polynomial form of Brandes et al. (2002):

$$r = 0.9951 + 0.0251D - 0.036\,44D^2 + 5.303 \times 10^{-3}D^3 - 2.492 \times 10^{-4}D^4 \quad (2.1)$$

where D is the equivolume diameter of the rain drop in mm. It should be noted that the coefficient of the cubic term above, 5.303×10^{-3}, is not the value given by Brandes et al. (2002). Both Brandes et al. (2002) and Brandes et al. (2004) give a value of 5.030×10^{-3}. However, this value results in a curve that does not match the plot given in Brandes et al. (2004), as shown in Figure 2.1; the value of 5.303×10^{-3}, however, does produce a matching plot. In addition to this relation, it is also possible to specify the use of the raindrop axis ratio relation introduced by Pruppacher and Beard (1970):

$$r = 1.030 - 0.062D \quad (2.2)$$

where D is again in mm.

Another required parameter for performing the scattering calculations is the refractive index (m) for water. The equations given by Ray (1972) are used to calculate the complex dielectric constant ($\epsilon_r + i\epsilon_i$) as a function of temperature (T, °C) and wavelength (λ, cm):

$$\epsilon_r = \epsilon_\infty + \frac{(\epsilon_s - \epsilon_\infty)[1 + (\lambda_s/\lambda)^{(1-\alpha)} \sin(\alpha\pi/2)]}{1 + 2(\lambda_s/\lambda)^{(1-\alpha)} \sin(\alpha\pi/2) + (\lambda_s/\lambda)^{2(1-\alpha)}} \quad (2.3)$$

$$\epsilon_i = \frac{(\epsilon_s - \epsilon_\infty)(\lambda_s/\lambda)^{(1-\alpha)} \cos(\alpha\pi/2)}{1 + 2(\lambda_s/\lambda)^{(1-\alpha)} \sin(\alpha\pi/2) + (\lambda_s/\lambda)^{2(1-\alpha)}} + \frac{\sigma\lambda}{18.8496 \times 10^{10}} \quad (2.4)$$

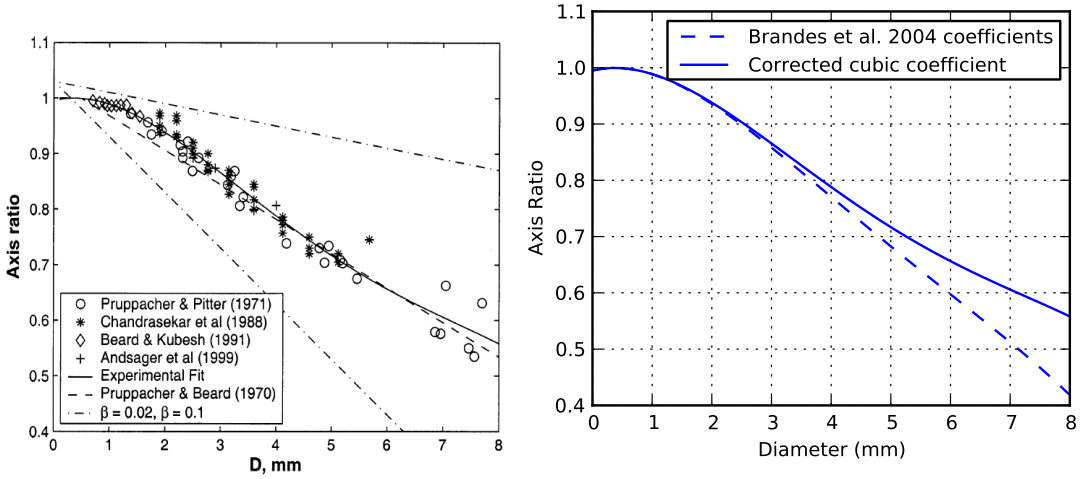

Figure 2.1: Left: As in Brandes et al. (2004) "Raindrop axis ratio as a function of drop equivalent volume diameter derived from measurements. The curved solid line shows an empirical fit [Eq. (21)]; the dashed line shows the linear relation of Pruppacher and Beard (1970); and the dashdot lines show the computational domain of Gorgucci et al. (2000)" Right: Comparison of drop axis ratio relations using the coefficients published in Brandes et al. (2004) (dashed) and with the corrected value (solid).

where ϵ_∞ is the high-frequency dielectric constant, ϵ_s is the static dielectric constant, λ_s is the relaxation wavelength, α is a spread parameter, and σ is a frequency-independent conductivity. These values are calculated as a function of temperature as:

$$\begin{aligned}\epsilon_s &= 78.54[1.0 - 4.579 \times 10^{-3}(T - 25.0) \\ &\quad + 1.19 \times 10^{-5}(T - 25.0)^2 - 2.8 \times 10^{-8}(T - 25.0)^3]\end{aligned} \tag{2.5}$$

$$\epsilon_\infty = 5.271\,37 + 0.021\,647\,4T + 0.001\,311\,98T^2 \tag{2.6}$$

$$\alpha = \frac{-16.8129}{T + 273} + 0.060\,926\,5 \tag{2.7}$$

$$\lambda_s = 0.000\,338\,36\ \exp\frac{2513.98}{T + 273} \tag{2.8}$$

$$\sigma = 12.5664 \times 10^8 \tag{2.9}$$

The index of refraction is found by taking the complex square root:

$$m = \sqrt{\epsilon_r + i\epsilon_i} \tag{2.10}$$

The use of these equations allow the simulator to capture the wavelength and temperature dependence of the index of refraction, avoiding the use of lookup tables with interpolation between fixed values for wavelength and temperature. This permits calculation of scattering using the temperature at each individual model grid point. Also, by having the wavelength dependence captured in a functional form, the simulator can be used at arbitrary wavelengths and not just be constrained to operating at general wavelengths appropriate to a given band (such as 3 cm for X-band).

All of the scattering calculations start from the scattering matrices in the forward ($\mathbf{S^f}$) and backward($\mathbf{S^b}$) scattering directions, given as:

$$\mathbf{S^f(D)} = \begin{bmatrix} S^f_{HH}(D) & S^f_{HV}(D) \\ S^f_{VH}(D) & S^f_{VV}(D) \end{bmatrix} \tag{2.11}$$

$$\mathbf{S^b(D)} = \begin{bmatrix} S^b_{HH}(D) & S^b_{HV}(D) \\ S^b_{VH}(D) & S^b_{VV}(D) \end{bmatrix} \tag{2.12}$$

where D is diameter and H and V in the subscript represent the polarization for the incident and scattered wave. The calculation of the scattering matrices depends on the scattering model used.

Rayleigh The Rayleigh approximation to the scattering from a dielectric sphere is the simplest, and the most familiar, method of calculating radar observables. Its inclusion within the simulator facilitates the use of the simulator as a teaching tool and also permits evaluation of the impacts of making the assumption that Rayleigh scattering is the dominant effect. The Rayleigh approximation is relatively accurate for scatterers whose size is small compared to the wavelength (Doviak and Zrnić 1993). Under this assumption, the effects of scattering are obtained by treating the sphere as a radiating dipole. This gives the following expressions for backscatter (σ_b), total scatter (σ_s), and absorption (σ_a) cross-sections:

$$|K|^2 = \left| \frac{m^2 - 1}{m^2 + 2} \right|^2 \tag{2.13}$$

$$\sigma_b = \frac{\pi^5}{\lambda^4} |K|^2 D^6 \tag{2.14}$$

$$\sigma_s = \frac{2}{3} \sigma_b \tag{2.15}$$

$$\sigma_a = \frac{\pi^2}{\lambda} \operatorname{Im} -KD^3 \tag{2.16}$$

H and V are omitted since Rayleigh scattering assumes spherical scatterers, and thus these scattering properties are identical for the two polarizations. For consistency with the other scattering calculations, these efficiencies are converted to their respective terms in the ($\mathbf{S^f}$) and backward($\mathbf{S^b}$) scattering matrices:

$$S^b_{HH}(D) = \frac{\sqrt{\sigma_b}}{4\pi} \tag{2.17}$$

$$S^b_{VV}(D) = S^b_{HH}(D) \tag{2.18}$$

$$\mathrm{Re}\, S^f_{HH}(D) = \mathrm{Re}\, S^b_{HH}(D) \tag{2.19}$$

$$\mathrm{Re}\, S^f_{VV}(D) = \mathrm{Re}\, S^b_{VV}(D) \tag{2.20}$$

$$\mathrm{Im}\, S^f_{HH}(D) = \frac{\sigma_s + \sigma_a}{2\lambda} \tag{2.21}$$

$$\mathrm{Im}\, S^f_{VV}(D) = \mathrm{Im}\, S^f_{HH}(D) \tag{2.22}$$

The expressions for the forward scattering matrices, while not fully correct (for the real part of the complex scattering matrix), allow the extinction cross-section to be calculated in accordance with optical theorem (Ishimaru 1991). This allows all of the different scattering models to use common code for obtaining relevant radar parameters from the scattering matrices in the forward and backward directions. The real portion of the forward scattering matrix would be used to obtain a propagation phase; since the differential between H and V polarizations is the quantity of interest, such a calculation is senseless with the Rayleigh approximation.

Rayleigh-Gans Rayleigh-Gans scattering extends Rayleigh scattering theory to non-spherical scatterers. This is achieved by adjusting the polarizability of the scatterer based on the orientation of the spheroid (prolate or oblate) and the polarization of the

incident wave (Bringi and Chandrasekar 2001). This theory gives the backscattering matrix as:

$$\mathbf{S^b}(\mathbf{D}) = \frac{\pi^2 D^3 (m^2-1)}{6\lambda^2} \begin{bmatrix} \Lambda & 0 \\ 0 & \Lambda_z \end{bmatrix} \tag{2.23}$$

$$\Lambda_{x,y,z} = \frac{1}{(m^2-1)\lambda_{x,y,z}+1} \tag{2.24}$$

$$\Lambda = \Lambda_x = \Lambda_y \tag{2.25}$$

$$\lambda_x = \lambda_y = \frac{1-\lambda_z}{2} \tag{2.26}$$

where $\lambda_{x,y,z}$ is the so-called depolarizing factor (Bringi and Chandrasekar 2001) in the x, y, z direction. These factors depend on the shape of the scatterer, and are given for oblate spheroids and spheres as:

$$\lambda_z(sphere) = \frac{1}{3} \tag{2.27}$$

$$\lambda_z(oblate) = \frac{1+f^2}{f^2}\left(1 - \frac{1}{f}\tan^{-1} f\right) \tag{2.28}$$

$$f^2 = \frac{1}{e^2} - 1 \tag{2.29}$$

where e is the eccentricity of the spheroid. It can be shown that λ_z for the sphere can be obtained by taking the limit as e goes to ∞. Using the value for a sphere, one obtains an identical expression as that given by unmodified Rayleigh theory.

Rayleigh-Gans theory gives the same matrix for the forward scatter direction as in the backscatter direction, with the exception of a flipped sign on the S_{HH} term.

However, as before, it is modified so that the proper extinction coefficients are obtained using optical theorem (Ishimaru 1991). In this case:

$$K_h = \frac{m^2 - 1}{(m^2 - 1)\lambda_x + 1} \tag{2.30}$$

$$\sigma_{sh} = \frac{2\pi^5}{3\lambda^4} |K_h|^2 D^6 \tag{2.31}$$

$$\sigma_{ah} = \frac{\pi^2}{\lambda} \operatorname{Im} -K_h D^3 \tag{2.32}$$

$$K_v = \frac{m^2 - 1}{(m^2 - 1)\lambda_z + 1} \tag{2.33}$$

$$\sigma_{sv} = \frac{2\pi^5}{3\lambda^4} |K_h|^2 D^6 \tag{2.34}$$

$$\sigma_{av} = \frac{\pi^2}{\lambda} \operatorname{Im} -K_h D^3 \tag{2.35}$$

These are used to adjust the forward scattering matrix as:

$$\operatorname{Im} S^f_{HH}(D) = \frac{\sigma_{sh} + \sigma_{ah}}{2\lambda} \tag{2.36}$$

$$\operatorname{Im} S^f_{VV}(D) = \frac{\sigma_{sv} + \sigma_{av}}{2\lambda} \tag{2.37}$$

Mie The Mie (1908) solution to the scattering problem is a relatively straightforward solution to the boundary value problem for the Laplace equation (see e.g Bringi and Chandrasekar 2001). This involves solving:

$$\epsilon_0 \nabla^2 \psi = \vec{\nabla} \cdot \vec{P} \tag{2.38}$$

subject to the boundary conditions:

$$\hat{n}_1 \times \vec{E}^{in}_T + \hat{n}_2 \times (\vec{E}^i + \vec{E}^s) = 0 \tag{2.39}$$

$$\hat{n}_1 \times \vec{B}^{in}_T + \hat{n}_2 \times (\vec{B}^i + \vec{B}^s) = 0 \tag{2.40}$$

where

$$\hat{n}_1 = \hat{r} \tag{2.41}$$

$$\hat{n}_2 = -\hat{r} \tag{2.42}$$

where $\vec{E}$ and $\vec{B}$ are the electric and magnetic fields, respectively, the superscript i and s denote the incident and scattered fields, respectively, and the superscript in and subscript T denote the total internal field. The solution proceeds by expanding the scattered field in terms of vector spherical harmonics:

$$\vec{E}^s(k_0 r, \theta, \phi) = 2\pi E_0 \sum_{n=1}^{\infty} (-\imath)^n \gamma_{1n}^{1/2} \vec{X}_{1n} \tag{2.43}$$

$$\vec{X}_{1n} = \left[\alpha_{o1n} \vec{M}_{o1n}(k_0 r, \theta, \phi) + \imath \beta_{e1n} \vec{N}_{e1n}(k_0 r, \theta, \phi) \right] \tag{2.44}$$

$$\gamma_{mn}^{1/2} = \sqrt{\frac{(2n+1)(n-m)! \epsilon_m}{4\pi(n+m)!}} \tag{2.45}$$

$$\epsilon_m = \begin{cases} 2 & m > 0 \\ 1 & m = 0 \end{cases} \tag{2.46}$$

where k_0 is the free-space wavenumber, k is the wavenumber within the sphere, and $\vec{M}$ and $\vec{N}$ are the vector spherical wave functions (also called multipoles). The Rg notation denote wave functions which are modified to be regular (finite) at the origin. The o and e subscripts denote represent whether the function is even or odd as a way of

eliminating the use of complex harmonics. The expansion coefficients, α_{o1n} and β_{e1n}, found using the boundary conditions, are:

$$\alpha_{o1n} = \frac{\rho j_n(\rho)[\rho_0 j_n(\rho_0)]' - \sqrt{\epsilon_r}\rho_0 j_n(\rho_0)[\rho j_n(\rho)]'}{\sqrt{\epsilon_r}\rho_0 h_n^{(2)}(\rho_0)[\rho j_n(\rho)]' - \rho j_n(\rho)[\rho_0 h_n^{(2)}(\rho_0)]'} \tag{2.47}$$

$$\beta_{e1n} = \frac{\rho_0 j_n(\rho_0)[\rho j_n(\rho)]' - \sqrt{\epsilon_r}\rho j_n(\rho)[\rho_0 j_n(\rho_0)]'}{\sqrt{\epsilon_r}\rho j_n(\rho)[\rho_0 h_n^{(2)}(\rho_0)]' - \rho_0 h_n^{(2)}(\rho_0)[\rho j_n(\rho)]'} \tag{2.48}$$

$$\rho_0 = k_0 a \tag{2.49}$$

$$\rho = \rho_0\sqrt{\epsilon_r} \tag{2.50}$$

$$[\rho z_n(\rho)]' = \frac{d\rho z_n(\rho)}{d\rho} \tag{2.51}$$

where j_n and $h_n^{(2)}$ are the spherical Bessel and (second kind) Hankel functions, respectively. Combining (2.46) and (2.51) gives the following expressions for the scattering matrices (Bringi and Chandrasekar 2001):

$$\mathbf{S} = \begin{bmatrix} \frac{i\cos\phi_s}{k_0} S_1(\theta_s) & \frac{-i\sin\phi_s}{k_0} S_1(\theta_s) \\ \frac{i\sin\phi_s}{k_0} S_2(\theta_s) & \frac{i\cos\phi_s}{k_0} S_2(\theta_s) \end{bmatrix} \tag{2.52}$$

$$S_1(\theta_s) = \sum_{n=1}^{\infty} \frac{2n+1}{n(n+1)} \left[\alpha_{o1n} \frac{P_n^1(\cos\theta_s)}{\sin\theta_s} + \beta_{e1n} \frac{dP_n^1(\cos\theta_s)}{d\theta_s} \right] \tag{2.53}$$

$$S_2(\theta_s) = \sum_{n=1}^{\infty} \frac{2n+1}{n(n+1)} \left[\alpha_{o1n} \frac{dP_n^1(\cos\theta_s)}{d\theta_s} + \beta_{e1n} \frac{P_n^1(\cos\theta_s)}{\sin\theta_s} \right] \tag{2.54}$$

where $P_n^m(\cos\theta)$ are the associated Legendre functions, and θ_s and ϕ_s define the scattering direction. For our purposes, ϕ_s is 0° and θ_s is 0 or π for forward scatter or backscatter, respectively. The actual implementation is a Python-based port of Matlab code written by Matzler (2002).

T-Matrix The extended boundary condition, or T-Matrix, method was first proposed to solve electromagnetic scattering problems by Waterman (1971). The approach is similar to that for Mie scattering, in that the incident and scattered fields are expanded

into various multipole terms, solving for coefficients of vector spherical wave functions. However, the T-matrix method is applicable to non-spherical scatterers which do not have a simple form in spherical coordinates. In such cases the boundary conditions do not lend themselves to a direct relation between the expansion coefficients of the incident field and those of the scattered field. Due to the linearity of Maxwell's equations and the boundary conditions themselves, the two sets of expansion coefficients can be related through a set of linear equations and matrix of coefficients.

In theory, this "transition" matrix (or T-matrix) is infinite in size; in practice, the procedure is iterated, increasing the number of terms until the results converge. The radar simulation code relies on the FORTRAN implementation from Mishchenko et al. (1996), which calculates the T-matrix for a fixed orientation; this has been wrapped in Python for convenience purposes. The reader is referred to Mishchenko et al. (1996) and the references therein for the lengthy theoretical derivation.

Canting Angle Distribution For T-matrix scattering calculations, the simulator has the option of including a non-zero canting angle distribution width. While the mean canting angle is assumed to be zero (a common assumption and a crucial one for the NEXRAD dual-polarization upgrade (Doviak et al. 2000)), the width of the distribution of angles can be changed to account for some random hydrometeor orientation due to turbulence. The simulation uses the axial distribution (Mardia 1972), which can be used to describe the distribution of a two-dimensional orientation angle in which

one of the components is fixed at 90°. Such a distribution is given by (Bringi and Chandrasekar 2001):

$$g_A(\theta) = b(\kappa) \exp(-\kappa \cos^2 \theta) \sin \theta \tag{2.55}$$

$$b(\kappa) = \frac{1}{2 \int_0^1 \exp(-\kappa t^2)\, dt} \tag{2.56}$$

where κ is the parameter that controls the width of the distribution. Figure 2.2 shows the axial probability density function for various values of κ.

To include the effects of the orientation angle distribution in the calculation of radar observables, all expected values are converted from single integrals over the drop size distribution to double integrals over both the DSD and the angular distribution. That is, integrals of the form:

$$A = \int f(D) N(D)\, dD \tag{2.57}$$

become:

$$A = \iint f(D, \theta) N(D) g_A(\theta)\, dD\, d\theta \tag{2.58}$$

Radar Observables By integrating various terms of these scattering matrices with respect to the drop size distribution, at each model grid point the relevant radar parameters can be calculated: reflectivity (η), backscatter differential phase shift (δ),

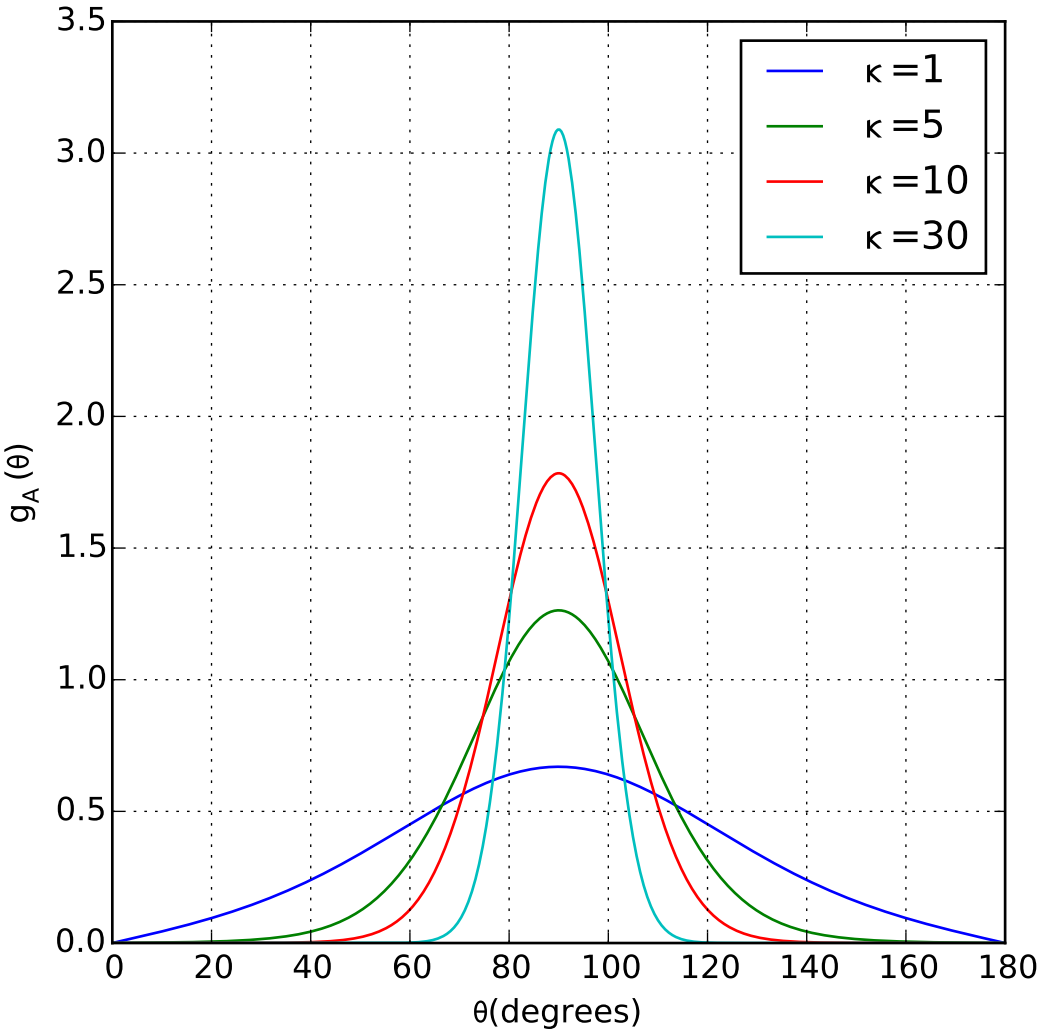

Figure 2.2: Axial probability density function for various values of the distribution width parameter, κ.

wavenumber perturbation (Δk, due to propagation through the medium), and expected cross-correlation coefficient ($|\rho_{hv}|$) (Bringi and Chandrasekar 2001, chap. 3 and 4):

$$\eta_H = 4\pi \int_0^{D_{max}} |S^b_{HH}(D)|^2 N(D)\, dD \tag{2.59}$$

$$\eta_V = 4\pi \int_0^{D_{max}} |S^b_{VV}(D)|^2 N(D)\, dD \tag{2.60}$$

$$\delta = arg(\int_0^{D_{max}} S^{b*}_{HH}(D) S^b_{VV}(D) N(D)\, dD) \tag{2.61}$$

$$\Delta k_H = \lambda \int_0^{D_{max}} S^f_{HH}(D) N(D)\, dD \tag{2.62}$$

$$\Delta k_V = \lambda \int_0^{D_{max}} S^f_{VV}(D) N(D)\, dD \tag{2.63}$$

$$|\rho_{HV}| = \frac{|\int_0^{D_{max}} S^f_{HH}(D) S^{f*}_{VV}(D) N(D)\, dD|}{\sqrt{\int_0^{D_{max}} |S^f_{HH}(D)|^2 N(D)\, dD \int_0^{D_{max}} |S^f_{VV}(D)|^2 N(D)\, dD}} \tag{2.64}$$

While it is customary for such analytic forms to integrate from 0 to ∞, this is not realistic, as there is a maximum size, D_{max}, above which drops will break up due to aerodynamic forces (Magarvey and Taylor 1956). A value of 1.0 cm is chosen here, which allows for a small number of large drops (depending on the actual drop size distribution). This limit both keeps the scattering calculation computationally tractable and eliminates contributions from non-realistic drops.

All of these calculations are performed for various values of temperature and microphysics parameters and written into lookup tables. This allows the calculations to be performed over the entire model domain much more rapidly than by calculating the scattering matrices at each grid point, especially in the case of T-matrix, which is the most computationally intensive of the scattering models. It should also be noted that one significant limitation is that the scattering calculations do not include mean canting at all–this includes the orientation of the particle relative to the radar beam as the radar points away from horizontal. To do this well would require adding the angle of

incidence of the radar beam relative to the axis of symmetry of the particles as another dimension for the lookup tables. This would make the memory requirements much larger as well as make the interpolation process take longer. While this is a significant limitation for simulating dual-polarization variables at high elevation angles, this is not significant for simulating data at low elevations, such as those used in radar QPE.

From the complex wavenumber perturbation, both the propagation phase shift (K) and attenuation (A) per unit range can be calculated:

$$K_H = 2\,\mathrm{Re}\,\Delta k_H \tag{2.65}$$

$$A_H = 4\,\mathrm{Im}\,\Delta k_H \tag{2.66}$$

$$K_V = 2\,\mathrm{Re}\,\Delta k_V \tag{2.67}$$

$$A_V = 4\,\mathrm{Im}\,\Delta k_V \tag{2.68}$$

Each value has a factor of 2 that converts it to a quantity representing the change over the two-way path. The attenuation terms have an additional factor of 2 that converts the attenuation from representing amplitude loss to representing a loss of power.

Drop Size Distributions Three different forms for drop-size distribution are permitted for calculating the integrals of (2.58) above: the (MP, Marshall and Palmer 1948) exponential distribution, the modified gamma distribution Ulbrich (1983), and the gamma distribution as used by Ziegler (1985). The choice of these distributions is motivated by the numerical simulation output that has been used to date. In order to generate the proper scattering fields, the drop size distribution needs to be calculated

at each model grid point, using the appropriate hydrometeor field. The MP distribution is given by:

$$N(D) = N_0 \exp(-\Lambda D) \tag{2.69}$$

where N_0 is the intercept parameter and has a value of $8000\,\mathrm{m}^{-3}\,\mathrm{mm}^{-1}$, D is the diameter in m, and Λ is the slope parameter in m^{-1}. Λ can be calculated from the model field rain concentration q_r:

$$\Lambda = \sqrt[4]{\frac{1000\,\pi\rho_l N_0}{q_r}} \tag{2.70}$$

where ρ_l is the density of liquid water ($1000\,\mathrm{kg\,m}^{-3}$) and the factor of 1000 converts N_0 to m^4.

The modified gamma distribution Ulbrich (1983) is given by:

$$N(D) = N_0 D^{\mu} \exp(-\Lambda D) \tag{2.71}$$

where μ is the so-called shape parameter. Note that in this case that N_0 has units that depend on μ and are different from those of the intecept parameter for the exponential distribution.

The gamma distribution of Ziegler (1985), henceforth called volume gamma, is given as follows:

$$N(V) = \frac{N(\nu+1)^{\nu+1}}{V_0\Gamma(\nu+1)} \left(\frac{V}{V_0}\right)^{\nu} \exp\left[-(\nu+1)\frac{V}{V_0}\right] \tag{2.72}$$

where ν is the shape parameter with a value of -0.8, V_0 is the mean drop volume, Γ is the Gamma function, and N is the number concentration, which is given by the numerical simulation. This can also be converted to terms of diameter instead of volume, making it more applicable to radar calculations:

$$N(D) = \frac{3N(\nu+1)^{\nu+1}}{D_0\Gamma(\nu+1)} \left(\frac{D}{D_0}\right)^{3\nu+2} \exp\left[-(\nu+1)\left(\frac{D}{D_0}\right)^{3}\right] \tag{2.73}$$

where D_0 is the mean drop diameter, rather than volume. The mean volume and diameter can be calculated from the simulation number concentration and rain concentration fields as:

$$V_0 = \frac{q_r}{\rho_l N} \tag{2.74}$$

$$D_0 = \sqrt[3]{\frac{6\, q_r}{\pi \rho_l N}} \tag{2.75}$$

Note that while this latter distribution is provided to maintain consistency with the numerical simulation input, its use in the calculation of radar observables is problematic. Figure 2.3 compares the volume gamma distribution with a modified gamma distribution, an exponential distribution, and a Marshal-Palmer distribution, all having the same total liquid water content, q_r. Additionally, with the exception of the Marshal-Palmer distribution, all have the same total number concentration. The volume gamma distribution shows a significant excess in the number of small drops, a lack of larger drops, and an overall character which does not match typical drop size distribution patterns. This has ramifications when calculating radar observables, especially Z_{DR}– the overabundance of small drops and lack of large drops would tend towards 0dB more than other distributions. This departure from a typical distribution shape results from its original formulation in terms of volume, which causes the cube of diameter to appear in the exponential; no set of coefficients for the modified gamma family of distributions for diameter can match this shape. The abundance of small drops, tending towards infinity as drop volume approaches 0, also creates problems when performing numerical integration of the distribution.

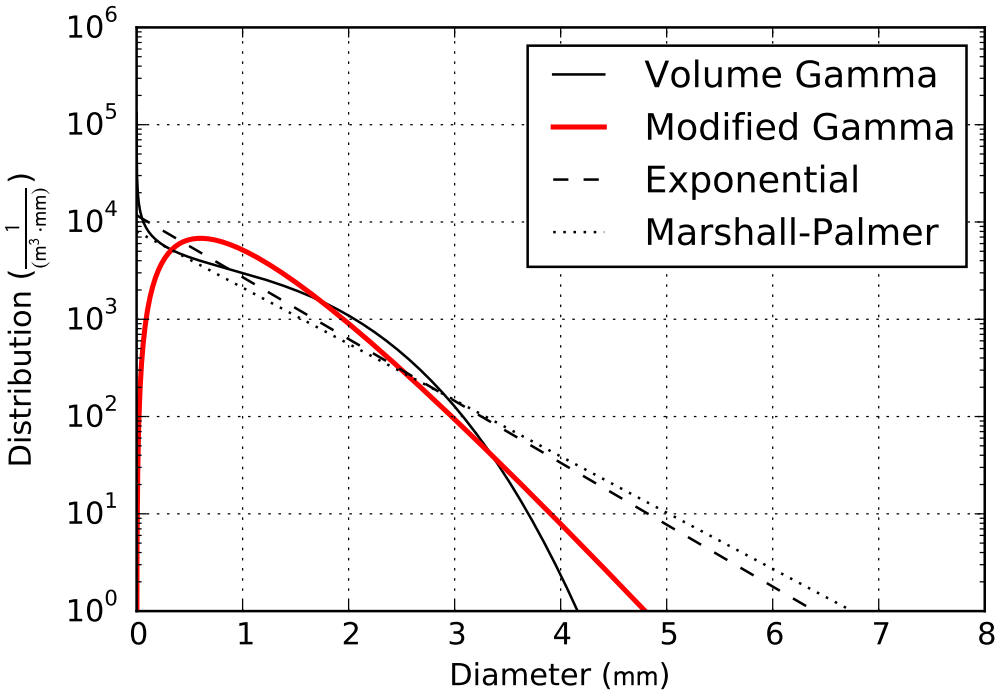

Figure 2.3: Comparison of drop size distributions as a function of diameter, D: Marshall-Palmer, dotted black line; Exponential, black dashed line; Volume Gamma, black solid line; Modified Gamma with fixed shape 1.8102, red solid line.

In order to address these shortcomings but also stay as consistent as possible with the original DSD shape used by the model (more complex shape than a simple exponential distribution), several attempts were made to fit the modified gamma distribution to the available parameters, N and q_r, which can be expressed in terms of the zeroth and third moments of the distribution, respectively. Starting from the expression for the moments of the modified gamma distribution:

$$\int_0^\infty N_0 D^n e^{-\Lambda D} dD = N_0 \Gamma(n+1) \Lambda^{-(n+1)} \tag{2.76}$$

and substituting for the zeroth and third moments yields:

$$N = \overline{D^0} \tag{2.77}$$

$$= N_0 \Gamma(1+\mu) \Lambda^{-(\mu+1)} \tag{2.78}$$

$$q_r = \frac{\rho_l \pi}{6} \overline{D^3} \tag{2.79}$$

$$= \frac{\rho_l \pi N_0}{6} \Gamma(4+\mu) \Lambda^{-(\mu+4)} \tag{2.80}$$

By taking the ratio of N and q_r the complex Γ functions (as well as N_0) can be eliminated:

$$\frac{q_r}{N} = \frac{\rho_l \pi}{6} (\mu+3)(\mu+2)(\mu+1) \Lambda^{-3} \tag{2.81}$$

In order to reduce this expression further, a set of constraints is needed to be able to calculate a unique set of distribution parameters from the model prognostic variables (this is an under-determined problem otherwise since there are three parameters but only two model variables).

One option for the constraint is the constrained gamma distribution of Zhang et al. (2001). This work demonstrated, using empirical data, that the value of shape of the distribution, μ, largely can be predicted using the slope, Λ:

$$\mu = -0.016\Lambda^2 + 1.213\Lambda - 1.957 \tag{2.82}$$

By substituting this into (2.81) above, a sixth order polynomial in Λ is obtained:

$$\begin{aligned} -4.096 \times 10^{-6}\Lambda^6 + 9.315\,84 \times 10^{-4}\Lambda^5 - 0.070\,592\,688\Lambda^4 + 1.779\,763\,33\Lambda^3 \\ +0.205\,717\,849\Lambda^2 - 1.206\,271\,49\Lambda - 0.042\,920\,493\,0 = \frac{6}{\rho_l \pi}\frac{q_r}{N}\Lambda^3 \end{aligned} \tag{2.83}$$

Solving this polynomial is problematic, since it potentially has six roots for a given q_r and N pair; fortunately, in practice, there are only up to two real, positive roots. This still leaves a problem of picking between one of two physically valid solutions. One possible strategy is to pick the value closest to a moderate value of Λ; we choose $10\,\mathrm{mm}^{-1}$ for illustration here, but others options tested include: maximum Λ, minimum Λ, closest to $10\,\mathrm{mm}^{-1}$, and closest to μ of 2, using (2.82). The value of 2 was chosen to reflect a representative value, chosen from the empirical data shown in Zhang et al. (2001).

Figure 2.4 shows the consequences of solving the sixth order polynomial to find the Λ value. While the other distributions (exponential, modified gamma with fixed shape, and volume gamma) show nearly identical distributions of radar reflectivity factor (calculated using a sample set of model liquid water content and number concentration), the constrained gamma distribution shows instead two distinct bands. It is likely that each of the two bands represent one of the families of roots being chosen from the two possible physical solutions to (2.83). This behavior is carried across all

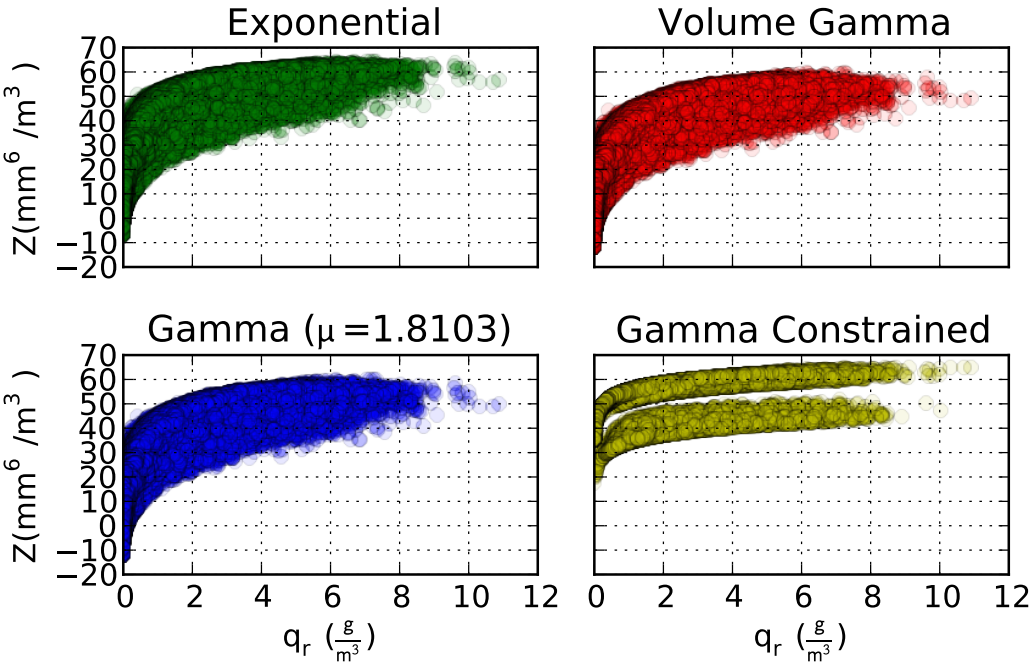

Figure 2.4: Comparison of radar reflectivity values calculated at X-band for different drop size distributions, using the same number concentration and liquid water content taken from sample model output. These distributions are: exponential distribution, upper left; volume gamma, upper right; modified gamma with fixed shape, lower left; gamma constrained, lower right.

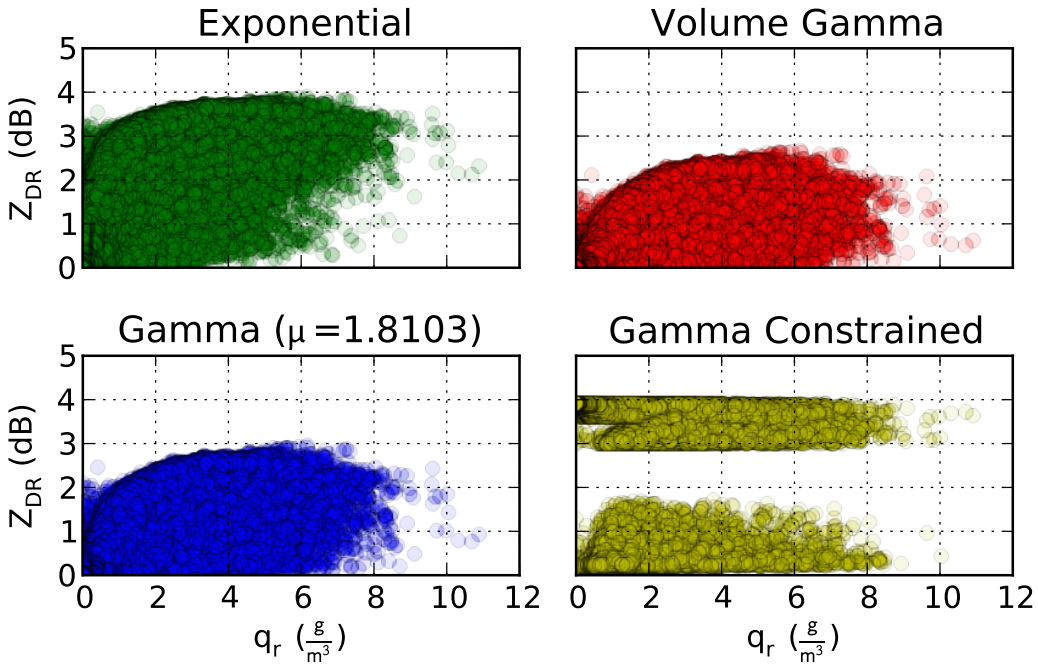

Figure 2.5: As in 2.4, but for calculated Z_{DR}.

of the moments: Z_{DR} (Figure 2.5), K_{DP} (Figure 2.6), A_H (Figure 2.7), and A_D (Figure 2.8). This behavior of two distinct bands of behavior is present regardless of the method used to choose between the two solutions, though the details of the bands do vary based on the method.

In light of the problems of using the $\Lambda - \mu$ relation of Zhang et al. (2001) to constrain the distribution, we chose instead to use the conservation of the sixth moment of the diameter distribution as the necessary constraint to allow calculating all three parameters of the distribution. This was chosen both because the combination of the zeroth, third, and sixth moments allows the math to be tenable and because conserving the sixth moment of the distribution is approximately the same as conserving the

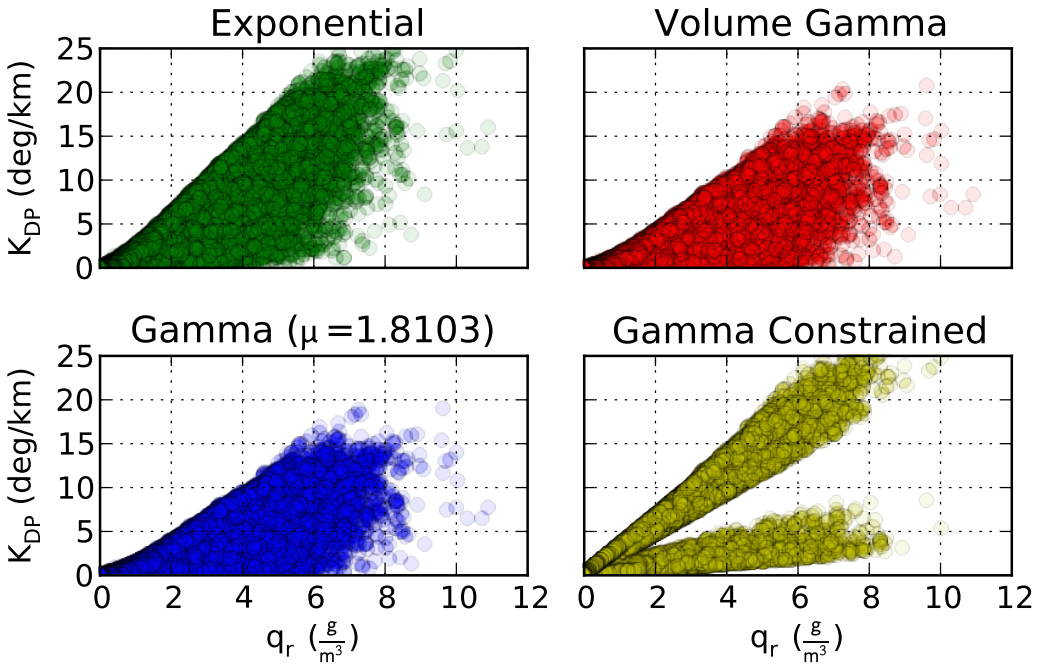

Figure 2.6: As in 2.4, but for calculated K_{DP}.

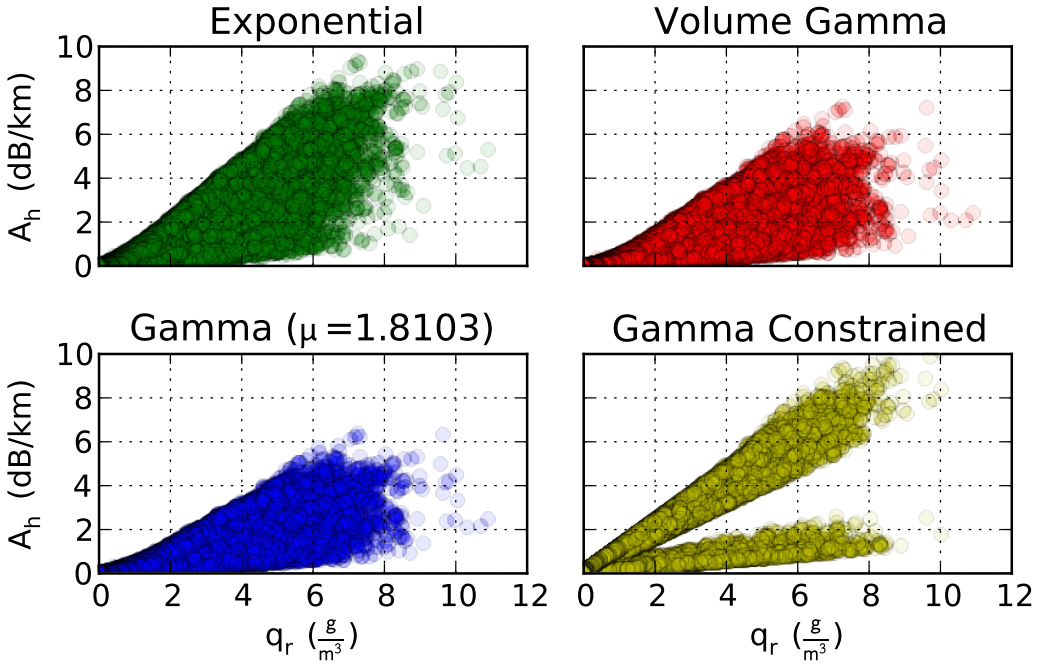

Figure 2.7: As in 2.4, but for calculated horizontal attenuation, A_H.

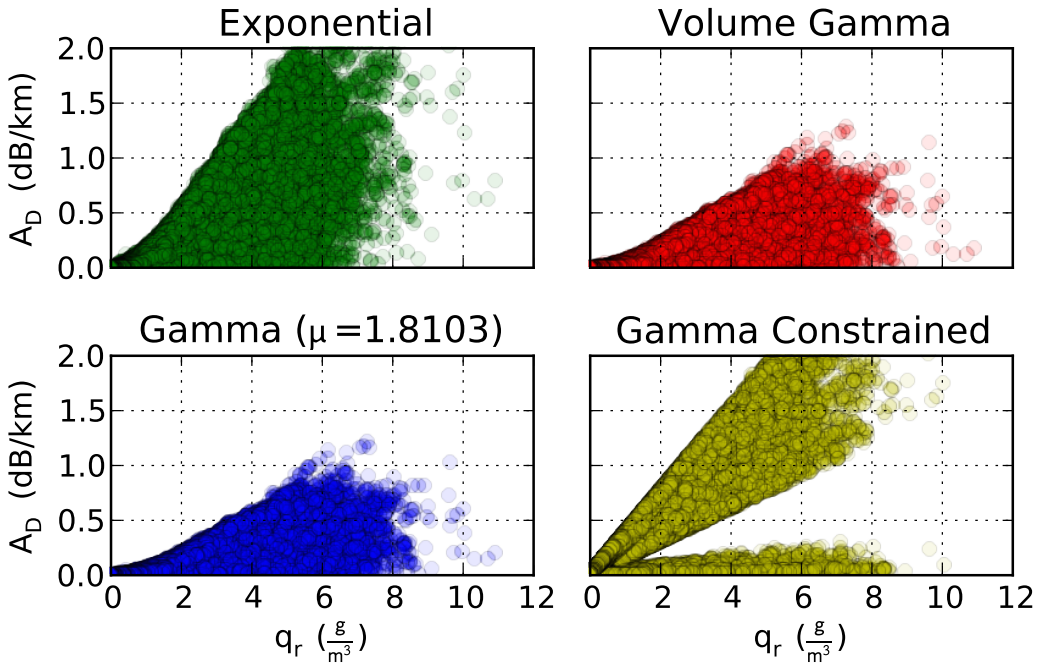

Figure 2.8: As in 2.4, but for calculated differential attenuation, A_D.

equivalent radar reflectivity factor (under the Rayleigh approximation). These three moments of the modified gamma distribution can be expressed as:

$$\overline{D^0} = N_0 \Gamma(\mu + 1) \Lambda^{-(\mu+1)} \tag{2.84}$$

$$\overline{D^3} = N_0 \Gamma(\mu + 4) \Lambda^{-(\mu+4)} \tag{2.85}$$

$$\overline{D^6} = N_0 \Gamma(\mu + 7) \Lambda^{-(\mu+7)} \tag{2.86}$$

In order to eliminate N_0 and Λ, these moments can be combined into a unitless ratio:

$$\frac{\overline{D^3}^2}{\overline{D^0}\,\overline{D^6}} = \frac{\Gamma(\mu + 4)\Gamma(\mu + 4)}{\Gamma(\mu + 1)\Gamma(\mu + 7)} \tag{2.87}$$

$$= \frac{(\mu + 3)(\mu + 2)(\mu + 1)}{(\mu + 6)(\mu + 5)(\mu + 4)} \tag{2.88}$$

In order to find a value for the left hand side of (2.88), we start by noting the following relation between the moments of the diameter distribution and the moments of the volume distribution

$$\overline{V^n} = \left(\frac{\pi}{6}\right)^n \overline{D^{3n}} \tag{2.89}$$

The relevant moments of the volume distribution from (2.72) above are:

$$\overline{V^0} = N \tag{2.90}$$

$$\overline{V^1} = NV_0 \tag{2.91}$$

$$\overline{V^2} = NV_0^2 \frac{\nu+2}{\nu+1} \tag{2.92}$$

Combining these with (2.89) yields the desired left hand side of (2.88):

$$\frac{\overline{D^3}^2}{\overline{D^0}\,\overline{D^6}} = \frac{\left(\frac{6}{\pi}\right)^2 (NV_0)^2}{N(\left(\frac{6}{\pi}\right)^2 NV_0^2 \frac{\nu+2}{\nu+1})} \tag{2.93}$$

which simplifies to:

$$\frac{\overline{D^3}^2}{\overline{D^0}\,\overline{D^6}} = \frac{\nu+1}{\nu+2} \tag{2.94}$$

Since ν is specified by the model (-0.8 here), this reduces (2.88) to a simple polynomial:

$$\frac{5}{6}\mu^3 + \frac{7}{2}\mu^2 - \frac{4}{3}\mu - 14 = 0 \tag{2.95}$$

This polynomial, fortunately, has only a single real root, $1.810\,283\,293\,877\,15$. Using this value for the shape parameter of the modified gamma distribution yields a distribution that matches the number concentration, liquid water content, and Rayleigh approximation radar reflectivity factor of the distribution of the model. Figure 2.9 provides evidence that this procedure works by comparing the liquid water content

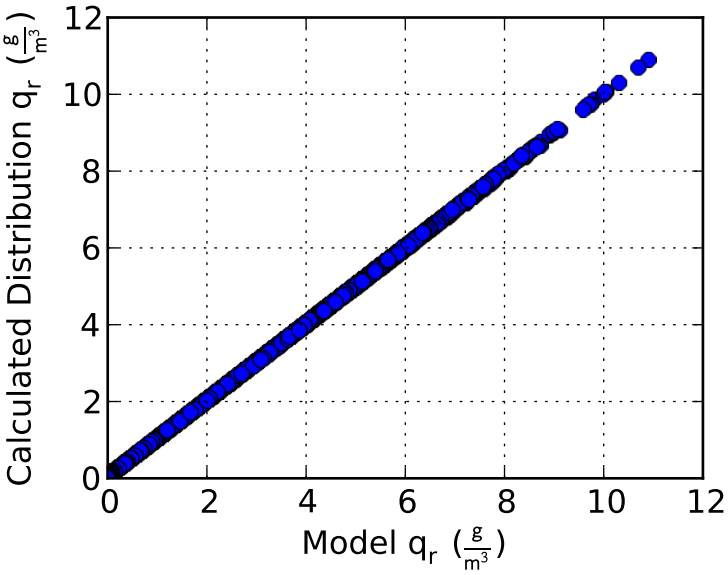

Figure 2.9: Comparison of liquid water content calculated from the fit modified gamma distribution with that of the original model. All values lie along the 1-1 line, indicative that the procedure works to conserve water content.

calculated from the fit distribution against that which was present in the original model output. All values lie along the 1-1 correspondence line, indicating that value used to calculate the parameters of the distribution are able to be retrieved again.

The improvement in the shape of the distribution obtained by using the modified gamma distribution is clear in Figure 2.3. By using this modified gamma distribution, the number of drops as a function of diameter has a subjectively better shape (c.f. Figure 2 in Ulbrich (1983)); the abundance of small drops is addressed, as is the lack of larger drops. Looking at the calculated dual-pol parameters, these changes to the distribution manifest in subtle ways. First, as shown in Figure 2.5, there is a $0.5\,$dB difference in peak Z_{DR} values; this is likely the product of shifting liquid water mass from small spherical drops to larger, aspherical drops. Both A_H (Figure 2.7) and K_{DP}

(Figure 2.6) have smaller values when using the modified gamma distribution as well. Z_H and A_D are relatively unaffected by changes between these distributions. Overall, this points to a sensitivity of the calculated moments to the drop size distribution; while not surprising, this does emphasize the importance of using a distribution that best matches real world observations. In this case, reality much better reflects the modified gamma distribution for diameter rather than the volume gamma distribution.

2.1.2.2 Atmospheric refractive index

To allow ray tracing of the radar pulse propagation path, the index of refraction is calculated from the model temperature, T, water vapor pressure, e, and air pressure, p, using the relation (Bean and Dutton 1966, chap. 1)

$$n = \left(\frac{C_d p}{T} + \frac{C_{w1} e}{T} + \frac{C_{w2} e}{T^2} \right) \times 10^{-6} + 1 \tag{2.96}$$

where C_d, C_{w1}, C_{w2}, have values $0.776\,\mathrm{K\,Pa^{-1}}$, $0.716\,\mathrm{K\,Pa^{-1}}$, and $3.7 \times 10^3\,\mathrm{K^2\,Pa^{-1}}$, respectively.

2.1.2.3 Radial velocity

To simplify calculations and reduce run-time memory requirements, the u, v, and w wind components are reduced to a radial velocity value based on the known location of the radar relative to the model grid. The radial velocity, V_r, is calculated by the projection of the total wind velocity vector onto the radar beam:

$$V_r = (u \sin\theta + v \cos\theta) \cos\phi + (w - w_t) \sin\phi \tag{2.97}$$

where u is the x-component of the wind, v is the y-component of the wind, w is the z-component of the wind, w_t is the average terminal fall speed for the hydrometeors, θ

is the azimuth angle measured clockwise from north, and ϕ is the elevation angle. The average hydrometeor terminal fall speed for the grid box is calculated as a backscatter cross-section-weighted average given by:

$$w_t = \eta^{-1} \int_0^{D_{max}} \sigma_b(D) V_t(D) N(D)\, dD \tag{2.98}$$

where η is the total reflectivity at the grid point, $\sigma_b(D)$ is the backscatter cross-section, and $V_t(D)$ is the terminal fall speed as a function of diameter, which is calculated using the fit of Brandes et al. (2002):

$$w_t(D) = -0.1021 + 4.932D - 0.9551D^2 + 0.079\,34D^3 - 2.362 \times 10^{-3} D^4 \tag{2.99}$$

By using a backscatter cross-section-weighted mean, the terminal velocity better reflects that which would be observed by the radar.

2.1.3 Sampling of input fields

To sample the virtual model atmosphere, the simulator calculates radar observables along the path of individual pulses at the interval specified by the pulse repetition time (PRT). This allows the input model fields, as well as the state of the radar (such as antenna pointing angle) to change for individual pulses. While the simulator is currently configured for a mechanically scanning antenna, pulse-by-pulse calculation can be used to simulate measurements for a phased-array radar as well. The pulse generated within the simulator defines the volume of space that contributes to a sample taken along the radar beam. It is bound in elevation and azimuth by a fixed multiple of the half-power beamwidth. This multiple is chosen based on the number of sidelobes that are desired for simulation in the antenna pattern. The pulse is bound in range

by the specified pulse length. This volume of space is subdivided into individual pulse elements, such that, at the maximum range from the radar, the dimensions of each pulse element are ten percent smaller than the model grid voxel at that range–ensuring that the pulse element spacing is always finer than the model grid spacing in any direction.

The pulse itself is propagated through the numerical grid using a ray-tracing technique. For each range gate, the height of each horizontal slice of pulse elements is determined separately by taking into account the atmospheric index of refraction experienced by that particular ray element. This allows for differential propagation across the vertical plane of the radar beam. Since any part of the pulse that encounters the ground stops propagating, this allows for partial beam blockage. This is more useful if terrain data are available rather than the uniform ground level present in most model simulations. The change in the height above ground, Δh, and change in range from the radar (along the surface of the Earth), Δr, can be calculated from the incremental change in range along the path, Δs, as

$$\Delta h = \sqrt{h^2 + \Delta s^2 + 2h\Delta s\sqrt{1 - \frac{C^2}{n^2 h^2}}} \tag{2.100}$$

$$\Delta r = a \arcsin\left(\frac{C\Delta s}{nh(h + \Delta h)}\right) \tag{2.101}$$

$$C = n_0 a \cos\phi \tag{2.102}$$

where a is the radius of the earth, h is the previous height of the element above ground, n is the index of refraction at height h, n_0 is the index of refraction at the radar, and ϕ is the initial elevation angle of the element (Doviak and Zrnić 1993). The element's range from the radar along the surface of the earth is then converted to standard two-dimensional Cartesian coordinates, which are used to determine the location of the element on the model grid.

The pulse volume is allowed to propagate through the environment as far as twice the unambiguous range, R_a,

$$R_a = \frac{cT_s}{2} \tag{2.103}$$

where T_s is the PRT and c is the speed of light. Allowing the pulse to propagate $2R_a$ from the radar means that after one PRT from the time the radar is started there are two pulses propagating through the model field at any given instant. When a sample is taken, the returns from both pulses are assigned to the gate, producing the effects of range aliasing.

During propagation, each pulse element is assigned values of attenuation, propagation phase shift, reflectivity, and backscatter phase shift for both horizontal and vertical polarizations, as well as values for radial velocity and co-polar cross-correlation coefficient. These values correspond to the grid point nearest to the element's location in space. Nearest neighbor sampling is chosen over trilinear (or other more sophisticated) interpolation to improve the computational efficiency of the simulator. Since the pulse elements are generally much smaller than the grid cells, this sampling method provides sufficient accuracy. The entire pulse volume is stepped forward in range while keeping track of the total attenuation and propagation phase shift along the path, for both polarizations. This running total is kept for each pulse element, which allows for the calculation of differential (in a geometric sense, not polarimetric) attenuation and phase shift across the pulse.

2.1.4 Sampling the pulse

As the pulse is propagated through the model grid of the simulated atmosphere, it is periodically sampled at an interval in range dictated by the specified gate spacing. This allows for the gate and pulse lengths to be independent. When a pulse sample is taken, two main processes happen: time series data are generated and pulse averaged values are calculated.

2.1.4.1 Time series generation

Time series data are generated by combining the approaches used by Muschinski et al. (1999) and Galati (1995); Torres and Zrnić (2003). The core of the procedure is to simulate radar returns for a volume of space by treating each element of the discretized pulse as a "scattering center" Muschinski et al. (1999) and assigning it a random, complex signal value.

The complex values from every pulse element are summed together and added to a complex random noise value to generate a single IQ sample (V) for the range gate for both horizontal and vertical polarization:

$$V_{h,v} = A_N e^{-j\theta_N} + \sum_k A_{k(h,v)} \tag{2.104}$$

where A_N is the noise amplitude, θ_N is the noise phase, and A_k is the complex signal amplitude of the k^{th} pulse element. A_N is calculated as the square root of a random value of noise power, which is generated from an exponential distribution with an expected value equal to the configured radar noise power (chosen to be the same as the minimum detectable signal). θ_N is randomly generated uniformly between $[0, 2\pi]$.

To control the correlation between the two polarizations, the value of the co-polar cross-correlation coefficient for the pulse element is used. This value is used as the expected value for the cross-correlation between the horizontal and vertical channels, and is used to combine two independent samples, w_1 and w_2, from a white, complex Gaussian distribution Galati (1995):

$$A_{kh} = \sqrt{P_{kh}} w_{1k} e^{-j\theta_k} \tag{2.105}$$

$$A_{kv} = \sqrt{P_{kv}} \left(\rho_{HVk} w_{1k} + \sqrt{1 - \rho_{HVk}^2} w_{2k} \right) e^{-j\theta_k} \tag{2.106}$$

$$\theta_k = \theta_k^n + \delta_k + \phi_k \tag{2.107}$$

$$\theta_k^n = \theta_k^{n-1} + \frac{4\pi V_{rk} T_s}{\lambda} \tag{2.108}$$

$$\theta_k^0 = 0 \tag{2.109}$$

where P_{kh} and P_{kv} are the horizontal and vertical power, θ_k^n is the initial phase for the current pulse n, δ_k is the backscatter phase shift, ϕ_k is the propagation phase shift, and the term involving V_{rk} (the radial velocity for the pulse element) represents the Doppler phase shift (due to moving scatterers). δ_k and ϕ_k are those appropriate for the pulse element being calculated. The phase of w_1 and w_2 for each pulse element is kept constant. This allows each individual pulse element to have a uniformly distributed random initial phase and to track the total phase shift due to the motion of scatterers (Muschinski et al. 1999). This approach for controlling the correlation of the horizontal and vertical channels assumes that each polarization has the same sample-time auto-correlation function and that the cross-correlation function is just the cross-correlation coefficient times the autocorrelation.

The horizontal and vertical powers are calculated as:

$$P_k = \frac{P_t g^2 \lambda^2 f^4(\theta_k, \phi_k) |W(r_0, r)|^2 \eta_k}{(4\pi)^3 l_k^2(r) r^2} \Delta r \sin\phi_k \, \Delta\phi \, \Delta\theta \tag{2.110}$$

where P_t is the transmitted power, g is the system gain, λ is the wavelength, r is range from the radar, l_k^2 is the two-way attenuation factor, f^2 is the normalized, one-way antenna pattern, θ_k is the azimuth angle relative to the beam center, ϕ_k is the elevation angle relative to beam center, η_k is the reflectivity (backscattering cross section per unit volume), and W is the range weighting function. Δr, $\Delta\phi$, and $\Delta\theta$ represent the spacing between pulse elements in range, elevation, and azimuth, respectively. This expression comes from making a discrete approximation to the integrand given by Doviak and Zrnić (1993), where the power, P, for a sample taken at range r_0 is given by:

$$P(r_0) = \iiint_V \eta(r) I(r_0, r) \, dV \tag{2.111}$$

where

$$I(r_0, r) = \frac{P_t g^2 \lambda^2 f^4(\theta, \phi) |W(r_0, r)|^2}{(4\pi)^3 l^2(r) r^4} \tag{2.112}$$

$$dV = r^2 \, dr sin(\phi) \, d\phi \, d\theta \tag{2.113}$$

All random values are generated using the Mersenne Twister pseudorandom number generator (Matsumoto and Nishimura 1998). This generator is chosen because it produces high-quality pseudorandom numbers with good run time performance and has readily available source code.

The simulator assumes a Gaussian range weighting function and a normalized antenna pattern with the following form (Doviak and Zrnić 1993, chap. 3)

$$f^2(\theta) = \left(\frac{8 J_2((\pi D_a \sin\theta)/\lambda)}{((\pi D_a \sin\theta)/\lambda)^2} \right)^2 \tag{2.114}$$

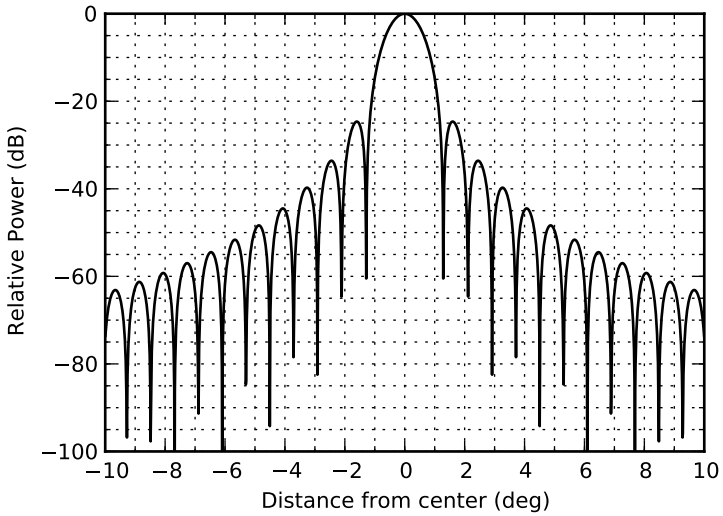

Figure 2.10: Simulator antenna pattern for a one-degree half-power beamwidth radar.

where J_2 is the second-order Bessel function of the first kind, θ is the angular offset from boresight and D_a is the diameter of the antenna. D_a for (2.114) above can be calculated from the half-power beamwidth, θ_1, as

$$D_a = \frac{1.27\lambda}{\theta_1} \tag{2.115}$$

where λ is the wavelength. Doviak and Zrnić (1993) state that (2.114) describes the antenna pattern for the first few sidelobes quite well for a parabolic antenna. However, it is limited in that it gives sidelobes of a fixed level and location (c.f. Figure 2.10), prohibiting configuration of sidelobes with arbitrary magnitude.

2.1.4.2 Pulse averaged values

Pulse averaged values are a way to generate a single data value for the pulse to represent a radar observable. These averages include the antenna and range weighting functions, as well as reflectivity weighting where appropriate. These are useful for inter-comparison with the time series data, as they are not contaminated with noise or

other artifacts that occur with IQ-based estimates. Consequently, they are useful for generating moments for use as truth fields representing the best case for radar observations. They are also useful if time-series data generation is not desired and the simpler averages give sufficient realism for the application.

Several values are calculated currently: power ($\overline{P}$, both horizontal and vertical), power-weighted average radial velocity ($\overline{V_r}$), power-weighted radial velocity variance (σ_{vr}), power-weighted average $\overline{K_{DP}}$, and power-weighted differential backscatter phase ($\overline{\delta_{hv}}$). The power-weighting for the latter two variables only include antenna and range weighting. $\overline{K_{DP}}$ is treated differently because it is a propagation-based variable. $\overline{\delta_{hv}}$ is so weighted because its use is not intended as true moment data, but rather as a diagnostic tool to see what areas might be impacted by its presence. Thus, only a representative average is needed. The power-weightings are performed over all of the pulse elements as follows, where P_k is as in (2.110):

$$\overline{P} = \sum_k P_k \tag{2.116}$$

$$\overline{V_r} = \frac{\sum_k P_k V_{rk}}{\overline{P}} \tag{2.117}$$

$$\sigma_{vr} = \frac{\sum_k P_k V_{rk}^2}{\overline{P}} - \overline{V_r}^2 \tag{2.118}$$

$$\overline{K_{DP}} = \frac{\sum_k f^4(\theta_k, \phi_k)|W(r_0, r)|^2 (K_{Hk} - K_{Vk})}{\sum_k f^4(\theta_k, \phi_k)|W(r_0, r)|^2} \tag{2.119}$$

$$\overline{\delta_{hv}} = \frac{\sum_k f^4(\theta_k, \phi_k)|W(r_0, r)|^2 (\delta_{Hk} - \delta_{Vk})}{\sum_k f^4(\theta_k, \phi_k)|W(r_0, r)|^2} \tag{2.120}$$

where quantities with the k subscript represent those for the k^{th} pulse element.

2.1.5 Moment calculation

The sampling of model data is repeated for the number of pulses that are to be averaged for a radial of data, as specified by the scanning strategy. Moment data (horizontal and vertical power, Doppler velocity, Doppler spectrum width, specific differential phase, and backscatter differential phase) are then generated at each range gate along the radial. Power, specific differential phase, and backscatter differential phase are calculated as the average of all their respective samples for the specified number of pulses at that range gate. Radial velocity is calculated as the power-weighted average of all velocity samples (one per pulse) at that range gate. To simulate velocity aliasing, this average is restricted to a value within the Nyquist interval and is given by:

$$V_a = V_r + 2nV_{NYQ} \tag{2.121}$$

where

$$n = \begin{cases} 0 & \text{for } |V_r| <= V_{NYQ} \\ \frac{V_{NYQ}-V_r}{2V_{NYQ}} - 1 & \text{for } V_r > V_{NYQ} \\ 1 - \frac{V_{NYQ}+V_r}{2V_{NYQ}} & \text{for } V_r < -V_{NYQ} \end{cases} \tag{2.122}$$

where V_a is the aliased velocity value, V_r is the original (unaliased) radial velocity, V_{NYQ} is the Nyquist (or aliasing) velocity, and n, an integer, is the number of Nyquist intervals by which the V_a differs from V_r. One advantage of simulated data is that the unaliased Doppler velocity is known and can be output as well. This is useful for testing dealiasing algorithms or when one wishes to eliminate velocity aliasing from the problem under consideration.

Spectrum width is calculated as the square root of the power-weighted average of the variance for each sample, which is the variance of all velocity values within

the pulse. Initial attempts at simulating spectrum width used only the variance of the individual velocity samples that were themselves an average over the entire pulse. That approach yielded unreasonably low spectrum width values. By taking into account the variance of all velocity values within all pulses, the spectrum width reflects the effects of antenna rotation and wind shear across the radar beam; however, the sub-grid scale atmospheric turbulence is neglected. Moreover, since this method does not use a true power spectrum at each range gate, this simulated spectrum width does not take into account a limited Nyquist interval. This option exists as a holdover from an earlier version and it is recommended to use spectrum width values generated from time-series data as they will be much more representative of real-world behavior.

In addition to the moments above, equivalent reflectivity factor (Z_e) is calculated from the average power using:

$$Z_e = \frac{2^{10} \ln 2 \lambda^2 r^2 \overline{P_r}}{\pi^3 P_t g^2 \theta_1^2 c\tau |K_W|^2} \tag{2.123}$$

where τ is the pulse duration.

To estimate moments from time series data, the standard autocorrelation-based methods are used. The single polarization moments, power ($\hat{P}$), mean Doppler velocity ($\hat{V}_r$), and Doppler spectrum width ($\hat{\sigma}_v$) are calculated as (Bringi and Chandrasekar 2001, chaps. 5 and 6):

$$\hat{R}(l) = \sum_{n=0}^{N-l-1} V(n+l)V^*(n) \tag{2.124}$$

$$\hat{P} = \hat{R}(0) \tag{2.125}$$

$$\hat{V}_r = \frac{-\lambda}{4\pi T_s} \arg \hat{R}(1) \tag{2.126}$$

$$\hat{\sigma}_v = \frac{\lambda}{2\pi T_s \sqrt{2}} \left[\ln \left| \frac{\hat{R}(0)}{\hat{R}(1)} \right| \right]^{\frac{1}{2}} \tag{2.127}$$

where $\hat{R}(l)$ is the autocorrelation at lag l. The dual-polarization moments are estimated as (Bringi and Chandrasekar 2001, chaps. 5 and 6):

$$\hat{R}_{v,h}(l) = \sum_{n=0}^{N-l-1} V_v(n+l)V_h^*(n) \tag{2.128}$$

$$\hat{Z}_{DR} = \frac{\hat{P}_h - \hat{N}_h}{\hat{P}_v - \hat{N}_v} \tag{2.129}$$

$$|\hat{\rho}_{co}| = \frac{|\hat{R}_{v,h}(0)|}{\sqrt{\hat{P}_h \hat{P}_v}} \tag{2.130}$$

$$\hat{\phi}_{DP} = \arg \hat{R}_{v,h}(0) \tag{2.131}$$

where $\hat{R}_{v,h}(l)$ is the co-polar cross-correlation and $\hat{N}_h$ and $\hat{N}_v$ are noise power estimates for the horizontal and vertical channels, respectively. The simulator's configured noise power is used for these values, which represents a best case scenario. In addition, K_{DP} is calculated as:

$$\hat{K}_{DP}(r) = \frac{\hat{\phi}_{DP}(r + \Delta r) - \hat{\phi}_{DP}(r - \Delta r)}{2\,\Delta r} \tag{2.132}$$

which is a centered-difference approximation to the 1^{st} derivative of $\hat{\phi}_{DP}$. This approach is chosen purely for ease of implementation to demonstrate the generation of $\hat{K}_{DP}$ data. Such estimates are not used in practice (and will not be used in future work) because the discrete difference amplifies the noise in the original data.

2.2 Demonstration

Simulated data were generated for different radar characteristics to illustrate the simulator's capabilities to simulate dual-polarization radar data as a function of radar wavelength. The source simulation used as input is a COMMAS model simulation of multicell convection. The COMMAS model is a storm-scale model that includes prognostic

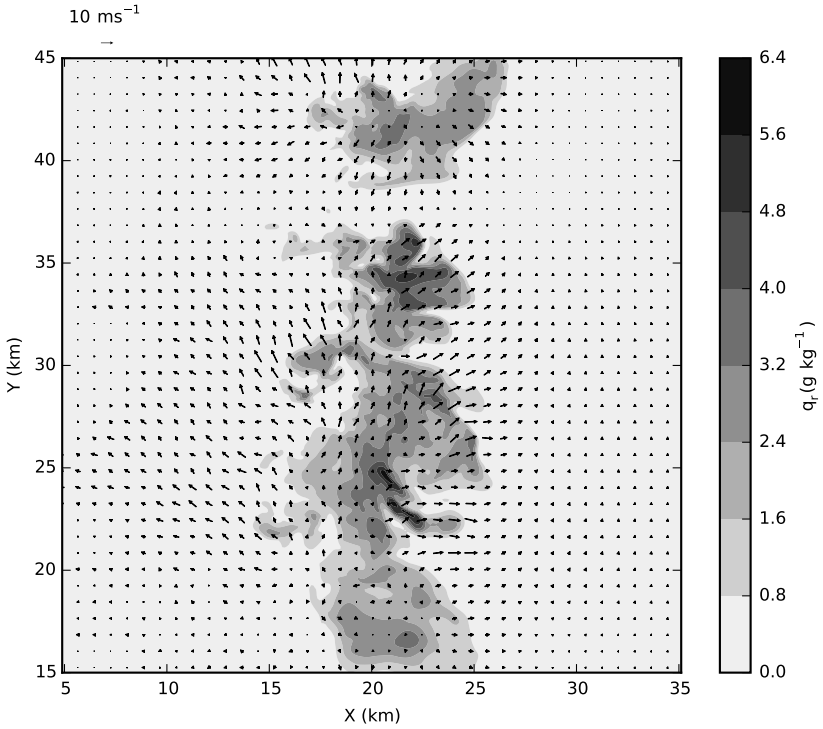

Figure 2.11: Rain water content, shaded contours, and horizontal wind, vectors, for the COMMAS simulation used to produce the sample datasets.

equations for momentum, pressure, potential temperature, and turbulent kinetic energy (Wicker and Wilhelmson 1995). This particular simulation was run on a grid with a uniform spacing of 100 m in x, y, and z, initialized using a series of buoyancy perturbations. The microphysics are a modified version of those described by Ziegler (1985), but include only liquid-phase hydrometeors. The simulated data here rely on a single time step 3600 s from the start of the simulation. A plot of the winds and rain concentration from 350 m AGL is shown in Figure 2.11.

Note that all radar simulations that follow were run using the same random number seed, 4346. This reduces variations due to different realizations of the sequence of random numbers in the Monte Carlo simulation. In fact, if the same number of

Antenna gain	45.5 dB
Peak power	250 kW
First range gate	500 m
Noise power	−113 dBm
Elevation	0.5°
PRT	0.667 ms
Rotation Rate	20 ° s^{-1}
Pulses per radial	75
Gate length	125 m
Antenna Limits	Main-lobe only

Table 2.2: Radar and scanning parameters common to the example simulations.

Experiment	C	CBW	CRW	S	X
Wavelength	5 cm	5 cm	5 cm	10 cm	3.21 cm
Beamwidth	1.0°	2.0°	2.0°	1.0°	1.0°
Radial Spacing	1.0°	1.0°	2.0°	1.0°	1.0°

Table 2.3: Parameters of note for the example simulations

random numbers are used (affected by number of pulses and number of sub elements in a pulse), there are no differences in the simulated output due to the Monte Carlo simulation. Table 2.2 lists the common parameters used to define the radar and scanning strategy for the examples that will be shown. The capabilities highlighted here focus on broad scale changes to radar capabilities: wavelength, beamwidth, antenna pattern, and radial size. The parameters varying across these examples are outlined in Table 2.2. The following sections examine the results from these simulations and

highlight features that capture effects observed in real-world data.

2.2.1 Wavelength

The experiments S, C, and X highlight the differences at these different respective wavelengths. The base configuration is for a typical radar with a 1.0° two-way $3\,$dB beamwidth, transmitting $250\,$kW of peak power.

At S-band, the horizontal reflectivity factor (Z_H) in Figure 2.12 shows a mutli-cell storm complex. The Doppler velocity field shows two distinct areas of surface divergence, evidenced by the couplets of in-bound, and then out-bound, velocities as one moves down the radial away from the radar. Looking at the PPI of horizontal attenuation, there is a peak in total attenuation of about $2.5\,$dB. Turning to the dual-polarization moments in Figure 2.13, the Z_{DR} field agrees well with that of Z_H, with higher values of Z_{DR}, indicative of more oblate drops, co-located with higher reflectivity values. For most of the area of weather signal, the values of Z_{DR} range from $0\,$dB to $2.5\,$dB. At the far range from the radar (along 0° azimuth), there are some negative values of Z_{DR}; these are not representative of intrinsic values from the precipitation particles, but rather are caused by differential attenuation. This is validated by panel (d) in Figure 2.13, where the A_D field shows a peak value of approximately $0.5\,$dB of attenuation. Along with the Z_{DR} field, the ρ_{HV} and Φ_{DP} fields look as typical for weather. The ρ_{HV} values are very close to 1.0 for the weather, with small departures, as low as 0.99. The Φ_{DP} field shows an overall monotonic increase with range from the radar.

Figure 2.14, for comparison, shows the same fields as Figure 2.12, but for a radar operating at C-band. Since the wind field in this multi-cell complex is relatively weak,

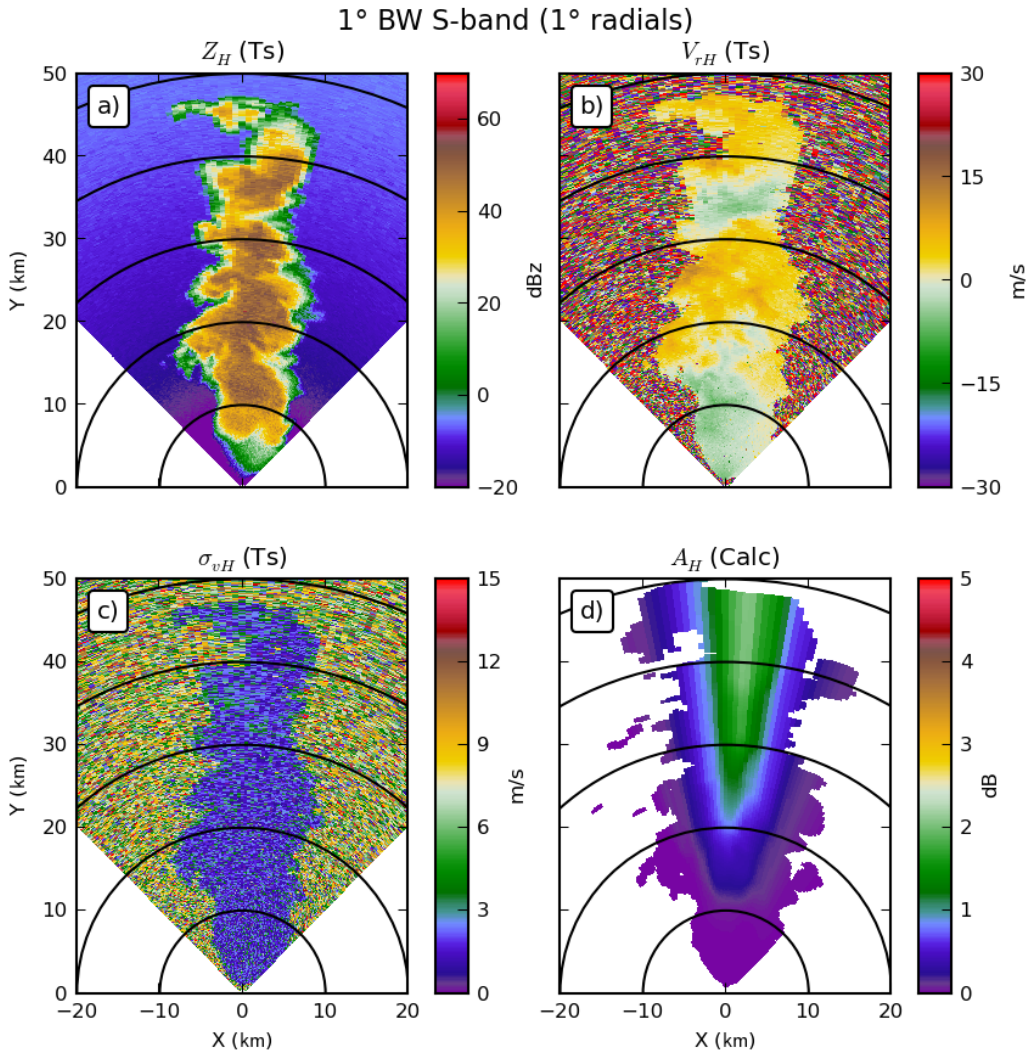

Figure 2.12: Plan Position Indicators (PPI) of the basic moment data for the base S experiment: (a) Horizontal Reflectivity Factor (Z_H) (b) horizontal Doppler velocity (V_{RH}) (c) horizontal Doppler spectrum width (σ_{vH}) (d) horizontal attenuation (A_H)

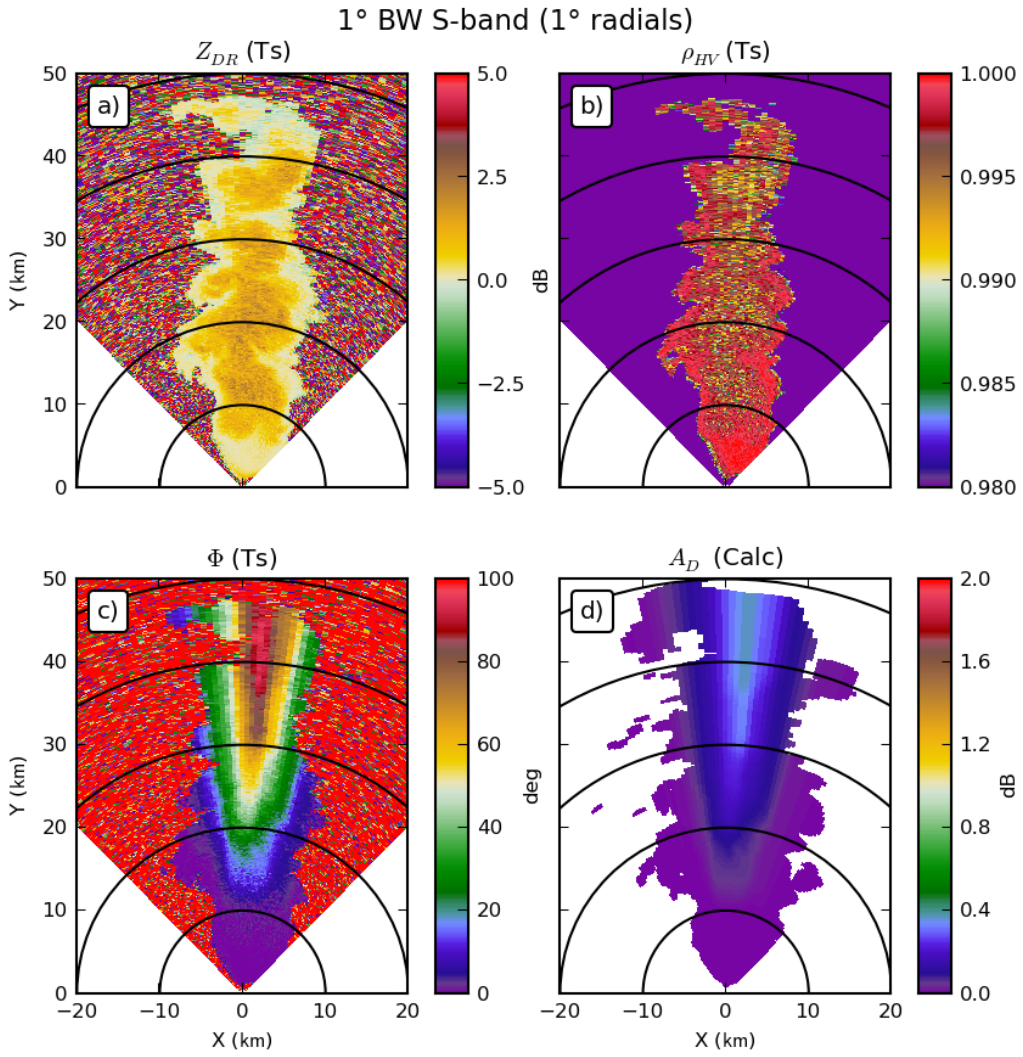

Figure 2.13: Plan Position Indicators (PPI) of the dual-polarization moment data for the S experiment: (a) Differential Reflectivity Factor (Z_{DR}) (b) differential phase (Φ_{DP}) (c) co-polar cross-correlation coefficient (ρ_{HV}) (d) differential attenuation (A_D)

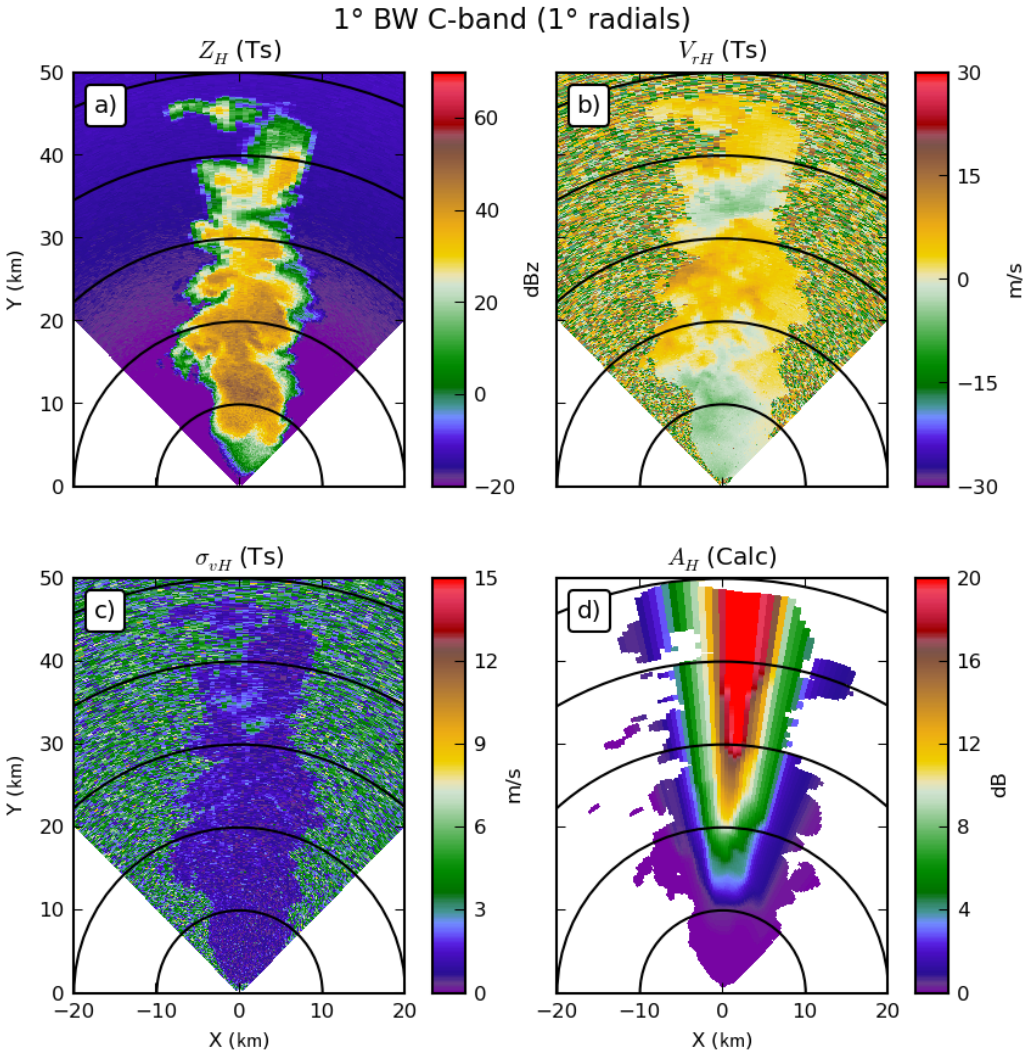

Figure 2.14: As in Figure 2.12, but for the C experiment.

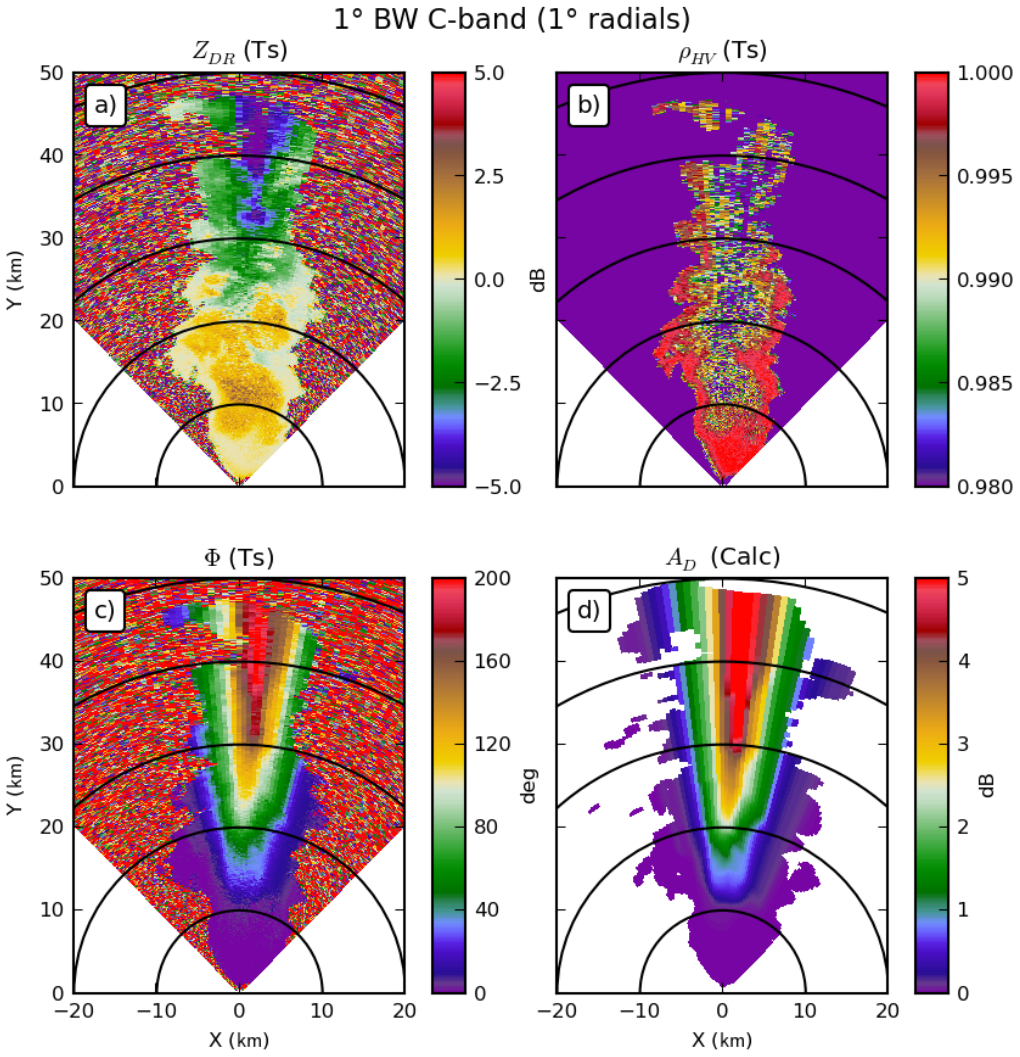

Figure 2.15: As in Figure 2.13, but for the C experiment.

the Doppler fields show no significant differences from those at S-band. However, the reflectivity field at C-band shows a pronounced decrease in intensity with range when compared to that for S-band. This is an effect of attenuation, which panel (d) in Figure 2.14 shows is over 20 dB. For the dual polarization moments, shown in Figure 2.15, the most prominent difference is the presence of differential attenuation, which is over 5 dB for a significant portion of the data around 0° azimuth. This greatly degrades the quality of the Z_{DR} data, which now drops to negative values beyond 10 km range. The ρ_{hv} field also shows some differences, with values around 0.98 within the weather. Much of this decrease is caused by noise biasing the ρ_{hv} estimates where attenuation has decreased the signal intensity. The PPI of Φ_{DP} also shows the impact of changing wavelength, where the peak values have doubled from 100° at S-band to 200° at C-band, which is consistent with scattering theory.

At X-band, the single polarization moments (Figure 2.16) show very large differences from S-band due to the effects of attenuation. The PPI of Z_H shows a swath of data along 0° azimuth where the signal is completely extinguished; the calculated attenuation in this region is up to 100 dB. As a result, the Doppler velocity and spectrum width moment data in this same region are unavailable, with only noise being detected. In Figure 2.17, the dual-polarization moment data also show the effects of increased attenuation. The field of Z_{DR} is almost entirely negative, owing to differential attenuation, which has a peak value of 16 dB. The field of Φ_{DP}, where the signal has not been extinguished, shows a peak of 250°.

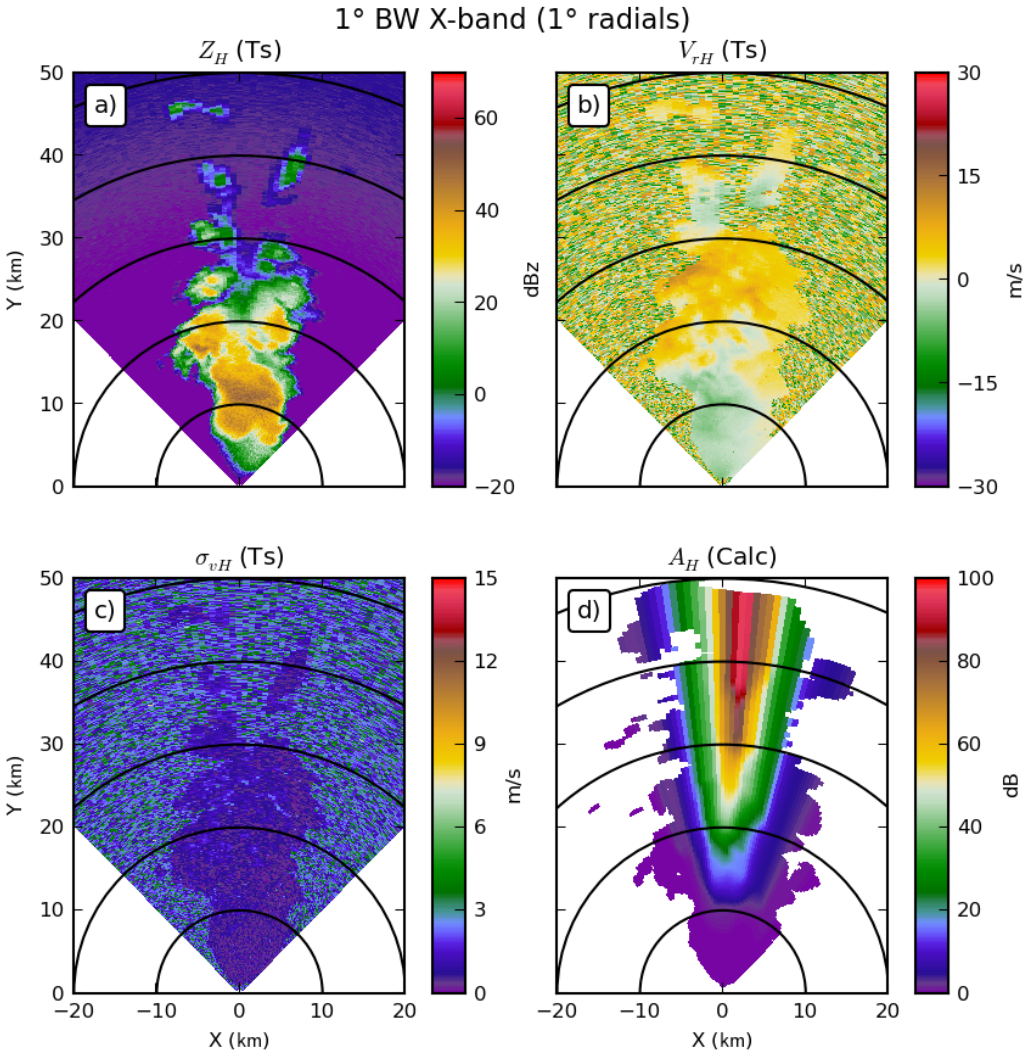

Figure 2.16: As in Figure 2.12, but for the X experiment.

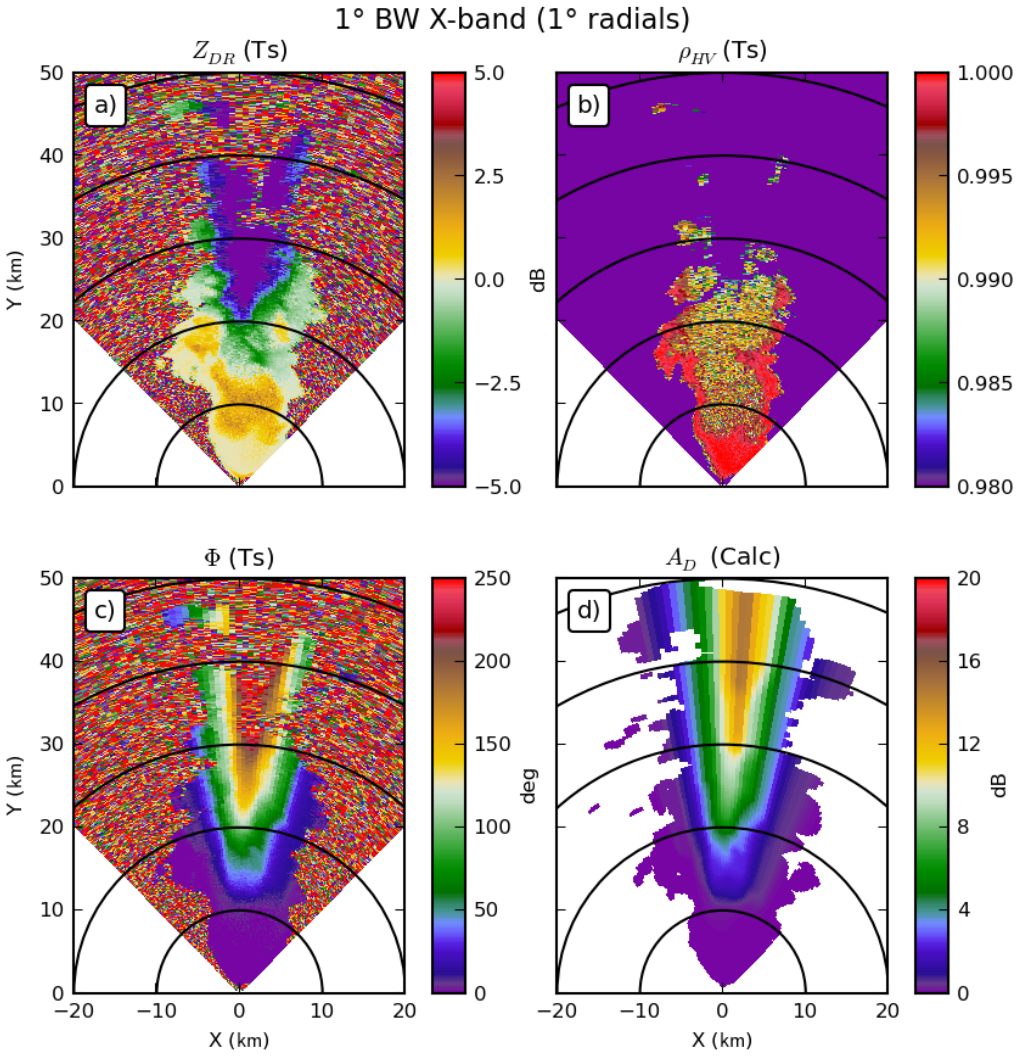

Figure 2.17: As in Figure 2.13, but for the X experiment.

2.2.2 Antenna

To demonstrate the impacts of changing antenna configuration, the configuration described as CBW in Table 2.3 changes the configured width of the mainlobe to 2°, while keeping the azimuthal sampling interval of the data at 1°.

Figure 2.18 shows the impact of this configuration change on the single polarization data, which is to smear the data across radials. This effect is most visible at the edges of the mutli-cell complex, where the change in beamwidth causes the apparent azimuthal extent of the complex to increase. One can also see areas of weak reflectivity in the original data (Figure 2.14) that are filled with larger values in the data taken with a larger beamwidth. The dual-polarization moments (Figure 2.19) show similar effects with regard to smearing. The ρ_{hv} data also show values with decreased magnitude as a result of the larger sampling volume.

2.2.3 Sampling

The last of the demonstration cases considered here examines changing the azimuthal sampling interval, independent of beamwidth, as specified by the CBW experiment. This experiment modifies the sampling width by just doubling the number of samples used to calculate the data for a radial, from 75 to 150; this changes the azimuthal sampling interval from 1.0° to 2.0°. For this configuration, the 2° beamwidth from the CBW experiment has been kept, so that these data have matching sampling interval and beamwidth. Figure 2.20 shows the single-polarization moment data for this configuration, while Figure 2.21 shows the dual-polarization data. Compared to the data for the CBW experiment shown in the previous section, these data generally look

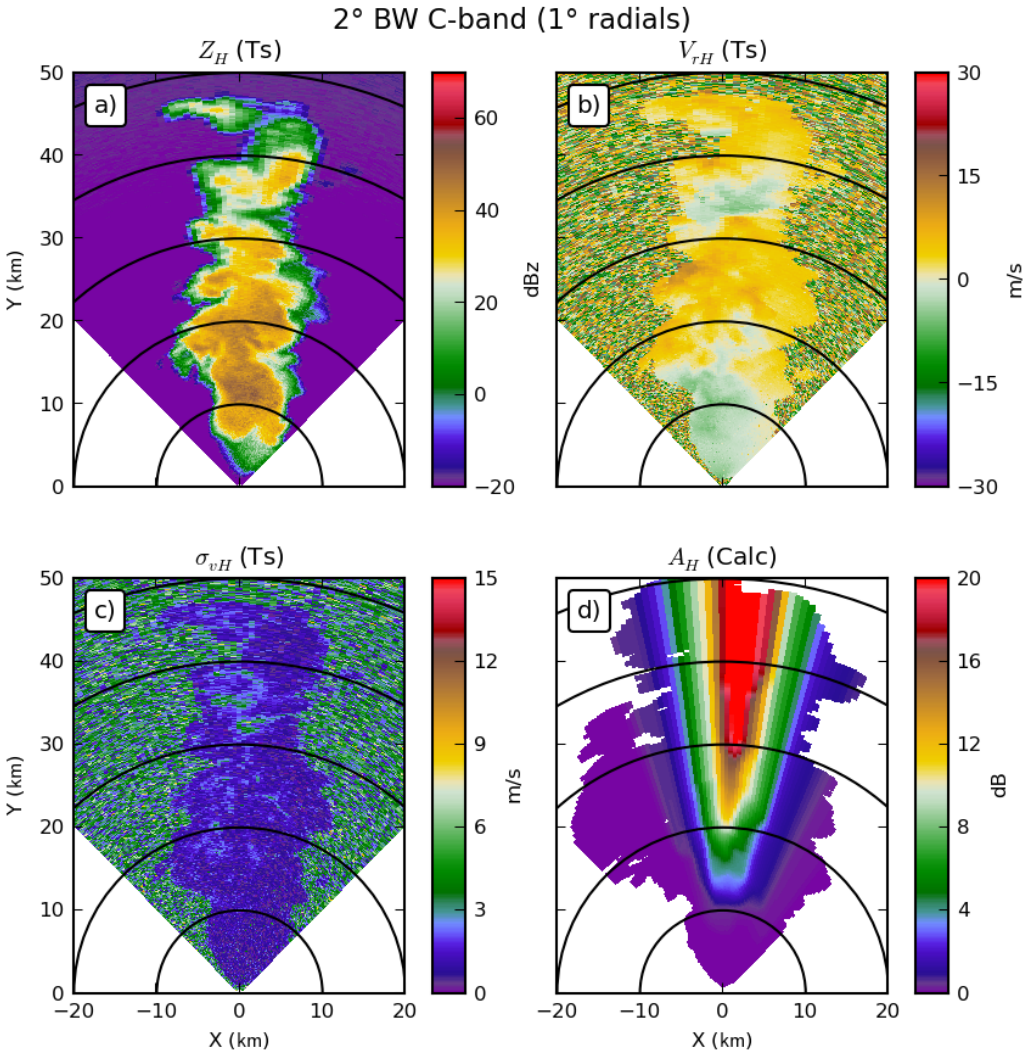

Figure 2.18: As in Figure 2.12, but for the CBW experiment.

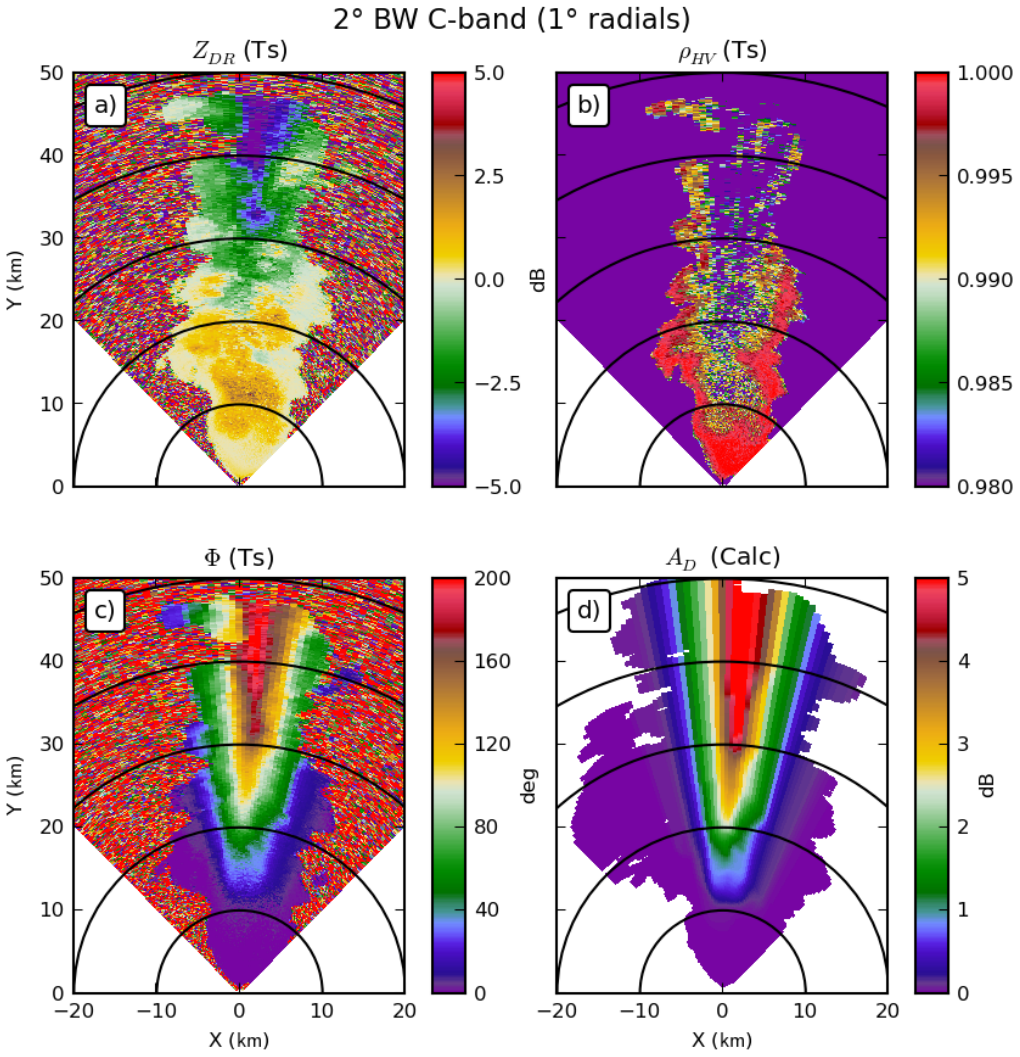

Figure 2.19: As in Figure 2.13, but for the CBW experiment.

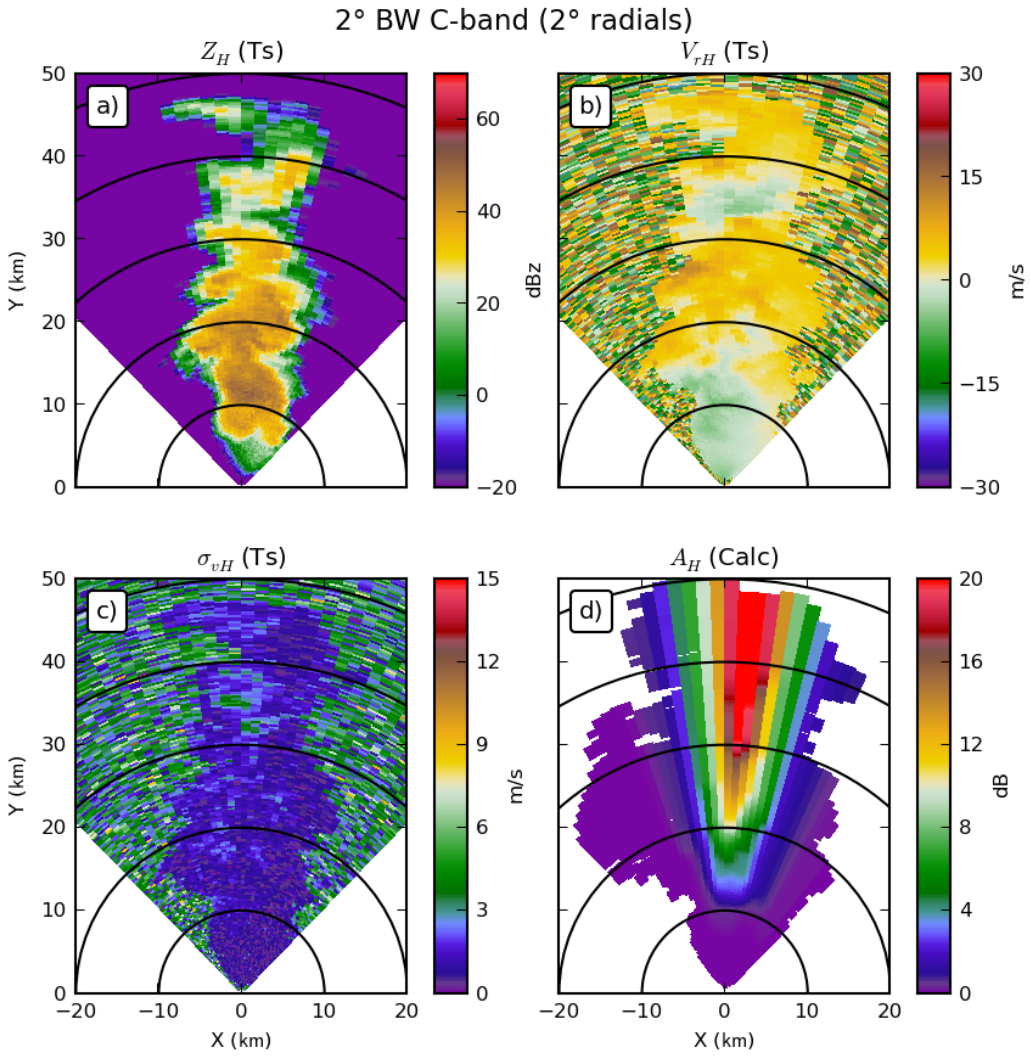

Figure 2.20: As in Figure 2.12, but for the CRW experiment

blurred, with features showing much less distinction. This makes sense since each radial in this data is the combination of two radials from the CBW data.

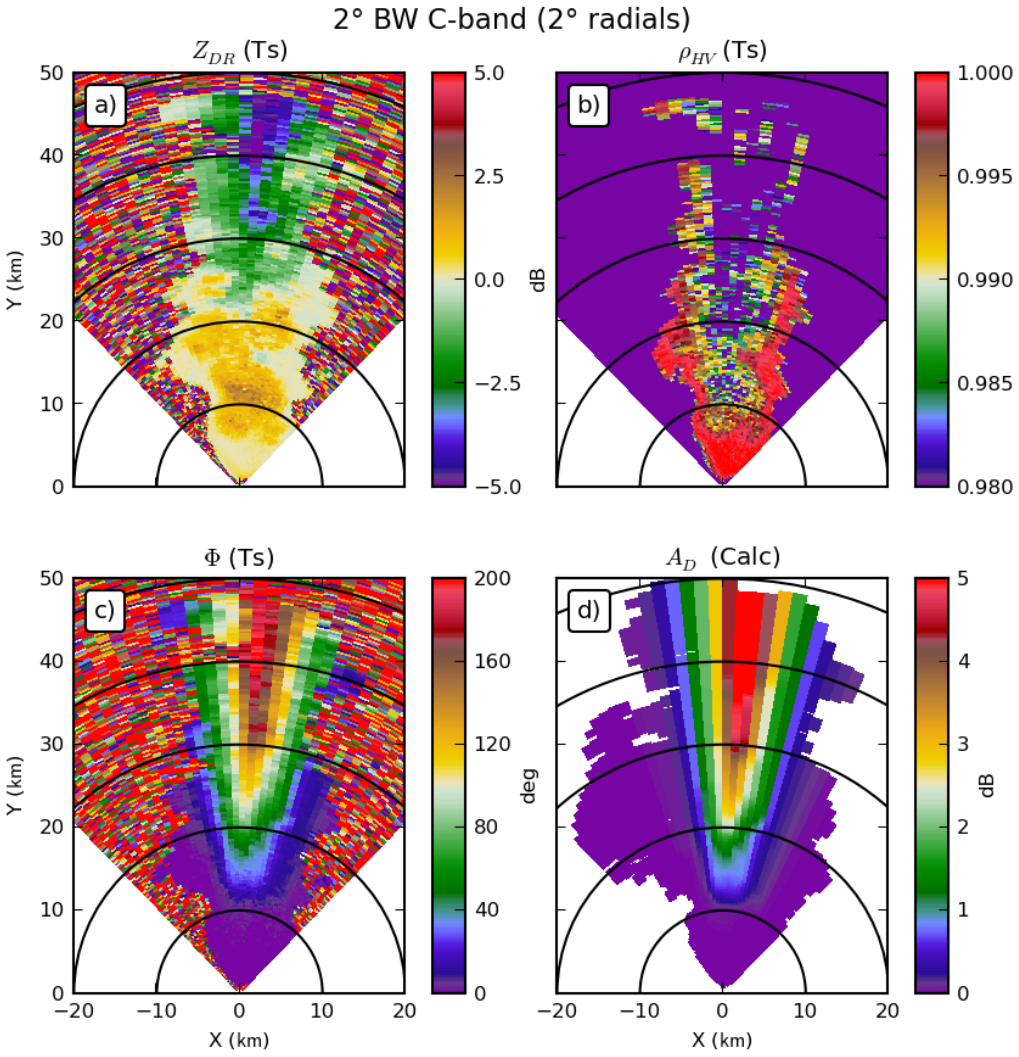

Figure 2.21: As in Figure 2.13, but for the CRW experiment

2.2.4 Time Series

As an example of time series data generation capabilities, Figure 2.22 shows the IQ data and power spectral density (PSD), for both the horizontally and vertically polarized channels, from an area around the main updraft of the storm for the S experiment. This region is chosen to give strong returns and moderate velocity. The PSD is calculated from the IQ data using the periodogram (Harris 1978) with a Hanning window and data padded to 128 samples. The PSD shows a distinct peak around $7\,\mathrm{m\,s^{-1}}$ with a shape around that peak that generally resembles a Gaussian distribution. The horizontal and vertical channels are slightly different in this case, with the vertical channel having slightly less power at all velocities, due to the intrinsic Z_{DR}. The fact that this occurs at all velocities is a consequence of the power from the main signal leaking into the other frequencies. This effect is not seen in Figure 2.23, which shows a similar plot for a region that does not contain any weather signal. Instead, the H and V channels show little correlation in the PSD, and there is no systematic bias between the channels.

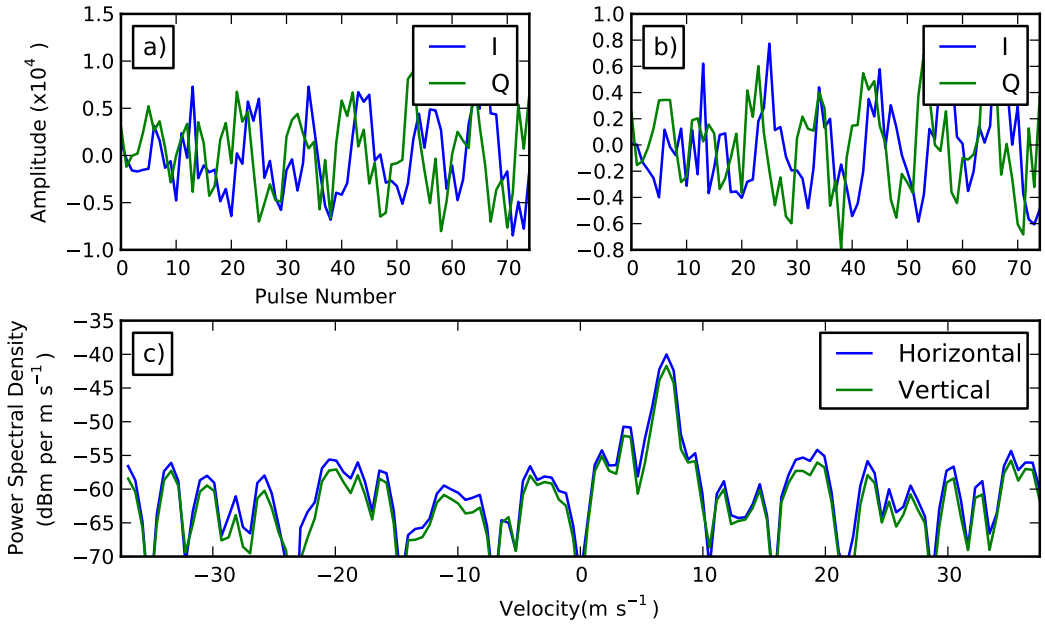

Figure 2.22: Plots of time series information for the S-band example. These data are from the main core of the storm at 355.5° azimuth and 25.5 km range. (a) Horizontal IQ data, (b) Vertical IQ data, (c) Power spectra for horizontal (blue) and vertical (green) channels.

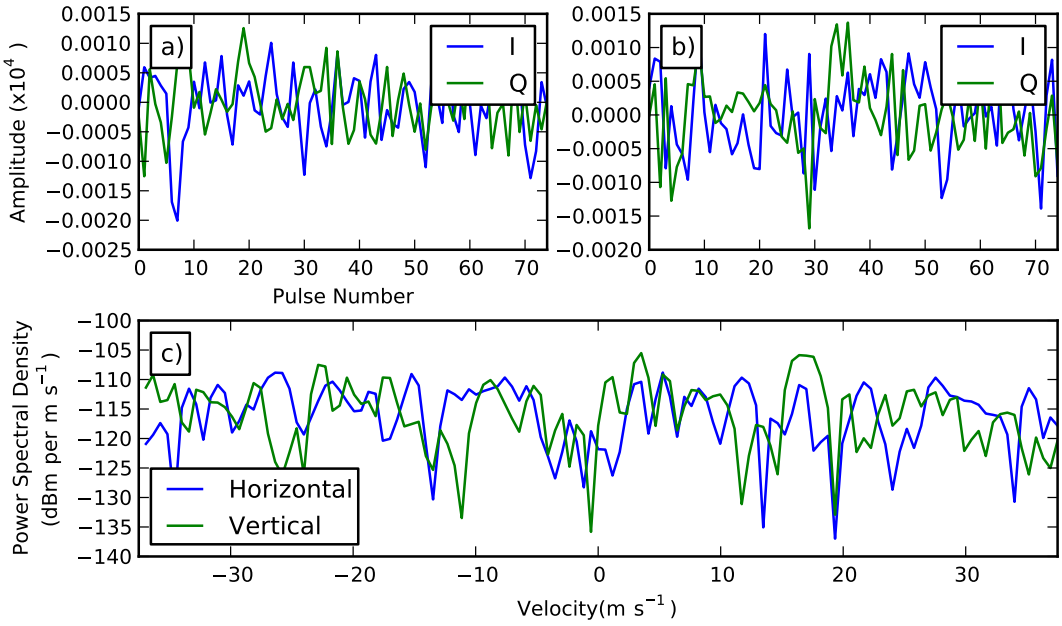

Figure 2.23: As in Figure 2.22, but at 342.5° azimuth, corresponding to an area devoid of weather echo, showing data for pure noise.

Chapter 3

Attenuation Correction

While significant research effort has been put into radar-based QPE, especially using dual-polarization radar data, there are still significant problems. Attenuation is an important problem in the use of dual-polarization radar data at any wavelength for QPE. Even at S-band, where attenuation of a single channel may not be significant, differential attenuation can significantly bias the calculation of differential reflectivity. When biased differential reflectivity values are fed into a power-law-based QPE algorithm, this bias is exacerbated. With the increasing use of radar systems at attenuating wavelengths (such as C- and X-band), the problem of correcting data for attenuation has been an area of active research.

3.1 Techniques

The basis for most radar rain attenuation correction schemes is in estimating the attenuation using other radar observables, such as reflectivity factor or, for dual-polarization radars, differential propagation phase. In this work, we examine several correction algorithms: Linear, ZPHI, Self-Consistent, and Modified Self-Consistent.

3.1.1 Linear

The Linear method, put forth by Bringi et al. (1990), is the most straight-forward of the attenuation-correction methods. This method uses a direct relationship between specific differential phase, K_{DP}, and both specific horizontal attenuation, A_H, and the specific differential attenuation, A_D:

$$A_H = \gamma_H K_{DP}^{\beta_H} \tag{3.1}$$

$$A_{DP} = \gamma_D K_{DP}^{\beta_D} \tag{3.2}$$

The coefficients in these relations are found by calculating the radar observables, combining theoretical scattering calculations and measured drop size distributions. For this algorithm, A_H and A_{DP} are regressed against K_{DP}, resulting in values for β_H and β_D that are close to 1.0, though not exact. By prescribing a value of 1.0 for the exponents in these relations, not only are the relations simplified, but the need to calculate K_{DP} is entirely removed. Then simple integration of (3.1) and (3.2) above results in the following set of equations:

$$a_H(r) = \gamma_H \Phi_{DP}(r) \tag{3.3}$$

$$a_D(r) = \gamma_D \Phi_{DP}(r) \tag{3.4}$$

Thus, (3.3) (and (3.4)) above describes a completely linear relation between the path integrated (differential) attenuation, a_H (and a_D) at a range, r, and the measured differential phase, Φ_{DP}, at that range. By eliminating the use of K_{DP}, the problem of estimating a derivative from noisy data is avoided. For this technique, there is one free parameter in each equation, γ, that relates attenuation (or differential attenuation) to Φ_{DP}; this parameter is empirically determined by a power-law regression on theoretical scattering calculations performed using drop size distribution data.

This technique has several shortcomings. First, the exponent in the best fit curve is not necessarily 1.0; by prescribing such a value, errors are necessarily introduced (albeit in the name of simplicity and operational robustness of the technique). Second, while K_{DP} calculation is avoided, with all its inherent challenges, the Φ_{DP} data can still be contaminated by effects of non-uniform beam-filling and differential backscatter phase. Quality control must be performed on the data to ensure that such effects do not result in anomalous attenuation correction. Finally, the relationship between attenuation and Φ_{DP} is sensitive to the assumptions made in the scattering calculations. If the actual atmospheric conditions and processes differ from those assumed (e.g. temperature or drop shapes), the Linear technique will be unable to compensate for these differences and thus yield less accurate results.

3.1.2 ZPHI

To address shortcomings in the Linear Φ_{DP} algorithm, Testud et al. (2001) proposed the ZPHI technique, based on an algorithm to correct for attenuation in satellite profiles. The core relation in this technique is between reflectivity and attenuation, as described by Hitschfeld and Bordan (1954). The Hitschfeld and Bordan (1954) algorithm is improved upon by providing a constraint for the total path attenuation. For

satellites, this is provided by the ground; for terrestrial radar applications, this constraint is provided by estimating the total path attenuation from the total change in Φ_{DP} along the path. The full technique is described by the following set of equations:

$$I(r, r_0) = 0.46b \int_r^{r_0} Z_a^b(s)\, ds \tag{3.5}$$

$$A(r_0) = \frac{Z_a^b(r_0)}{I(r_1, r_0)}\{10^{0.1b\gamma\Delta\Phi} - 1\} \tag{3.6}$$

$$A(r) = \frac{Z_a^b(r)}{I(r_1, r_0) + \{10^{0.1b\gamma\Delta\Phi} - 1\}I(r, r_0)} \times \{10^{0.1b\gamma\Delta\Phi} - 1\} \tag{3.7}$$

Essentially, the technique works by calculating the total attenuation from the total path change in Φ_{DP}, and distributing the total attenuation along the path based on the (attenuated) reflectivity values. It should be noted that the process of relating the total path-integrated attenuation to Φ_{DP} implicitly makes use of the same assumptions as the Linear Φ_{DP} algorithm. To correct for differential attenuation, the horizontal and vertical reflectivities can be corrected for attenuation separately; then corrected differential reflectivity can be calculated from the individual reflectivities.

This technique has several strengths versus the Linear Φ_{DP} algorithm. By relying on the relationship between reflectivity and attenuation, the ZPHI algorithm is much less sensitive to assumptions made about the scattering process. This dependence is captured by b, which is a free parameter that is empirically determined from scattering calculations. Also, by using Φ_{DP} only to calculate the total path attenuation, the problems of non-uniform beam-filling and differential backscatter phase are limited; only the total change in Φ_{DP} is needed, nominally reducing the requirements to two good values of Φ_{DP}.

However, the technique is not immune to the problems of invalid scattering assumptions. The γ above is the same as that for the linear Φ_{DP} algorithm; the same sensitivity to assumptions is present in estimating the total attenuation from Φ_{DP}. Thus, depending on actual atmospheric conditions, the total attenuation may be under- or over-estimated.

3.1.3 Self-Consistent

The self-consistent attenuation correction algorithm was introduced by Bringi et al. (2001) as an improvement on ZPHI. As the name suggests, this method relies on the internal consistency of the data, in particular attenuation and Φ_{DP}. This method iteratively performs the ZPHI correction to try to find an optimal value for the γ coefficient, attempting to address the sensitivity to scattering processes. The "optimal" value of γ is found by minimizing the mean absolute difference between the true profile of Φ_{DP} and a calculated profile of Φ_{DP}; this profile is calculated from the algorithm's estimated profile of attenuation using an inverted form of the Linear Φ_{DP} relation with the value of γ being tested. The procedure is explicitly defined as:

$$\phi^c_{DP}(r;\gamma) = 2\int_{r_0}^{r} \frac{A_h(s;\gamma)}{\gamma}\, ds \tag{3.8}$$

$$\gamma_{min} \leq \gamma \leq \gamma_{max} \tag{3.9}$$

$$Error = \sum_{j=1}^{N} \left| \Phi^{filt}_{DP}(r_j) - \Phi^c_{DP}(r_j;\gamma) \right| \tag{3.10}$$

The advantage of this technique is its ability to address the sensitivity of the algorithms to assumptions about scattering processes; however, only the γ coefficient (relating attenuation to Φ_{DP}) is optimized. The b coefficient (relating attenuation and reflectivity) remains fixed; while this coefficient is much less sensitive to scattering

assumptions, this is a limitation to the adaptiveness of the technique. Additionally, by using the linear Φ_{DP} relation, there is still the assumption that the power in the power law relation between K_{DP} and attenuation is 1.0; such an assumption is a limitation to the attenuation model prescribed by the equations and cannot be addressed by the adaptive procedure. Also, while this technique is robust in theory, in our testing we have observed that the technique can have convergence problems, especially on rays with limited data. Such problems are not limited to individual rays, unfortunately, but extend across small regions. For such rays, the procedure is not truly converging, but is stopping at the bounds prescribed by the algorithm's optimization procedure.

3.1.4 Modified Self-Consistent

In the course of examining the behavior and performance of the self-consistent method, some artifacts were observed. One problem was that for rays with little data coverage (and small total attenuation and Φ_{DP}), the errors were drastically larger. The poor performance for these rays comes as a result of the optimization procedure not being able to converge to a value within the specified bounds for γ; consequently, an anomalously large or small value for γ results. The second problem observed was that the algorithm showed an oscillating pattern as a function of azimuth, alternating between slightly greater and slightly less than true attenuation for several rays at a time. Figure 3.1 shows the values of the optimized γ as a function of azimuth. Comparing the estimated values to true values calculated from simulated data, the rays with bad (non-converged) values are clearly visible. One can also see changes in the converged value of γ_h that do not correspond to changes in the true optimal value of γ_h.

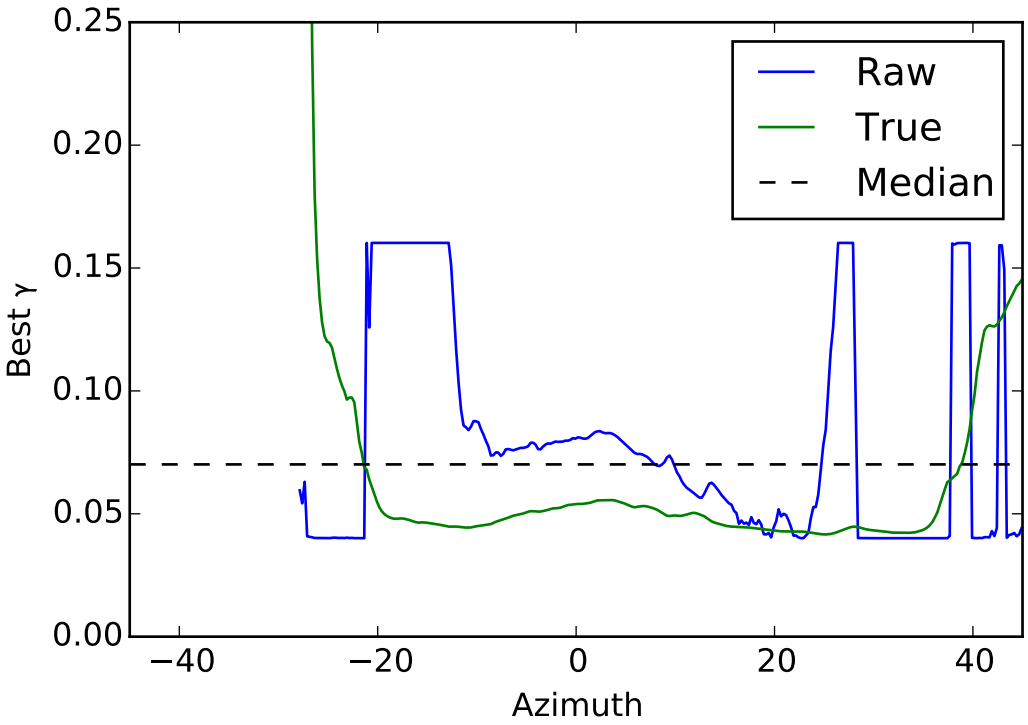

Figure 3.1: Distribution of γ_h values as a function of azimuth. Values obtained from optimization in the self-consistent algorithm are in blue, while true values are in green. The median of the optimized values is given by the dashed black line.

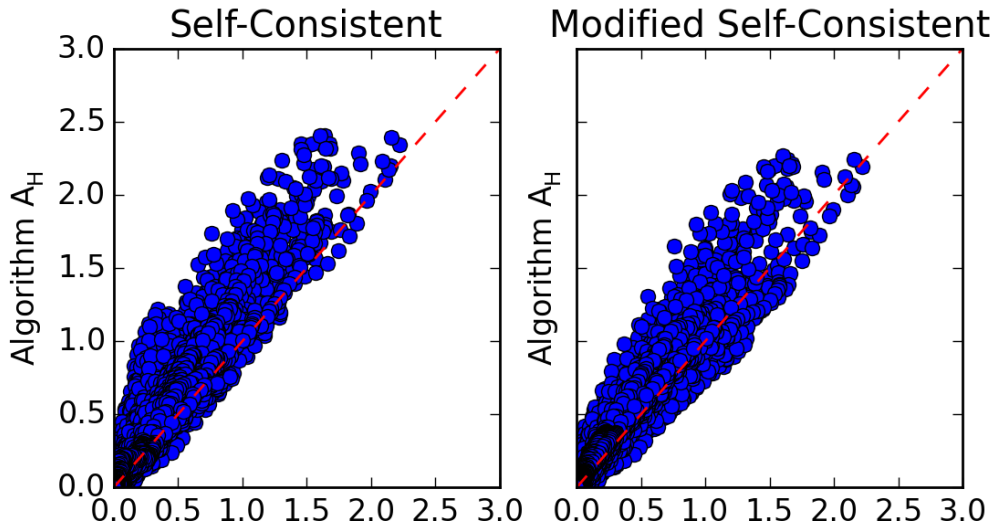

Figure 3.2: Scatter plots of estimated specific attenuation for self-consistent (left) and modified Self-Consistent (right) versus true specific attenuation values.

To address these shortcomings and increase the robustness of the Self-Consistent algorithm, we introduce a Modified Self-Consistent algorithm. In this version, the optimal values of γ_h from all rays is collected and the median γ_h value is calculated. This median is used then as the optimal value of γ_h for all rays. As an example, the median for the γ_h values given in Figure 3.1 is plotted as a horizontal line. While this value is clearly greater than the true value in places (and less in others), it has the beneficial behavior of removing outlier values as well as producing smoother results. Figure 3.2 compares the estimates of specific attenuation for horizontal attenuation (at C band) for both the modified and un-modified Self-Consistent algorithms. The modified method shows a tighter clustering of values, due to the reduction in outlier points. It also appears that the modified procedure introduces a slight negative bias, with more points below the one-to-one correspondence line.

The performance of this algorithm versus that of the unmodified Self-Consistent method will be discussed further in later chapters.

3.2 Finding Coefficients

All of the algorithms described previously rely on free parameters to relate attenuation to radar observables (i.e., reflectivity and Φ_{DP}). The original works (Bringi et al. (1990), Testud et al. (2000), and Bringi et al. (2001)) determined these coefficients empirically using regression on calculated radar observables. However, there are two obstacles to the use of these values here. First, the scattering calculations used to generate these parameters were based on datasets of drop size distributions; because these data would not match the prescribed drop size distribution that underlies the model simulation, their use could introduce errors in the attenuation correction. While certainly such errors exist in real world applications of these techniques, the goal here is to provide a best-case scenario for these techniques. As such, differences in assumptions between the algorithms and the radar data simulation are minimized where possible. The second challenge is that the original works have differing, or even undocumented, assumptions regarding their scattering calculations; it is difficult to create a set of radar simulation parameters that is known to completely match those assumptions made by several different works.

The challenges with using exiting published coefficients necessitates the development of a procedure for calculating a new set of regression parameters. This procedure has the benefit of creating parameters that represent a best case scenario for algorithm performance; since the assumptions used in generation of the parameters can be

matched exactly in the process of radar data simulation, resulting errors are inherent to the attenuation correction algorithm itself. Having such coefficients with precisely known assumptions also allows for systematic testing of how violating these assumptions affects algorithm performance; this is the subject of the next chapter.

3.2.1 Scattering Calculations

To generate empirical fits between radar observables (i.e., K_{DP} and reflectivity) and (differential) attenuation values, we start with a set of scattering matrices calculated using the T-matrix method, as outlined in the previous chapter. The relevant assumptions for the scattering calculations are given in Table 3.1. Using these assumptions, the scattering matrices are calculated across a range of diameters from 0.01 to 8 mm.

Wavelength	5.5 cm, 3.21 cm
Temperature	283 K
Canting Angle Distribution Width	10
Shape Model	Brandes et al. (2004)

Table 3.1: Parameters used in scattering calculations for regression coefficients

To turn the scattering matrices into K_{DP}, reflectivity, attenuation, and differential attenuation, we use equations (2.58) and (2.68), just as in the radar simulation. The model simulation grid, which gives a set of rain water concentration (q_r) and number concentration (N_0) values, functions as a set of relevant DSD data. Even when the grid is thresholded to contain measurable rain ($q_r > 0.5\,\mathrm{kg\,m^{-3}}$ and $N_0 > 100\,\mathrm{m^{-3}}$), there are still too many points to work with; as a result, we arbitrarily subset those points by a factor of 100. In Figure 3.3 the resulting subset of the data is shown. These

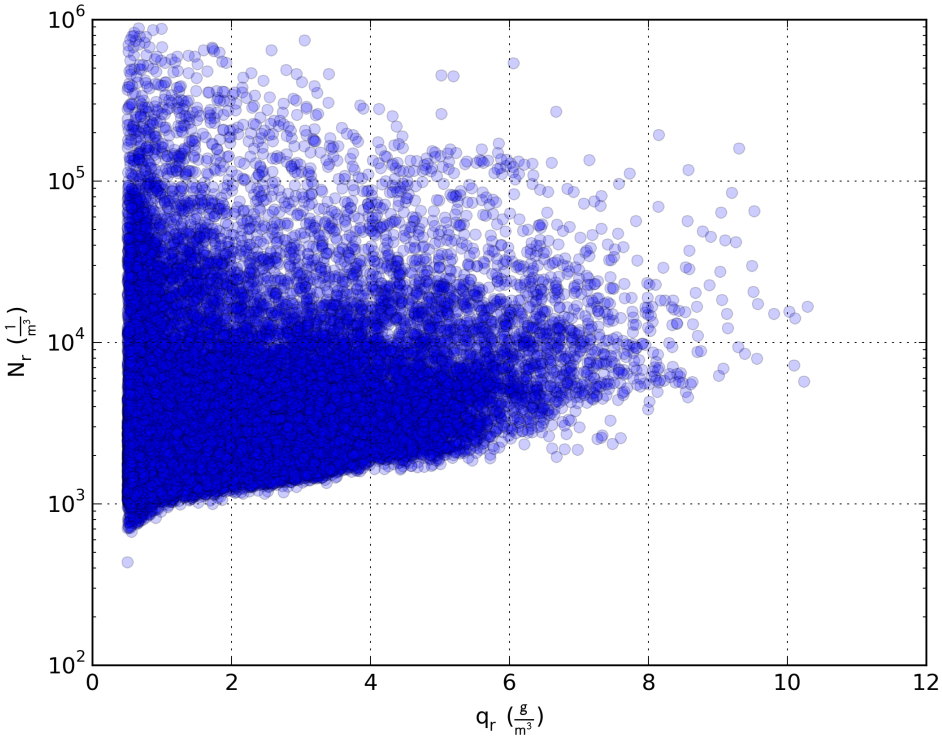

Figure 3.3: Scatter plot of rain water parameters used for regressions. Rain water content (g m^{-3}) is plotted along the x-axis and number concentration (m^{-3}) is plotted logarithmically along the y-axis.

data represent a wide spread of number concentration values, with the higher rainwater content values clustered around a number concentration of $10\,000\,\mathrm{m}^{-3}$. To turn these two parameters into actual drop size distributions, a modified gamma distribution, as described previously, is prescribed. Using the model-appropriate fixed shape parameter of 1.81, we have sufficient information to generate a unique drop size distribution for each rain content-number concentration pair.

3.2.2 Regressions

For the attenuation correction techniques described previously, the following set of empirical relations are required:

$$A_H = \gamma_H K_{DP} \tag{3.11}$$

$$A_V = \gamma_V K_{DP} \tag{3.12}$$

$$A_H = a_H Z_H^{b_H} \tag{3.13}$$

$$A_V = a_V Z_V^{b_V} \tag{3.14}$$

$\gamma_{H,V}$ and $b_{H,V}$ are the empirical coefficients that need to be determined through regressions on sets of $A_{H,V}$, $Z_{H,V}$, and K_{DP} provided by the scattering calculations ($a_{H,V}$ are unused in the algorithms). $\gamma_{H,V}$ can be found in a straightforward fashion using linear regression, while the $b_{H,V}$ can be found by using logarithms to transform the power law regression into a linear regression problem. Figure 3.4 shows the results of the regression (for both C- and X-bands) between reflectivity factor (Z_H) and specific attenuation (A_H) at horizontal polarization. Qualitatively, the resulting fit does not appear to capture well the relationship between Z_H and A_H, especially at C-band; the increasing error with increasing values of A_H confirms this. Figure 3.5 shows similar problems with the fit for vertical polarization. Figures 3.6 and 3.7 show the same analysis, but for the regression between specific differential phase (K_{DP}) and specific attenuation at horizontal and vertical polarizations, respectively. The results here are much less problematic; overall the curves seem to fit the raw values relatively well, though for horizontal polarization the slope of the line looks, qualitatively, to be too small.

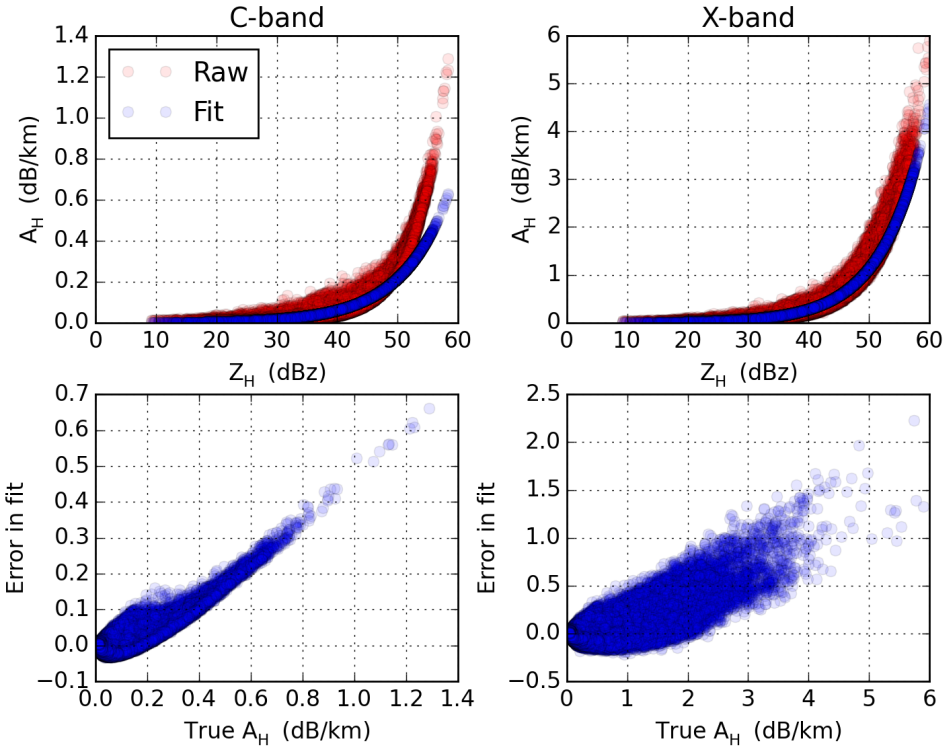

Figure 3.4: Results of applying regression on scattering data for C-band (left) and X-band (right). The top panels show the raw calculated specific attenuation (A_H) values (red), as well as those calculated from the regression (blue), as a function of reflectivity factor (Z_H), for horizontal polarization. The bottom panels show the resulting error as a function of the true specific attenuation values.

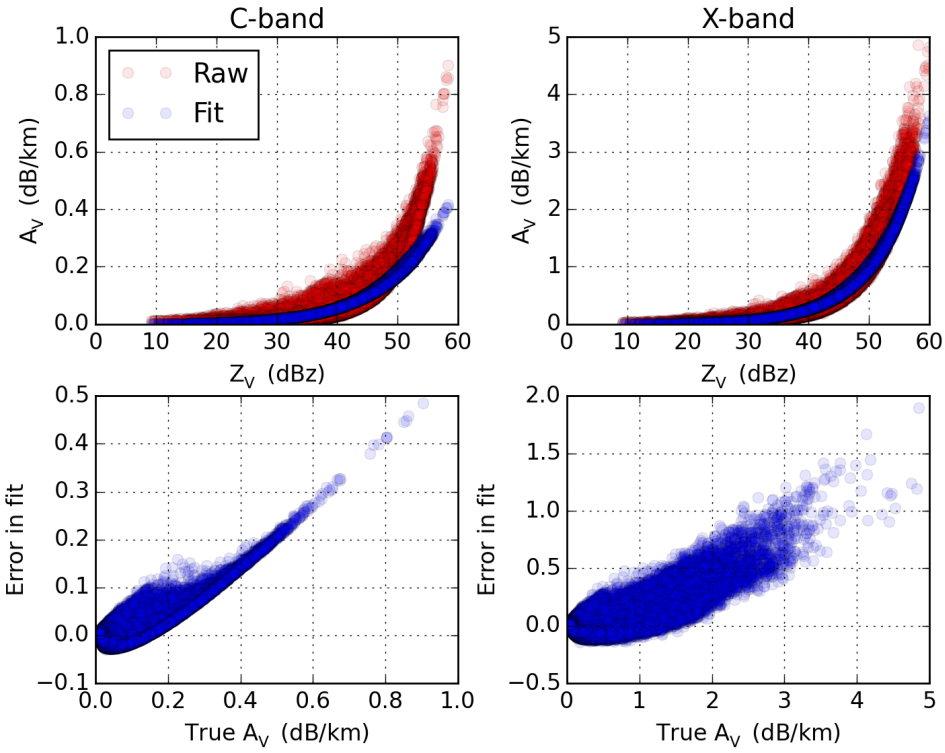

Figure 3.5: As in Figure 3.4, but for vertical polarization.

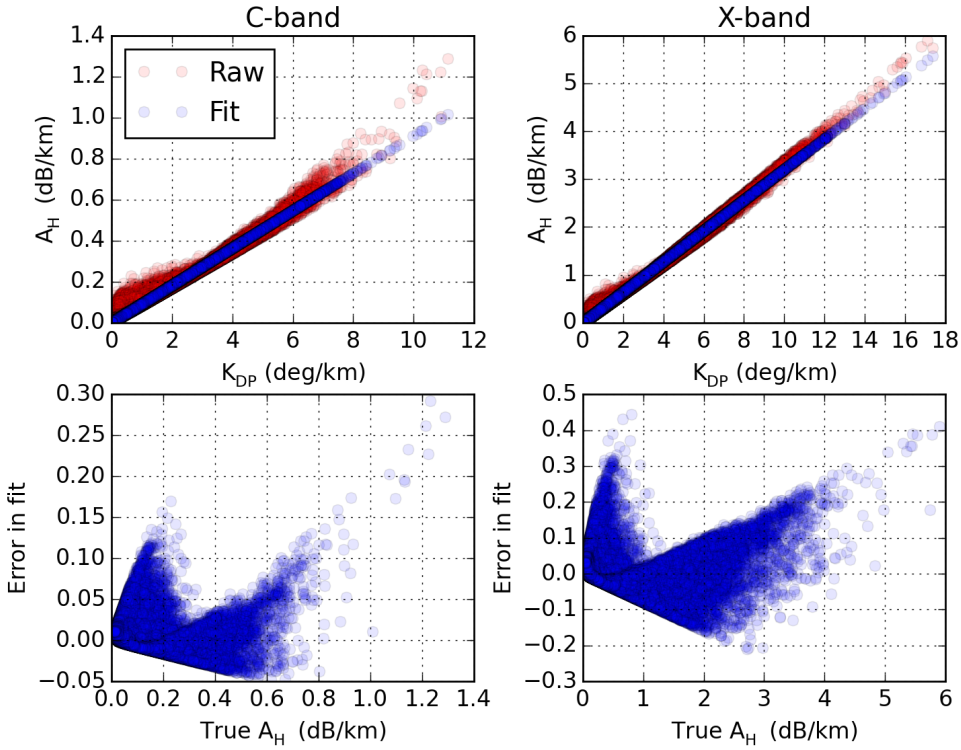

Figure 3.6: Results of applying regression on scattering data for C-band (left) and X-band (right). The top panels show, for horizontal polarization, the raw calculated specific attenuation (A_H) values (red), as well as those calculated from the regression (blue), as a function of specific differential phase (K_{DP}). The bottom panels show the resulting error as a function of the true specific attenuation values.

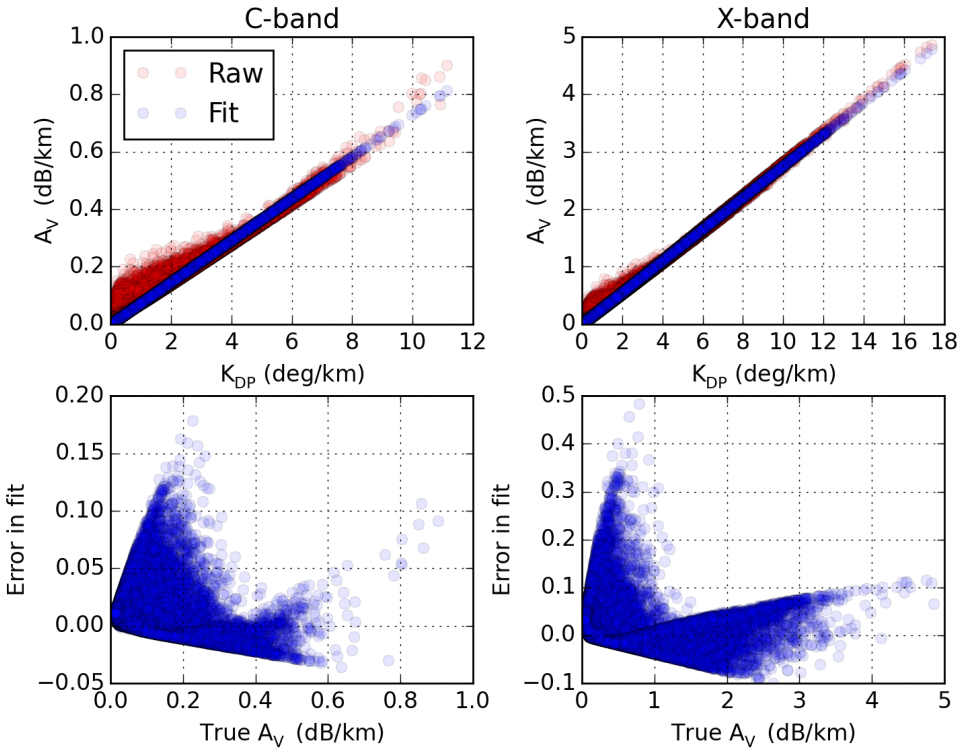

Figure 3.7: As in Figure 3.6, but for vertical polarization.

There are two main reasons for the poor regression fits. First, the set of points used in the regression is dominated by points corresponding to low attenuation values; this is a direct consequence of using the model grid's precipitation fields as the source of DSD data, as most of the model field that has precipitation is only filled with light rain. Combined with the mathematics of linear regression, the curve that minimizes the RMS error fits, for the most part, the numerous points at low attenuation values. The errors from the lack of fit at high attenuation value are more than countered by the fact that the line fits many points at low values. This particular problem affects both the regressions using K_{DP} and $Z_{H,V}$.

The second problem, which only affects the regressions on $Z_{H,V}$, come from the reformulation of the power law fit as a linear regression. The logarithmic transformation of the data (to make it a linear problem), changes the measurement of errors. The deviations of the regression curve from the data (i.e., subtraction between points) in logarithmic space, actually represent ratios in the space of the original points being fit with a power law. Effectively, the regression is minimizing the RMS of relative error rather than that of absolute error. This has the effect of reducing the error contribution of points at higher attenuation values. This effect explains why the regressions for $Z_{H,V}$ were, qualitatively, less good than those for K_{DP}.

One method to try to improve these fits would be to resample the model DSD fields to remove the over-represented low attenuation values. To do so objectively would not be simple; more importantly, this would not address all of the problems for the power law regressions. Instead, we have chosen to use weighted linear regression, using the

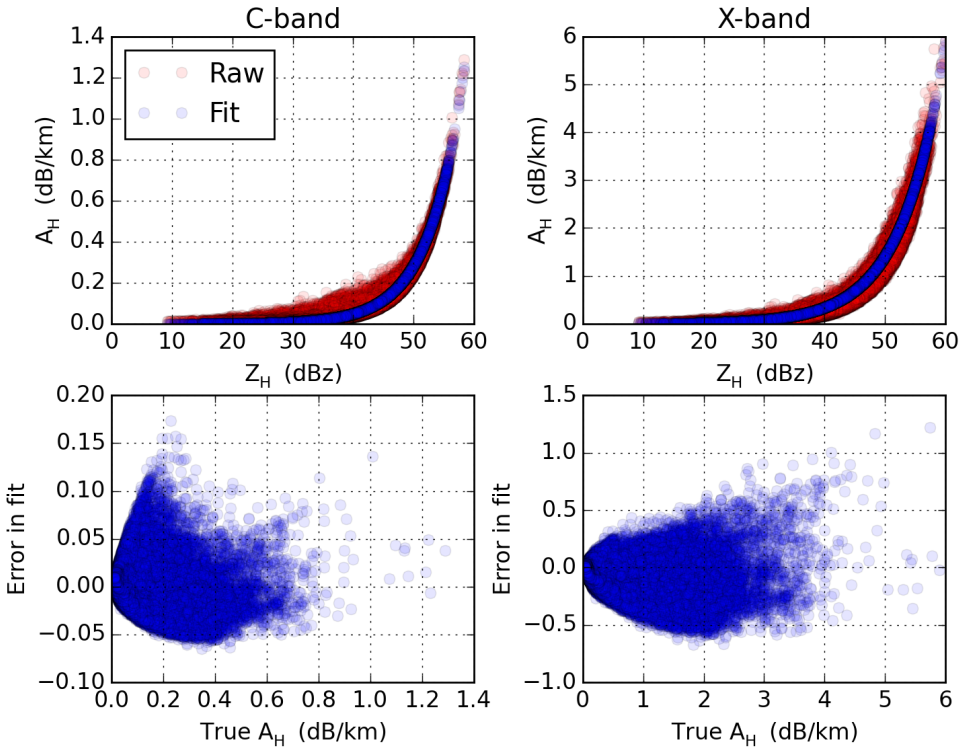

Figure 3.8: As in Figure 3.4, but for weighted regression.

square of the attenuation value as the weights. Doing so makes the larger attenuation values have a greater impact on the regression, countering both the problems of numerous low values and the logarithmic scaling.

Figure 3.8 shows the results when weighting is applied in the regression between specific attenuation and reflectivity factor at horizontal polarization. Qualitatively, the resulting curves do a much better job of capturing the relationship between A_H and Z_H, especially at C-band. Quantitatively, the errors for high attenuation values are greatly reduced, without greatly increasing the errors for small values of A_H. The results for vertical polarization (Figure 3.9) show similar improvements. Figures 3.10 and 3.11 do not show the same clear gains for the regression between K_{DP} and A_H, though there do appear to be slight improvements. Overall, the effect of weighting in

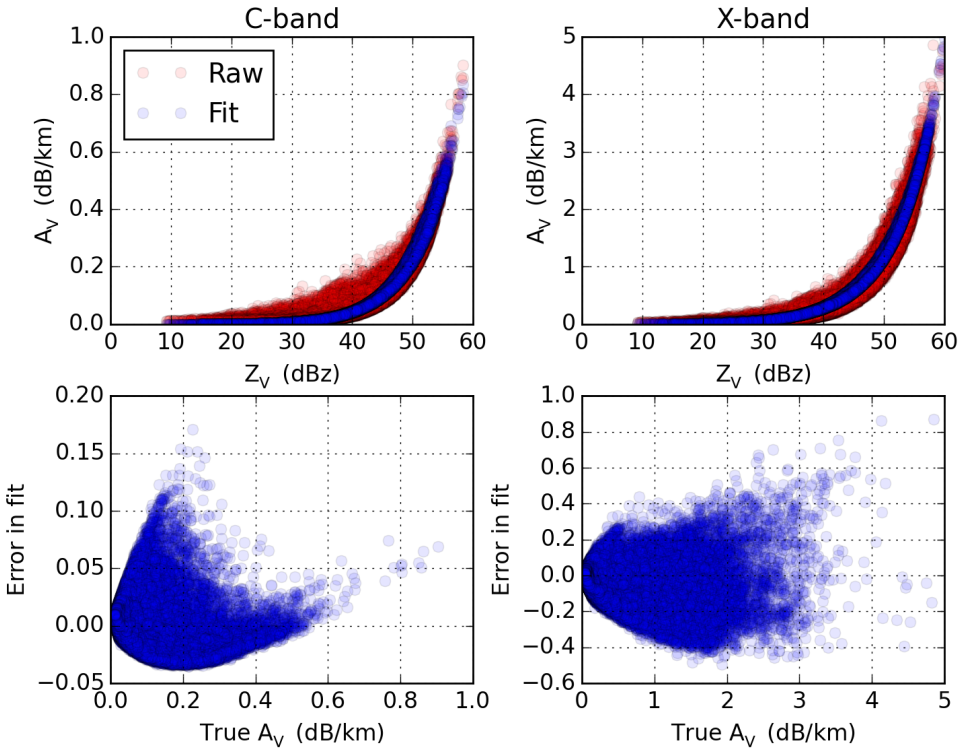

Figure 3.9: As in Figure 3.5, but for weighted regression.

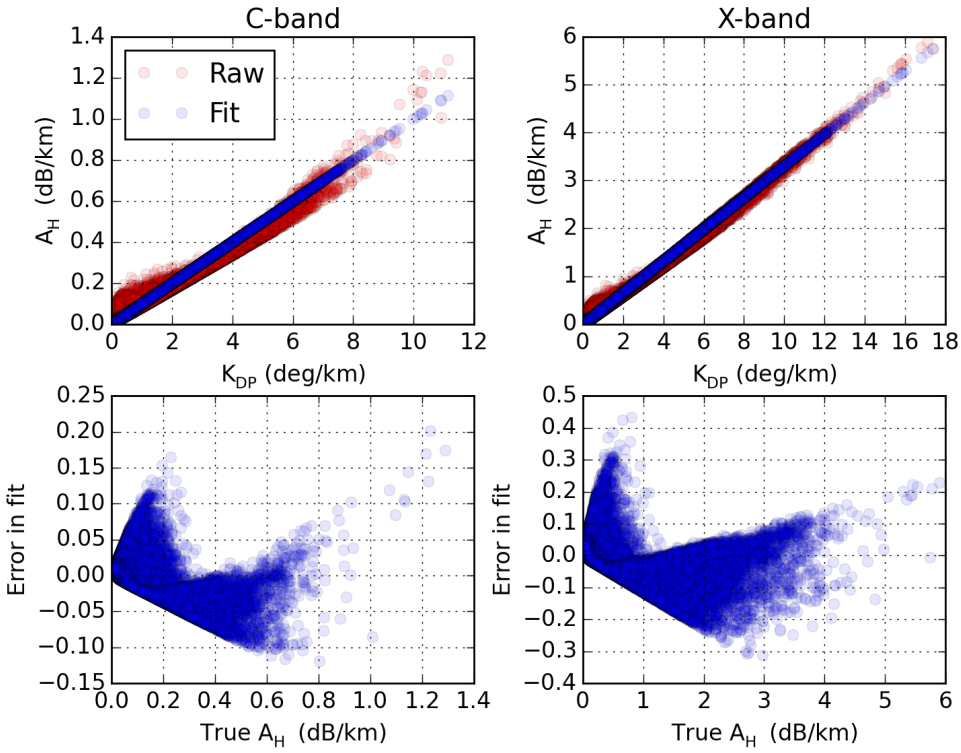

Figure 3.10: As in Figure 3.6, but for weighted regression.

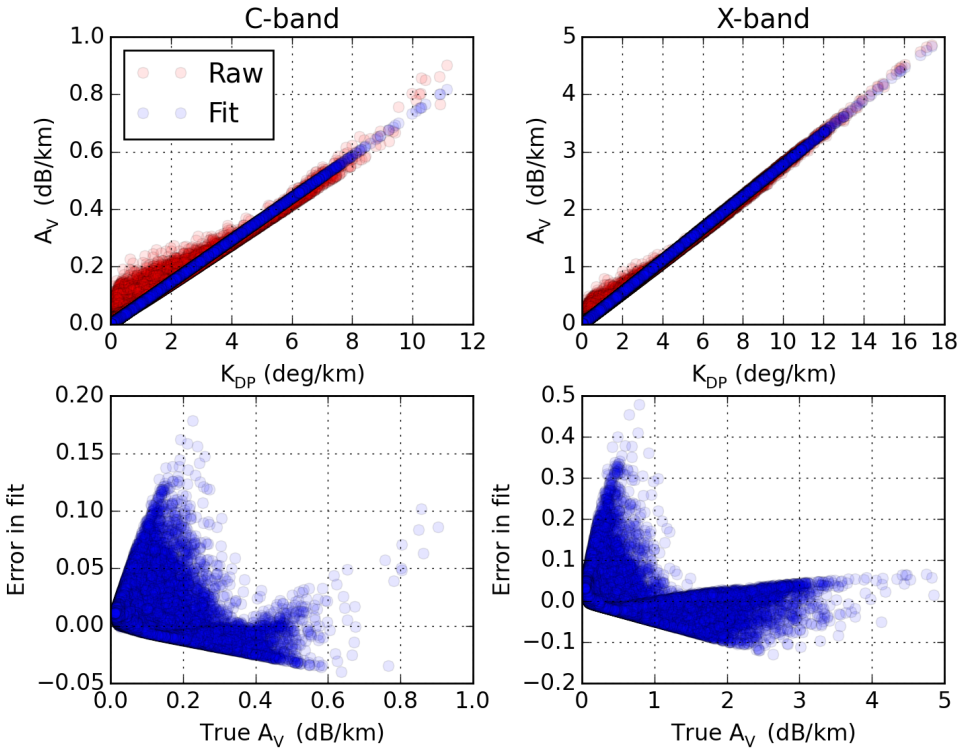

Figure 3.11: As in Figure 3.7, but for weighted regression.

the regression has been to create fits to the data that provide useful estimates for the parameters needed in (3.14) above; the weighted regressions appear to capture well the relationships between the radar observables. The final values for these parameters, which will be used in the later chapters, are presented in Table 3.2.

	C-band	**X-band**
β_H	$0.770\,618\,335$	$0.621\,43$
β_V	$0.812\,085\,167$	$0.681\,336\,195$
γ_H	$0.100\,147\,590\,397\,957\,04$	$0.331\,560\,153\,770\,154\,5$
γ_V	$0.073\,427\,838\,671\,551\,96$	$0.278\,886\,861\,638\,882\,65$

Table 3.2: Final parameter values from regression.

Chapter 4

Modeling Errors in Attenuation Correction

The goal here is to examine and quantify the sensitivity of the previously described algorithms to the assumptions made in calculating the coefficients used in those techniques. Thus, it explores the impact of errors in modeling the relationships between the radar variables. Such sensitivity of radar parameters has previously been demonstrated by Aydin et al. (1989), Bringi et al. (1990), and Carey et al. (2000), among others. The work here, carries the study of such sensitivity further by using fully-simulated radar data as well as full algorithm implementations.

To perform this study, the radar data simulation procedure described previously is used to generate data using different sets of assumptions. For each of these sets, the attenuation correction algorithms are run to generate estimates of the attenuation field, which are compared against the true attenuation field, as calculated by the radar simulation. These comparisons are done for both C- and X-band, which permits exploration of any differences between the two bands.

Table 4.1 lists the parameters common across all of the experiments involved in studying the effects of modeling errors. To limit the impact of radar sampling geometry on the results, the radar and scanning configuration is chosen to produce very high-resolution data, higher than usually is encountered in real data; the effects of sampling will be explored later. These parameters give radials with a spacing of 0.25°, matching the 3 dB beamwidth.

Antenna gain	45.5 dB
Antenna 3 dB Beamwidth	0.25°
Antenna Limits	Main-lobe only
Peak power	250 kW
First range gate	500 m
Noise power	−113 dBm
Elevation	0.5°
PRT	0.667 ms
Rotation Rate	15 ° s^{-1}
Pulses per radial	25
Gate length	100 m

Table 4.1: Radar and scanning parameters common to the simulations

Experiment	Wavelength	Canting Width	Temperature	Shape Model
Control	5.5 cm, 3.21 cm	10	283 K	Brandes
Canting	5.5 cm, 3.21 cm	20	283 K	Brandes
Shape	5.5 cm, 3.21 cm	10	283 K	Pruppacher
Temperature	5.5 cm, 3.21 cm	10	Grid (295 K)	Brandes
Wavelength	5.0 cm, 3.0 cm	10	283 K	Brandes
Combined	5.0 cm, 3.0 cm	20	Grid (295 K)	Pruppacher

Table 4.2: Parameters differing between different experiments

Table 4.2 lists the parameters for the various experiments that are examined here. The Control experiment serves as the baseline of performance for the algorithms, where the assumptions used in simulating the radar data match those used to find the coefficients for the algorithms; as such, it also represents a best case for performance. The other experiments, Canting, Shape, Temperature, and Wavelength, are chosen to systematically test how algorithm performance varies as assumptions involving these aspects of scattering are varied. The final experiment, Combined, is essentially the opposite of the Control experiment, in that all of the assumptions are violated; as such, it might be considered to represent, theoretically, a worst case scenario for algorithm performance.

To frame the results from the experiments, Figures 4.1 and 4.2 show plots of attenuation as a function of both reflectivity factor and specific differential phase, for both horizontal and vertical polarizations. These plots give some expectation of the results of the experiments, while making a simplifying assumption of a Marshall et al. (1947) drop size distribution; this implies that they do not reflect completely the results from the full simulation (using a modified gamma distribution). For reference, the curve corresponding to the regression coefficients (for the correction algorithms) is also plotted.

In Figure 4.1, it is apparent that at C-band the relationship between reflectivity factor and attenuation, for both polarizations, is relatively immune to the assumptions made; the biggest change comes from switching the wavelength. It is also seems from these plots that the regression coefficient between reflectivity and attenuation captures the various relationships relatively well. The relationship between specific differential phase and attenuation, however, varies much more with changing assumptions. Again,

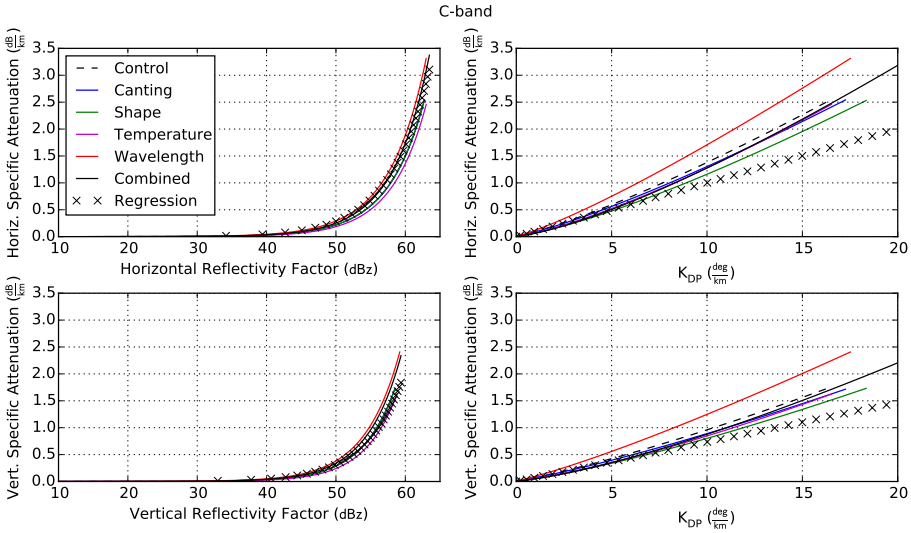

Figure 4.1: Top Left: Specific attenuation as a function of reflectivity factor for horizontal polarization. Top Right: Specific attenuation at horizontal polarization as a function specific differential phase. Bottom Left: Specific attenuation as a function of reflectivity factor for vertical polarization. Bottom Right: Specific attenuation at vertical polarization as a function of specific differential phase. All calculations assume a C-band wavelength.

the greatest impact seems to come from switching wavelength, though the effect is even greater than for reflectivity factor. It should also be noted that the effect of changing wavelength was of the opposite sign to the effects of changing every other assumption. Consequently, the curve for the Combined experiment lies very close to that of Control, a result of the errors for changing the various assumptions canceling out. The regression coefficient curve in this case is well below the others, as well. This hints that calculating attenuation using differential phase may result in underestimation; or it may just be a product of using the Marshall et al. (1947) drop size distribution here, while the coefficient was optimized for a modified gamma distribution. The results of the individual experiments answer this question.

At X-band, in Figure 4.2, the relationship between reflectivity factor and attenuation seems to be more sensitive to the assumptions made than at C-band. Also, the regression coefficient curve in this case seems to be noticeably different than the other curves; again, this could be caused by the difference in the drop size distribution used. Looking at the relations between attenuation and specific differential phase, it is apparent that the assumptions made greatly impact the result. As before, for the case of the Combined experiment the errors seem to cancel out, leaving the Control and Combined curves very close. For horizontal polarization, the regression curve is right along the Control (and Combined); at vertical polarization the regression curve is not as good a match for Control. The results from the experiments with the full simulation are needed to see whether this is an artifact of the drop size distribution difference.

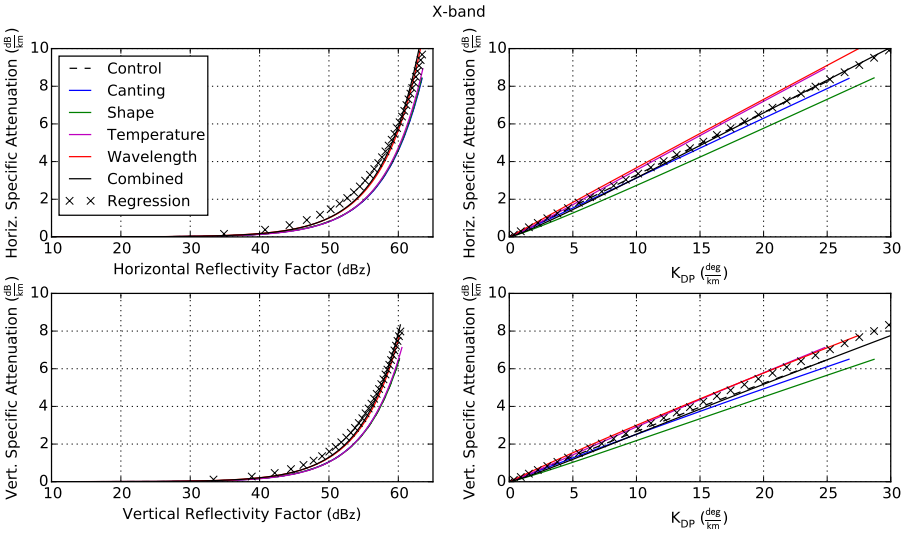

Figure 4.2: As in Figure 4.1, but for X-band.

4.1 Control

As mentioned previously, the Control experiment is designed to represent a best case for algorithm performance, where the parameters used to simulate the radar data match the assumptions made when calculating the coefficients for the attenuation correction algorithms. The parameters include fairly routine assumptions, such as fixed temperature (283 K) and the Brandes et al. (2002) shape model (as described in (2.1)). Given the matching assumptions and the high resolution data, any errors here reflect fundamental limitations of the algorithms due to the assumptions made about power law relationships between the variables, as well as any errors introduced by the radar's sampling process.

4.1.1 C band

Figure 4.3 shows the fields of horizontal attenuation that result from running the various algorithms, as well as the true field of attenuation. Overall, all algorithms show

good agreement. The greatest values of attenuation are found at the far range due north from the radar. Here, the Linear and ZPHI algorithms have noticably higher values compared to the truth field; the Modified Self-Consistent (MSC) algorithm, on the other hand, underestimates the attenuation values. The Self-Consistent (SC) algorithm appears to capture the true attenuation almost perfectly.

These observations are largely corroborated by Figure 4.4, which shows the output from the algorithms with the true attenuation field subtracted, aiding in highlighting the areas that differ. The differences for Linear and ZPHI are in the range of $2\,$dB too high in the core, while MSC only shows a slight low bias of approximately $0.5\,$dB. SC shows fluctuations of some rays with low values and some with high, with the magnitude of the differences on the order of $1\,$dB; overall, the output field from SC appears unbiased. As mentioned before, the radial-to-radial variation for SC is a consequence of the independent optimization for γ that is applied to each radial, and is the impetus for the development of the MSC. In this case, MSC does not show the oscillatory behavior, but still manages to show an overall field that appears unbiased with regards to estimates of attenuation.

Figures 4.5 and 4.6 show similar analyses for vertical polarization. Here, all of the algorithms, overall, demonstrate accuracy in estimating the amount of attenuation. The Linear and ZPHI algorithms yield an overall overestimate of attenuation, up to $1\,$dB. MSC, conversely, shows an overall slight underestimation of attenuation, on the order of about $0.5\,$dB. SC displays changes on a per radial basis; while the mean of its field appears that it could be comparable to the others, the individual radials show errors larger than the other algorithms.

2D histograms of the specific attenuation at horizontal and vertical polarizations, shown in Figures 4.7 and 4.8, respectively, help to examine the algorithm performance better by focusing on the accuracy on a gate by gate basis. At horizontal polarization, the bias in the Linear algorithm is evidenced by the ribbon of largest values being located above one-to-one line. This is also true for ZPHI, though in this case, the algorithm shows two distinct maximal bands in specific attenuation, and the one-to-one line goes between them; the band with the highest counts sits above the line, indicating a slight high bias. SC and MSC also demonstrate this two-banded structure; however, for these algorithms, especially MSC, the band of highest point counts lies along the one-to-one line. It should also be mentioned that all of the ZPHI-based algorithms (ZPHI, SC, MSC) show a universal underestimation of higher values of specific attenuation, though these values are less common. At vertical polarization, all of the histograms tighten up, showing less overall spread. All of the algorithms have greater concentrations of points along the one-to-one line, reinforcing the notion that all of the algorithms have decreased errors for vertical polarization. These results are reflected in Table 4.3, which shows that SC and MSC have the lowest biases at horizontal polarization, while all algorithms show lower values of mean squared-error (MSE) at vertical polarization.

Based on these results, it is also instructive to look at the results for differential attenuation, since it is more directly related to biases in Z_{DR}. Figures 4.9 and 4.10 show PPIs of differential attenuation and its difference from the true value, respectively. Here the Linear algorithm shows a clear high bias, of approximately $1.2\,\mathrm{dB}$, which would be a significant bias for Z_{DR}. ZPHI shows a decreased bias with respect

to this, though the errors still approach 1.0 dB. The SC algorithm again shows an overall unbiased field, with significant spatial variability in the errors. MSC appears to smooth this out well, though it is still showing errors of approximately 0.5 dB outside of the core, where there are slightly negative errors. The 2D histogram of specific differential attenuation, Figure 4.11, shows these same patterns of biases, including the negative biases of SC and MSC at higher values. Again, the calculated bias and MSE values (Table 4.3) favor the results of the SC and MSC algorithms.

Overall, all of the algorithms perform relatively well when the coefficients used agree with the nature of the data. Linear begins to show some problems correcting differential attenuation, as the resulting bias is high relative to the magnitude of Z_{DR}. It should also be noted that, given its better performance at vertical polarization, the problem stems from its bias at estimating horizontal attenuation. The Control experiment also demonstrates that the optimization procedure for SC does well at reducing the bias from the ZPHI algorithm, and subsequently the MSC does well at smoothing out the results from SC.

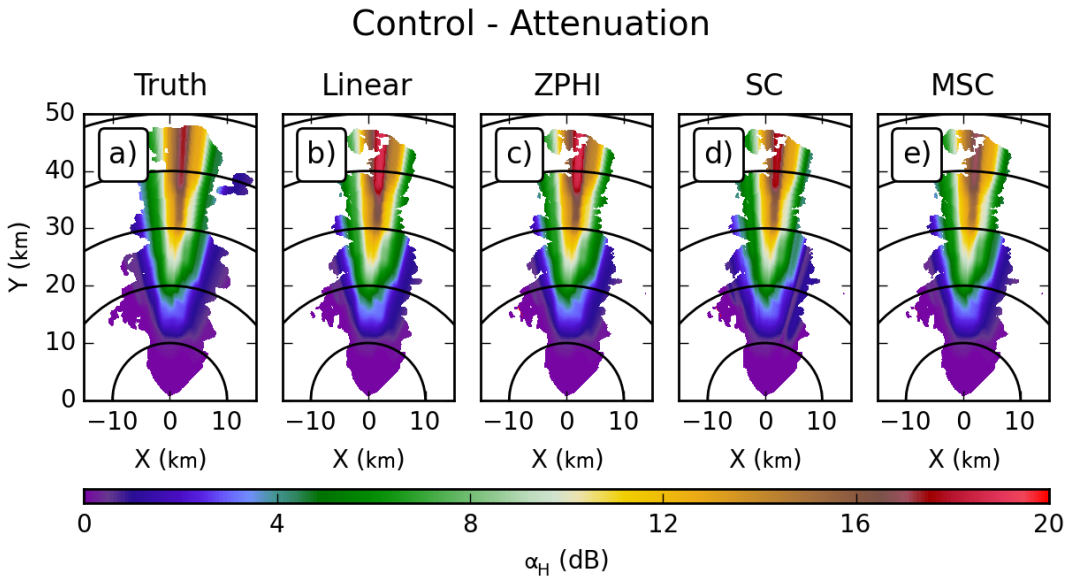

Figure 4.3: Plan Position Indicators (PPIs) of attenuation for horizontal polarization at C-band for the Control experiment from various sources: (a) True field calculated from model (b) Linear algorithm (c) ZPHI algorithm (d) Self-Consistent algorithm (e) Modified Self-Consistent algorithm. Range rings are plotted every 10 km from the radar.

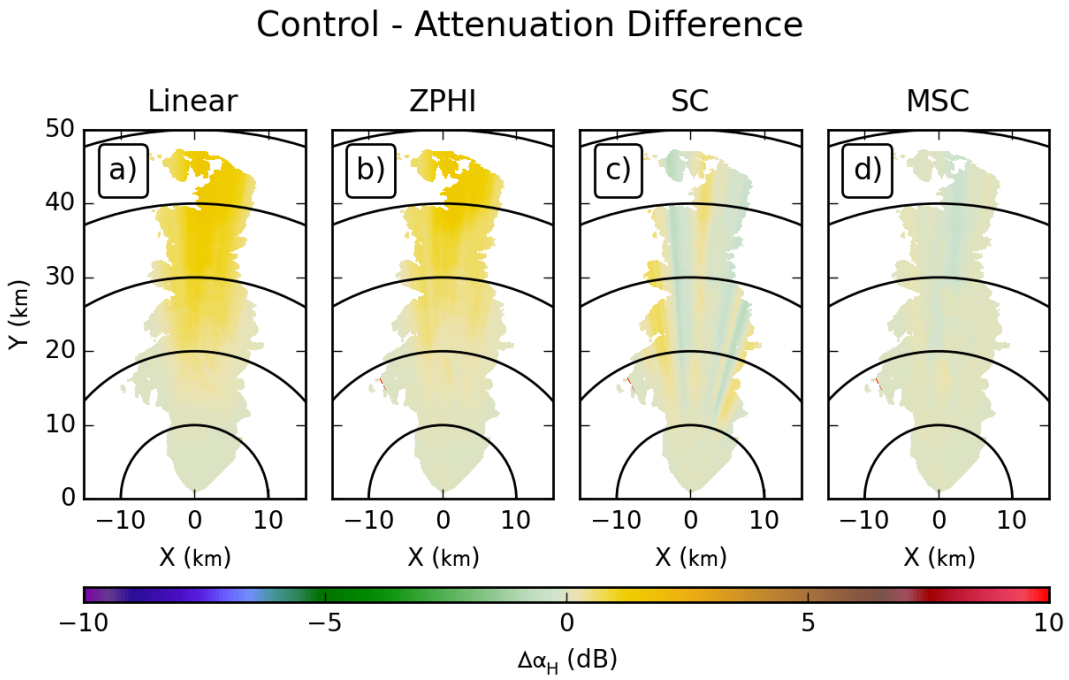

Figure 4.4: Plan Position Indicators (PPIs) for the Control experiment of the difference between the true horizontal attenuation values (from the model) at C-band and those calculated by algorithms: (a) Linear algorithm (b) ZPHI algorithm (c) Self-Consistent algorithm (d) Modified Self-Consistent algorithm. Range rings are plotted every 10 km from the radar.

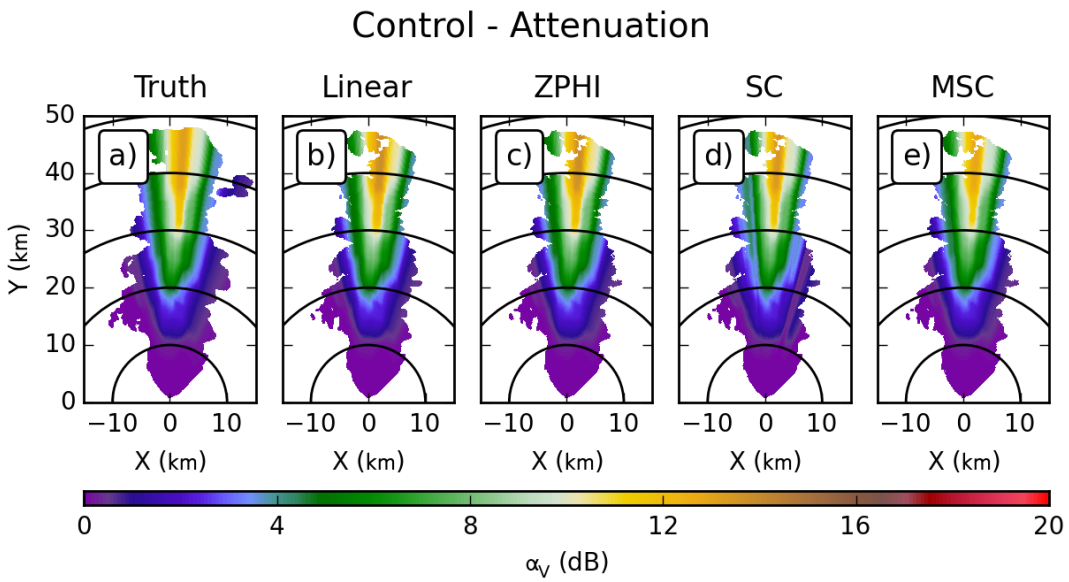

Figure 4.5: As in Figure 4.3, but for vertical polarization.

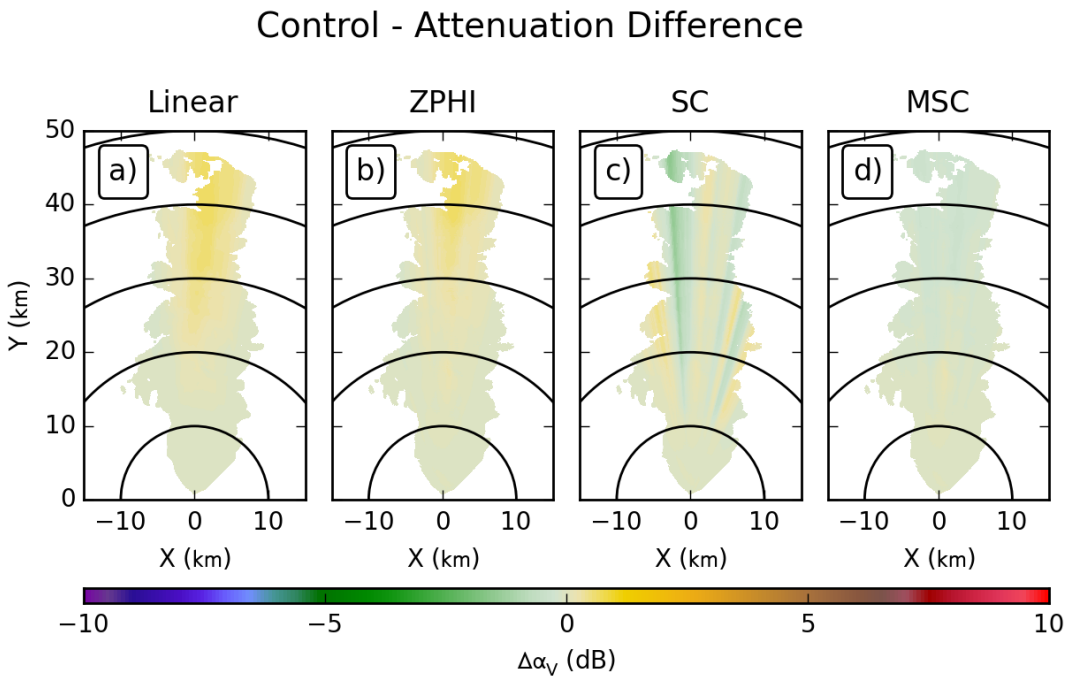

Figure 4.6: As in Figure 4.4, but for vertical polarization.

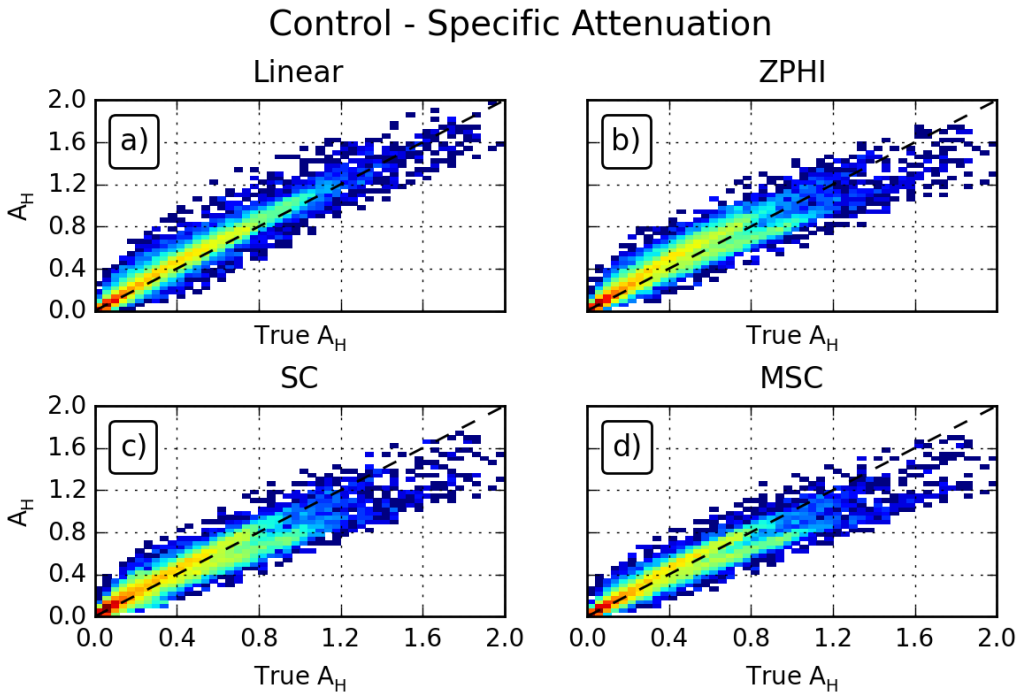

Figure 4.7: 2D histograms for the C-band Control experiment of true specific horizontal attenuation (x-axis) and calculated specific horizontal attenuation (y-axis) for: (a) Linear algorithm (b) ZPHI algorithm (c) Self-Consistent algorithm (d) Modified Self-Consistent algorithm.

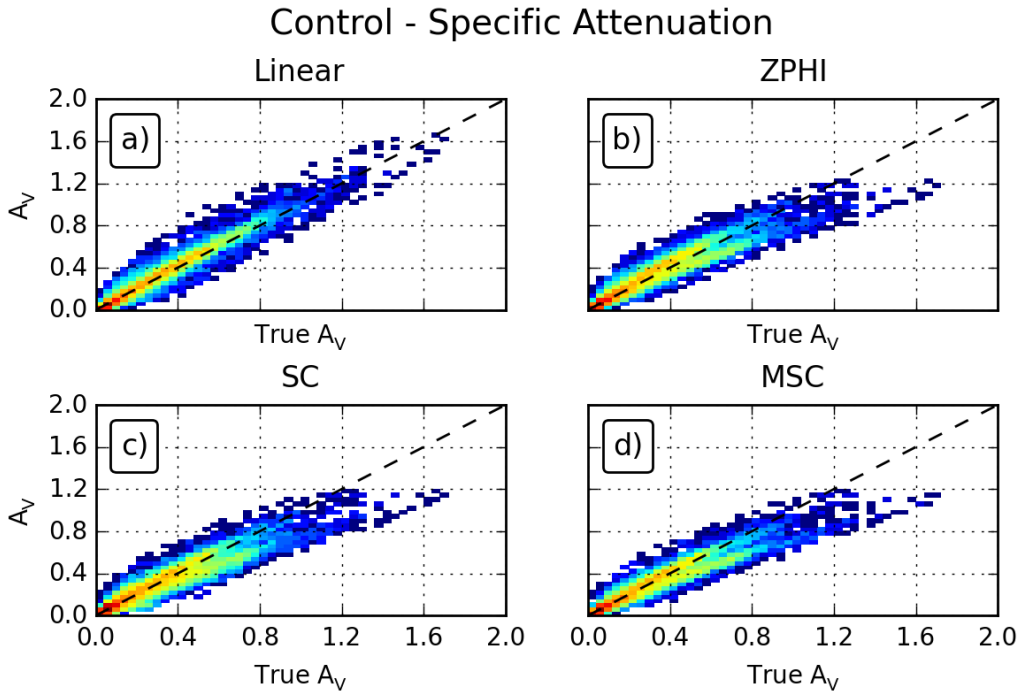

Figure 4.8: As in Figure 4.7 but for vertical polarization.

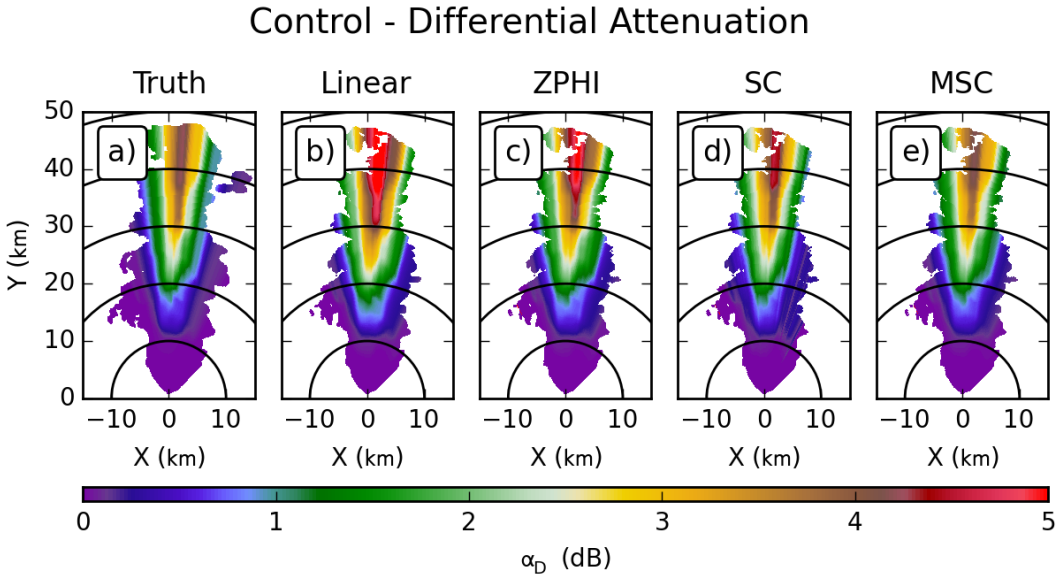

Figure 4.9: As in Figure 4.3 but for differential attenuation.

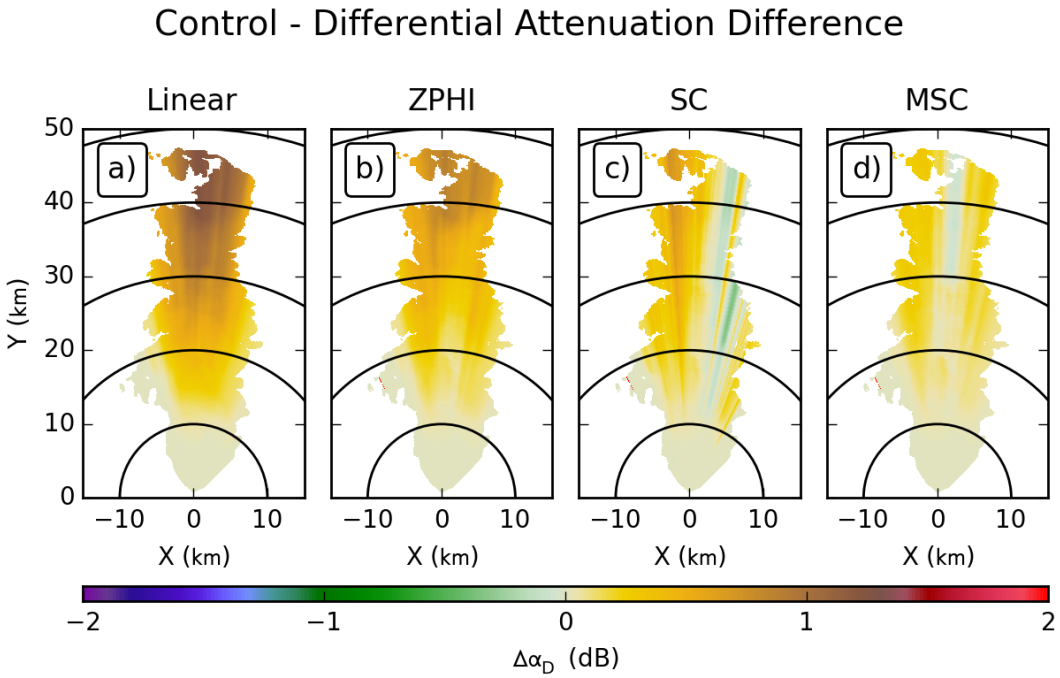

Figure 4.10: As in Figure 4.4 but for differential attenuation.

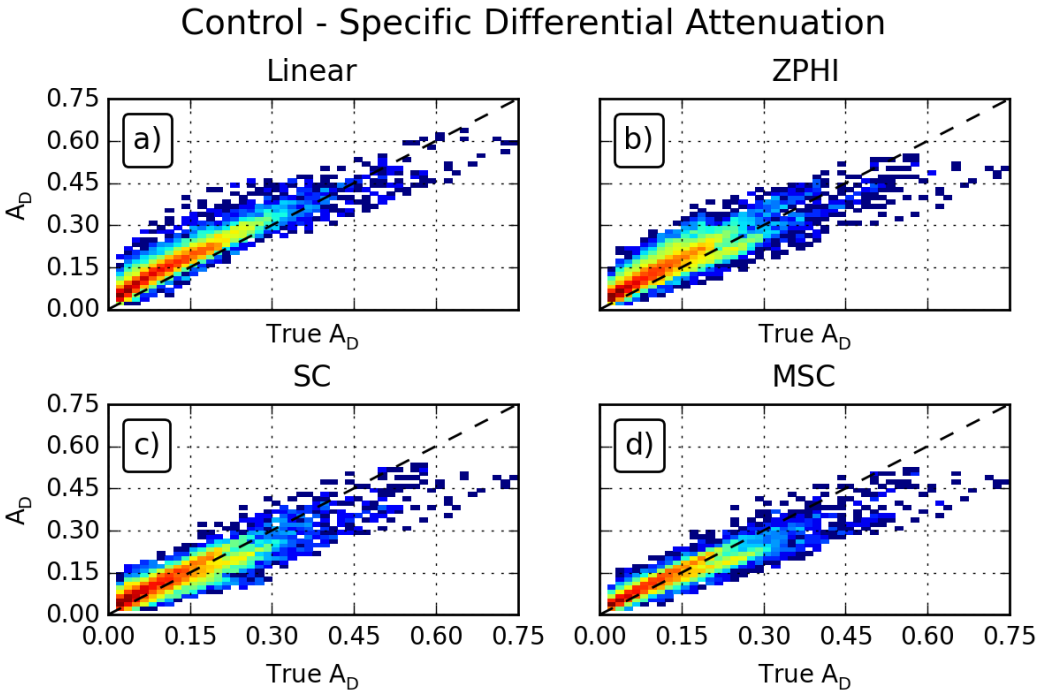

Figure 4.11: As in Figure 4.7 but for specific differential attenuation.

Algorithm	Bias (dB/km)	MSE (dB^2/km^2)	r^2
Horizontal			
Linear	0.0310	0.0047	0.9612
ZPHI	0.0281	0.0070	0.9233
SC	0.0074	0.0070	0.9173
MSC	-0.0009	0.0059	0.9305
Vertical			
Linear	0.0095	0.0020	0.9639
ZPHI	0.0071	0.0033	0.9240
SC	-0.0027	0.0042	0.9061
MSC	-0.0087	0.0034	0.9257
Differential			
Linear	0.0410	0.0023	0.9021
ZPHI	0.0287	0.0019	0.8291
SC	0.0091	0.0012	0.8315
MSC	0.0064	0.0009	0.8896

Table 4.3: Bias, mean squared-error, and r^2 for the specific attenuation results for the Control experiment at C-band.

4.1.2 X band

At X-band, the pattern of horizontal attenuation looks similar to that at C-band, as shown by the PPIs in Figure 4.12. One difference is that the core of highest attenuation values (now peaking around 100 dB) is in the area of missing data for the algorithms, since the actual data are completely attenuated here; the signal is well below the noise. As a result, the algorithms have no chance of matching truth here. For the ZPHI algorithms, it is also clear that they are not able to match the high values calculated by the Linear algorithm. From Figure 4.13 it is apparent, based on the differences when the true attenuation values are subtracted, that the Linear algorithm is doing much better than the other algorithms in this area along the outside of the core. This is likely caused by ZPHI's reliance on reflectivity data, which while above the noise threshold, are still heavily contaminated by the amount of attenuation incurred. Even outside these regions, the Linear algorithm appears to be doing the best job, though the other algorithms demonstrate more reasonable performance outside the heavily attenuated area. Once again, the radial-to-radial variations are clear in the differences for SC, which are eliminated by the MSC algorithm.

At vertical polarization, similar behavior is exhibited by the algorithms' base results (Figure 4.14) and the differences (Figure 4.15), though the errors (outside of the heavy attenuation zone) are reduced in magnitude. Looking at the 2D histograms of specific attenuation for both horizontal and vertical polarization in Figures 4.16 and 4.17, respectively, it is clear that the Linear algorithm matches the true attenuation values very well, with only slight underestimation at the highest values. For the ZPHI-based algorithms, again the two-banded structure is evident, with one band on either side of the one-to-one line.

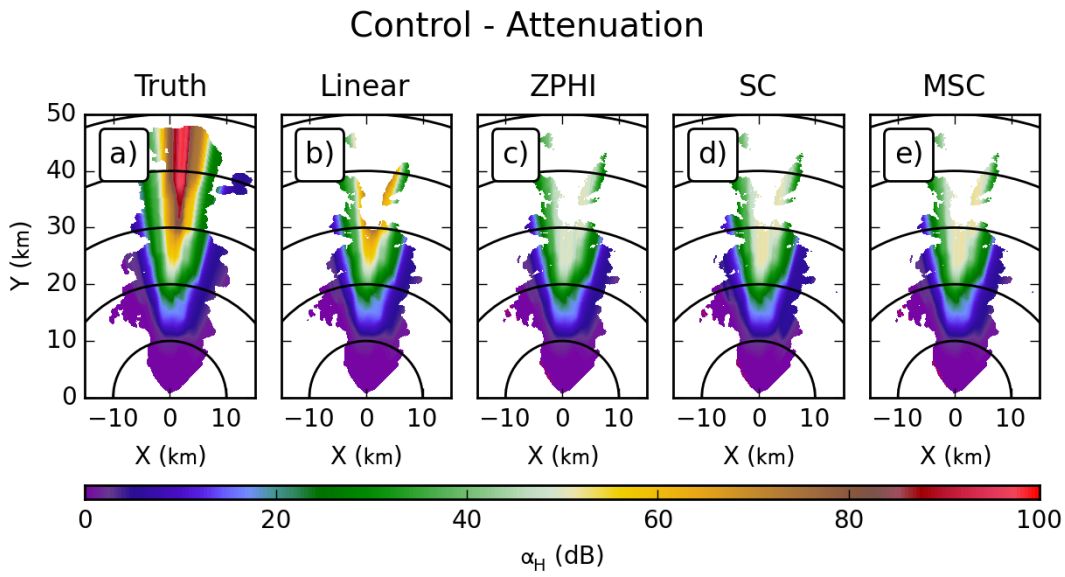

Figure 4.12: As in Figure 4.4 but for X-band.

The computed bias and MSE values for this experiment (Table 4.4) agree with these observations. While the Linear algorithm does not have the lowest bias, it is comparable to that of the other algorithms. The MSE for the Linear algorithm, is the lowest of all algorithms. It should also be noted that the difference in r^2 values between the Linear and ZPHI-based algorithms reflects the two-band structure present in the specific attenuation results.

For differential attenuation, the results in Figure 4.18 look very similar to those for the individual polarizations. In the differences from the true field (Figure 4.19), the zone where the ZPHI algorithms have problems has increased slightly in size; it now starts at 20 km range. Outside of this area, all of the algorithms look comparable, exhibiting a high bias in the estimated attenuation, with peak errors around 1.2 dB. In the 2D histograms for specific differential attenuation in Figure 4.20, these high

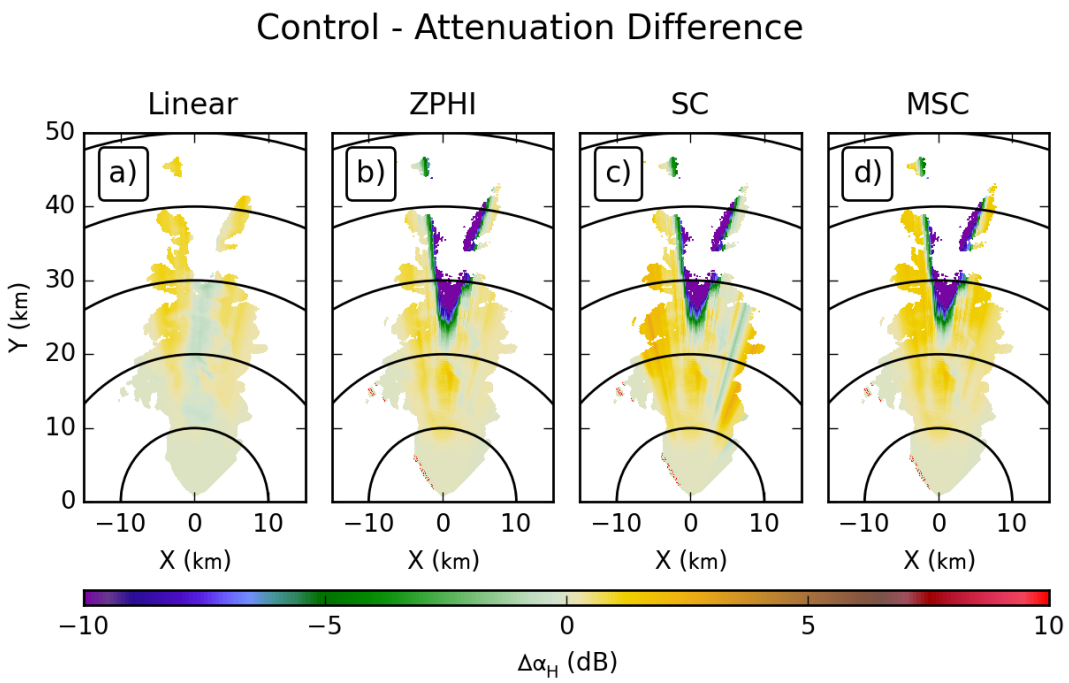

Figure 4.13: As in Figure 4.3 but for X-band.

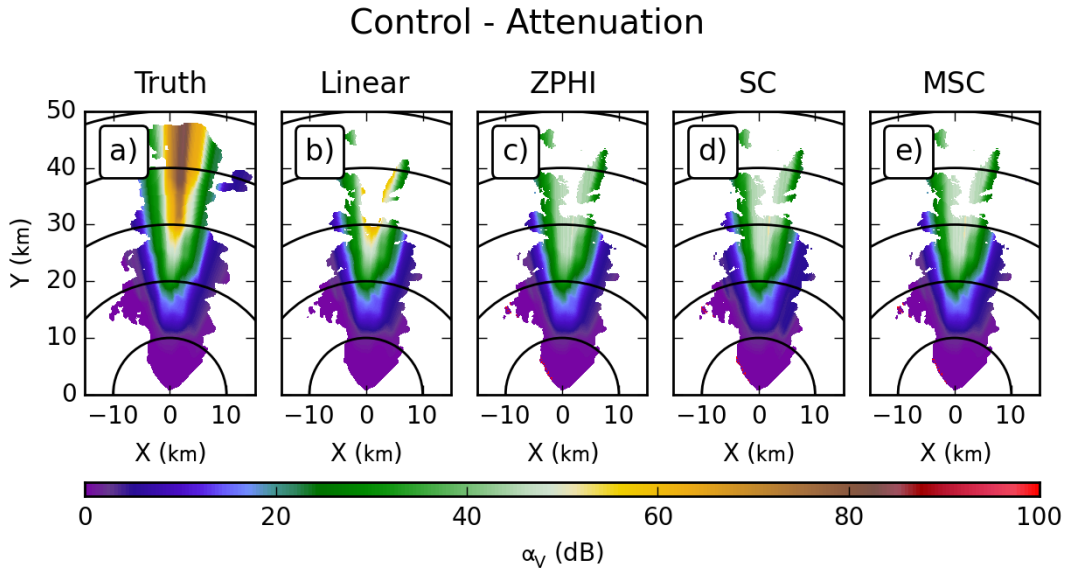

Figure 4.14: As in Figure 4.12 but for vertical polarization.

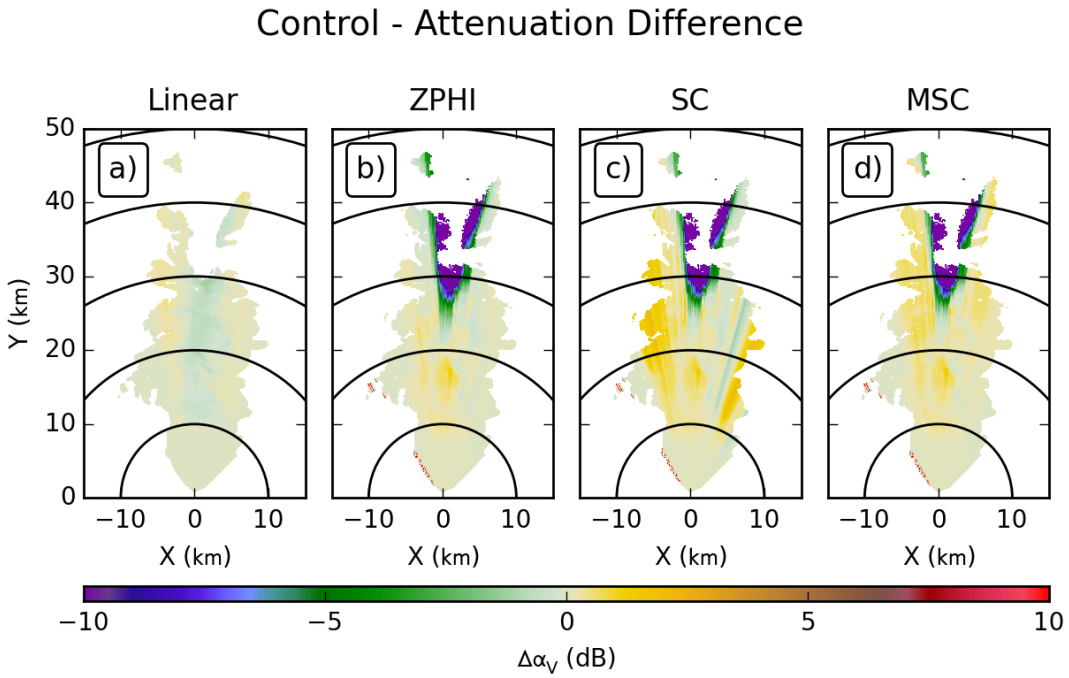

Figure 4.15: As in Figure 4.13 but for vertical polarization.

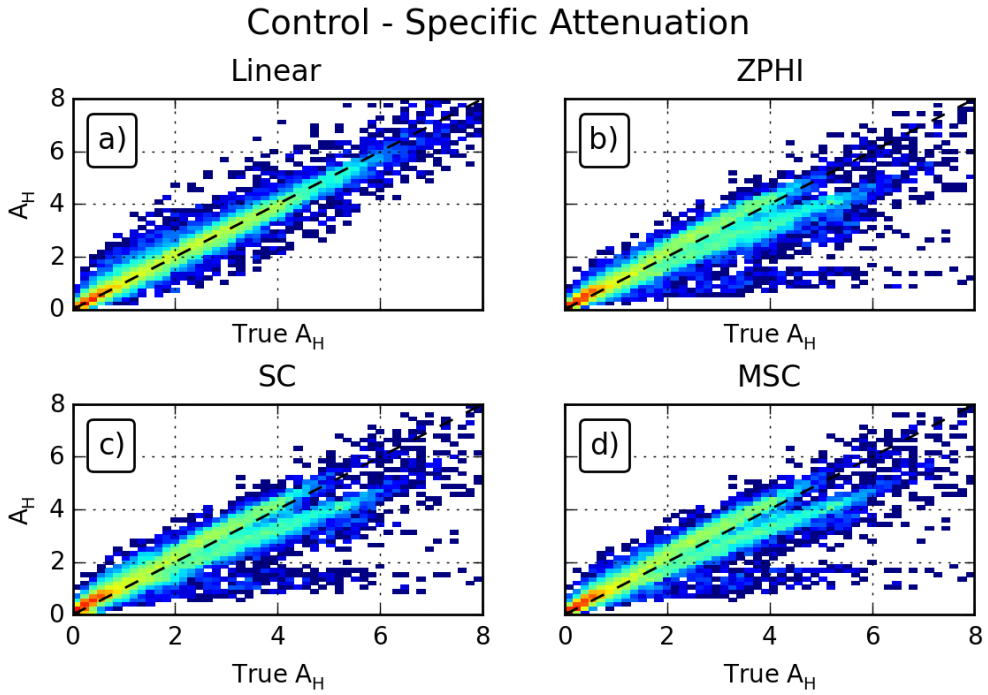

Figure 4.16: As in Figure 4.7 but for X-band.

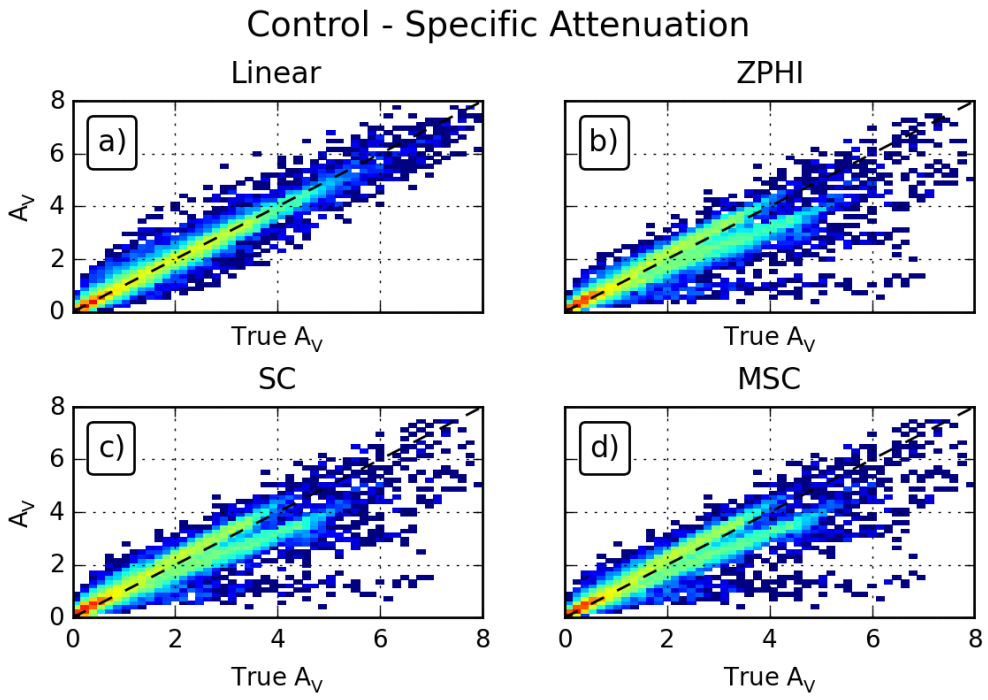

Figure 4.17: As in Figure 4.16 but for vertical polarization.

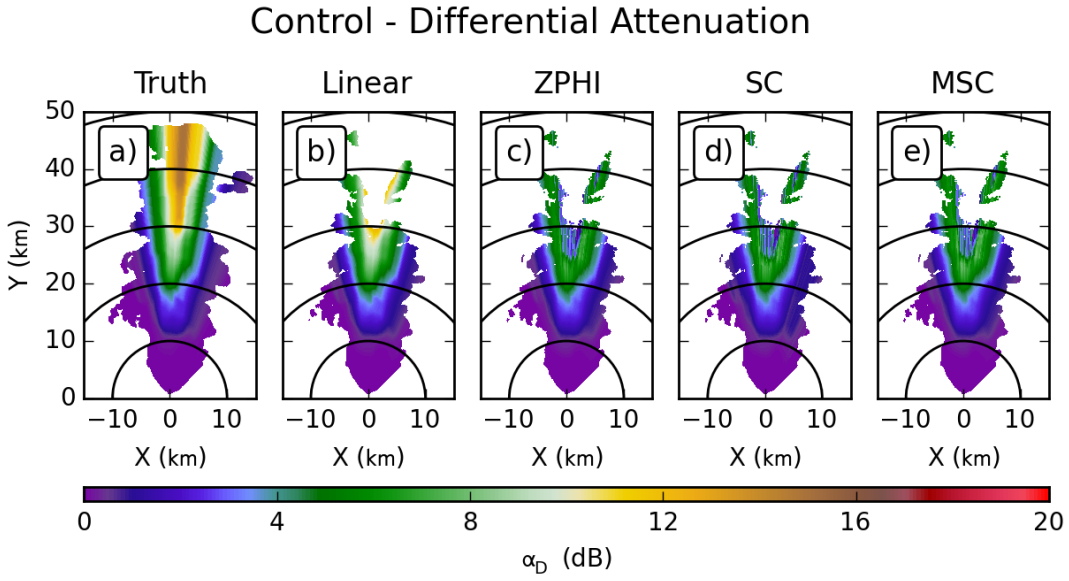

Figure 4.18: As in Figure 4.12 but for differential attenuation.

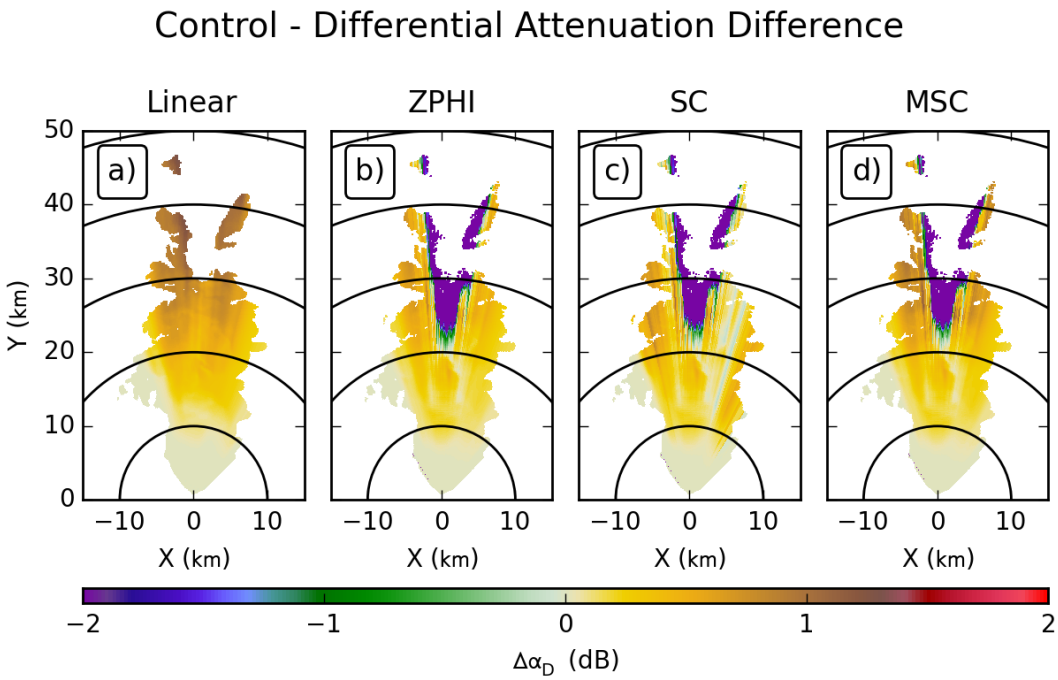

Figure 4.19: As in Figure 4.13 but for differential attenuation.

biases are clearly evident, with all of the algorithms having most of the values above the one-to-line.

Overall, for the Control experiment, the Linear algorithm shows the most success estimating attenuation at X-band, as its sole reliance on differential phase makes it more robust than the ZPHI-based algorithms, at least in this case. It should also be noticed that the performance of these latter algorithms were all very similar. This is unsurprising since SC and MSC do not need to optimize away from the base value; this value is already optimal for the assumptions used to simulate the data.

Algorithm	Bias (dB/km)	MSE (dB^2/km^2)	r^2
Horizontal			
Linear	0.0237	0.0722	0.9708
ZPHI	-0.0327	0.2279	0.9058
SC	0.0151	0.2200	0.9082
MSC	0.0079	0.1985	0.9157
Vertical			
Linear	-0.0004	0.0500	0.9712
ZPHI	-0.0414	0.1607	0.9071
SC	0.0036	0.1533	0.9098
MSC	-0.0115	0.1418	0.9160
Differential			
Linear	0.0384	0.0044	0.9561
ZPHI	0.0063	0.0120	0.8136
SC	0.0106	0.0118	0.8197
MSC	0.0216	0.0117	0.8201

Table 4.4: Bias, mean squared-error, and r^2 for the specific attenuation results for the Control experiment at X-band.

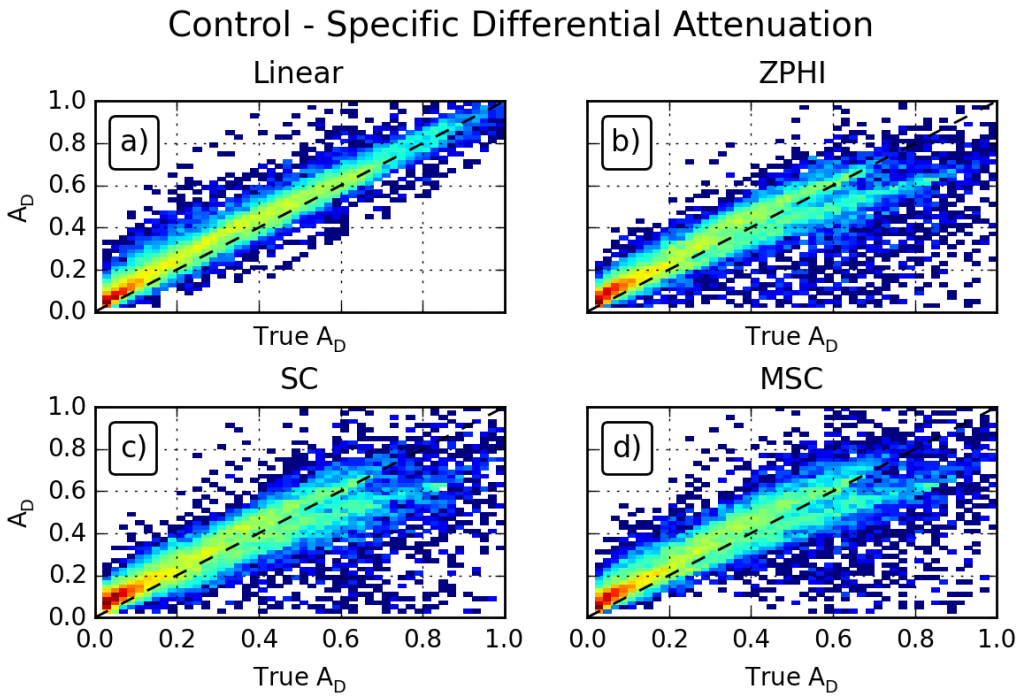

Figure 4.20: As in Figure 4.16 but for specific differential attenuation.

4.2 Canting

The Canting experiment modifies the Control experiment by changing the prescribed width of the canting angle distribution (κ in (2.56)) for the simulation from 10 to 20, changing the standard deviation of canting angles from $13.2°$ to $9.2°$. There still is no mean canting, only a narrower range of orientations distributed around $0°$. The effect of this decreased spread is to make the scatterers appear less isotropic to the radar, slightly increasing the magnitude of the dual-polarization signatures. Previously, Aydin et al. (1989), with an assumed Gaussian distribution of canting angles, found a $6\,\%$ error in K_{DP} resulted when increasing the standard deviation of canting angle from $0°$ to $10°$.

4.2.1 C band

In the Canting experiment, the horizontal attenuation estimates (Figure 4.21) show markedly higher values for the Linear and ZPHI algorithms, while SC and MSC show practically identical output compared to the Control experiment. The same is also true at vertical polarization (Figure 4.23). With the narrower distribution of angles, the intrinsic values of K_{DP}, and hence Φ_{DP} increase, causing the Linear and ZPHI algorithms to estimate more total path attenuation. The SC and MSC algorithms, however, by virtue of the optimization procedure, adjust their internal γ coefficient to account for the change in canting.

The impacts of this change are quite evident in the difference fields for horizontal (Figure 4.22) and vertical (Figure 4.24) polarizations. For the Linear and ZPHI algorithms, the errors increase to 3 dB, gaining around 1 dB in error from a simple change in canting; SC and MSC, conversely, show the same pattern of errors as in Control. These errors are also reflected in the histograms of specific attenuation at horizontal and vertical polarizations (Figures 4.25 and 4.26, respectively). Here the points for the Linear and ZPHI algorithms shift upwards, indicating a more pronounced positive bias. In contrast, the SC and MSC algorithms show qualitatively the same spread of points as in the Control experiment. The computed bias values (Table 4.5) for the SC and MSC algorithms are much lower for both polarizations; this decrease in bias comes with comparable (SC), or even slightly better (MSC), values for MSE.

For differential attenuation, Figure 4.27 shows an increase in attenuation as well, though this time the increase is for all algorithms, as well as the truth field. This increase in differential attenuation was likely concealed by the larger range of values at the individual polarizations. The differences from truth (Figure 4.28), show that

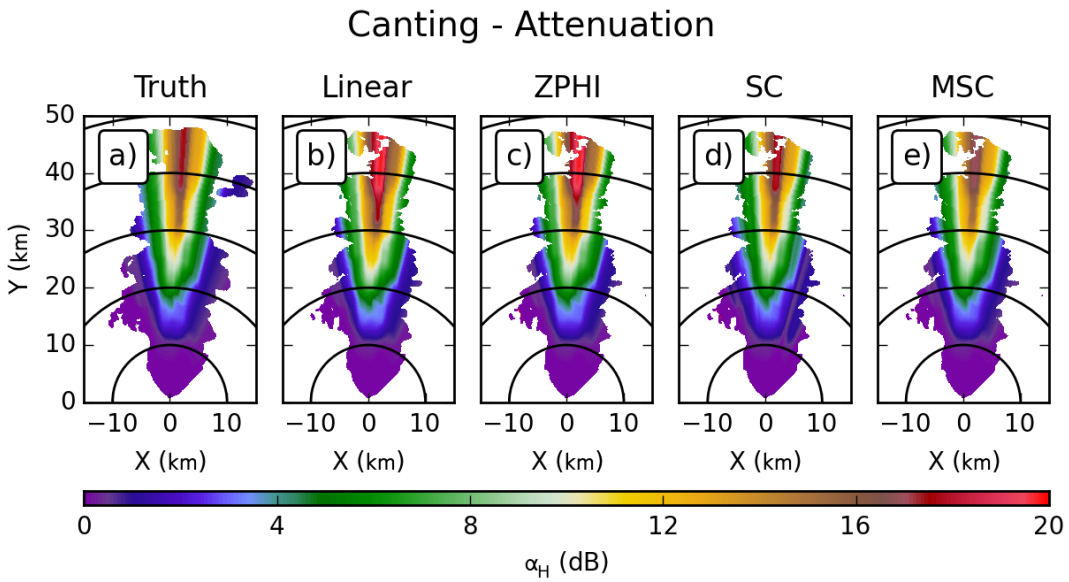

Figure 4.21: As in Figure 4.3 but for the Canting experiment.

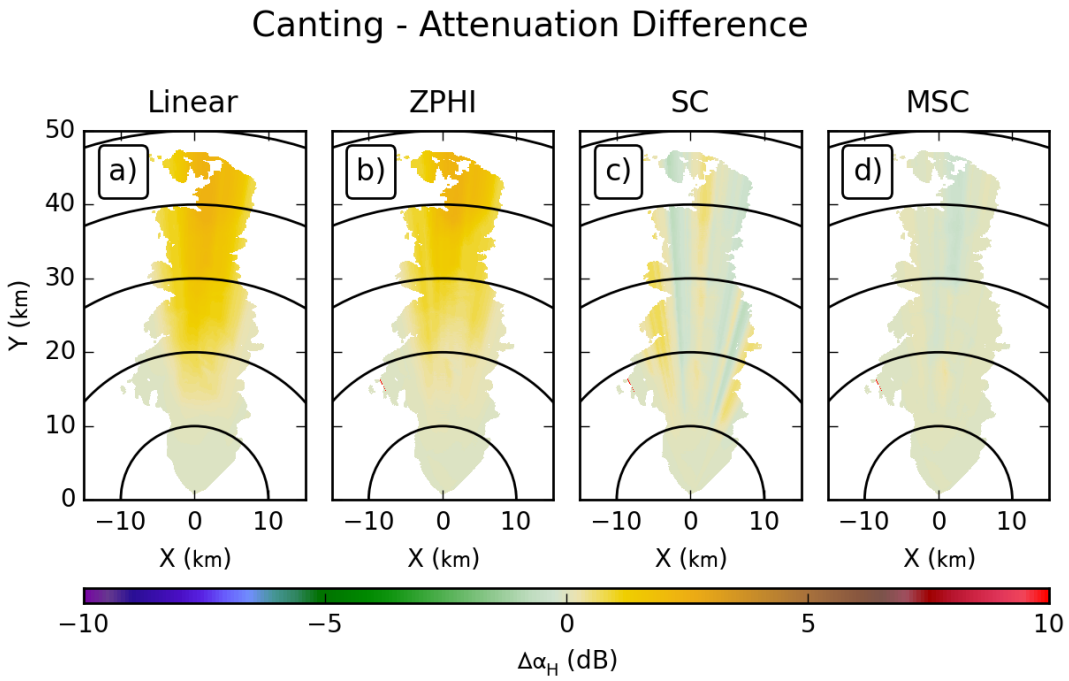

Figure 4.22: As in Figure 4.3 but for the Canting experiment.

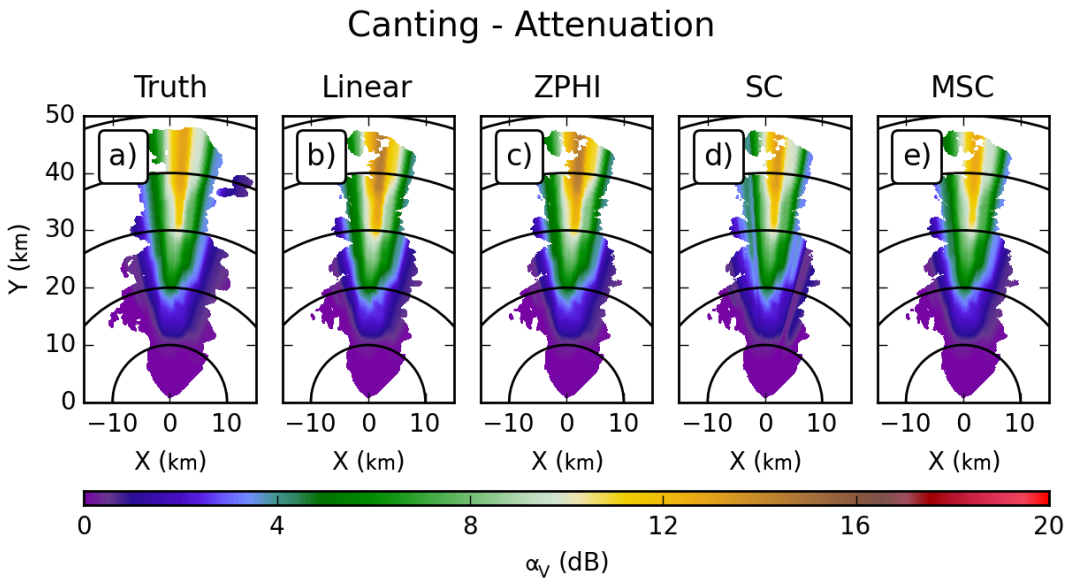

Figure 4.23: As in Figure 4.21 but for vertical polarization.

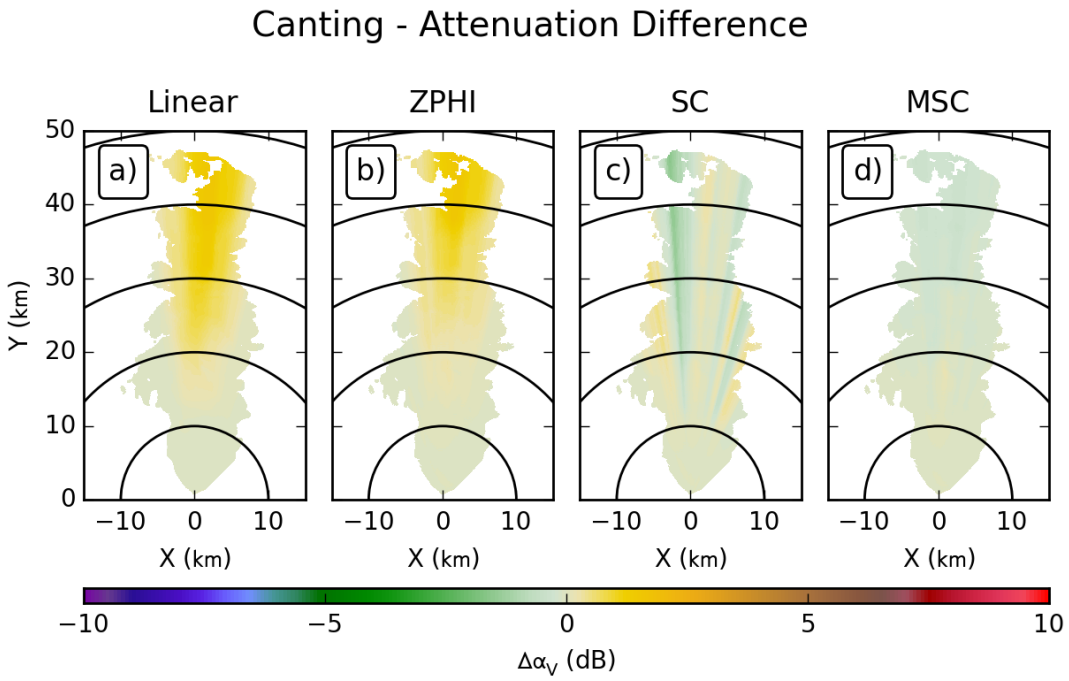

Figure 4.24: As in Figure 4.22 but for vertical polarization.

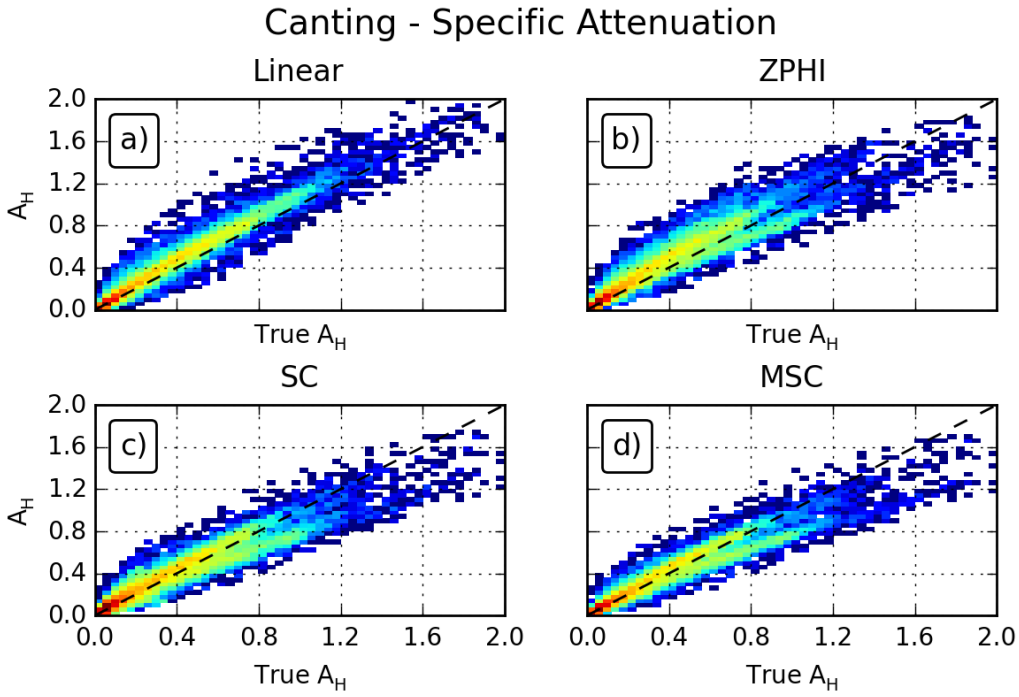

Figure 4.25: As in Figure 4.7 but for the Canting experiment.

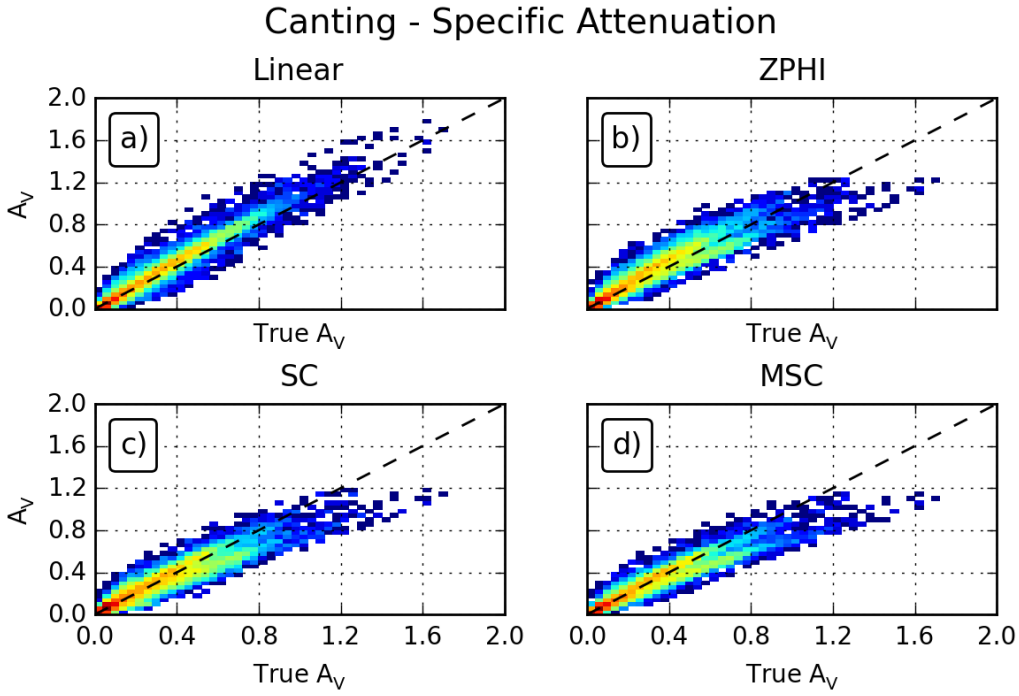

Figure 4.26: As in Figure 4.25 but for vertical polarization.

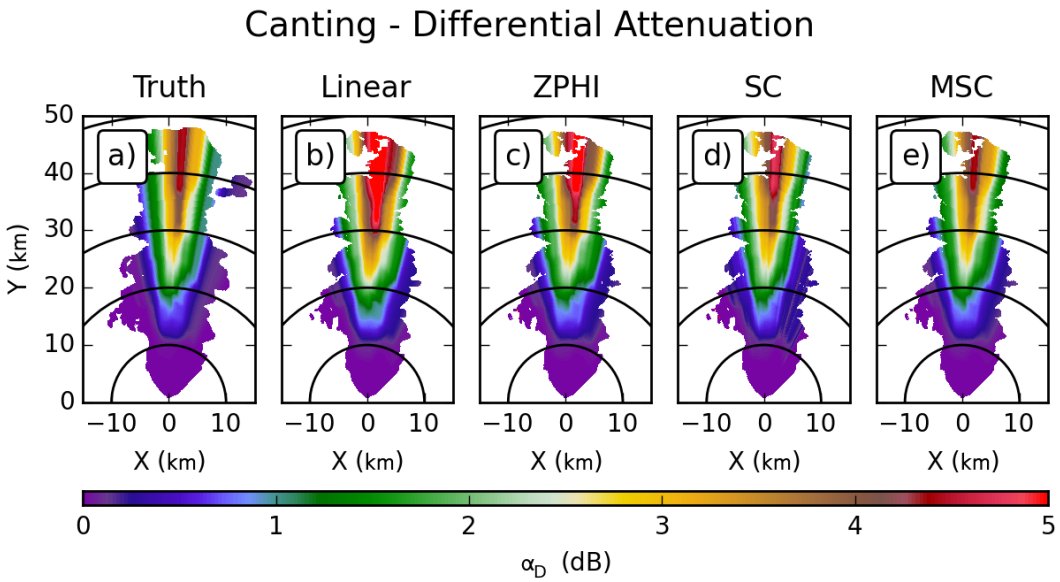

Figure 4.27: As in Figure 4.21 but for differential attenuation.

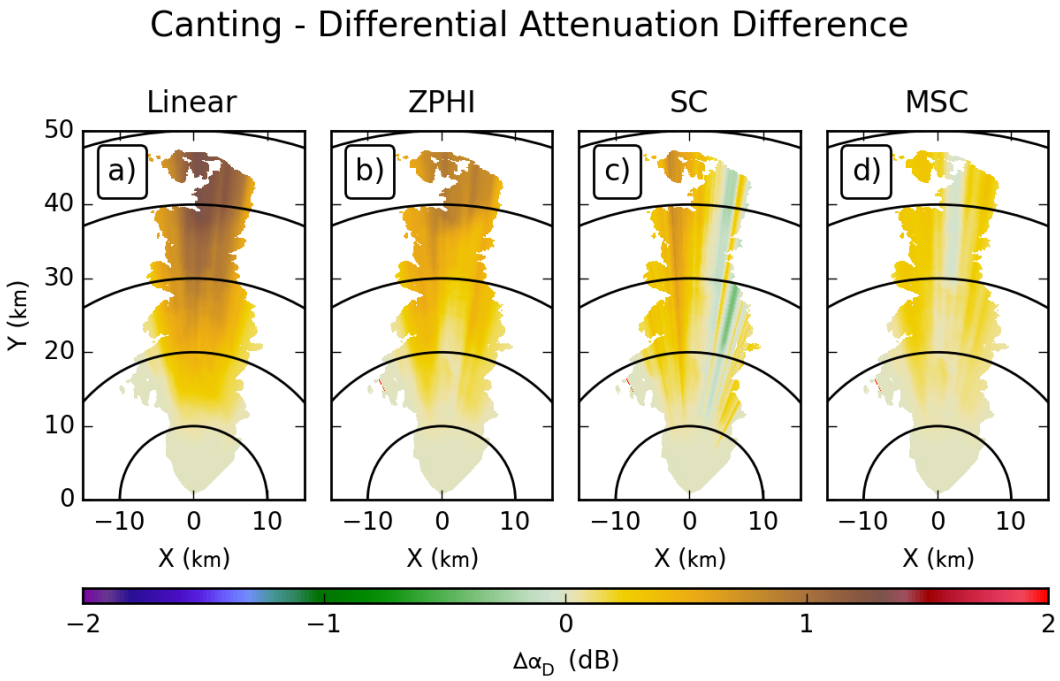

Figure 4.28: As in Figure 4.22 but for differential attenuation.

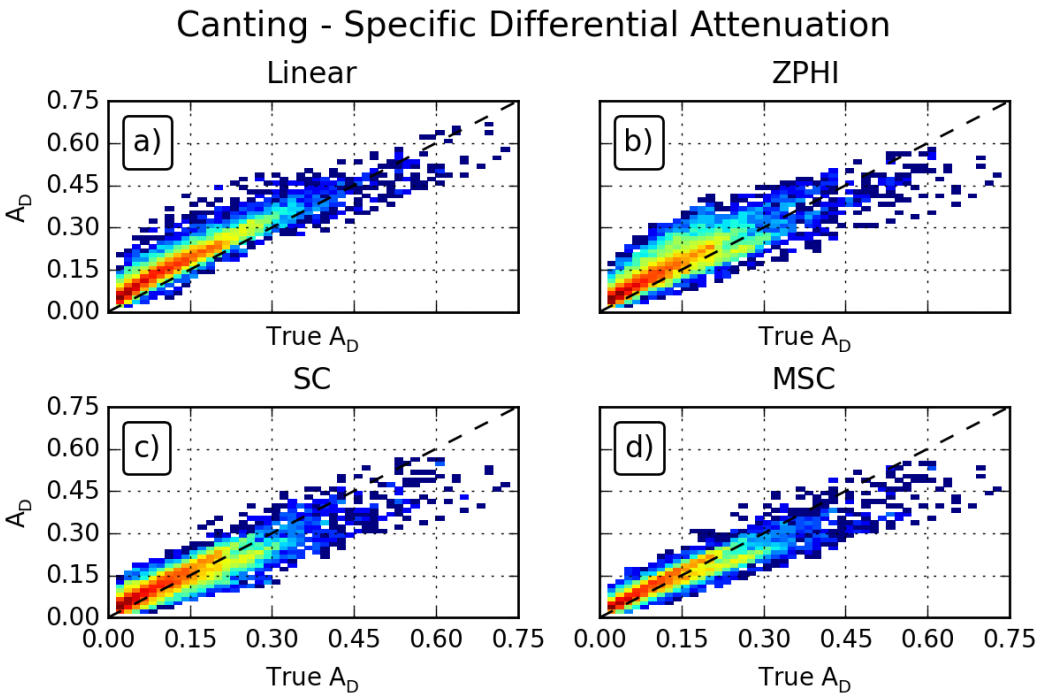

Figure 4.29: As in Figure 4.25 but for specific differential attenuation.

this increase in differential attenuation was well captured by all the algorithms. SC and MSC show only minor changes; Linear and ZPHI show slight increases in errors, on order of 0.2 dB, maintaining their overall positive bias. It should be noted, though, that this is not a negligible bias for Z_{DR}. The histogram of specific differential attenuation agrees with this, showing no shifts in the distributions of points. However, there are appreciable increases in the spread of points away from the one-to-one ratio line for the Linear and ZPHI algorithms; this indicates an overall reduction in accuracy for these algorithms.

Algorithm	Bias (dB/km)	MSE (dB^2/km^2)	r^2
Horizontal			
Linear	0.0465	0.0068	0.9612
ZPHI	0.0432	0.0094	0.9136
SC	0.0082	0.0071	0.9165
MSC	-0.0009	0.0060	0.9306
Vertical			
Linear	0.0243	0.0032	0.9642
ZPHI	0.0214	0.0041	0.9173
SC	-0.0024	0.0042	0.9037
MSC	-0.0096	0.0034	0.9254
Differential			
Linear	0.0430	0.0026	0.9035
ZPHI	0.0304	0.0024	0.8030
SC	0.0098	0.0013	0.8336
MSC	0.0077	0.0010	0.8916

Table 4.5: As in Table 4.3, but for the Canting experiment.

4.2.2 X band

The results at X-band mirror those for C-band, following from the same increase in differential phase due to the decrease in spread of canting angles. At both horizontal, Figure 4.30, and vertical, Figure 4.32, polarizations, the Linear and ZPHI algorithms show an increase in the calculated attenuation, while the SC and MSC algorithms show no perceptible changes; more importantly, the true attenuation does not change perceptibly. The difference fields in Figure 4.31 clarify this, showing that both Linear and ZPHI have a positive bias in their estimates of horizontal attenuation, with errors on the order of $3\,\mathrm{dB}$. This is a marked change from the Control experiment where both of these algorithms had results that were closer to being unbiased. There is an especially large change for the Linear algorithm due north from the radar, where the change is approximately $5\,\mathrm{dB}$. This same pattern is evident for vertical polarization in Figure 4.33, though the change for the Linear algorithm is more stark given the minimal errors that were present in its output for the Control experiment. The histograms for specific attenuation at horizontal, Figure 4.34, and vertical, Figure 4.35, polarizations show a shift in points upwards for the Linear and ZPHI algorithms, agreeing with the observed increase in bias. The histograms for the SC and MSC show no qualitative changes, which is also in agreement with the PPIs of attenuation; the computed bias values (Table 4.6) change much more for the Linear and ZPHI algorithms than for the SC and MSC algorithms.

The results for differential attenuation also agree with those at C-band. While the actual differential attenuation values in Figure 4.36 show moderately larger value across the board, the difference from the true values in Figure 4.37 show no appreciable difference from the results for the Control experiment. The results for ZPHI show

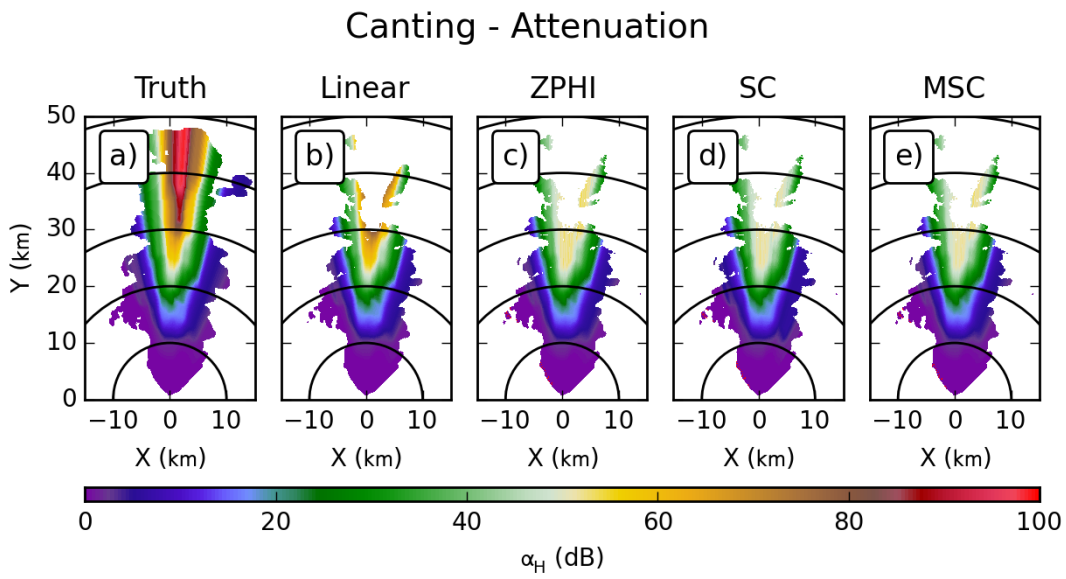

Figure 4.30: As in Figure 4.21 but for X-band.

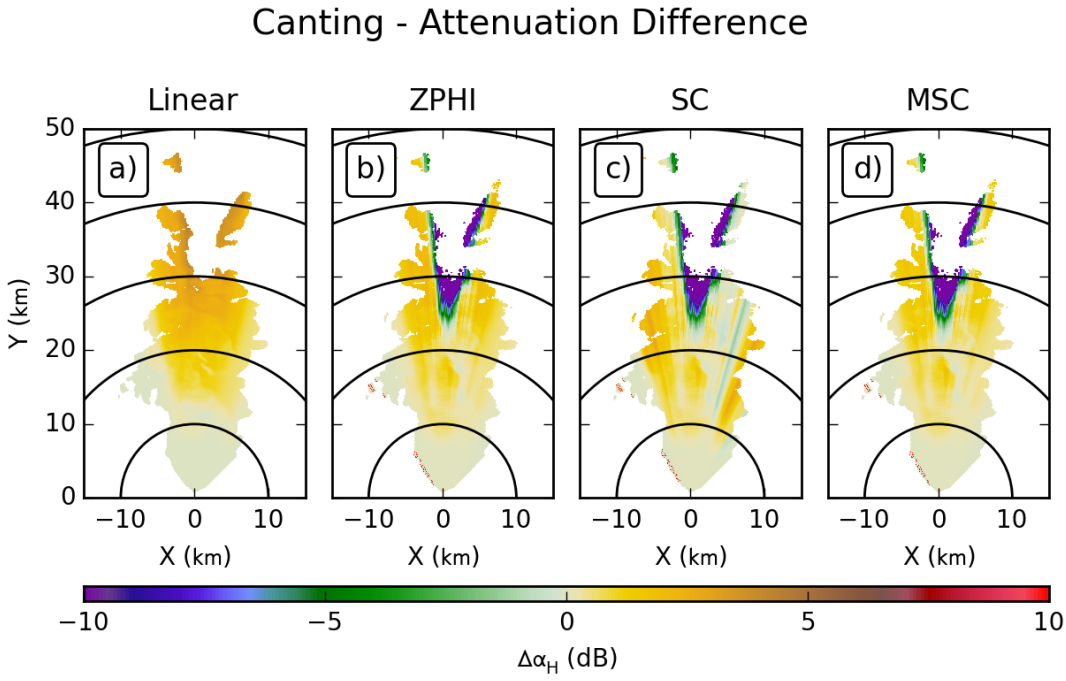

Figure 4.31: As in Figure 4.22 but for X-band.

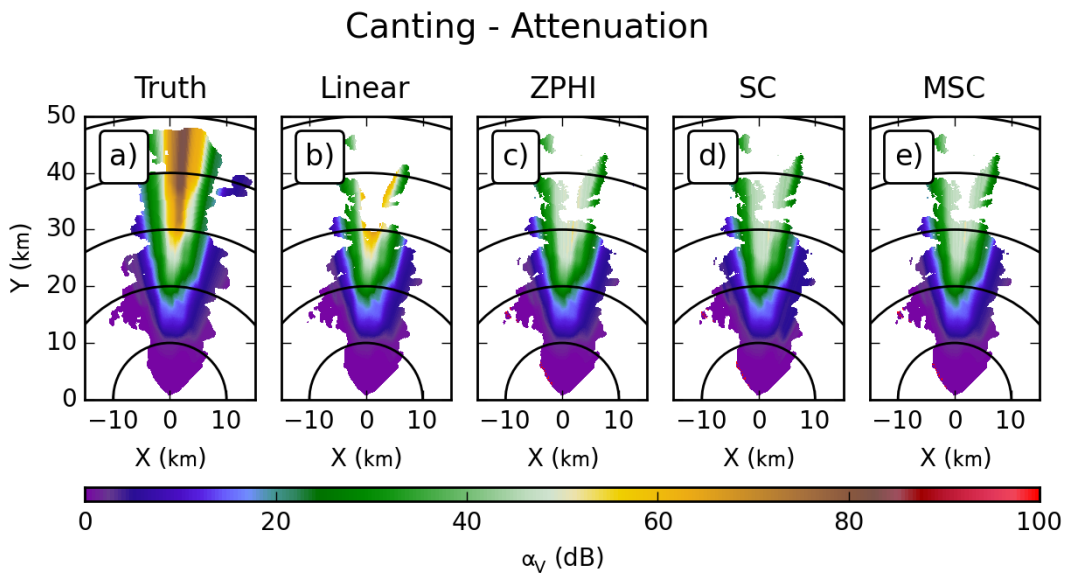

Figure 4.32: As in Figure 4.30 but for vertical polarization.

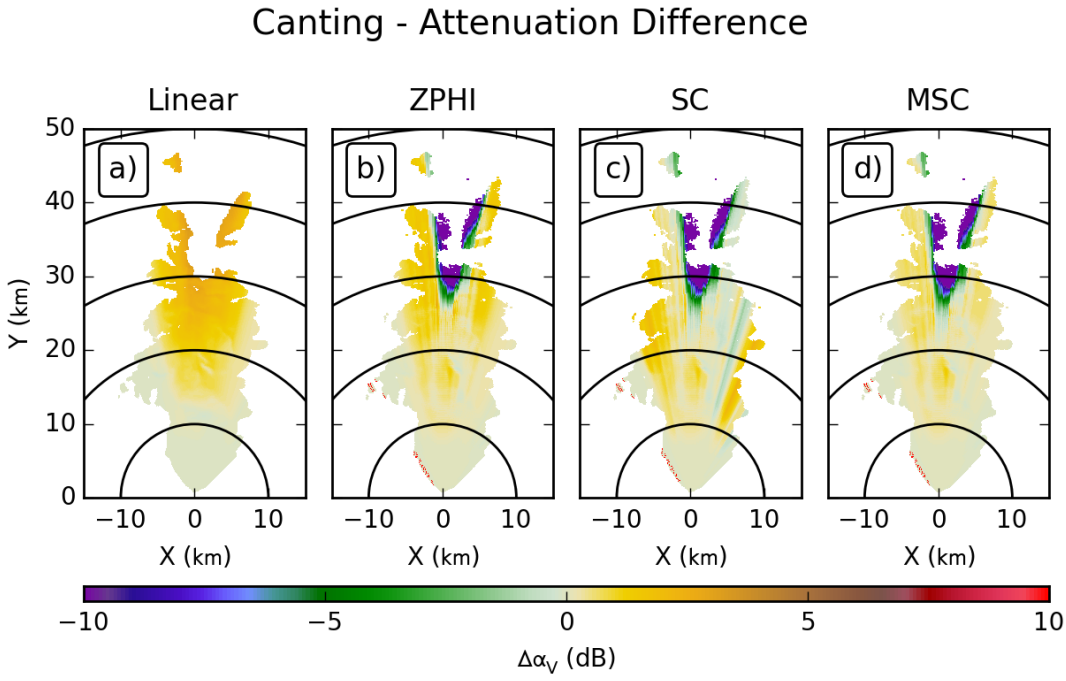

Figure 4.33: As in Figure 4.31 but for vertical polarization.

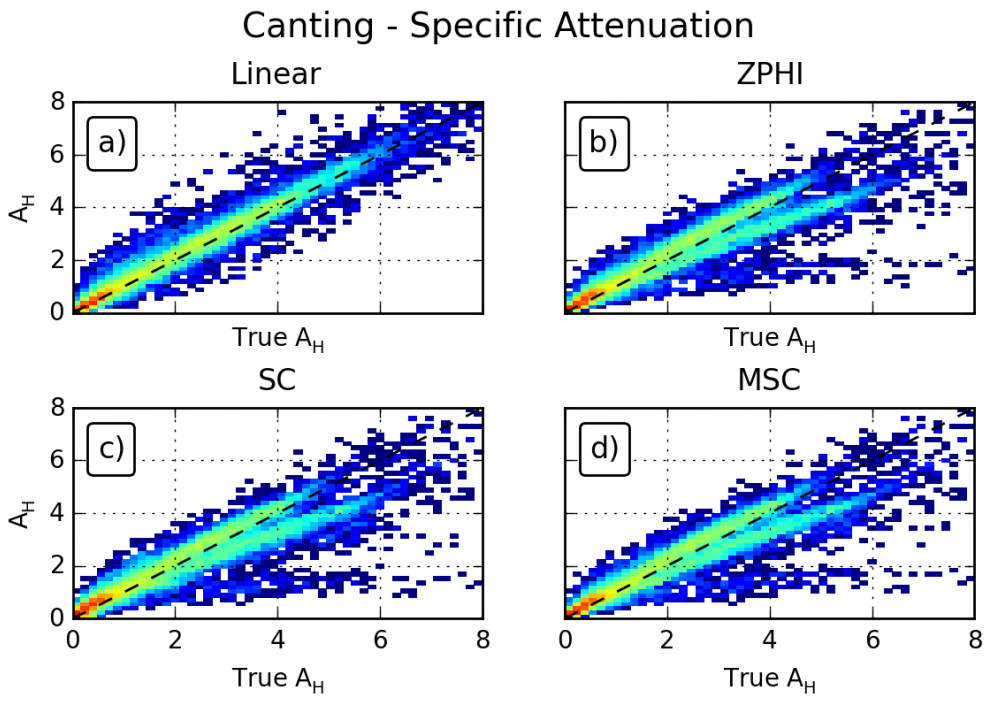

Figure 4.34: As in Figure 4.25 but for X-band.

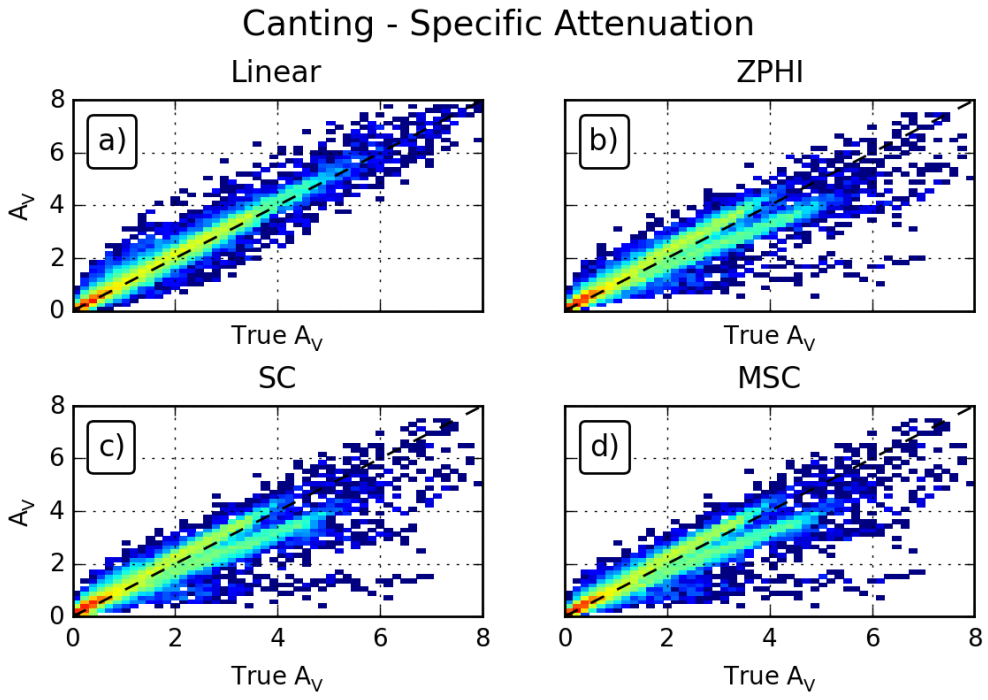

Figure 4.35: As in Figure 4.34 but for vertical polarization.

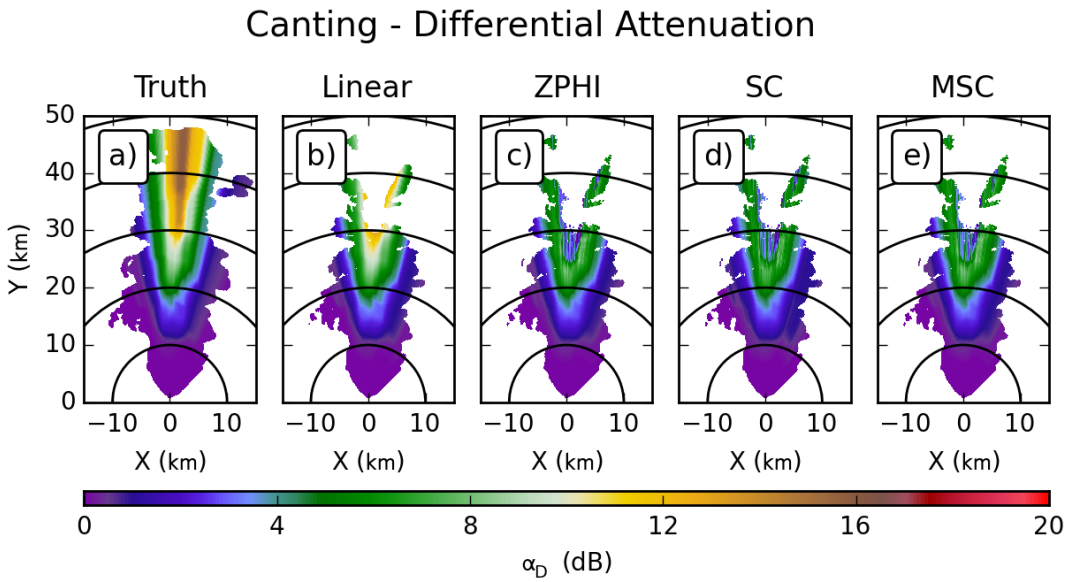

Figure 4.36: As in Figure 4.30 but for differential attenuation.

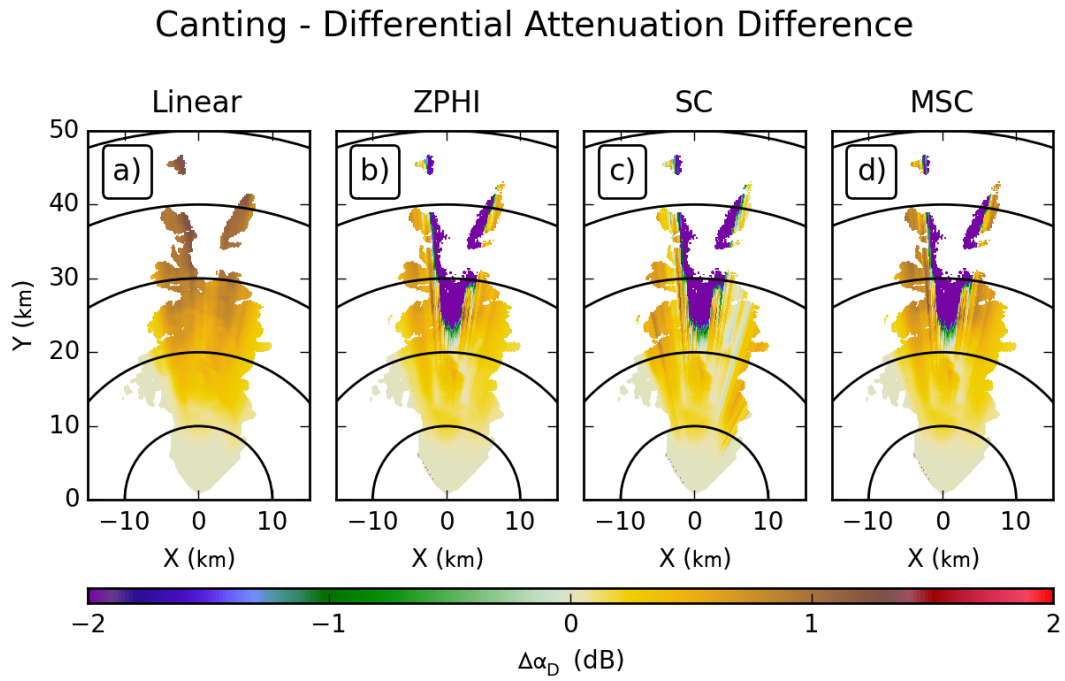

Figure 4.37: As in Figure 4.31 but for differential attenuation.

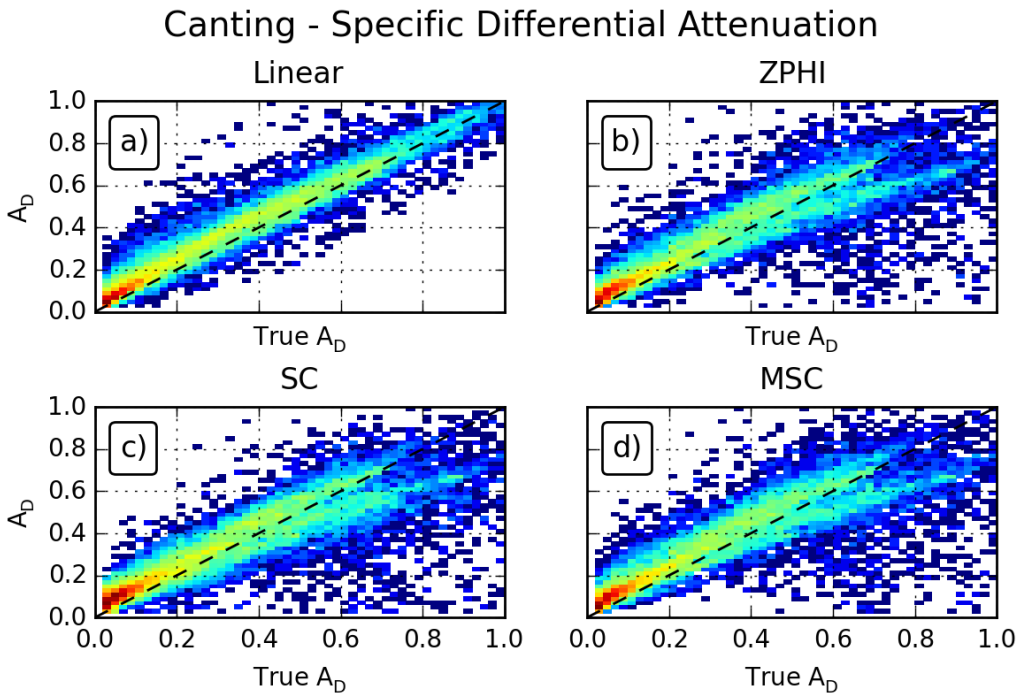

Figure 4.38: As in Figure 4.34 but for specific differential attenuation.

some changes in the highest core of attenuation, but this is on the fringes of the fully-extinguished signal, so values here are likely sensitive to the signal-to-noise ratio. This change does produce a difference in the histogram of specific differential attenuation, in Figure 4.38. Here the ZPHI algorithm has noticeably shifted many points from well below the one-to-one line to above, and the core bands have shifted upwards as well; this is likely a reflection of moving some of the anomalously low points closer to their true values. The effect of this change is an increase in the net bias for the ZPHI algorithm (Table 4.6); this increase is the largest of any of the algorithms.

Algorithm	Bias (dB/km)	MSE (dB^2/km^2)	r^2
Horizontal			
Linear	0.0960	0.0862	0.9709
ZPHI	0.0330	0.1882	0.9200
SC	0.0185	0.2225	0.9080
MSC	0.0096	0.1977	0.9167
Vertical			
Linear	0.0716	0.0597	0.9713
ZPHI	0.0250	0.1284	0.9219
SC	0.0066	0.1530	0.9091
MSC	-0.0102	0.1392	0.9166
Differential			
Linear	0.0404	0.0049	0.9564
ZPHI	0.0182	0.0120	0.8322
SC	0.0107	0.0129	0.8219
MSC	0.0220	0.0129	0.8216

Table 4.6: As in Table 4.4, but for the Canting experiment.

4.3 Shape

The Shape experiment modifies the Control experiment by changing the prescribed shape model (i.e., the relationship between drop axis ratio and size) from the Brandes et al. (2002) polynomial model to the Pruppacher and Beard (1970) model. Given that both models are empirical fits to data, neither one represents a guaranteed match to natural processes. Instead, this experiment is designed to highlight the sensitivity of the algorithms (through the coefficients) to the chosen drop shape model by examining how performance changes when the assumption is violated.

4.3.1 C band

In the Shape experiment, the results for horizontal attenuation in Figure 4.39 for the Linear and ZPHI algorithms show very pronounced increases from the values in the Control experiment. These values are well excess of those shown by the true attenuation field. The SC algorithm shows only a minor increase over the results from the Control experiment, while the MSC algorithm actually shows a decrease. For vertical polarization, in Figure 4.41, the results are similar. For the difference from the true values of horizontal attenuation, Figure 4.40 shows that the errors for Linear and ZPHI have increased to almost $6\,\mathrm{dB}$ (from initial errors around $1\,\mathrm{dB}$). For SC, while the errors of individual rays have changed, the overall error field remains unbiased, with a slight increase in the amount of negative departure for some rays. The MSC algorithm now shows a negative bias, with the peak of errors now approaching $1\,\mathrm{dB}$,

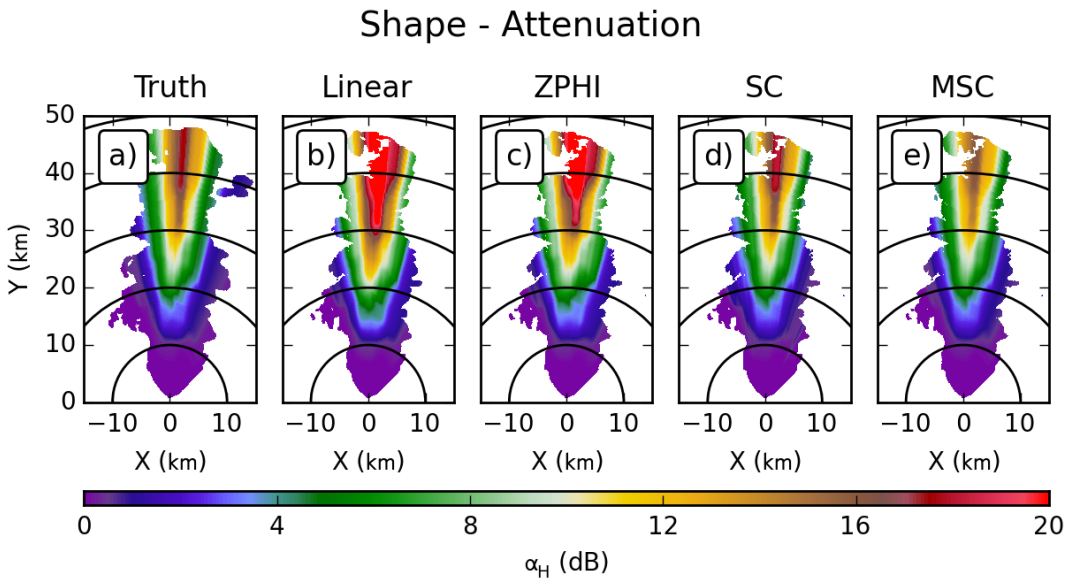

Figure 4.39: As in Figure 4.3 but for the Shape experiment.

in contrast with errors very close to 0 dB for the Control experiment. For vertical polarization (Figure 4.42), the results are qualitatively identical, though the magnitudes of the errors are slightly smaller.

Looking at the histograms of specific attenuation for horizontal and vertical polarizations, in Figures 4.43 and 4.44, respectively, the pronounced bias for the Linear algorithm is clearly visible. For the ZPHI algorithm, not only is the increase in bias visible, but the points are much more spread out. The SC algorithm does not show any significant changes, though there is a small region of points that now extend above the main core of points; this was not present in the Control experiment. For the MSC algorithm, the curve of points now slopes slightly further down, agreeing with the observation of the increase in negative bias.

The results at horizontal and vertical polarizations lead to a similar pattern of results for differential attenuation. The PPIs of the raw data in Figure 4.45 show the

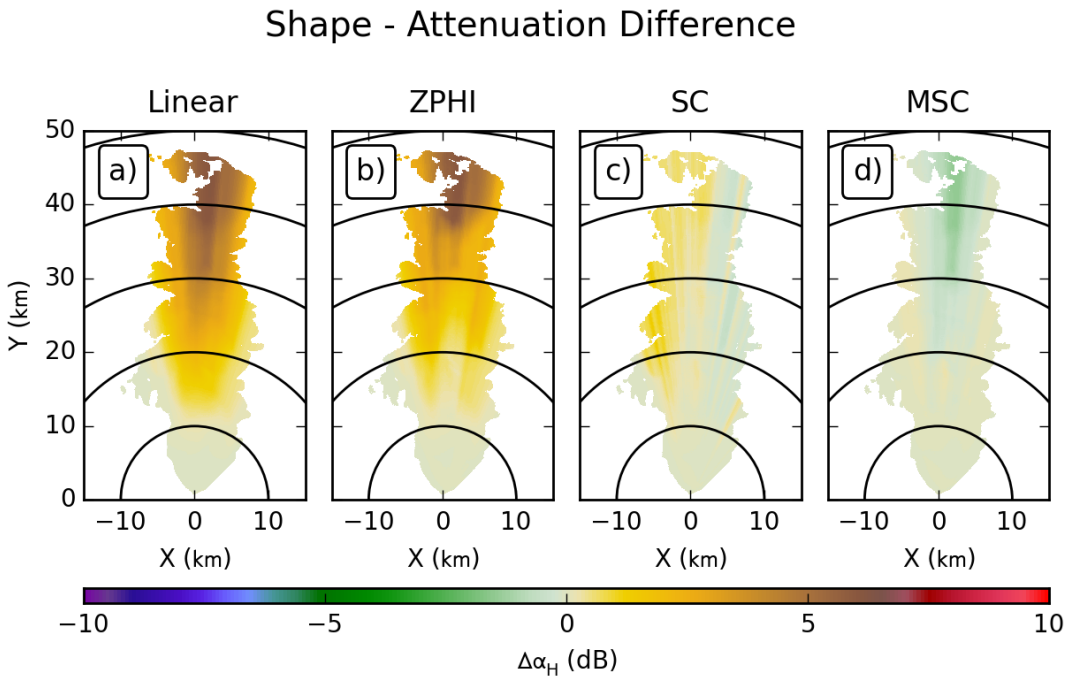

Figure 4.40: As in Figure 4.4 but for the Shape experiment.

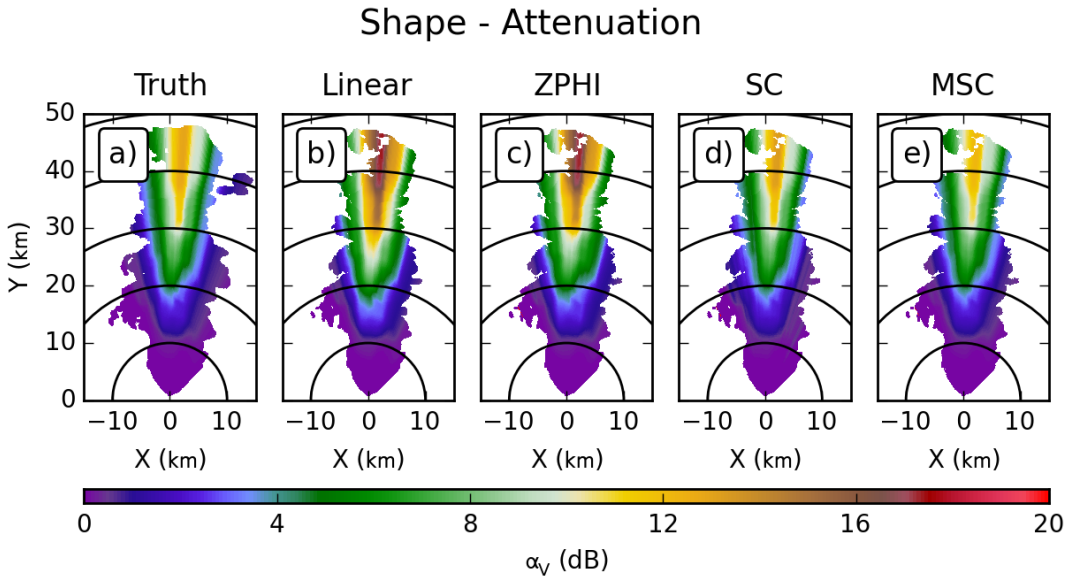

Figure 4.41: As in Figure 4.39 but for vertical polarization.

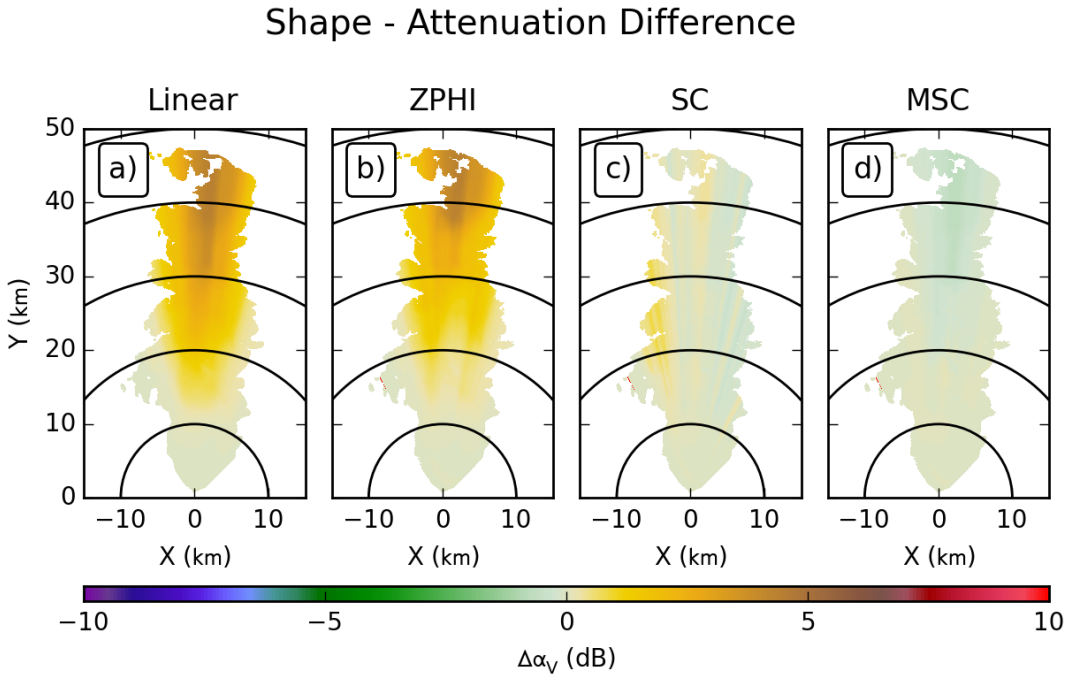

Figure 4.42: As in Figure 4.40 but for vertical polarization.

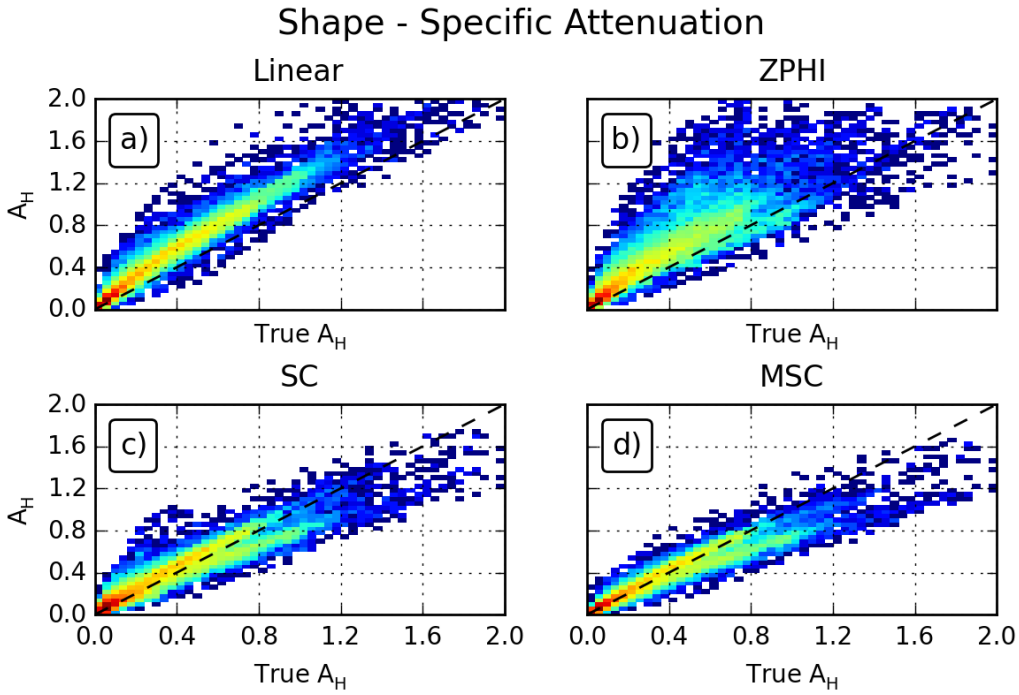

Figure 4.43: As in Figure 4.7, but for the Shape experiment.

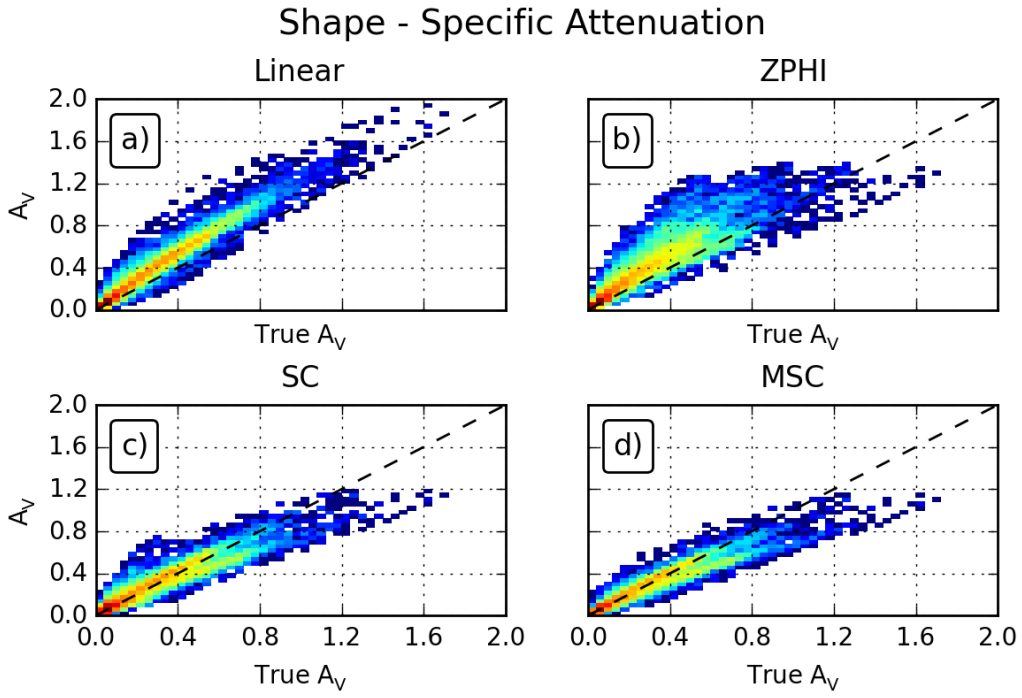

Figure 4.44: As in Figure 4.43, but for vertical polarization.

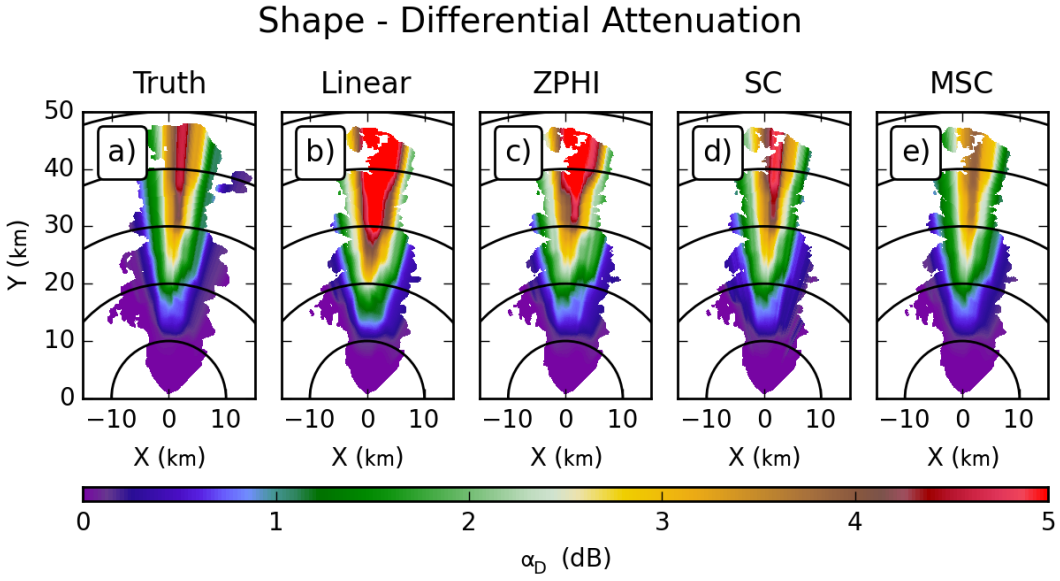

Figure 4.45: As in Figure 4.39, but for differential attenuation.

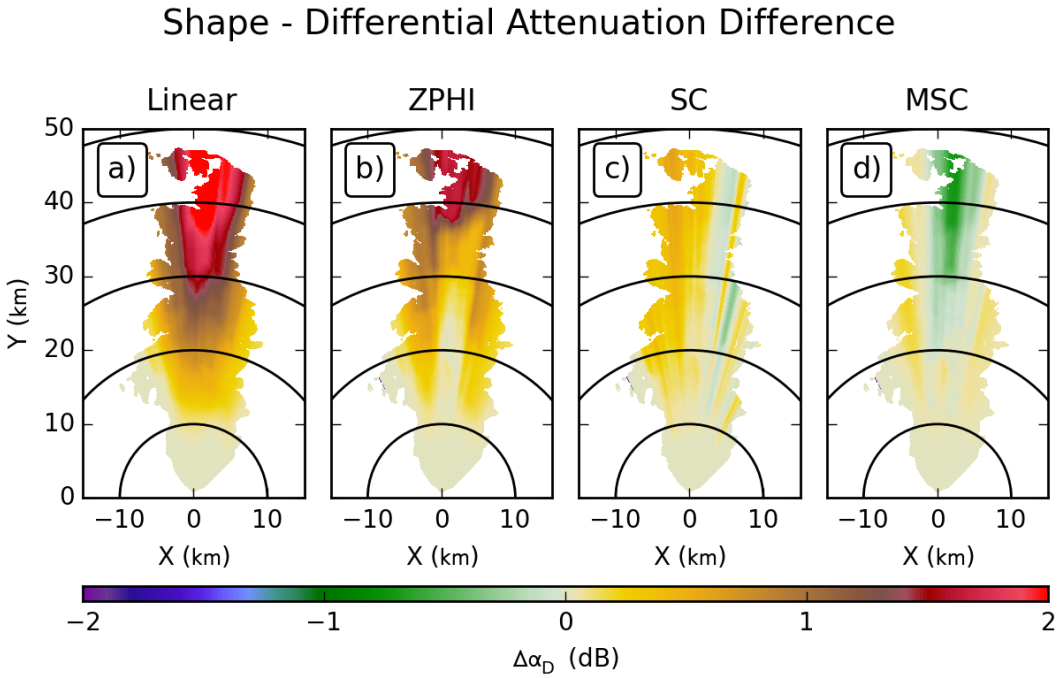

Figure 4.46: As in Figure 4.40, but for differential attenuation.

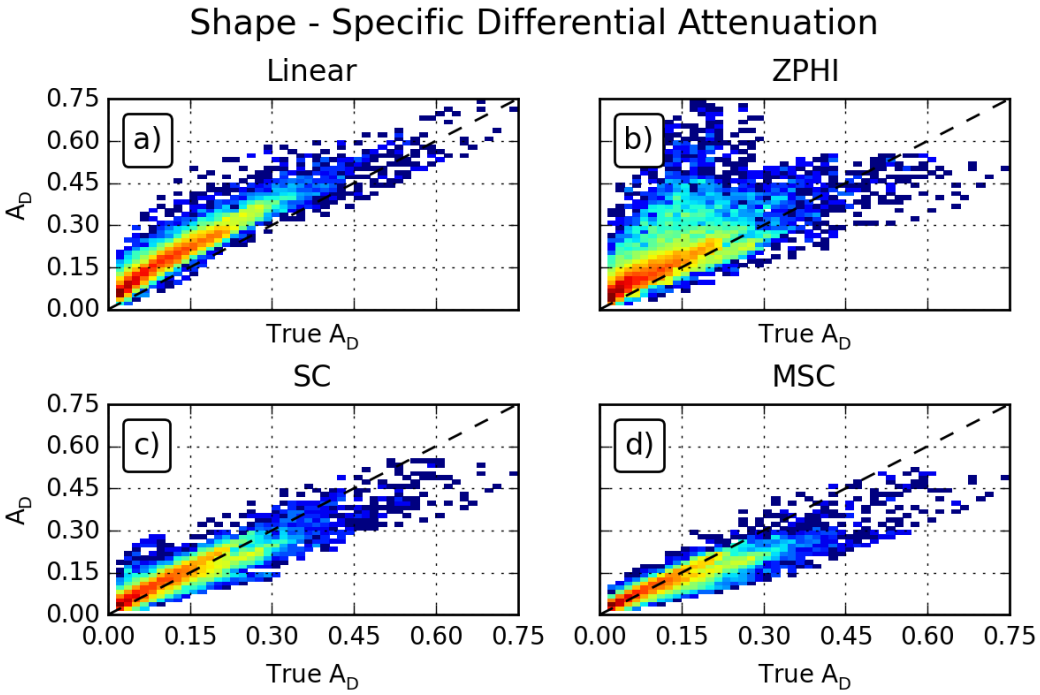

Figure 4.47: As in Figure 4.43 but for specific differential attenuation.

same large increase in values for the Linear and ZPHI algorithms, as well as a slight decrease in differential attenuation calculated by the MSC algorithm. Looking at the differences from truth in Figure 4.46, it is clear that the Linear algorithm has a large area where the bias in differential attenuation is well over $2\,\mathrm{dB}$. For ZPHI, the errors are less but have increased to $1.5\,\mathrm{dB}$. While the SC algorithm's results are mostly unchanged from the Control experiment, the MSC algorithm now has a large negative bias around $1\,\mathrm{dB}$. The histogram of specific differential attenuation in Figure 4.47 is consistent with the PPIs, and matches what was seen for specific attenuation for the individual polarizations, including the large increase in the spread of points for the ZPHI algorithm.

Overall, changing the shape model from the Brandes et al. (2002) model to the Pruppacher and Beard (1970) model drastically increased the errors for the algorithms using fixed coefficients at C-band. Since the Pruppacher and Beard (1970) model yields more oblate drops, this change increases the magnitude of the polarimetric variables; consequently, this increases the magnitude of the Φ_{DP} data without an increase in the reflectivity field. Together, this leads the Linear and ZPHI algorithms to increased estimations of attenuation. The SC algorithm, as in the Canting experiment, is able to compensate for this through its optimization procedure. The MSC also benefits from this optimization, but the changes made to filter the optimized coefficients have introduced a significant negative bias.

The computed bias and MSE values (Table 4.7) show that the SC and MSC algorithms are clearly the best performers, having the lowest values for both columns. Between the two algorithms, neither demonstrates consistently better performance across all polarizations. For r^2 values, while the SC and MSC are not able to produce values

higher than those of Linear, the differences are decreased over those in the Control experiment.

Algorithm	Bias (dB/km)	MSE (dB^2/km^2)	r^2
Horizontal			
Linear	0.1191	0.0251	0.9560
ZPHI	0.1171	0.0379	0.8265
SC	0.0170	0.0079	0.9083
MSC	-0.0088	0.0070	0.9279
Vertical			
Linear	0.0819	0.0128	0.9621
ZPHI	0.0803	0.0167	0.8616
SC	0.0070	0.0040	0.9055
MSC	-0.0074	0.0034	0.9273
Differential			
Linear	0.0683	0.0056	0.8986
ZPHI	0.0535	0.0082	0.5224
SC	0.0087	0.0012	0.8437
MSC	-0.0082	0.0014	0.8586

Table 4.7: As in Table 4.3, but for the Shape experiment.

4.3.2 X band

At X-band the results are similar to those at C-band. The PPIs of both horizontal and vertical attenuation, Figures 4.48 and 4.50, respectively, show very large increases in the estimated attenuation for the Linear and ZPHI algorithms. Again, this comes from the increased differential phase that results from using the Pruppacher and Beard (1970) shape model. Looking at the differences from the true values in Figures 4.49 and 4.51, the errors for the Linear algorithm have increased to well over 10 dB, while ZPHI has errors peaking at 10 dB. The SC and MSC see increases in errors as well, though these increases are much less drastic; the MSC algorithm increases to around 3 dB (from around 1 dB). The SC algorithm's estimate of attenuation, overall, shows no net increase; however, there are now some individual areas that have errors up to 5 dB. Indeed, it was this problem with some rays showing larger errors that motivated the development of MSC. The histograms of specific attenuation values, for both polarizations in Figures 4.52 and 4.53, match those at C-band.

For differential attenuation, Figure 4.54 shows that for the Shape experiment, differential attenuation increases for all, including the true values. Looking at the difference from truth (Figure 4.55), the errors for Linear and ZPHI increase as well; for Linear the errors are now up to 2 dB (up from 1 dB), and ZPHI has errors up to 1.5 dB, which is an increase from around 0.5 dB for the Control experiment. This is discounting the area where extinction of the signal is causing problems. As at the individual polarizations, SC shows an increase in errors for some rays, but no systematic increase, while MSC shows an overall increase in its positive bias, though of much less magnitude than Linear and ZPHI. Figure 4.56 shows the histogram of specific differential phase, which matches well those from horizontal and vertical polarizations.

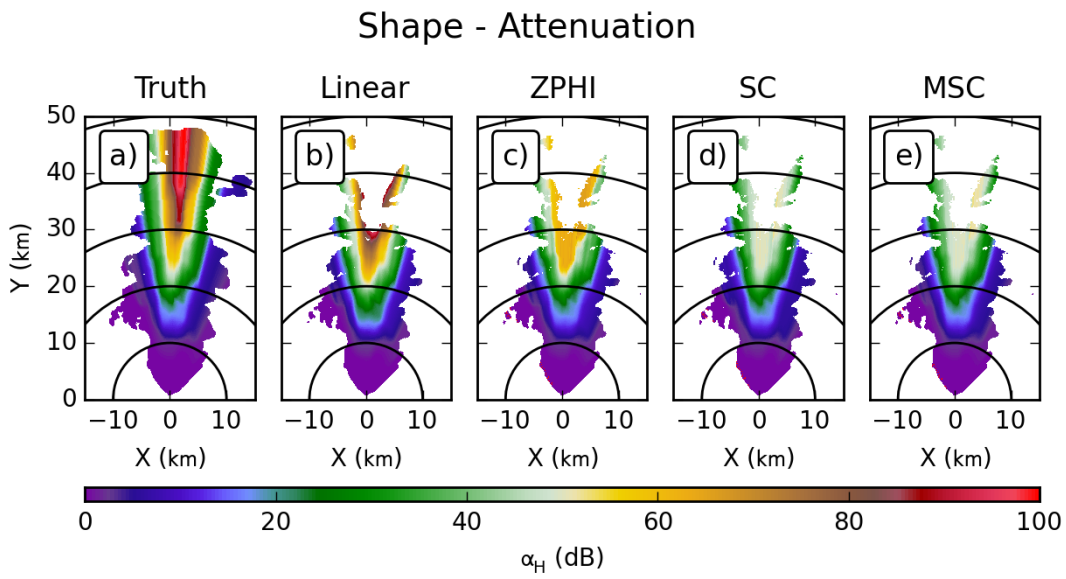

Figure 4.48: As in Figure 4.39, but for X-band.

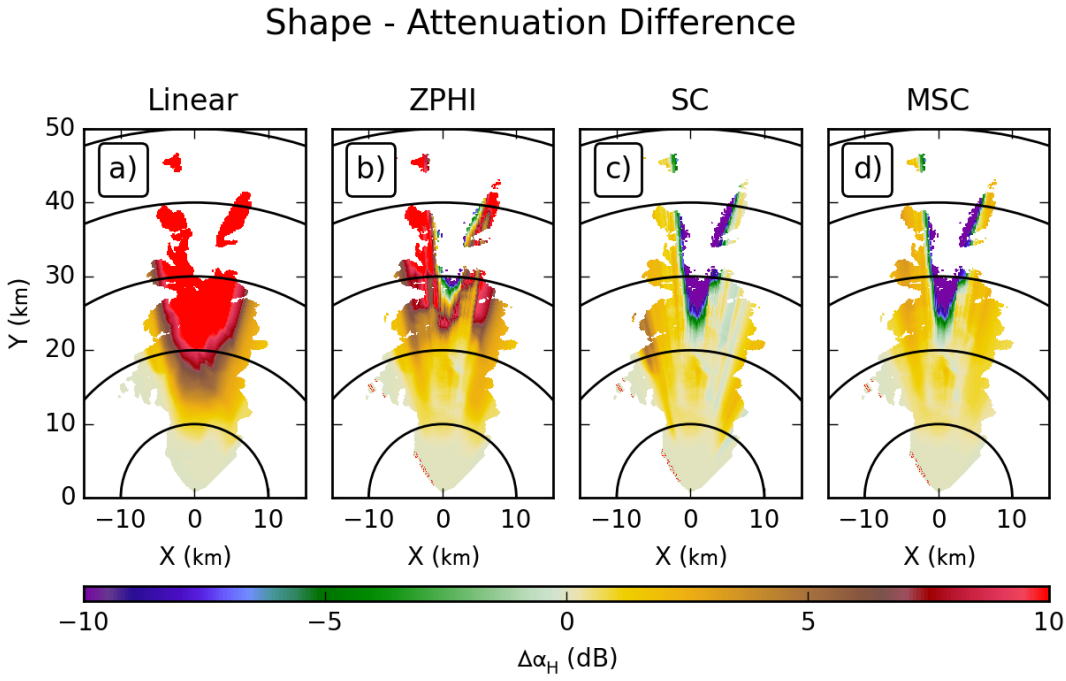

Figure 4.49: As in Figure 4.40, but for X-band.

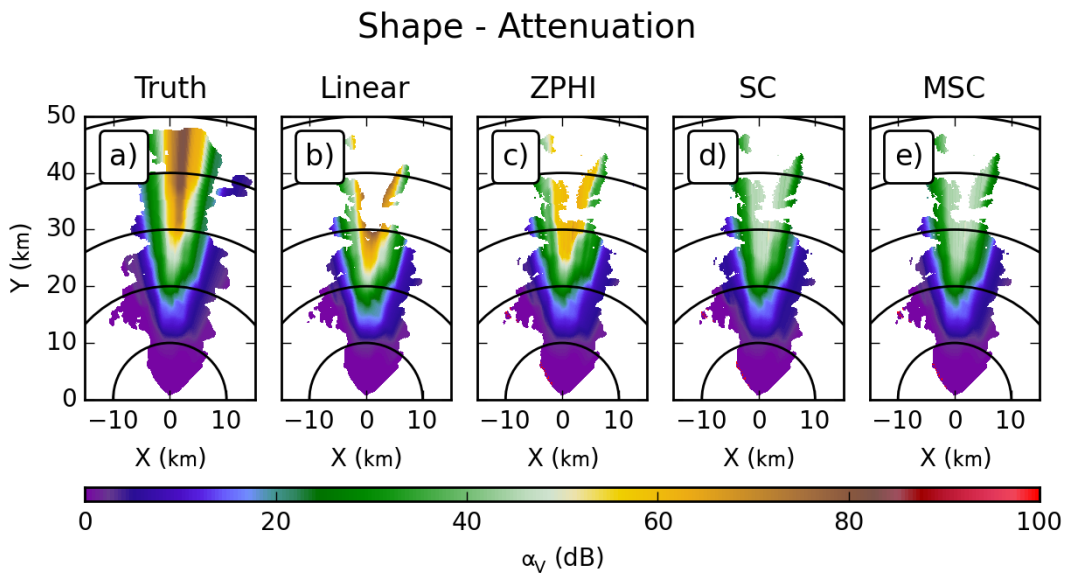

Figure 4.50: As in Figure 4.48, but for vertical polarization.

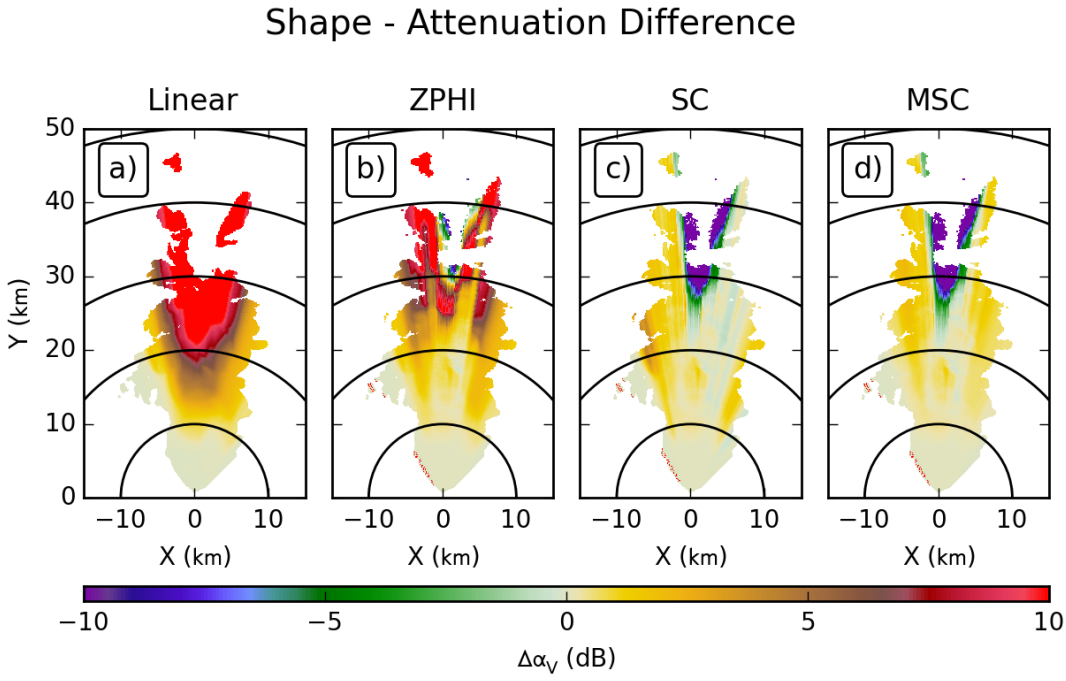

Figure 4.51: As in Figure 4.49, but for vertical polarization.

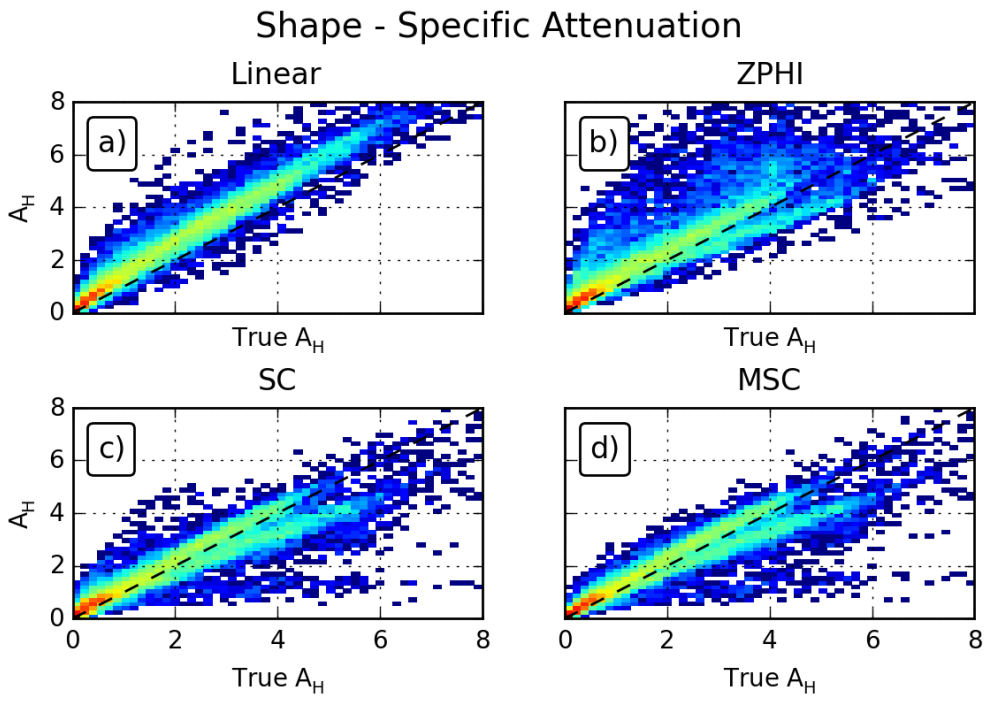

Figure 4.52: As in Figure 4.43, but for X-band.

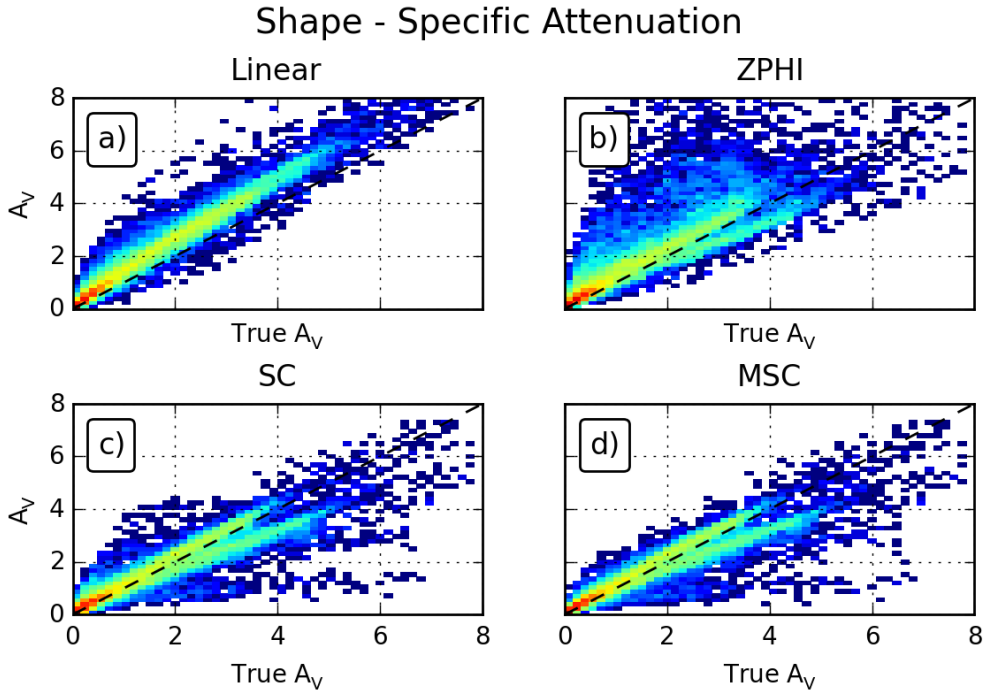

Figure 4.53: As in Figure 4.53, but for vertical polarization.

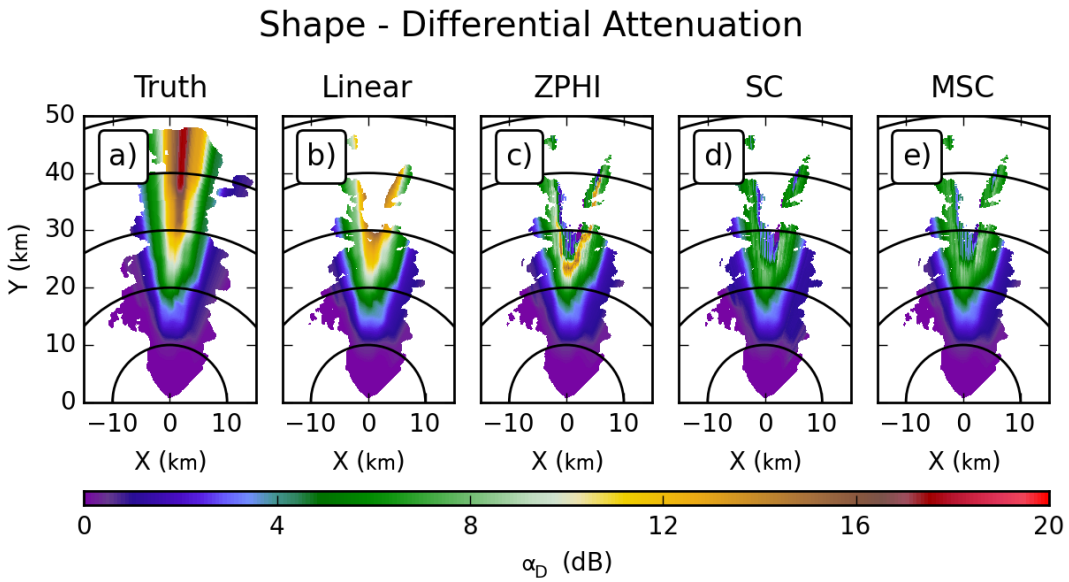

Figure 4.54: As in Figure 4.48, but for differential attenuation.

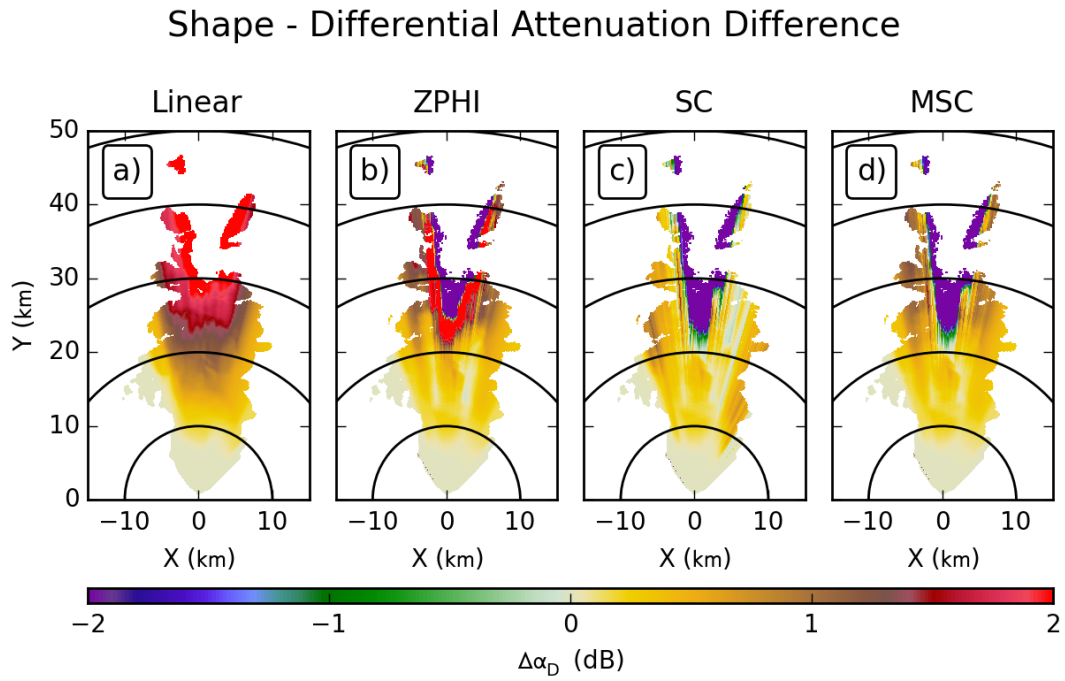

Figure 4.55: As in Figure 4.49, but for differential attenuation.

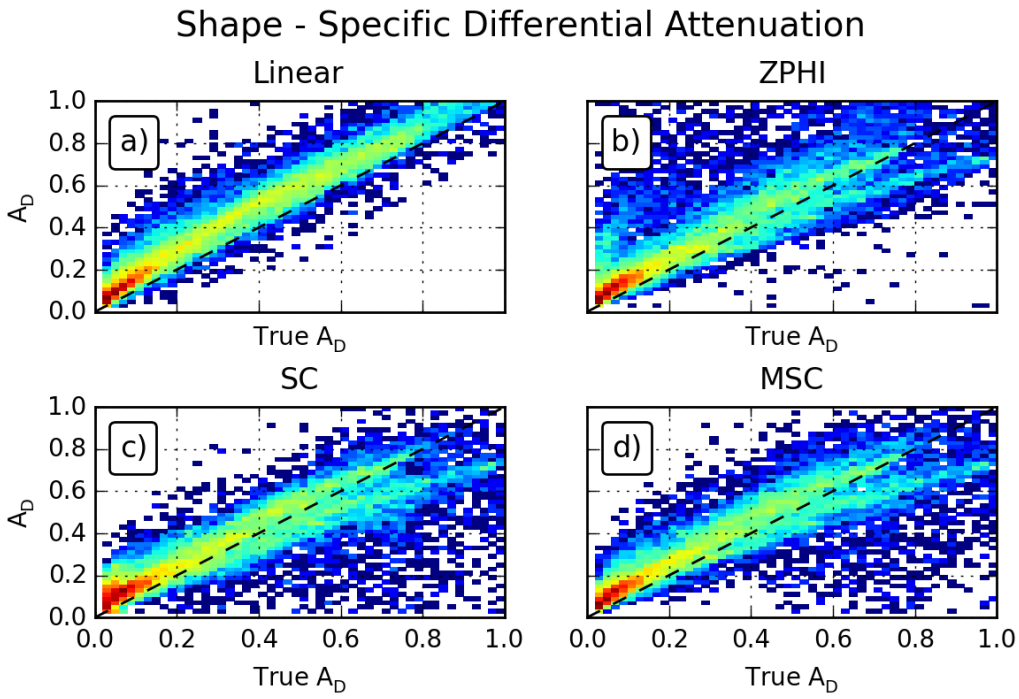

Figure 4.56: As in Figure 4.52, but for specific differential attenuation.

In terms of bias and MSE, the SC and MSC algorithms stand out from the other algorithms (Table 4.8). Between the two algorithms, in this experiment, the results from the MSC algorithm appear slightly better, as they yield a smaller MSE while having comparable biases.

Algorithm	Bias (dB/km)	MSE (dB^2/km^2)	r^2
Horizontal			
Linear	0.4642	0.4232	0.9667
ZPHI	0.3904	0.9875	0.7668
SC	0.0334	0.2623	0.8933
MSC	0.0360	0.2282	0.9066
Vertical			
Linear	0.4093	0.3313	0.9678
ZPHI	0.3619	0.9809	0.7046
SC	0.0232	0.1687	0.8981
MSC	0.0090	0.1530	0.9078
Differential			
Linear	0.0841	0.0116	0.9537
ZPHI	0.1683	0.3639	0.3179
SC	0.0116	0.0172	0.7968
MSC	0.0259	0.0169	0.8008

Table 4.8: As in Table 4.4, but for the Shape experiment.

4.4 Temperature

The Temperature experiment is designed to explore the sensitivity of the algorithms to changes in temperature; such sensitivity arises from the use of a fixed temperature when calculating the regression coefficients. In this experiment, instead of prescribing a fixed temperature for simulating the radar data, the temperature from the model grid is used. Figure 4.57 shows the actual field of temperatures that is used; the field of temperatures is generally around 295 K, though there is some spatial variability. However, this variability is smaller than the magnitude of the change from the fixed temperature of 283 K that was used to generate the regression coefficients.

Temperature sensitivity of the relationship between attenuation and differential phase was previously mentioned by Bringi et al. (1990), and its impact on attenuation correction was briefly described by Carey et al. (2000) and Aydin et al. (1989). The aim here is to quantify this effect within the context of actual algorithms run on (simulated) data.

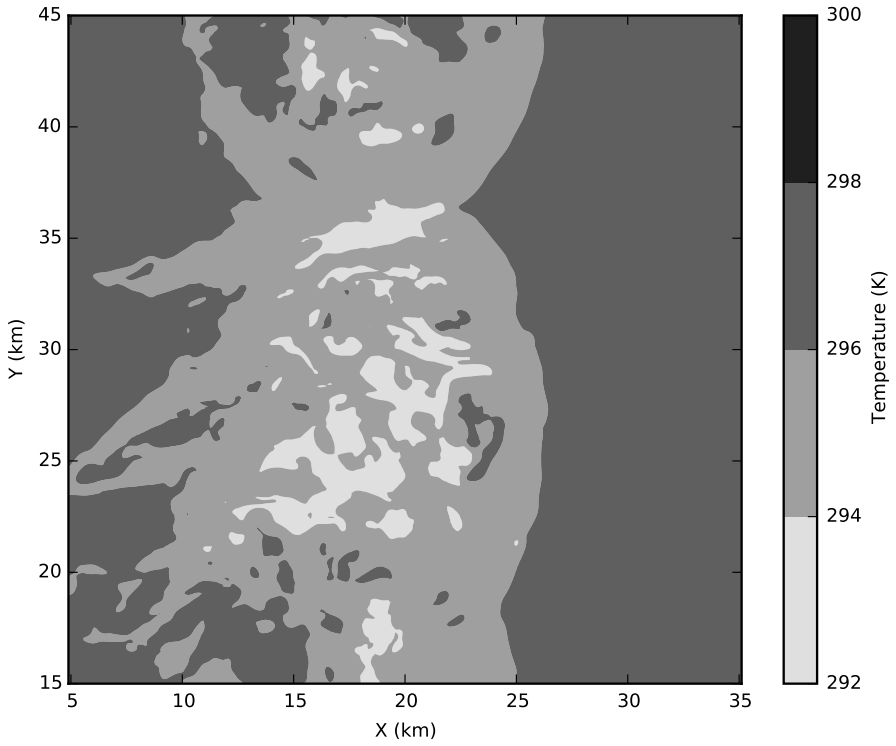

Figure 4.57: Temperature near the surface of the model grid used to simulate radar data.

4.4.1 C band

For the Temperature experiment at C-band, the PPIs of attenuation for horizontal, Figure 4.58, and vertical, Figure 4.60, show clear decreases in attenuation in both SC and MSC algorithms, as well as the true attenuation, that result from the increase in temperature. Subtracting out the true values, the corresponding differences in Figures 4.59 and 4.61 show that the decrease in SC and MSC capture well the real change in intrinsic attenuation, as they show no significant increase in errors; MSC shows a small increase in its negative bias, on order of 0.1 dB, while SC shows some rays that increase the magnitude of their errors by a similar amount, with no systematic changes. The attenuation estimates from Linear and ZPHI, however, now show almost 5 dB of error. The histograms of specific attenuation for both polarizations, in Figures 4.62 and 4.63, show clearly the biases of Linear and ZPHI, as the bands of most points shift noticeably upwards above the one-to-one ratio line. For SC and MSC, the change between the Control and Temperature experiments is to drastically shorten the maximum range of values, but there is no observable change in terms of shifts relative to the one-to-one line; there is a clear negative bias at higher values of specific attenuation, though this is consistent between the experiments.

Looking at differential attenuation now, the PPIs for the Temperature experiment in Figure 4.64 do not show significant changes. The true values exhibit only a small decrease, which from this figure appears to be matched by all algorithms, with the exception of a slight increase in the differential attenuation estimated by the Linear algorithm. Consequently, this causes the Linear algorithm to show the greatest increase in errors when comparing the differences from truth in Figure 4.65 to the results from the Control experiment. The Linear algorithm's error has increased from around 1.2 dB

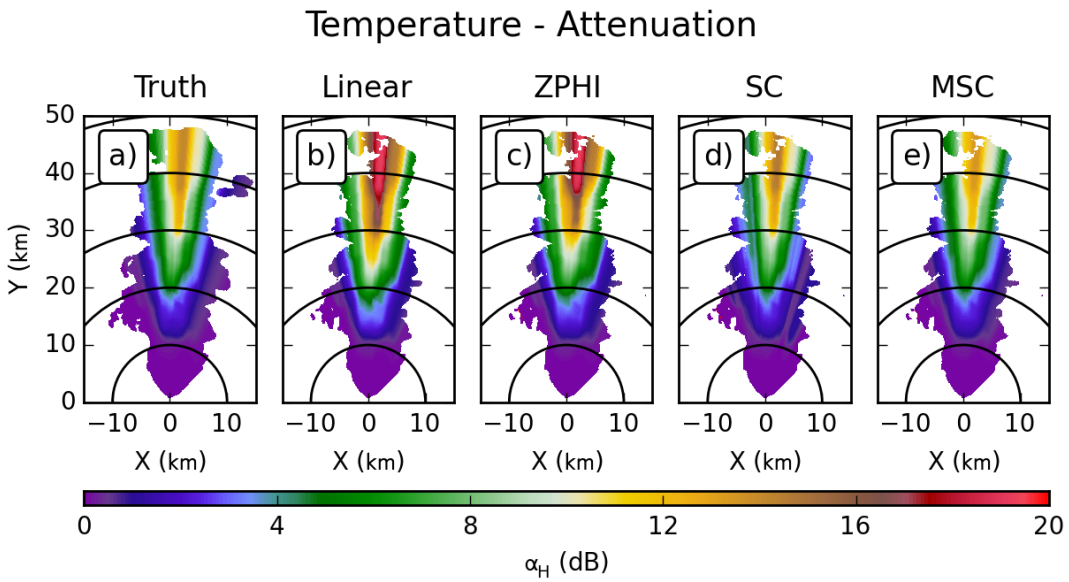

Figure 4.58: As in Figure 4.3, but for the Temperature experiment.

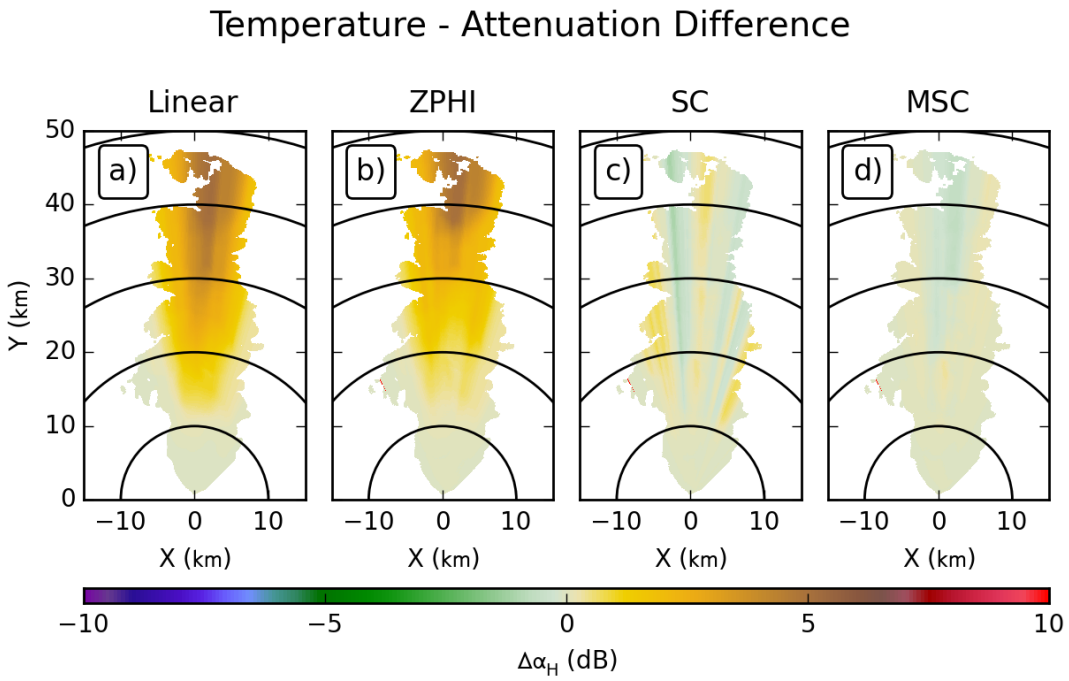

Figure 4.59: As in Figure 4.4, but for the Temperature experiment.

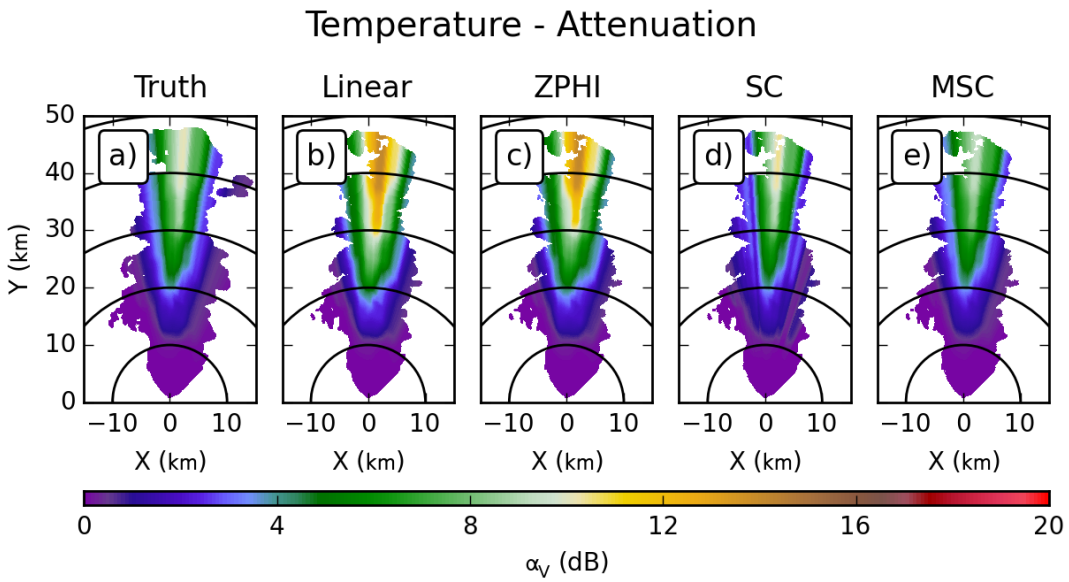

Figure 4.60: As in Figure 4.58, but for vertical polarization.

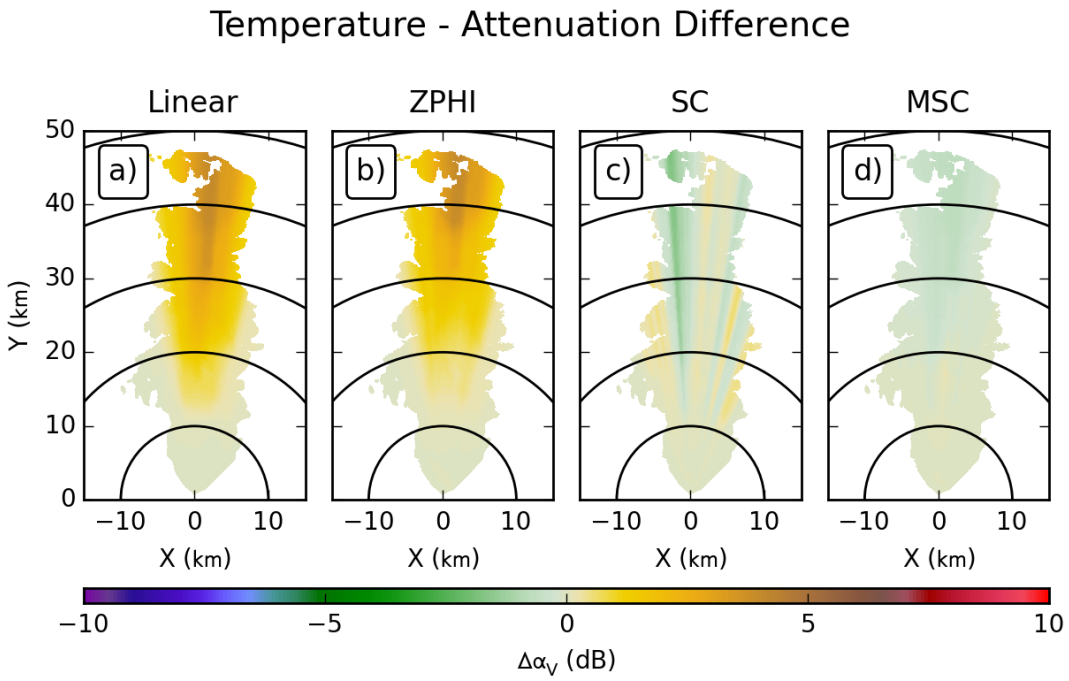

Figure 4.61: As in Figure 4.59, but for vertical polarization.

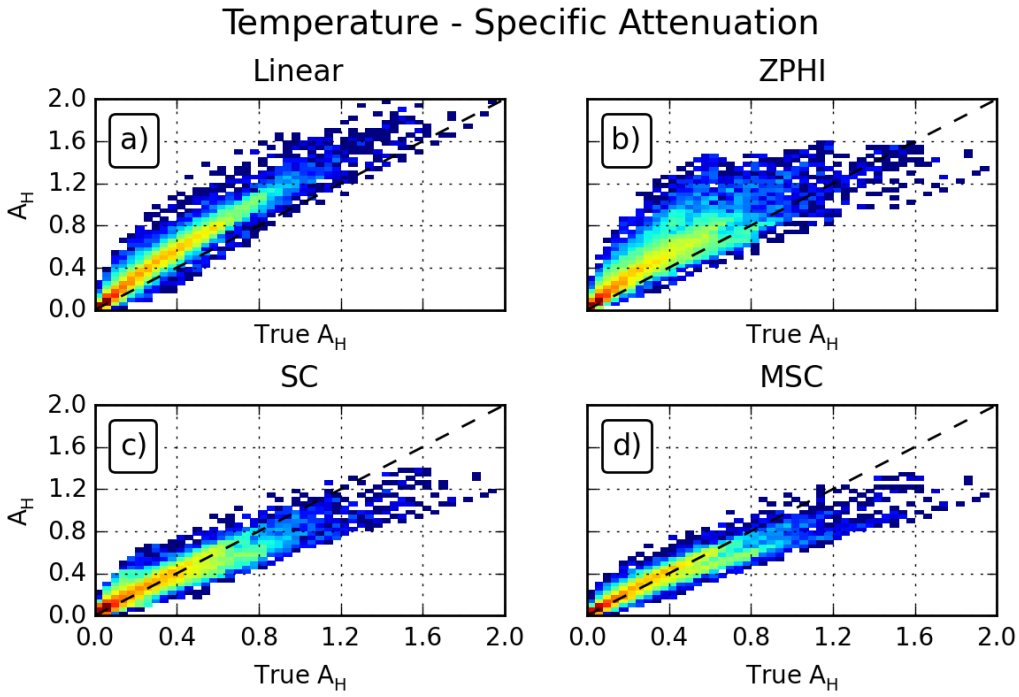

Figure 4.62: As in Figure 4.7, but for the Temperature experiment.

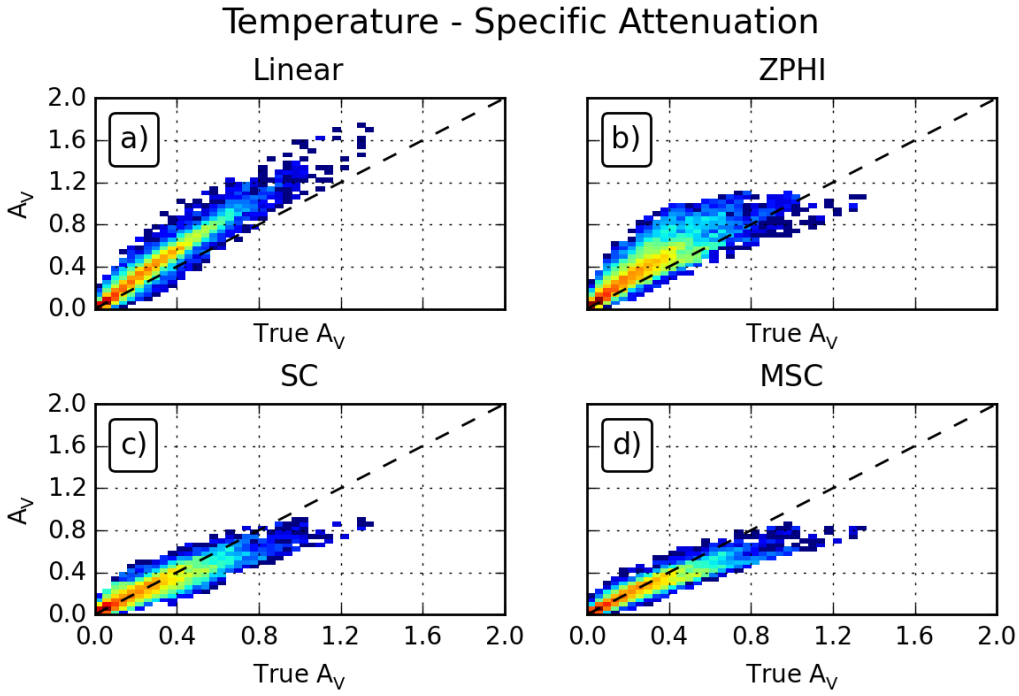

Figure 4.63: As in Figure 4.62, but for vertical polarization.

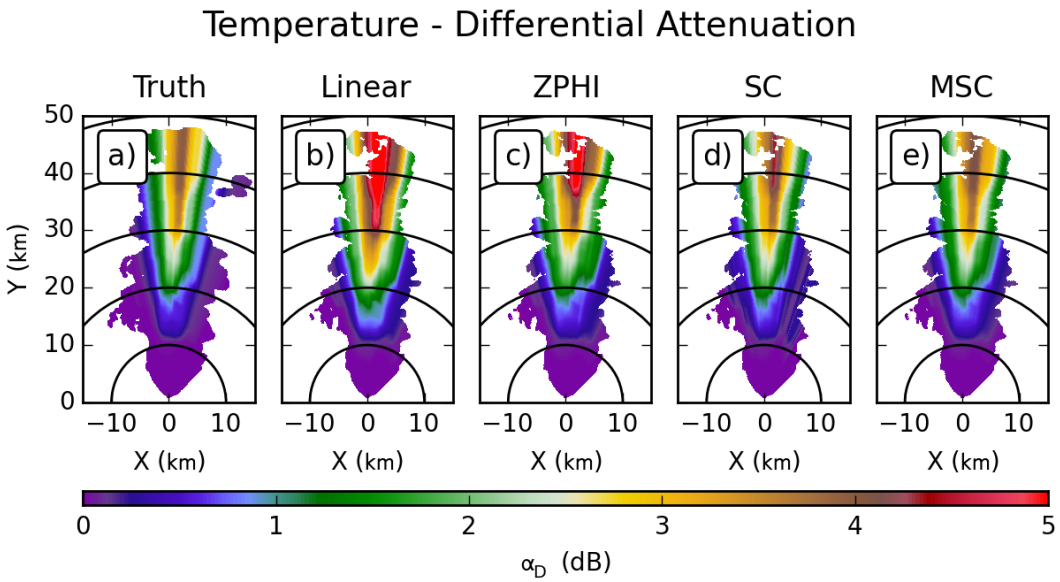

Figure 4.64: As in Figure 4.58, but for differential attenuation.

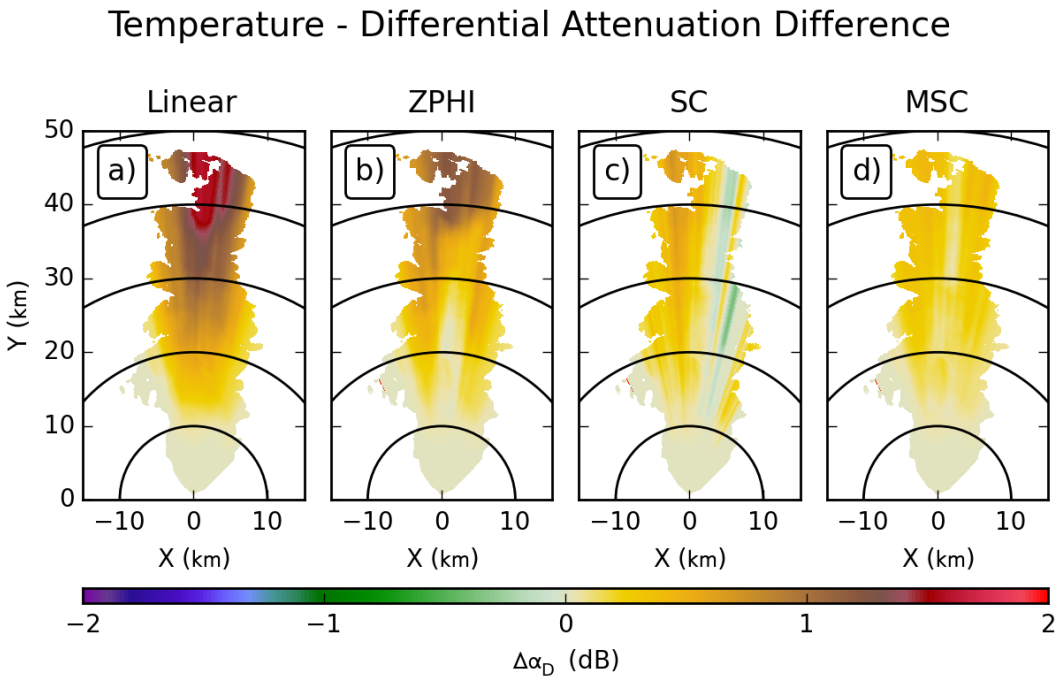

Figure 4.65: As in Figure 4.59, but for differential attenuation.

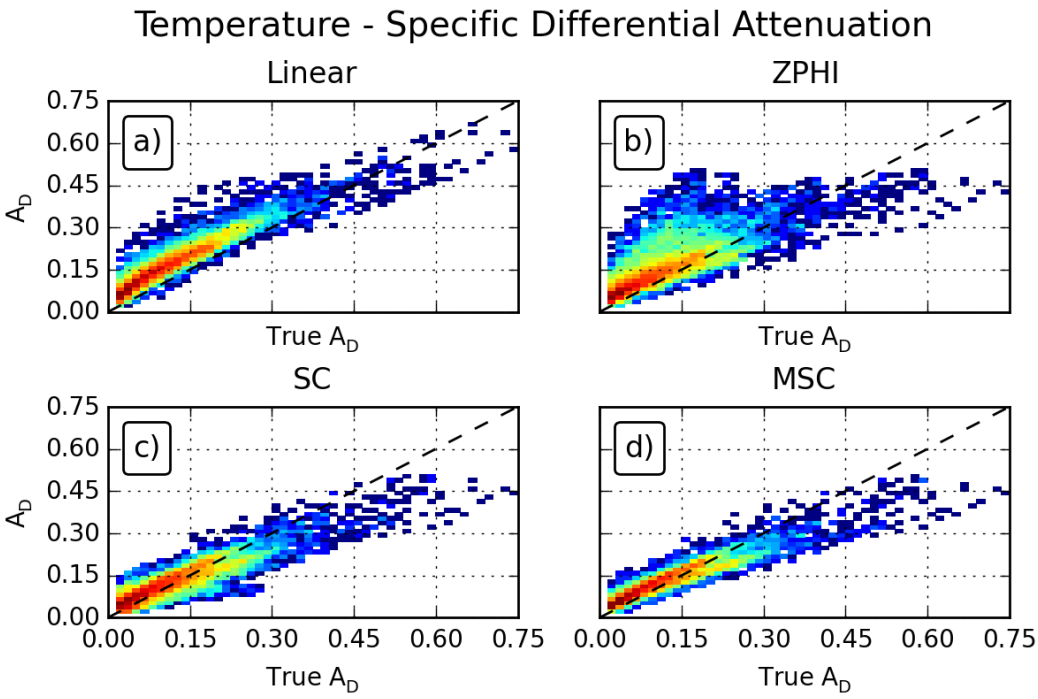

Figure 4.66: As in Figure 4.62, but for specific differential attenuation.

to 1.5 dB. The ZPHI algorithm's errors, in comparison with the Control experiment also show an increase. Conversely, the SC algorithm shows almost no change in errors, while the MSC shows only a minor increase in its positive bias by around 0.1 dB. In Figure 4.66, the histograms of specific differential attenuation largely match these minor changes, with a few notable exceptions. For the Linear algorithm, the band of points shifts upwards, giving the positive bias. Conversely, the band for ZPHI develops a negative bias that increases with increasing values of specific differential attenuation; this is countered by an increase spread of points above the one-to-one line, resulting in the net increase in positive bias seen in the PPIs of integrated attenuation. The SC and MSC algorithms also show the same increase in negative bias at larger values.

Overall, again the fixed coefficient algorithms at C-band show significant increases in errors in estimating attenuation for individual polarizations. The adaptive algorithms, SC and MSC, are able to adjust well for these changes with only minor increases in errors. It is worth noting that while the errors for the polarizations greatly increase for Linear and ZPHI, the increase in errors for differential attenuation is not nearly as great. This is because the changes in intrinsic horizontal and vertical attenuation were close in magnitude, resulting in only small changes to the differential attenuation. In this experiment, the difference between the algorithms is quite pronounced. The biases for the SC and MSC algorithms (Table 4.9) are almost an order of magnitude less than those of the Linear and ZPHI algorithms; this is achieved while also having a smaller MSE.

Algorithm	Bias (dB/km)	MSE (dB^2/km^2)	r^2
Horizontal			
Linear	0.1009	0.0191	0.9554
ZPHI	0.0968	0.0230	0.8453
SC	0.0087	0.0062	0.8974
MSC	-0.0009	0.0050	0.9235
Vertical			
Linear	0.0727	0.0111	0.9617
ZPHI	0.0689	0.0112	0.8652
SC	-0.0022	0.0036	0.8695
MSC	-0.0135	0.0028	0.9175
Differential			
Linear	0.0540	0.0037	0.8869
ZPHI	0.0392	0.0043	0.6153
SC	0.0081	0.0013	0.8099
MSC	0.0118	0.0010	0.8850

Table 4.9: As in Table 4.3, but for the Temperature experiment.

4.4.2 X band

At X-band, increasing the temperature increases the intrinsic attenuation at both polarizations, seen in Figures 4.67 and 4.69, as opposed to decreases as observed at C-band. The corresponding differences from the intrinsic value, in Figures 4.68 and 4.70, show a significant increase in the errors for the Linear algorithm, with pronounced negative bias around $5\,\mathrm{dB}$. All of the ZPHI-based algorithms, conversely, do not show significant increases in errors. ZPHI and MSC do show increases in magnitude to about $1\,\mathrm{dB}$, but these increases occur in both positive and negative directions, leaving their respective fields unbiased. These observations match the histograms for specific attenuation at horizontal and vertical polarizations, shown in Figures 4.71 and 4.72, respectively. The Linear algorithm shows an increased negative bias for higher attenuation values, versus the results from the Control experiment. This agrees with not only the large negative value for the path through the core of reflectivity, but also with the fact that the negative bias vanishes for smaller attenuation values along the edges of the storms. The ZPHI-based algorithms show increases in the spread of points, but no significant shifts in the bands of points, with the ZPHI and MSC algorithms showing the greatest spread. The computed values of bias and MSE (Table 4.10) agree with this observation. Here, the values for the Linear algorithm show the greatest change from the Control experiment, with the other algorithms' error statistics remaining much more stable.

For differential attenuation, the PPIs in Figure 4.68 show only small increase across the board, with the exception of a small decrease for the Linear algorithm. The differences in Figure 4.74 show that this results in an increased negative bias for the Linear

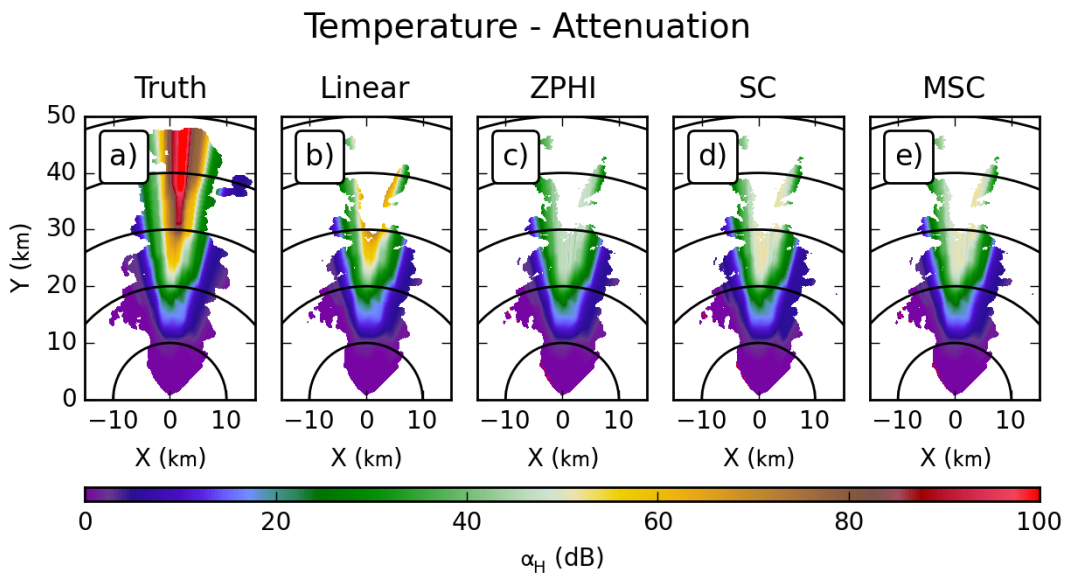

Figure 4.67: As in Figure 4.58, but for X-band.

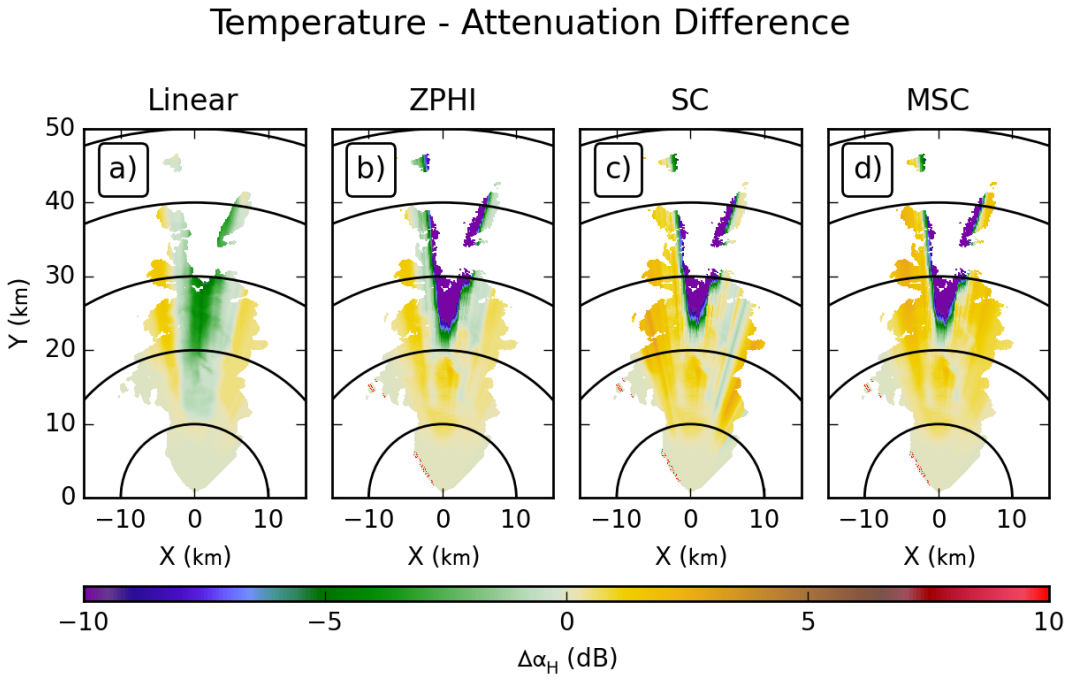

Figure 4.68: As in Figure 4.59, but for X-band.

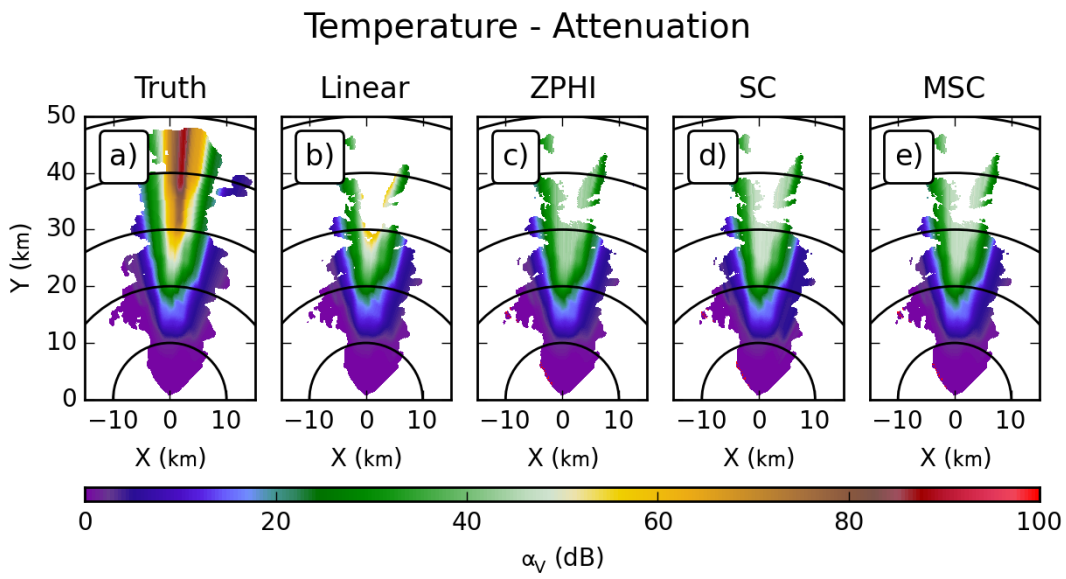

Figure 4.69: As in Figure 4.67, but for vertical polarization.

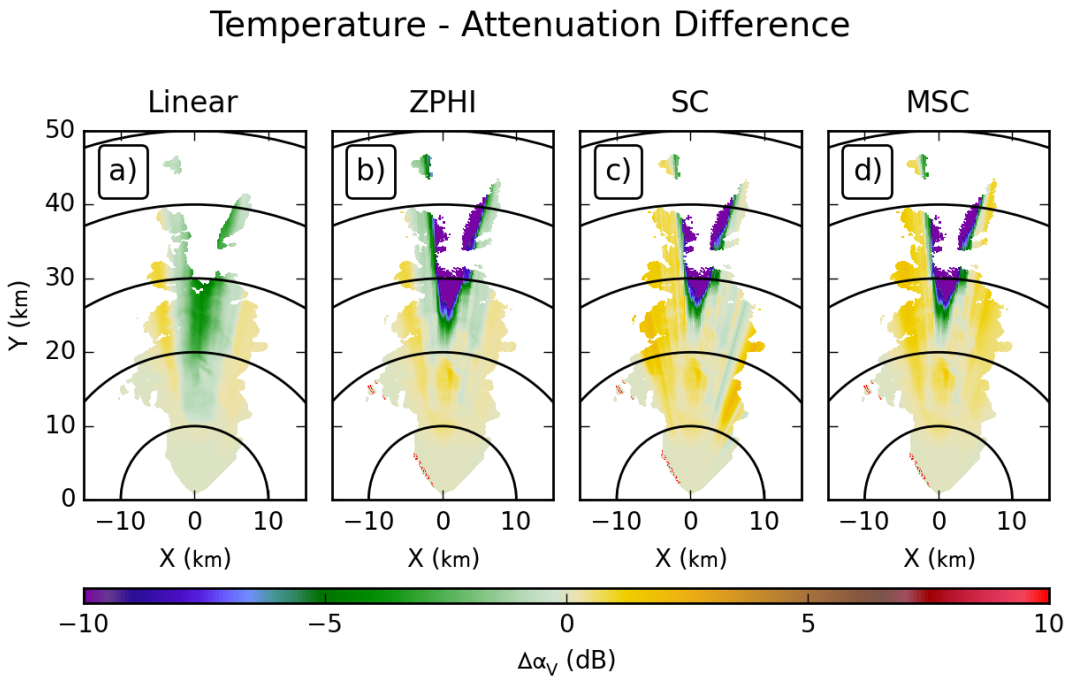

Figure 4.70: As in Figure 4.68, but for vertical polarization.

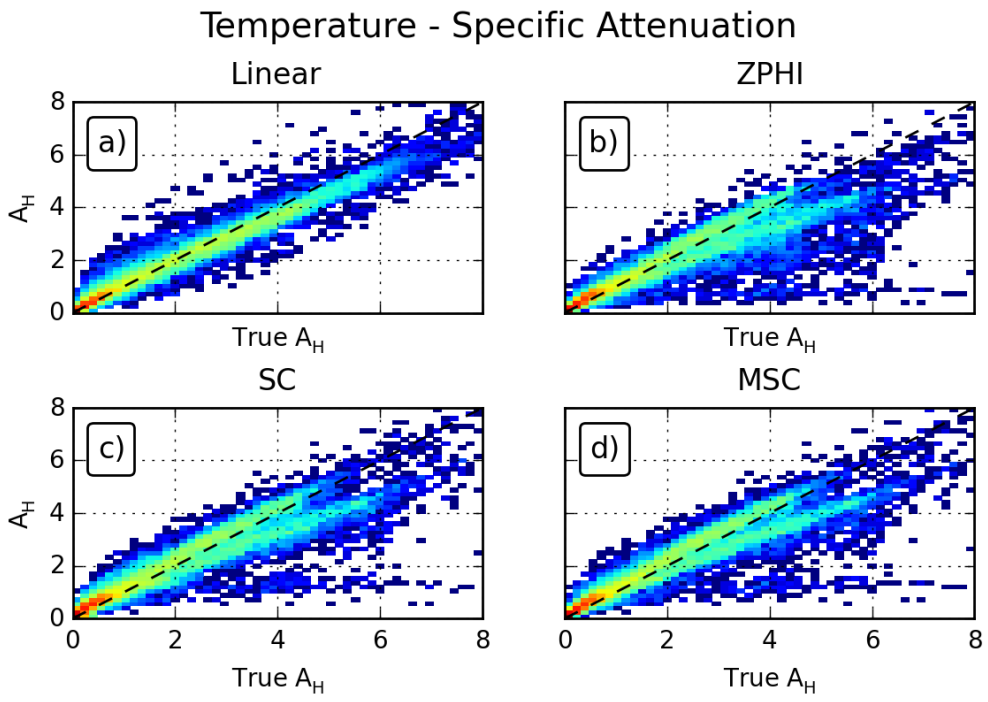

Figure 4.71: As in Figure 4.62, but for X-band.

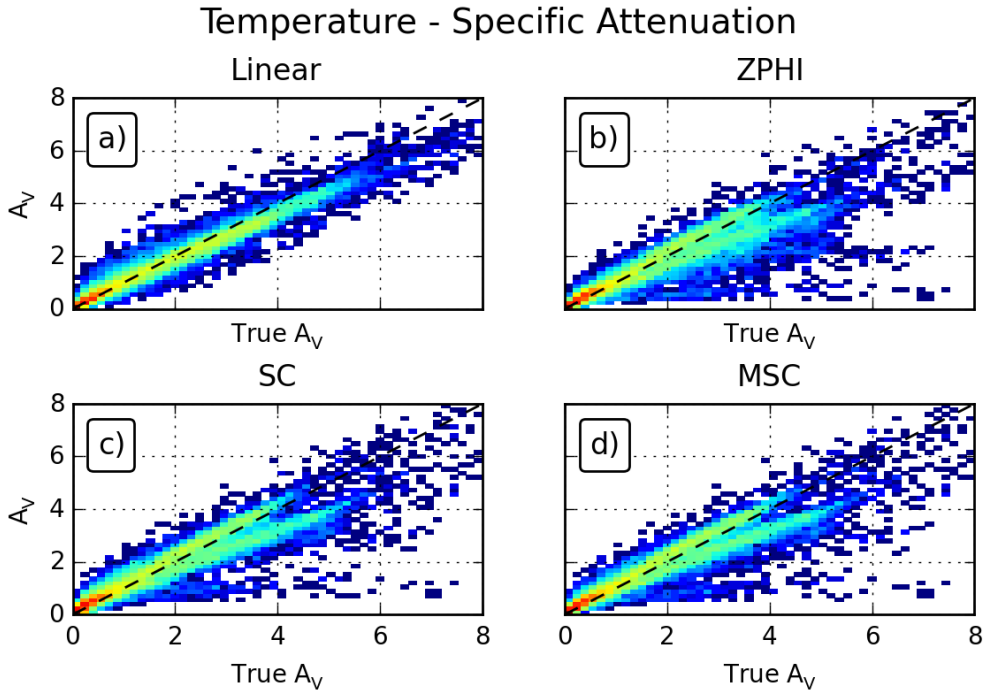

Figure 4.72: As in Figure 4.71, but for vertical polarization.

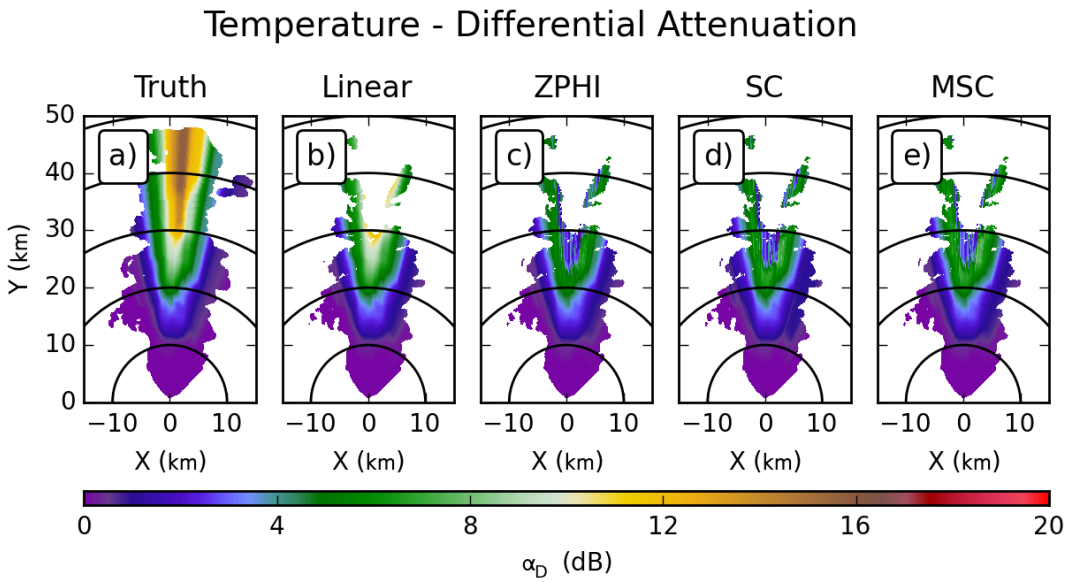

Figure 4.73: As in Figure 4.67, but for differential attenuation.

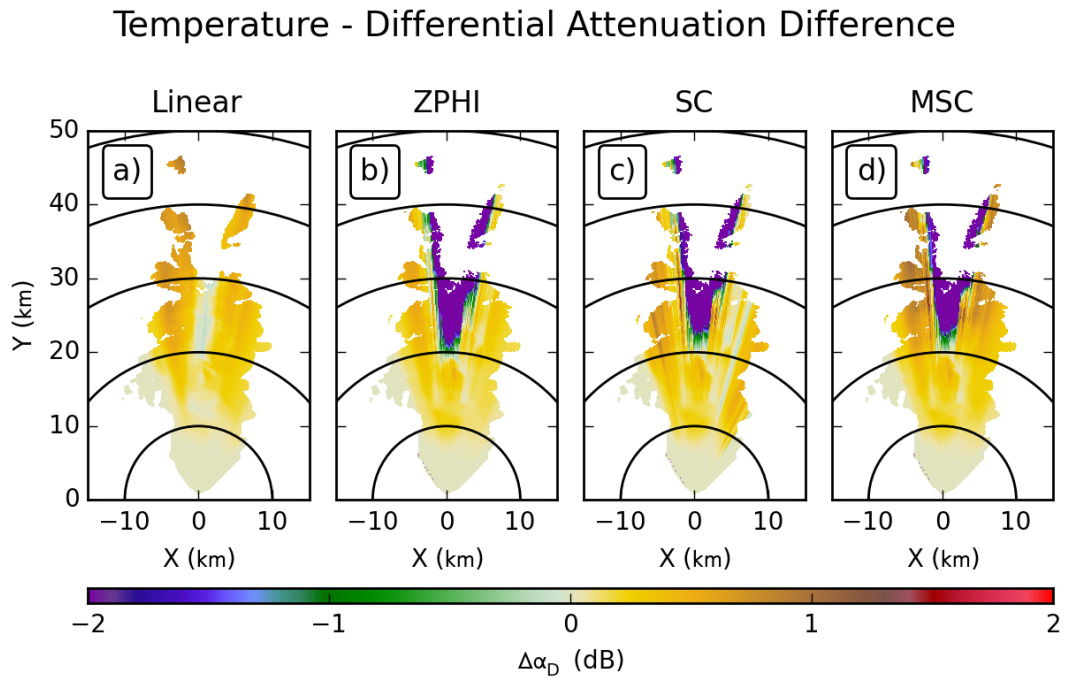

Figure 4.74: As in Figure 4.68, but for differential attenuation.

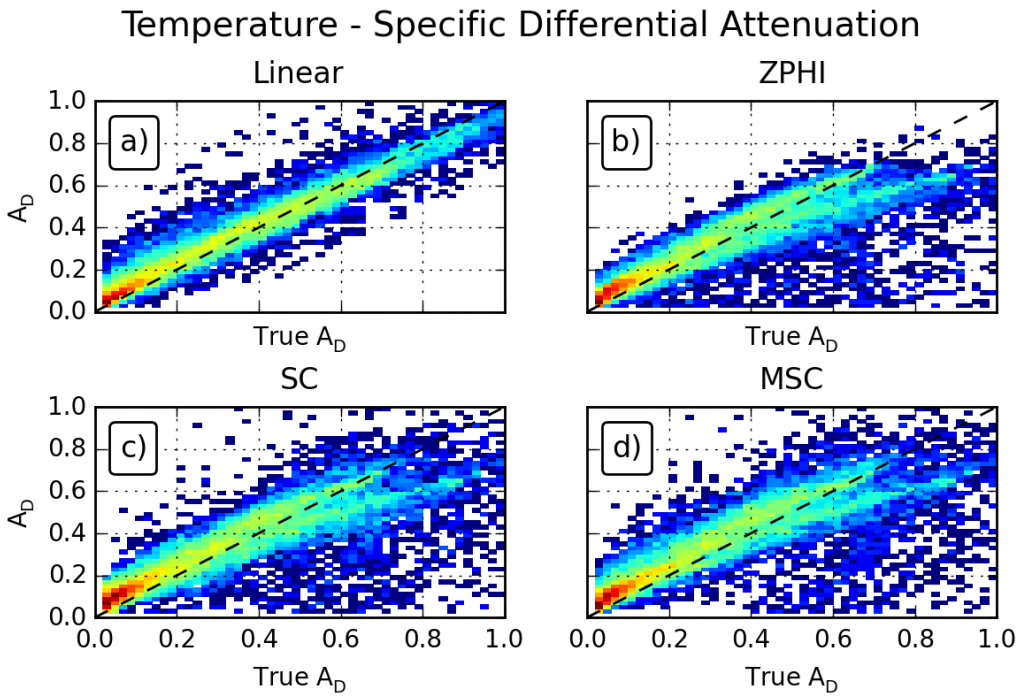

Figure 4.75: As in Figure 4.71, but for specific differential attenuation.

algorithm, similar to what was observed for the individual polarizations. The ZPHI-based algorithms remain largely unchanged in regards to errors, with only a small decrease in the errors for the ZPHI algorithm. The histograms of specific differential phase in Figure 4.75 show that the increase in negative bias, as well as ZPHI's decreased errors, are a result of a negative bias for larger values of attenuation.

4.5 Wavelength

The Wavelength experiment examines the impact of changing the wavelength while staying within the same band. While attenuation is clearly a function of wavelength, evidenced by the definitive changes going from S- to C- to X-band, within these bands

Algorithm	Bias (dB/km)	MSE (dB^2/km^2)	r^2
Horizontal			
Linear	-0.0239	0.1073	0.9682
ZPHI	-0.0773	0.3614	0.8760
SC	0.0174	0.2654	0.9053
MSC	0.0178	0.2546	0.9081
Vertical			
Linear	-0.0363	0.0770	0.9687
ZPHI	-0.0767	0.2473	0.8821
SC	0.0064	0.1798	0.9101
MSC	-0.0043	0.1772	0.9114
Differential			
Linear	0.0215	0.0039	0.9565
ZPHI	-0.0067	0.0166	0.7636
SC	0.0086	0.0148	0.7909
MSC	0.0184	0.0151	0.7834

Table 4.10: As in Table 4.4, but for the Temperature experiment.

changes in attenuation are often neglected. This experiment aims to quantify the effect of this assumption by changing the wavelength from the Control values, 5.5 cm and 3.21 cm for C- and X-bands, to 5.0 cm and 3.0 cm, respectively. These represent changes of only 10 %.

4.5.1 C band

In the Wavelength experiment, the PPIs of attenuation at horizontal and vertical polarization, in Figures 4.76 and 4.78, respectively, exhibit large increases in the amount of attenuation. The change in the intrinsic attenuation due to the decrease in wavelength appears to be captured well by the SC and MSC algorithms. The Linear and ZPHI algorithms do increase as well, though the magnitude of their increase is much less than the intrinsic values. This is reflected in Figures 4.77 and 4.79, which show the differences from truth at horizontal and vertical polarizations, respectively. For both polarizations, the Linear and ZPHI algorithms show significant negative biases of around 5 dB; this is a large change from the smaller 1 dB positive bias shown in the Control experiment. Conversely, the SC and MSC algorithms show no significant biases, nor any significant changes from the Control experiment. The histograms of specific attenuation at these two polarizations, in Figures 4.80 and 4.81, show large shifts down in the main band(s) of points, compared to the Control experiment for the Linear and ZPHI algorithms; this is a reflection of the negative bias in the Wavelength experiment. SC and MSC, show no perceptible shift, but only an expansion of the set of points out to larger values, due to the overall increase in attenuation with lesser wavelength.

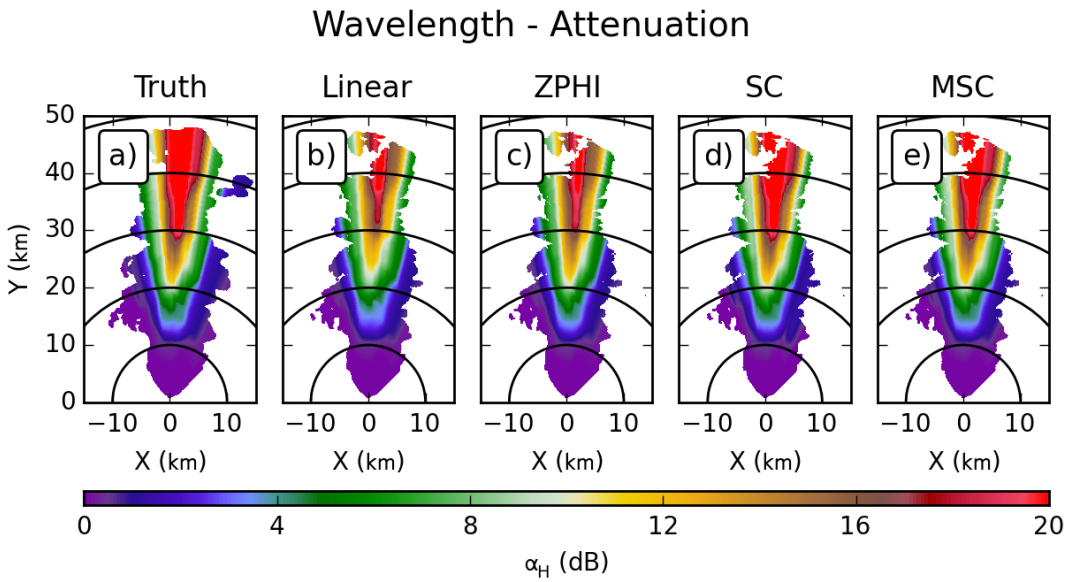

Figure 4.76: As in Figure 4.3, but for the Wavelength experiment.

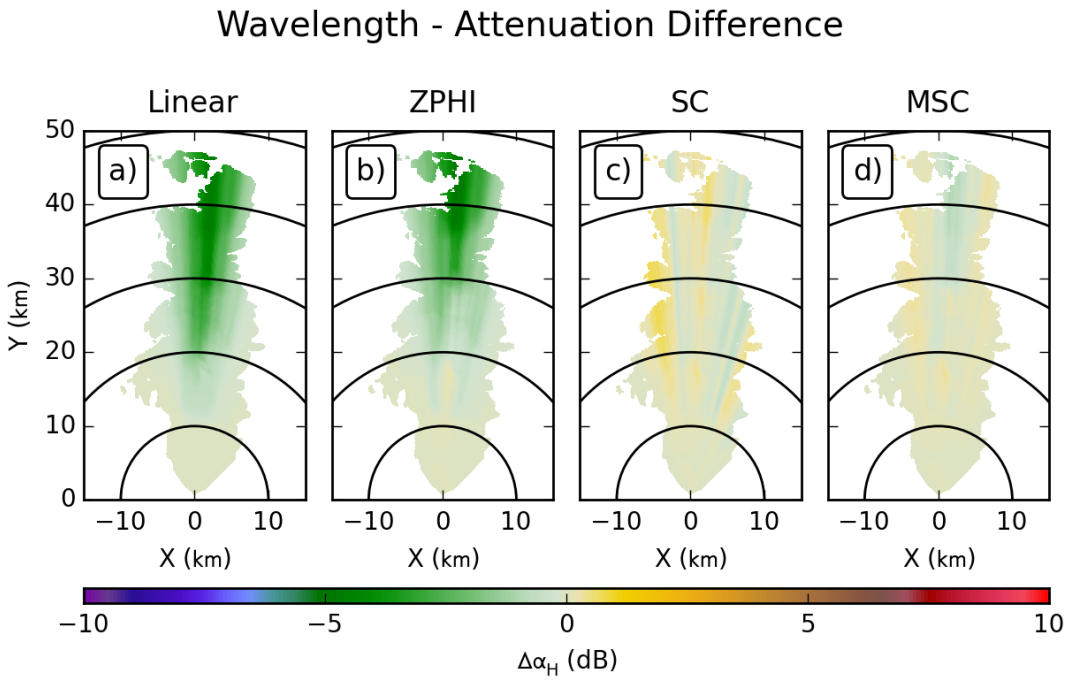

Figure 4.77: As in Figure 4.4, but for the Wavelength experiment.

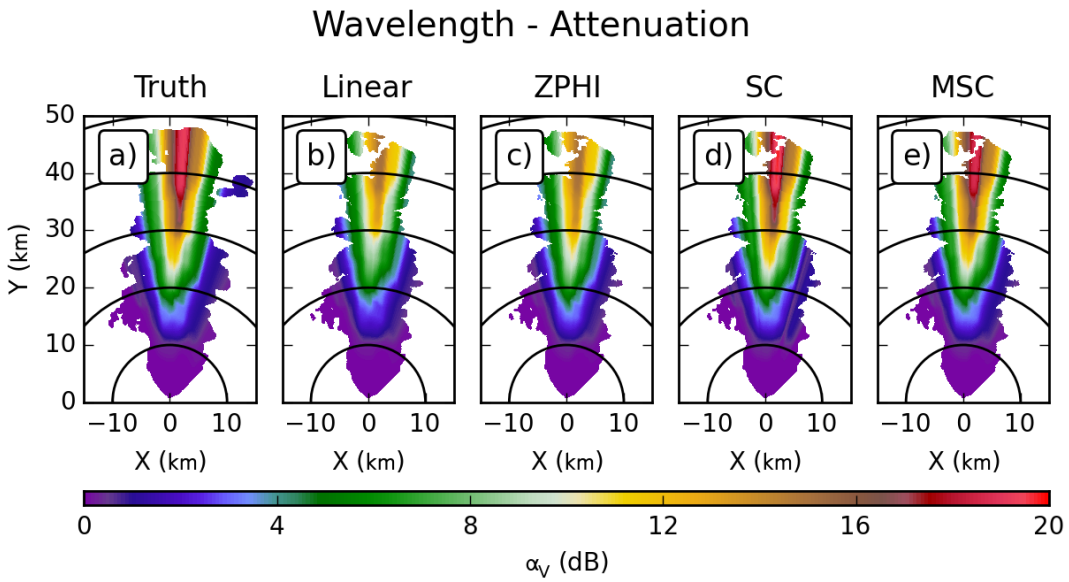

Figure 4.78: As in Figure 4.76 but for vertical polarization.

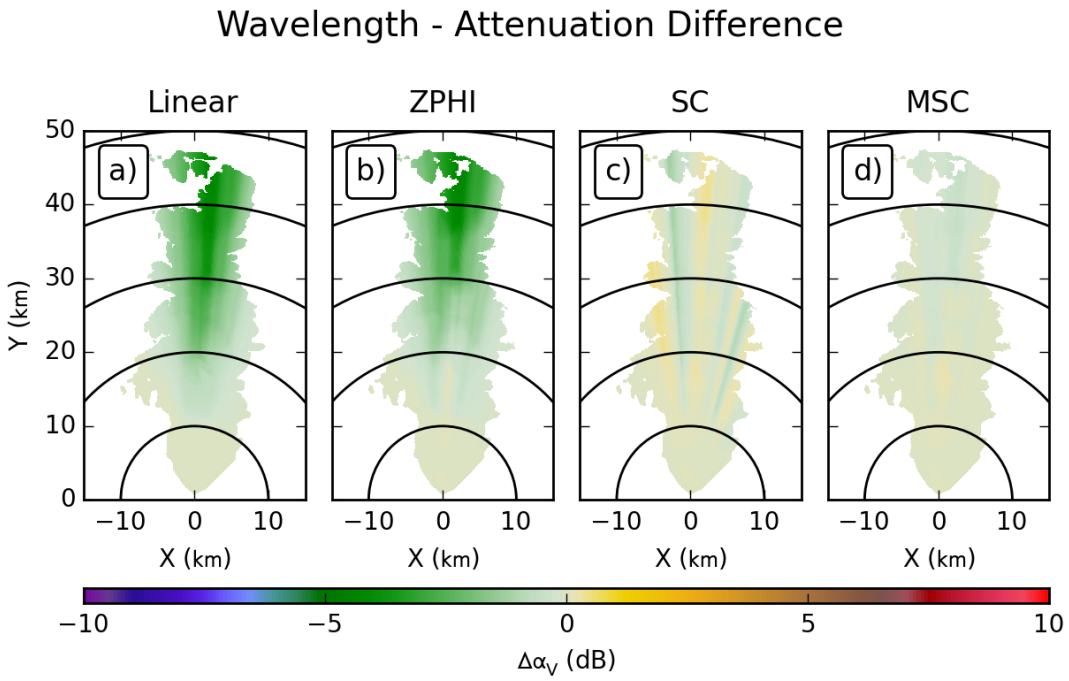

Figure 4.79: As in Figure 4.77, but for vertical polarization.

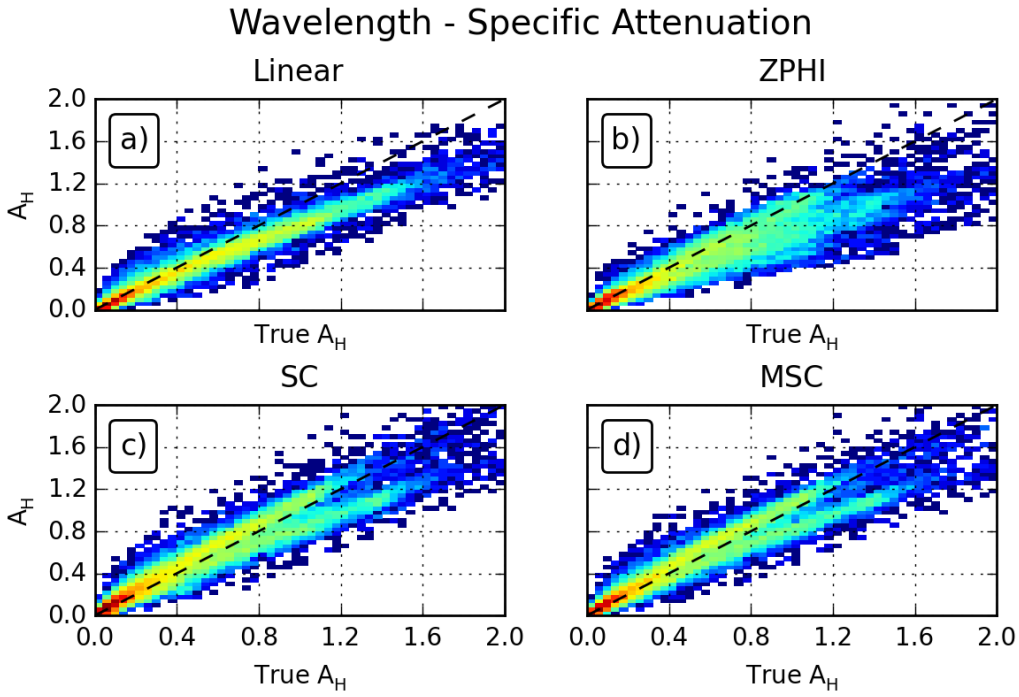

Figure 4.80: As in Figure 4.7, but for the Wavelength experiment.

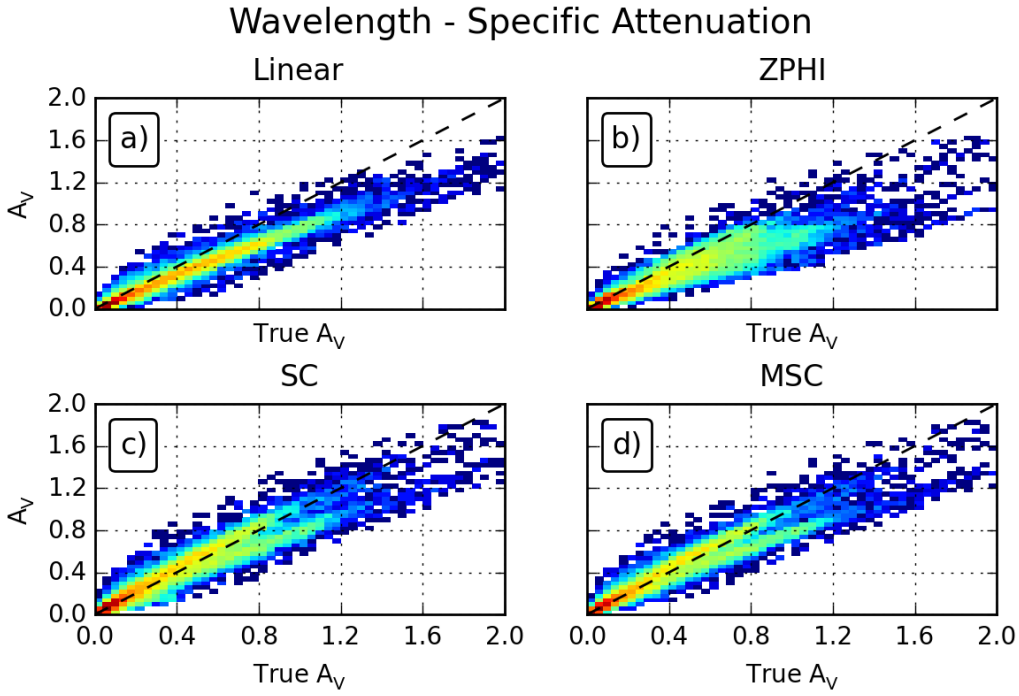

Figure 4.81: As in Figure 4.80, but for vertical polarization.

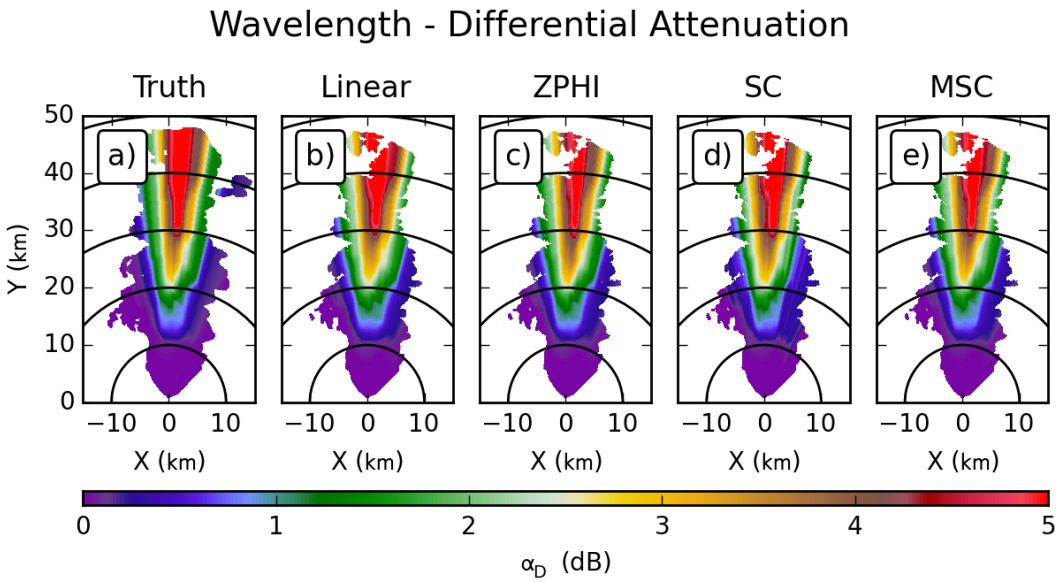

Figure 4.82: As in Figure 4.76, but for differential attenuation.

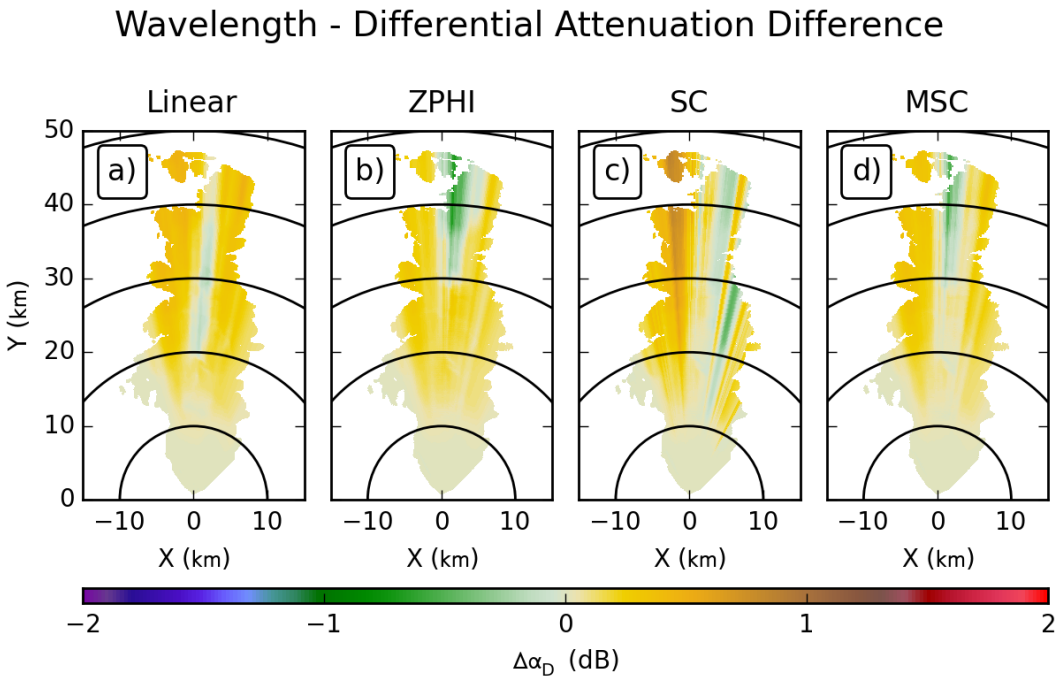

Figure 4.83: As in Figure 4.77, but for differential attenuation.

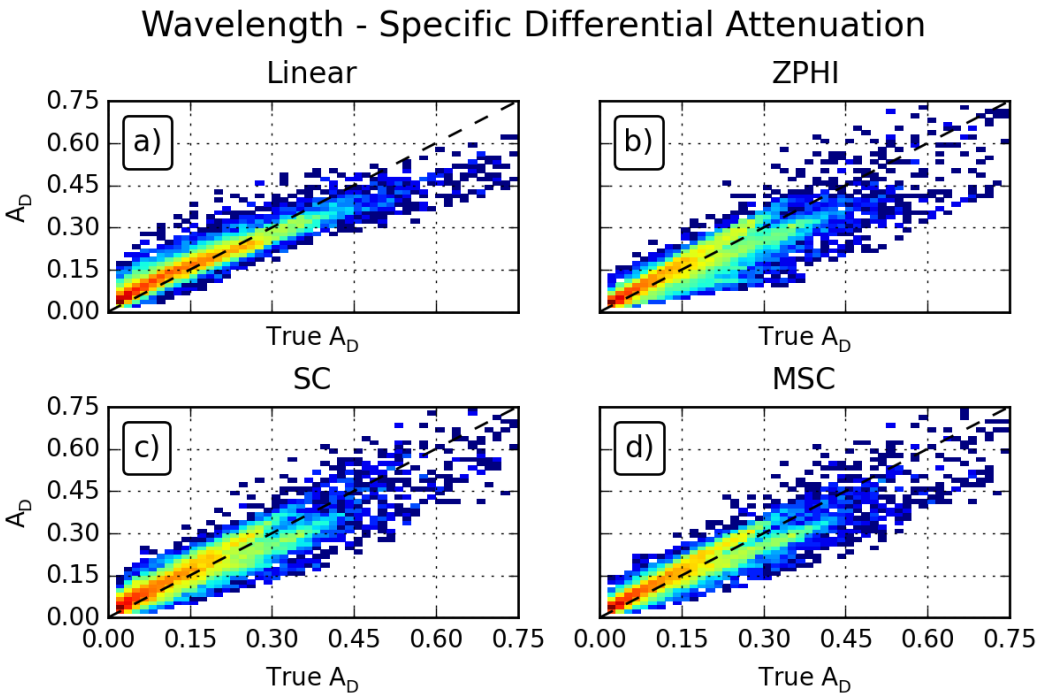

Figure 4.84: As in Figure 4.80, but for specific differential attenuation.

For differential attenuation, the same large increase in attenuation is observable for all PPIs in Figure 4.82 in comparison with the Control experiment. In contrast to the results for the individual polarizations, here the Linear and ZPHI match much better the intrinsic results as well as the performance of the SC and MSC algorithms. The difference from the true values, shown in Figure 4.83, show that with the exception of SC, all of the algorithms exhibit a pattern of a small positive bias along the edges of the reflectivity structure (smaller intrinsic differential attenuation), with a small negative bias in the middle of the reflectivity (larger intrinsic differential attenuation). For MSC, this represents an increase in the negative bias by about 0.5 dB. For the Linear and ZPHI algorithms this is a much greater change; before these algorithms had positive biases of approximately 1 dB, but now show negative biases. The SC algorithm shows no change in its overall bias, but individual rays show increases in errors

in both directions. The histograms of specific differential attenuation, Figures 4.84 reflect these changes in bias. The ZPHI and Linear algorithms show large downward shifts in the main bands of points; however, since the results for the Control experiment had a pronounced positive bias, the downward shift brings the results closer to the one-to-one ratio line, at least for lower attenuation values. The plot for the Linear algorithm shows a significant downward tilt at higher values of specific differential attenuation, which results in the negative bias in the core of reflectivity. For ZPHI, there is no noticeable curve to the points, but rather there is an overall increase in the number of points below the one-to-one line. The SC and MSC algorithms show no appreciable shift, but only an expansion to larger values.

The stark contrast in performance between the SC and MSC algorithms is likely a reflection of the limits of how attenuation is modelled in the ZPHI algorithm. In the SC approach, when the γ coefficient can vary on a per ray basis, the algorithm can compensate for the change between the high and low attenuation regimes better; this comes at the cost of more radial-to-radial variation. In the MSC approach, having a fixed coefficient across the field limits the ability of the algorithm to adjust between regimes, and instead the results show regions with both positive and negative biases.

Overall, the change in wavelength within C-band has a large impact on the results. Again, the SC and MSC algorithms' optimization procedure largely compensates for this effect, yielding lower biases and MSE values (Table 4.11). Linear and ZPHI, on the other hand show large changes, with especially large errors at calculating the attenuation for individual polarizations, which are reflected in the much greater biases for specific attenuation.

Algorithm	Bias (dB/km)	MSE (dB^2/km^2)	r^2
Horizontal			
Linear	-0.0629	0.0171	0.9596
ZPHI	-0.0641	0.0259	0.9002
SC	0.0076	0.0123	0.9304
MSC	0.0013	0.0117	0.9351
Vertical			
Linear	-0.0704	0.0125	0.9627
ZPHI	-0.0701	0.0191	0.8922
SC	-0.0020	0.0074	0.9244
MSC	-0.0063	0.0069	0.9318
Differential			
Linear	0.0124	0.0015	0.9129
ZPHI	0.0010	0.0019	0.8474
SC	0.0099	0.0018	0.8652
MSC	0.0068	0.0014	0.8895

Table 4.11: As in Table 4.3, but for the Wavelength experiment.

4.5.2 X band

At X-band, the results of changing the wavelength are similar to those observed at C-band. The PPIs of horizontal attenuation in Figure 4.85 show a large increase in the intrinsic attenuation. The algorithms show some changes from the results in the Control experiment, but in these images it is difficult to tell the exact nature due to the area of completely extinguished signal. Results at vertical polarization, Figure 4.87, are similar. The corresponding PPIs of the difference from truth, shown in Figures 4.86 and 4.88, show large changes for the Linear and ZPHI algorithms and minimal changes in the errors for the SC and MSC algorithms. The Linear algorithm fares very badly in changing the wavelength at X-band, with errors approaching 8 dB at both polarizations before the signal completely extinguishes; this is an exceedingly large change in performance given that this algorithm shows the least errors (nearly 0 dB) of all the algorithms in the Control experiment. ZPHI also shows a large increase in errors, with errors approaching 5 dB (discounting the fringes around the areas of extinguished signal). SC and MSC show no significant changes in the errors in these same areas, in comparison with the Control experiment. The histograms for specific attenuation (in Figures 4.89 and 4.90 for horizontal and vertical polarizations, respectively), show that for the Linear algorithm, the band of points has rotated to the right of the one-to-one ratio line. ZPHI develops a large area of points below the one-to-one line in comparison with the Control experiment results. These effects cause both the bias and MSE for the algorithm (Table 4.12) to increase greatly from their respective values in the results for the Control experiment; these results are also in agreement with the observed changes in the PPIs of attenuation. For the SC and MSC algorithms, there are no significant changes other than the expanded range due to larger values of attenuation; there are

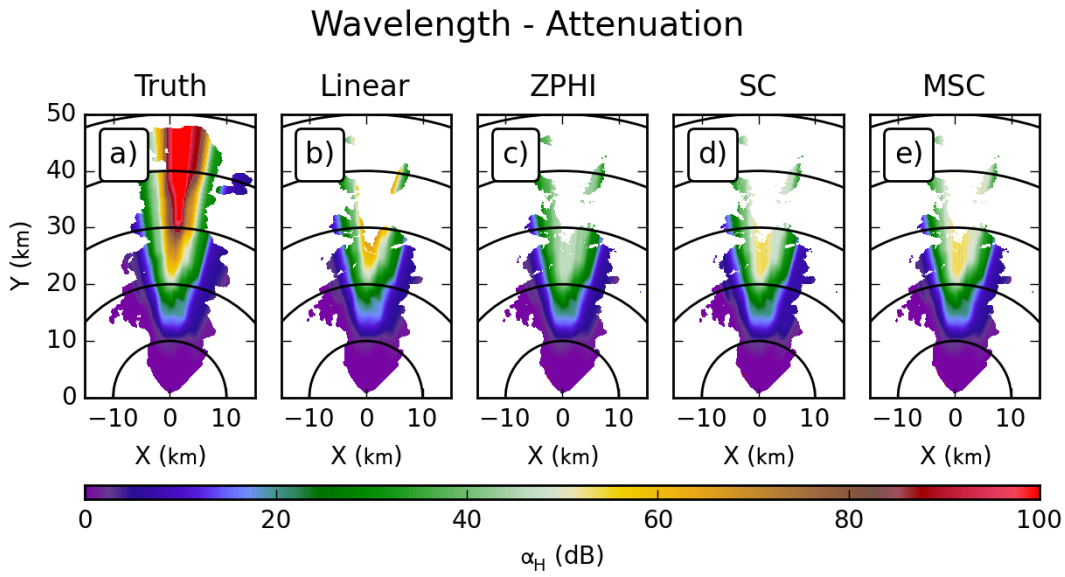

Figure 4.85: As in Figure 4.76, but for X-band.

no changes relative to the one-to-one line. There are, however, modest changes to the computed bias and MSE values for the algorithms (Table 4.12).

In comparison with the results at the individual polarizations, the results for differential attenuation are much less drastic. The PPI of the intrinsic attenuation in Figure 4.91 shows that the Wavelength experiment has slightly increased intrinsic differential attenuation in comparison with the Control experiment. The differences from the true values, in Figure 4.83, show that the only algorithm that experiences any significant change from the Control experiment is the Linear algorithm. The Linear algorithm, as in the Wavelength experiment at C-band, exhibits a decrease in errors in estimating differential attenuation in comparison with results for the Control experiment, with peak errors decreasing from $1.0\,$dB to $0.5\,$dB. The histogram of specific differential attenuation (Figure 4.93) shows that this decrease is the result from a small

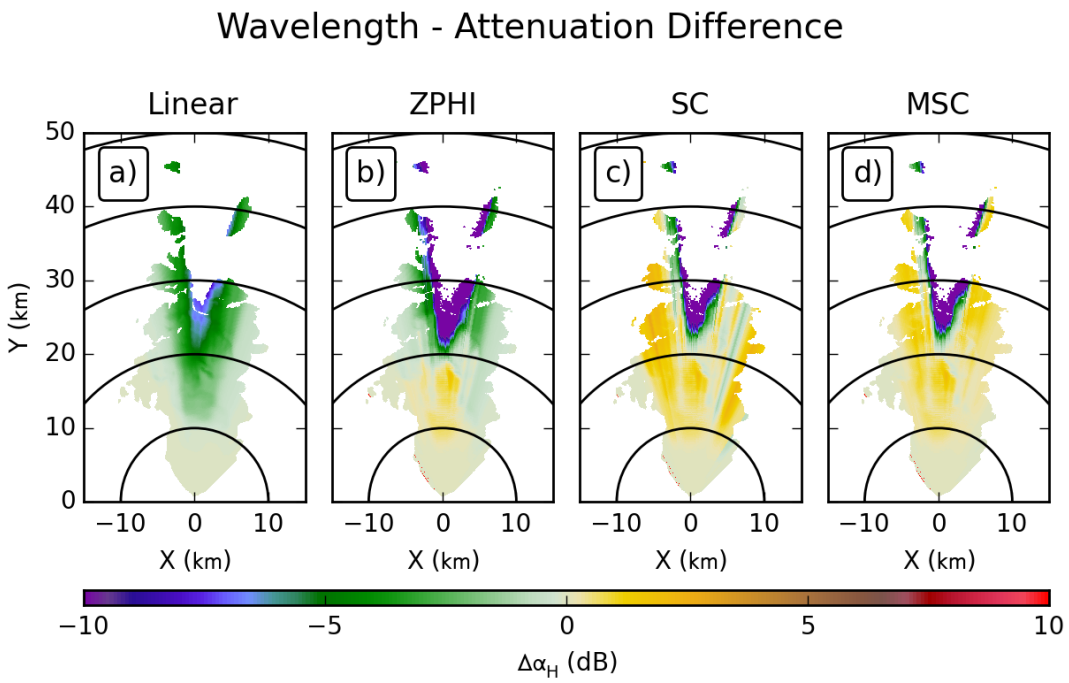

Figure 4.86: As in Figure 4.77, but for X-band.

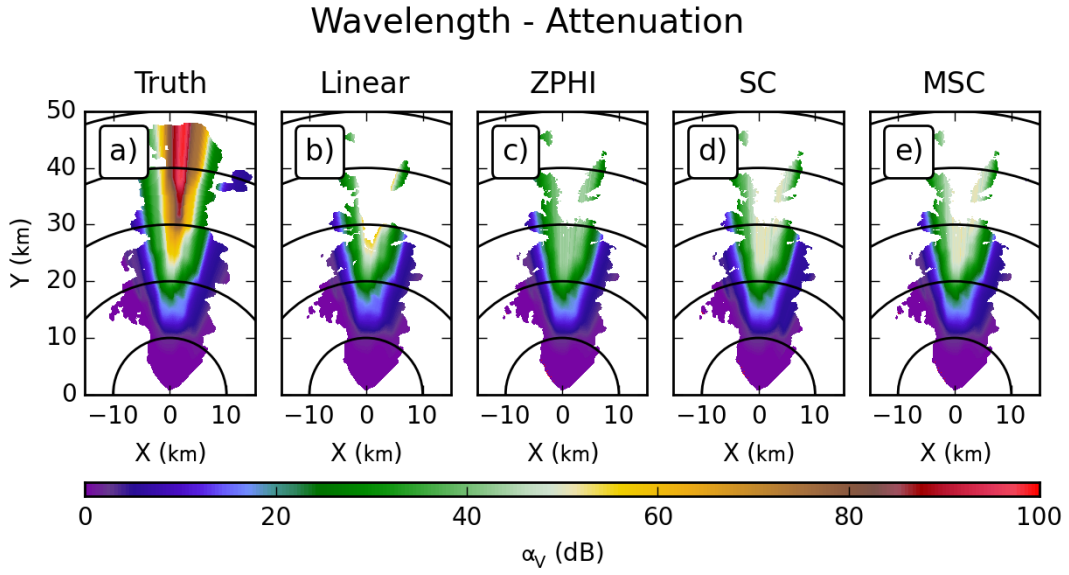

Figure 4.87: As in Figure 4.85, but for vertical polarization.

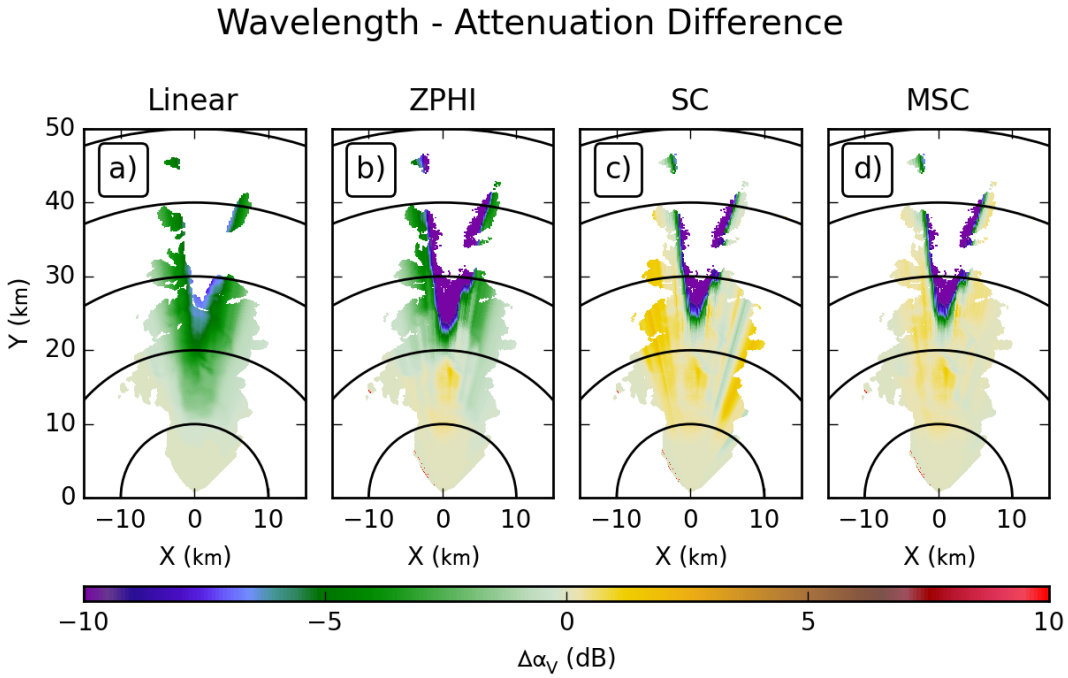

Figure 4.88: As in Figure 4.86, but for vertical polarization.

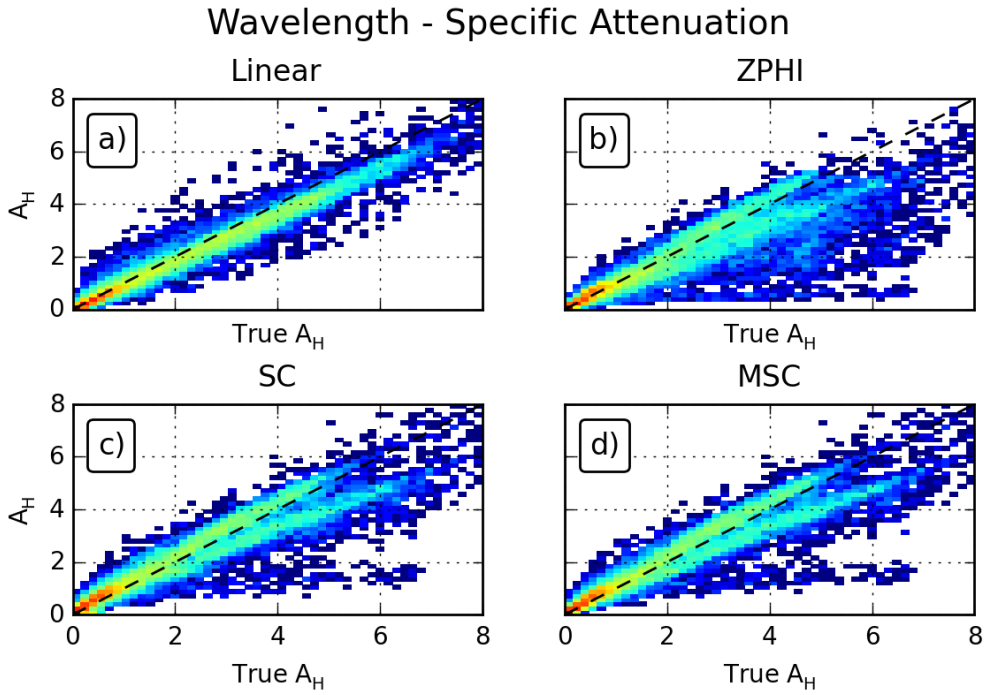

Figure 4.89: As in Figure 4.80, but for X-band.

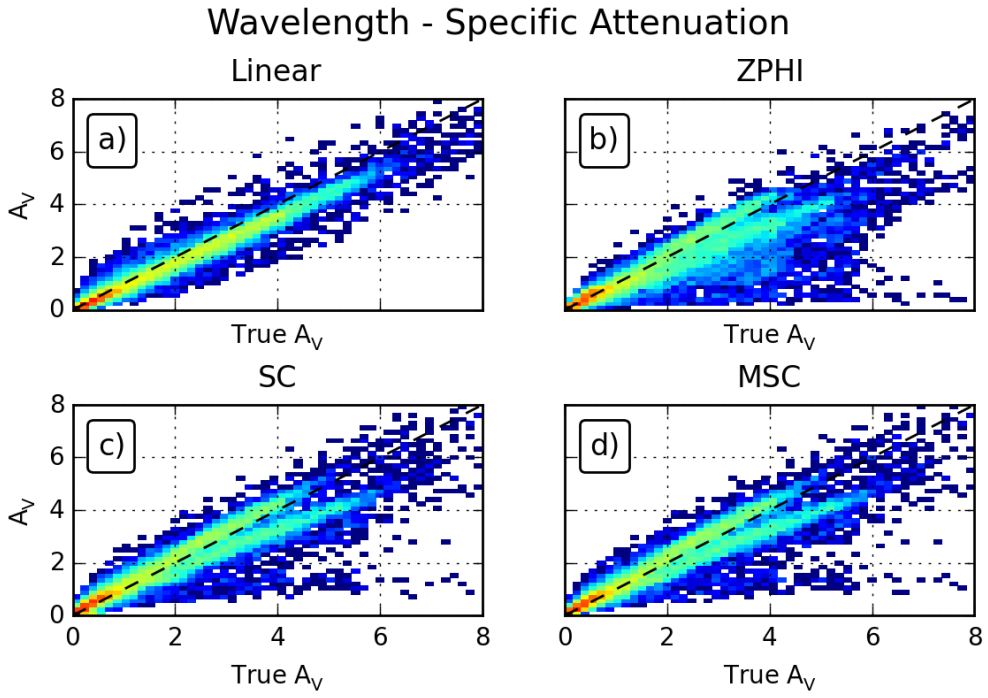

Figure 4.90: As in Figure 4.89 but for vertical polarization.

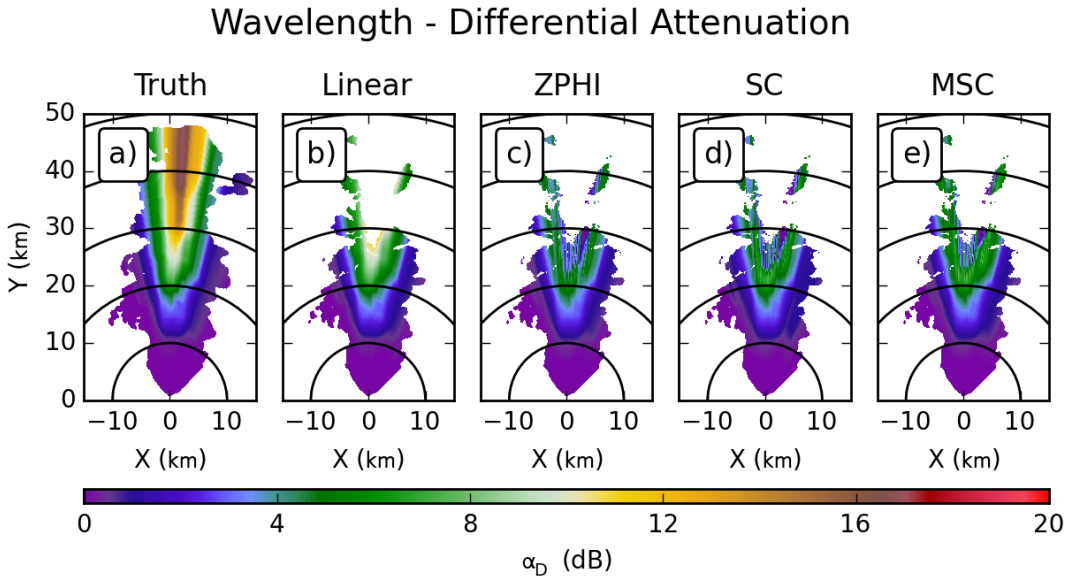

Figure 4.91: As in Figure 4.85, but for differential attenuation.

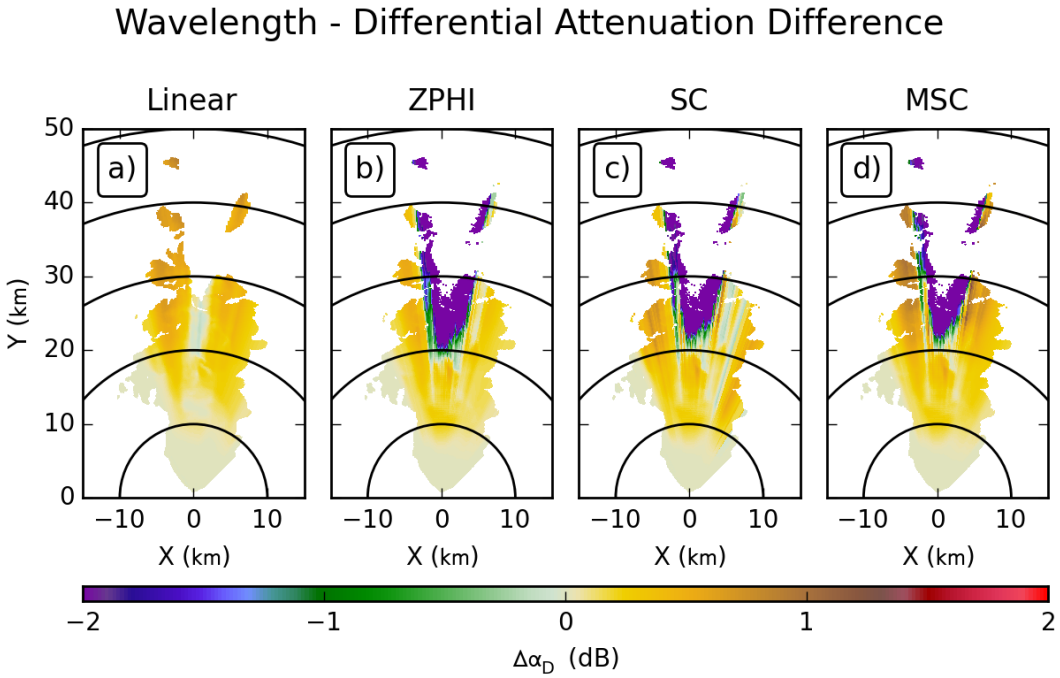

Figure 4.92: As in Figure 4.86, but for differential attenuation.

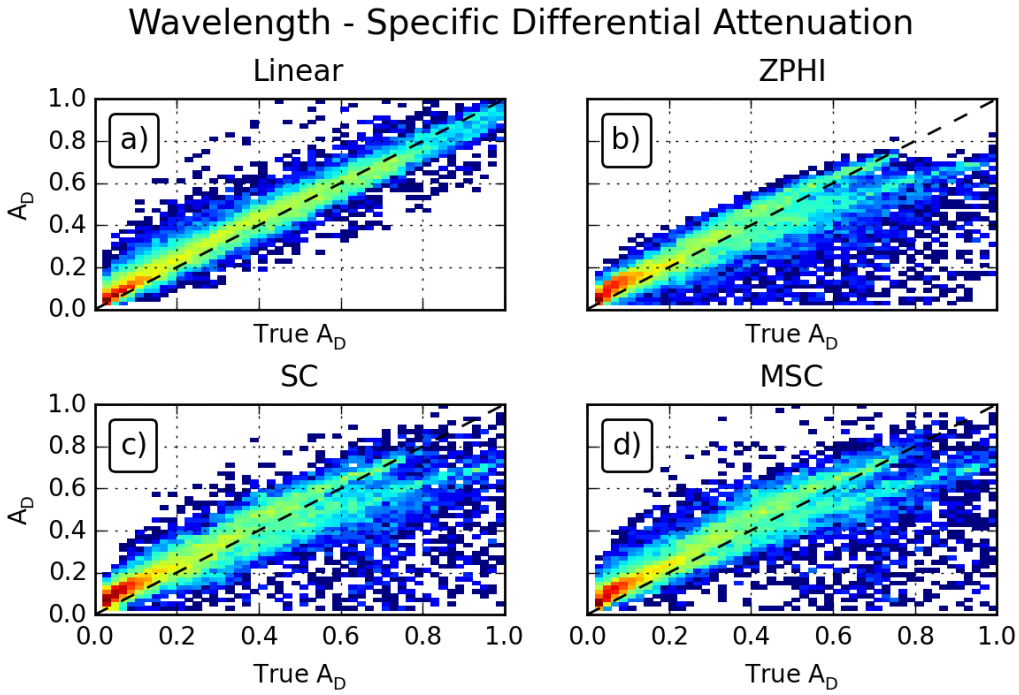

Figure 4.93: As in Figure 4.89, but for specific differential attenuation.

shift in the band of points, such that more of the band lies along the one-to-one ratio line, with a small negative bias at the highest values of specific differential attenuation.

4.6 Combined

Based on the all of the previous experiments, the Combined experiment examines a kind of "worst-case" scenario; whereas the previous experiments systematically probe the effects of violating individual assumptions, this experiment simultaneously violates all of the assumptions. By combining all of the effects, the experiment seeks to identify how errors may increase further with more incorrect assumptions. In considering this a "worst-case", this implicitly assumes that the errors stack together; as will be shown, it is just as possible that errors are of opposite sign and cancel.

Algorithm	Bias (dB/km)	MSE (dB^2/km^2)	r^2
Horizontal			
Linear	-0.1385	0.1323	0.9726
ZPHI	-0.1923	0.5343	0.8485
SC	0.0003	0.2619	0.9178
MSC	-0.0077	0.2398	0.9233
Vertical			
Linear	-0.1521	0.1064	0.9727
ZPHI	-0.1931	0.4143	0.8389
SC	-0.0081	0.1994	0.9123
MSC	-0.0267	0.1900	0.9161
Differential			
Linear	0.0220	0.0040	0.9585
ZPHI	-0.0168	0.0211	0.7163
SC	0.0009	0.0167	0.7992
MSC	0.0109	0.0163	0.7970

Table 4.12: As in Table 4.4, but for the Wavelength experiment.

4.6.1 C band

In the Combined experiment, the base field of horizontal attenuation, in Figure 4.94, shows large increases across the board. Visually, the increase in intrinsic attenuation seems to be best matched by the SC algorithm. The Linear and ZPHI algorithms show large increases, much higher than the intrinsic values, while the MSC algorithm does not appear to increase enough. These results are mirrored at vertical polarization, shown in Figure 4.96. These observations are confirmed in the differences from the intrinsic values for horizontal and vertical polarizations, shown in Figures 4.95 and 4.97, respectively. Linear shows the greatest amount of error, around 5 dB. ZPHI follows closely with errors of the same magnitude but showing less total area with that magnitude. The results from MSC, unlike the others, show the development of a pronounced negative bias, around 2 dB at both polarizations, in the core of the reflectivity structure. Since SC does not show any such bias, this is likely a result of a fixed coefficient across the domain being unable to match well the intrinsic relationships between radar observables and attenuation. The histograms of specific attenuation for both polarizations, in Figures 4.98 and 4.99, show the upward shift of the points for both Linear and ZPHI, which causes the observed positive bias. These histograms also show a slight difference between the SC and MSC algorithms; while the histogram of points for SC is balanced around the one-to-one ratio line, the MSC algorithm has more points below, as well as a band of points curving away from this line at higher values of specific attenuation. All of these effects contribute to the observed negative bias for MSC. This behavior is not evident, however, in the bias and MSE values for the experiment (Table 4.13), which are not significantly changed from the values for

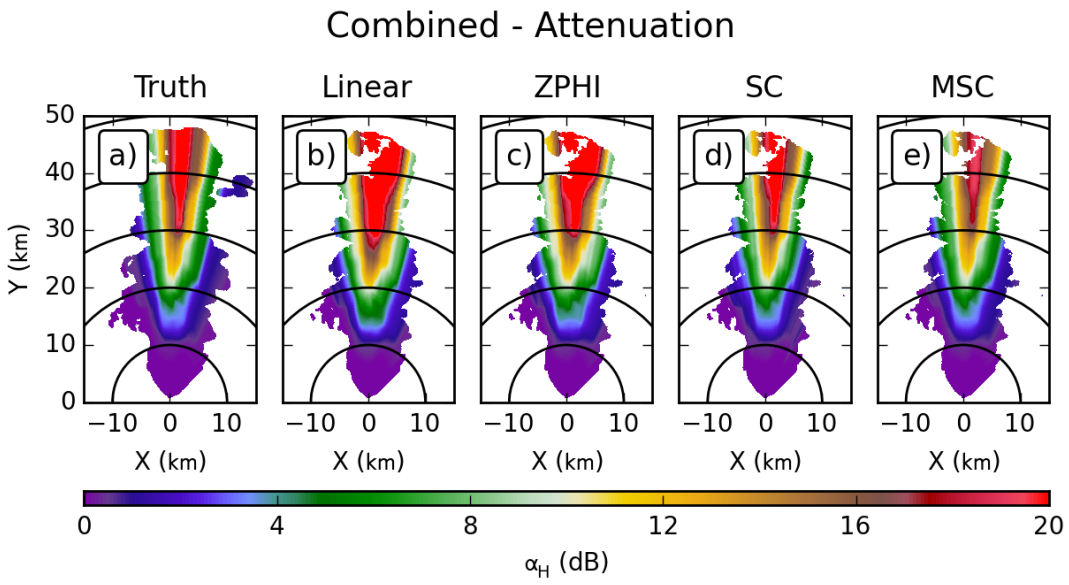

Figure 4.94: As in Figure 4.3, but for the Combined experiment.

MSC in the Control experiment. The bias values for the ZPHI and Linear algorithms are much larger.

For differential attenuation, the PPIs across the board show an increase in magnitude in Figure 4.100. The relative size of the increase matches those from the individual polarizations, with SC visually matching the intrinsic values best, Linear and ZPHI being too high, and MSC being not high enough. The differences from truth in Figure 4.101 quantify these errors. Here, the MSC algorithm shows the biggest errors as well as the biggest change; the pronounced negative bias of approximately $1.3\,\text{dB}$ represents a large change from the almost $0\,\text{dB}$ error observed in the same region in the Control experiment. Again, this is different from the SC algorithm, where the only change is slight increases to the magnitude of errors in individual rays but no change in overall bias. The Linear algorithm also shows an increase in its positive bias, changing from approximately $1\,\text{dB}$ in the Control experiment to $1.5\,\text{dB}$ here.

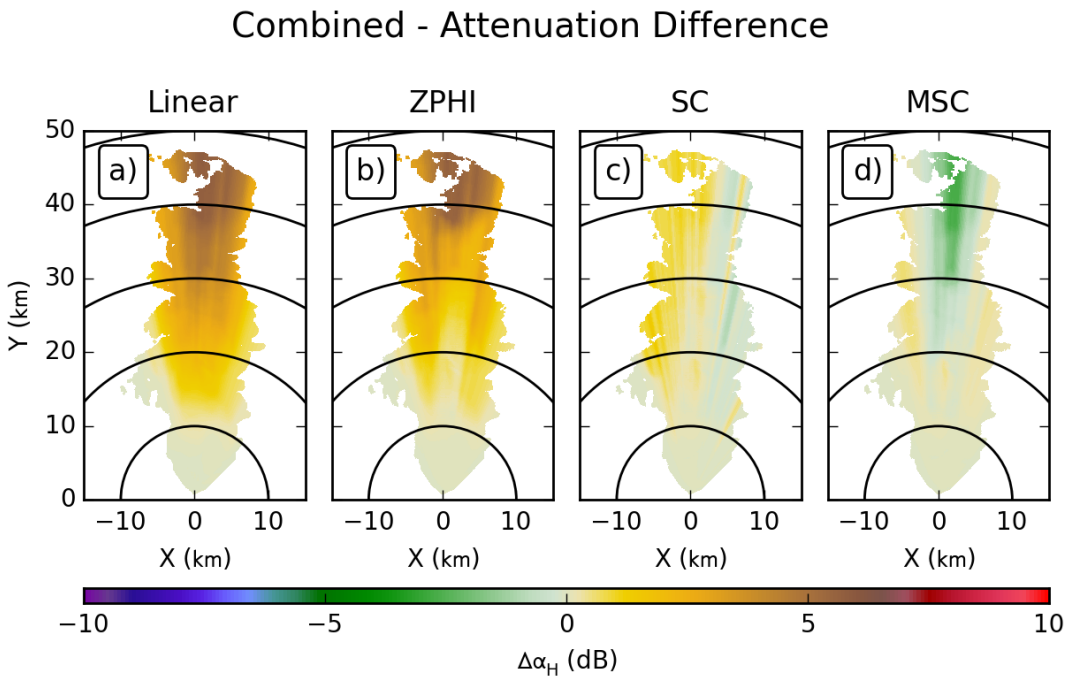

Figure 4.95: As in Figure 4.4, but for the Combined experiment.

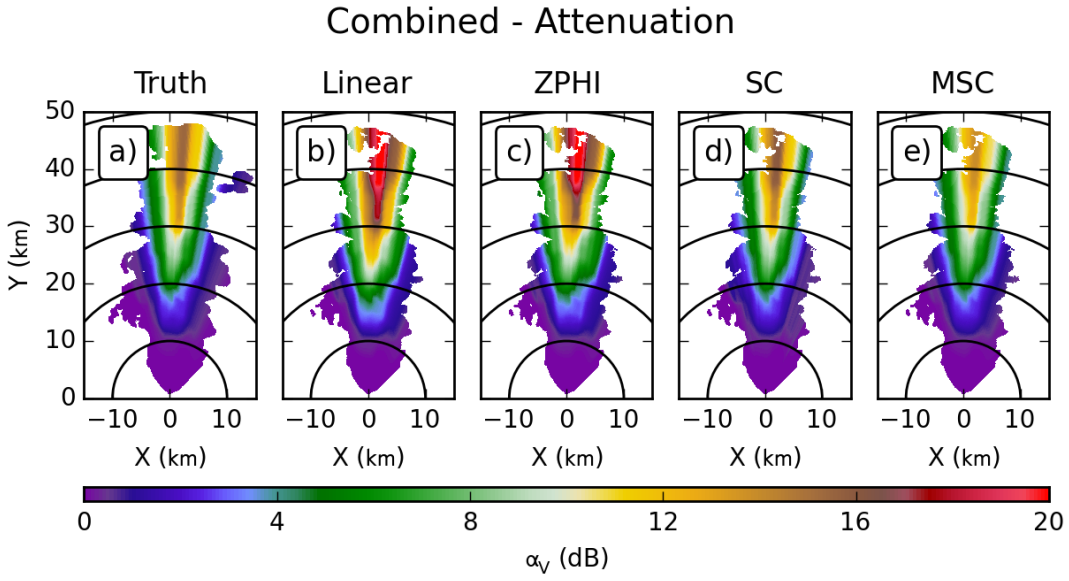

Figure 4.96: As in Figure 4.94, but for vertical polarization.

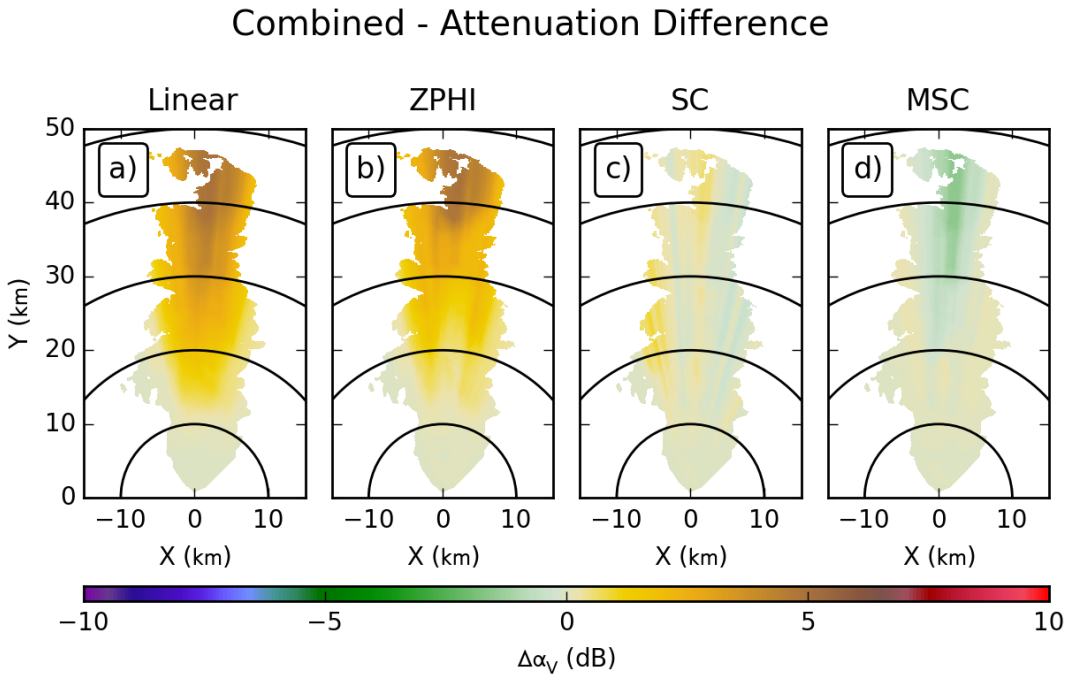

Figure 4.97: As in Figure 4.95, but for vertical polarization.

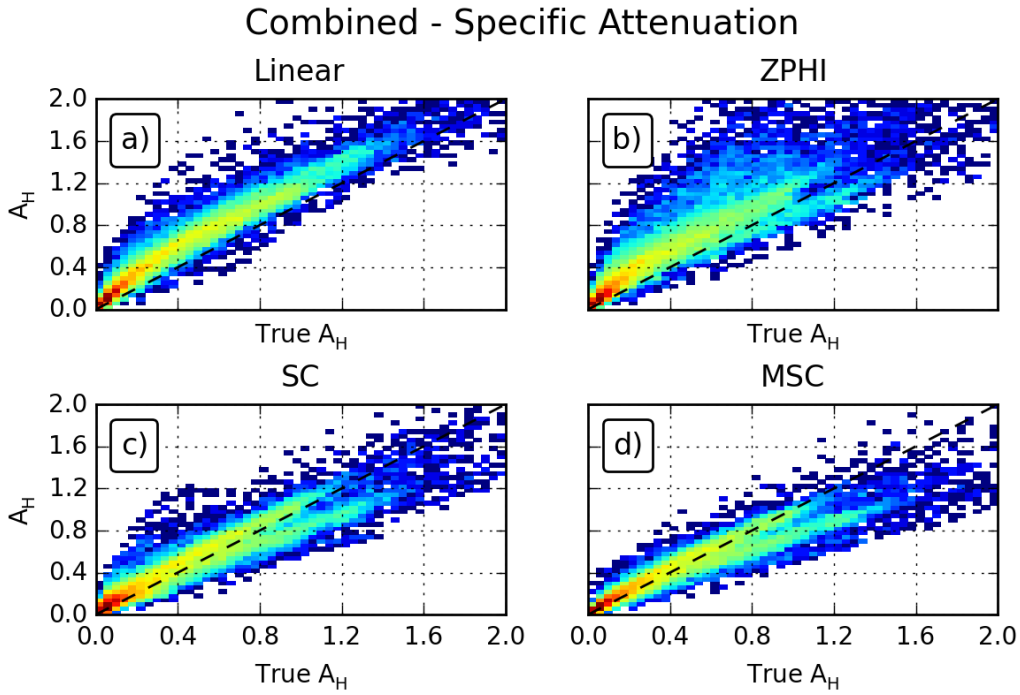

Figure 4.98: As in Figure 4.7, but for the Combined experiment.

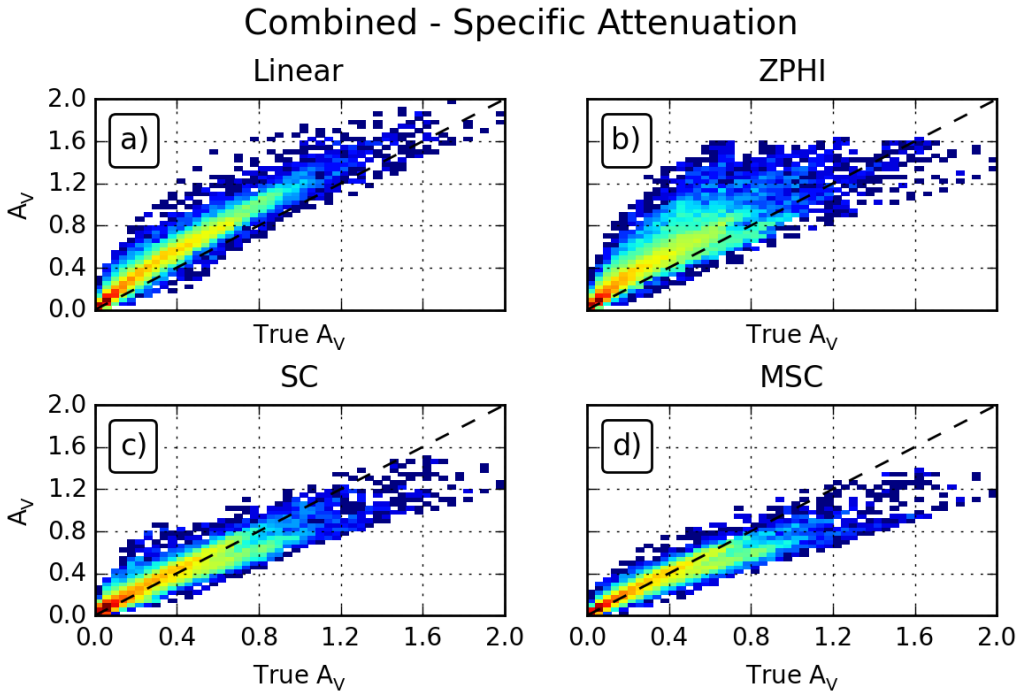

Figure 4.99: As in Figure 4.98, but for vertical polarization.

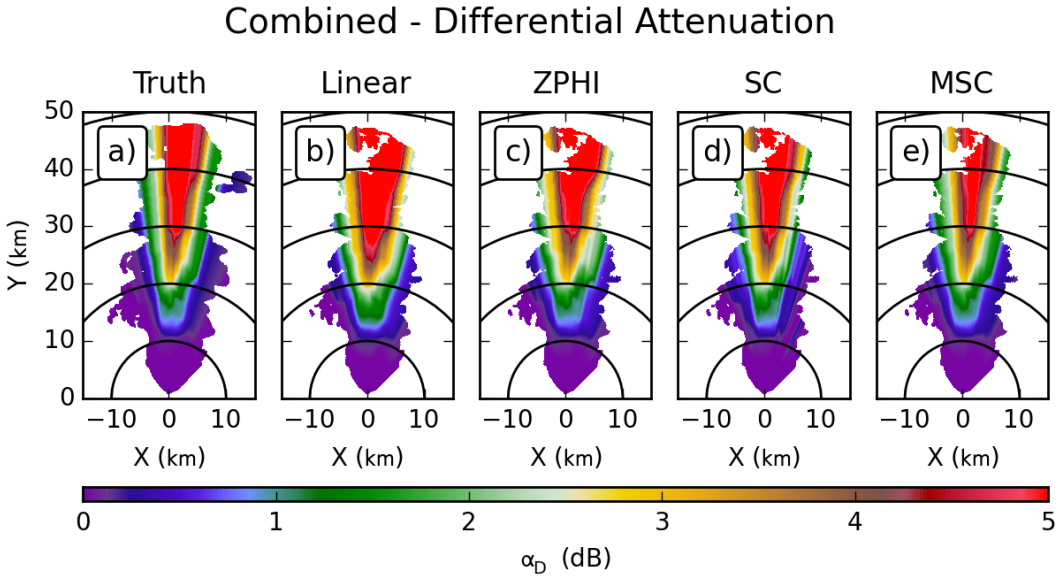

Figure 4.100: As in Figure 4.94 but for differential attenuation.

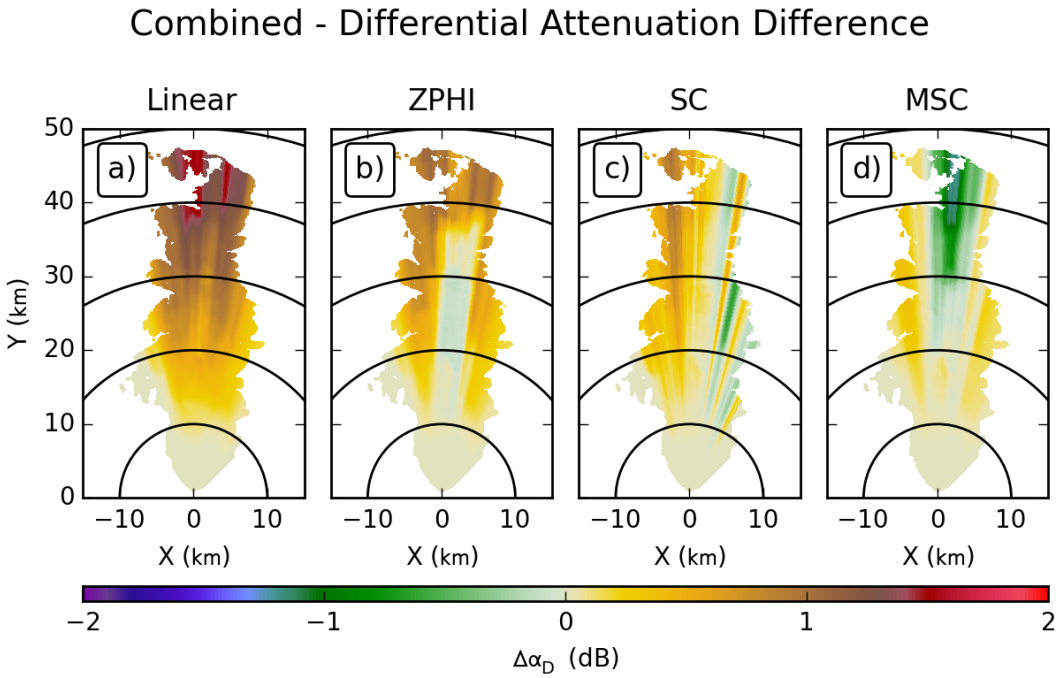

Figure 4.101: As in Figure 4.95, but for differential attenuation.

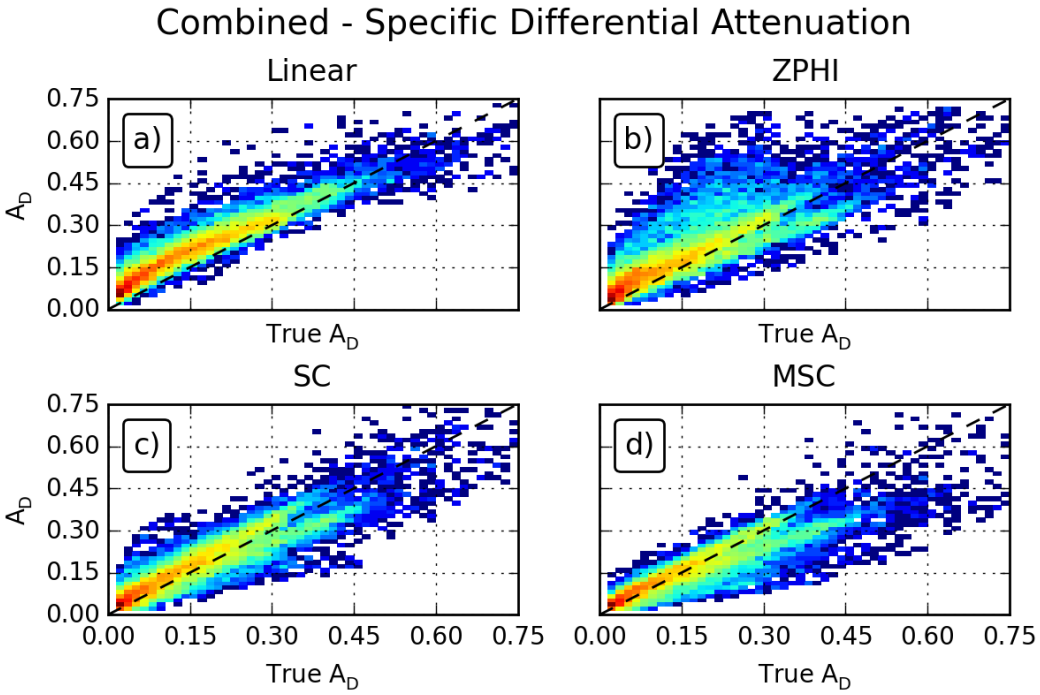

Figure 4.102: As in Figure 4.98, but for specific differential attenuation.

The ZPHI shows a two-fold change in its behavior. Along the edges of the reflectivity structure, where attenuation is less, the positive bias increases from around 0.5 dB to approximately 1.0 dB. In the core of the storm, the bias switches from slightly positive to slightly negative. This behavior is reflected in the histogram of specific differential attenuation shown in Figure 4.102. In comparison with the same histogram for the Control experiment, the ZPHI algorithm here shows a much larger region of points above the one-to-one line for small attenuation values, while an increase in negative bias for larger values. For the Linear algorithm, the histogram shows the shift in points corresponding to the increased positive bias. Conversely, the MSC algorithm shows an increase in the area of points below the line, a change not observed in the plot for SC; this corresponds to the increasing negative bias for MSC in the Combined experiment.

Algorithm	Bias (dB/km)	MSE (dB^2/km^2)	r^2
Horizontal			
Linear	0.1335	0.0302	0.9418
ZPHI	0.1311	0.0478	0.8375
SC	0.0221	0.0132	0.9128
MSC	-0.0104	0.0143	0.9202
Vertical			
Linear	0.1050	0.0187	0.9512
ZPHI	0.1027	0.0259	0.8402
SC	0.0107	0.0063	0.9085
MSC	-0.0093	0.0065	0.9221
Differential			
Linear	0.0512	0.0044	0.8924
ZPHI	0.0375	0.0063	0.7293
SC	0.0119	0.0025	0.8605
MSC	-0.0088	0.0029	0.8465

Table 4.13: As in Table 4.3, but for the Combined experiment.

4.6.2 X band

At X-band, the Combined experiment shows, in Figures 4.103 and 4.105, a pronounced increase in attenuation over the Control results for both polarizations. For the Linear algorithm, the differences from true attenuation for the Combined experiment (Figures 4.104 and 4.106 for horizontal and vertical polarizations, respectively) exhibit a very large increase; here the errors have increased to a peak magnitude of 10 dB, up from around 1 dB for the Control experiment. The ZPHI algorithm results also show a large, although lesser, increase, with errors now approaching almost 7.5 dB. The SC and MSC algorithms show smaller increases, with errors near 0 dB for the Control experiment now approaching 2 dB. These large increases in error are reflected in the histograms of specific attenuation for both polarizations in Figures 4.107 and 4.108; here the results for Linear and ZPHI both show large shifts in points upwards above the one-to-one ratio line, consistent with the large positive biases exhibited. The computed bias values for these two algorithms in this experiment are over ten times as large as those for the Control experiment (Table 4.14). Another feature of these histograms is a bulge in some points upwards in the results for the SC algorithm. These are a reflection of degraded results for some of the rays. MSC, through its use of smoothing the optimized coefficients, is able to avoid such rays.

Figure 4.109 shows that the results for differential attenuation are similar, with an increase in differential attenuation across the board, both intrinsic and calculated. The PPIs of the differences from the true values, in Figure 4.110, show that SC, having the lowest overall errors, does the best job of capturing these changes. The MSC and ZPHI algorithms are close, but they show increases in errors along the edges of the storms; here the errors have increased to over 1.2 dB, up from less than 1 dB in the Control

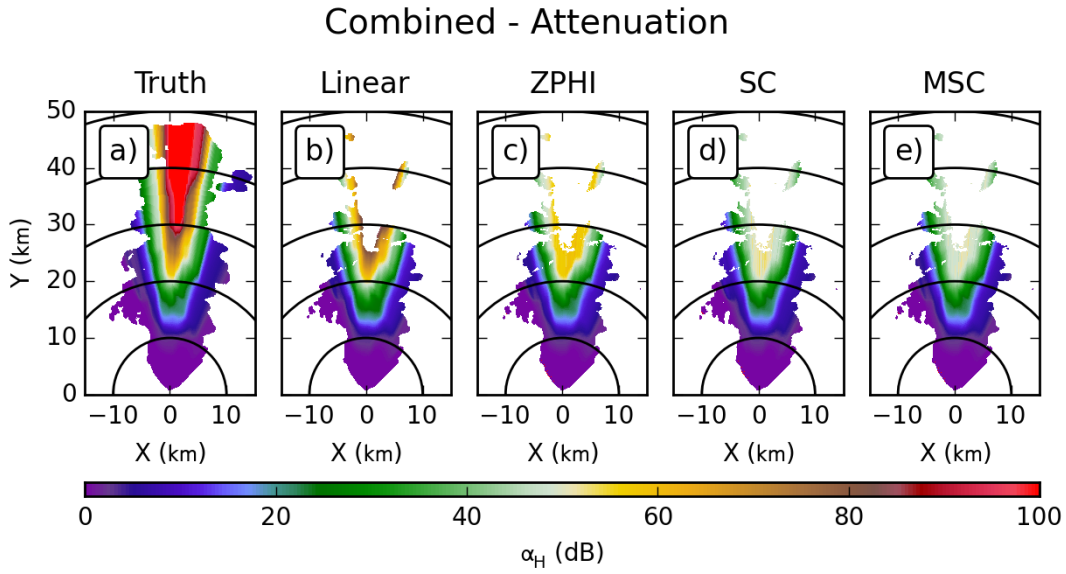

Figure 4.103: As in Figure 4.94, but for X-band.

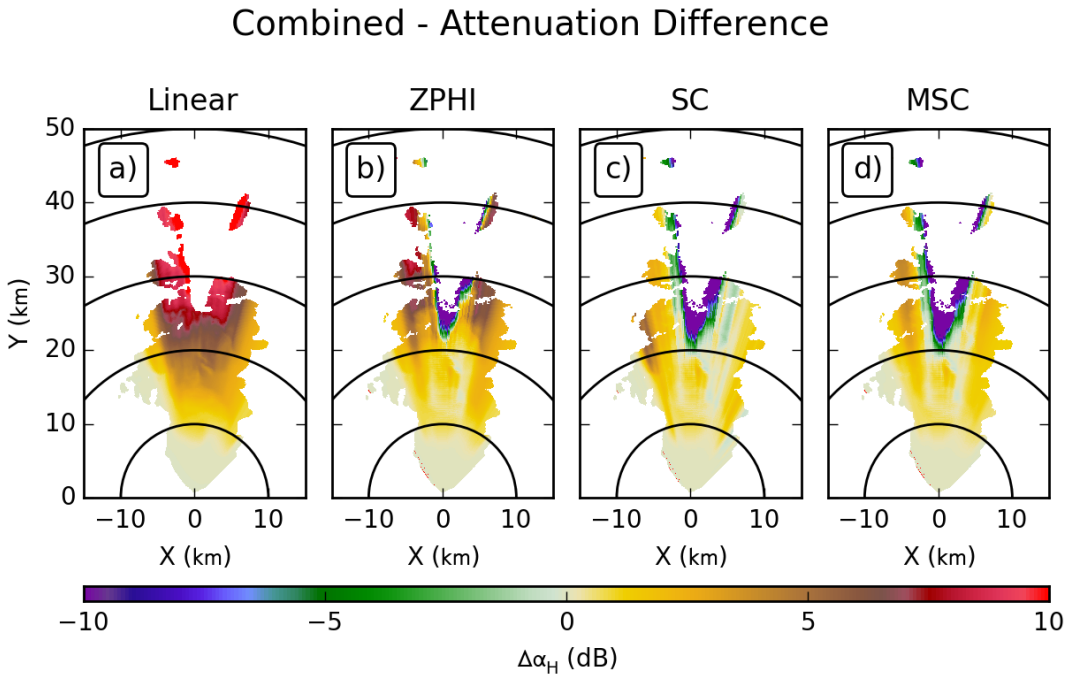

Figure 4.104: As in Figure 4.95, but for X-band.

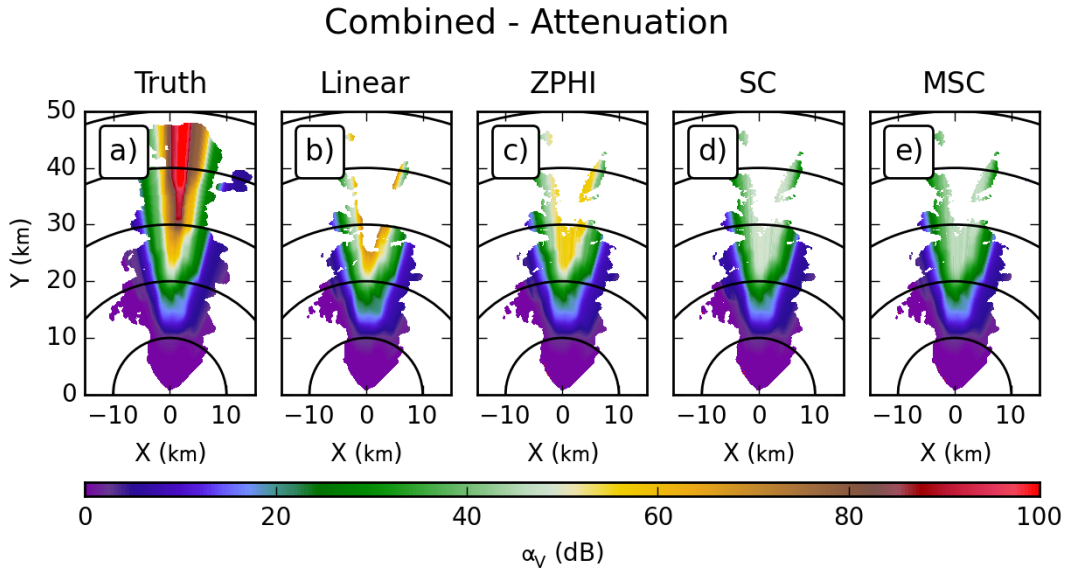

Figure 4.105: As in Figure 4.103, but for vertical polarization.

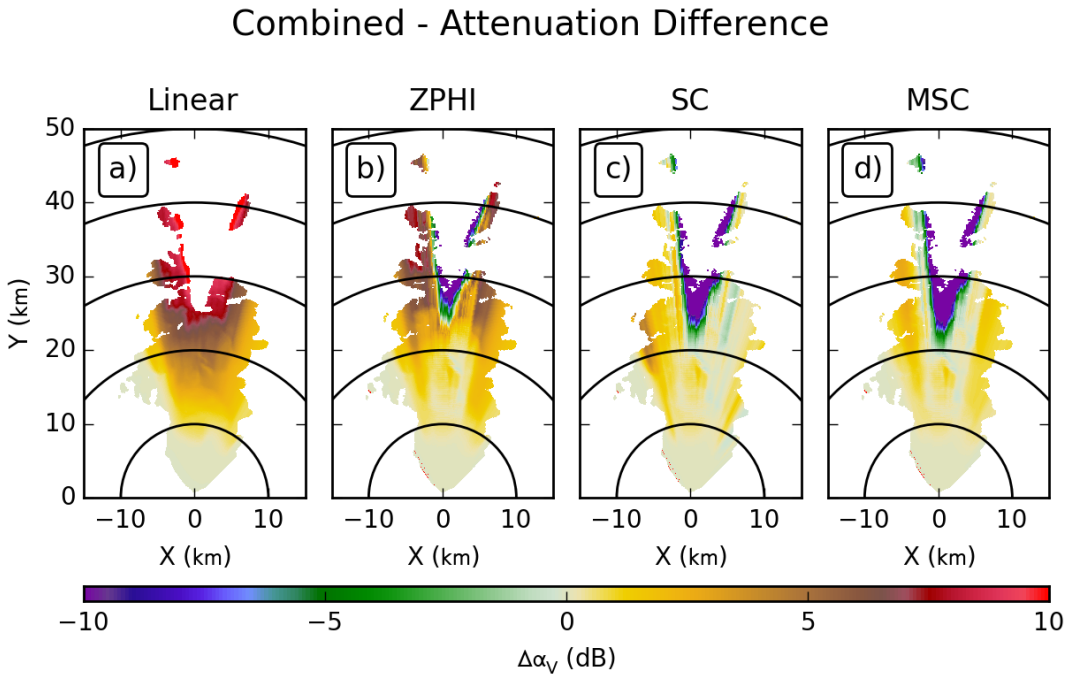

Figure 4.106: As in Figure 4.104, but for vertical polarization.

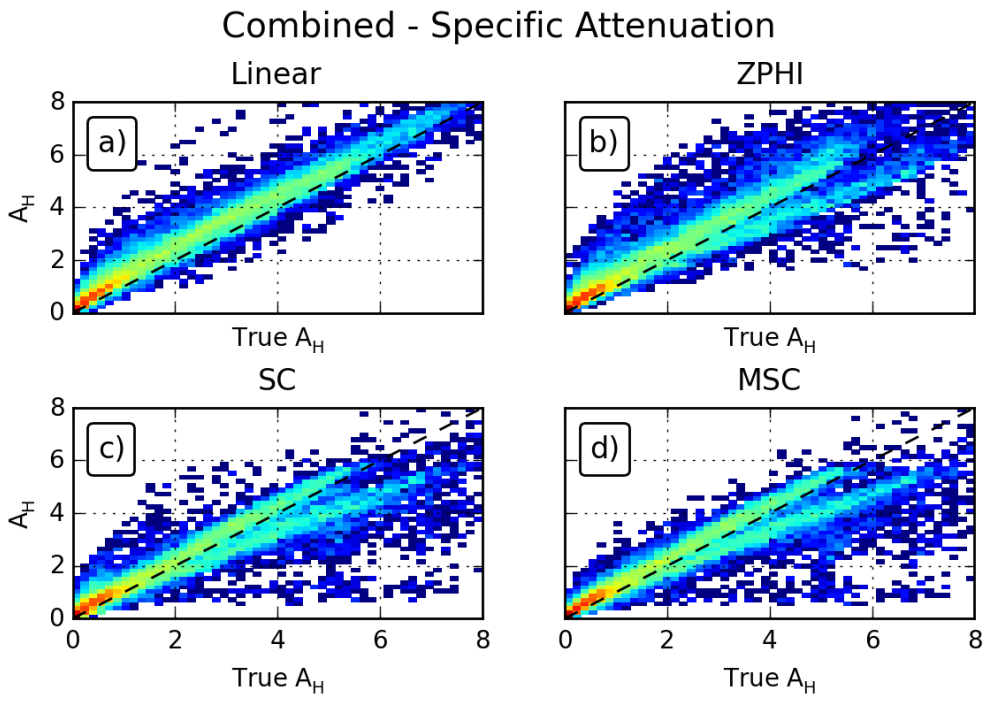

Figure 4.107: As in Figure 4.98, but for X-band.

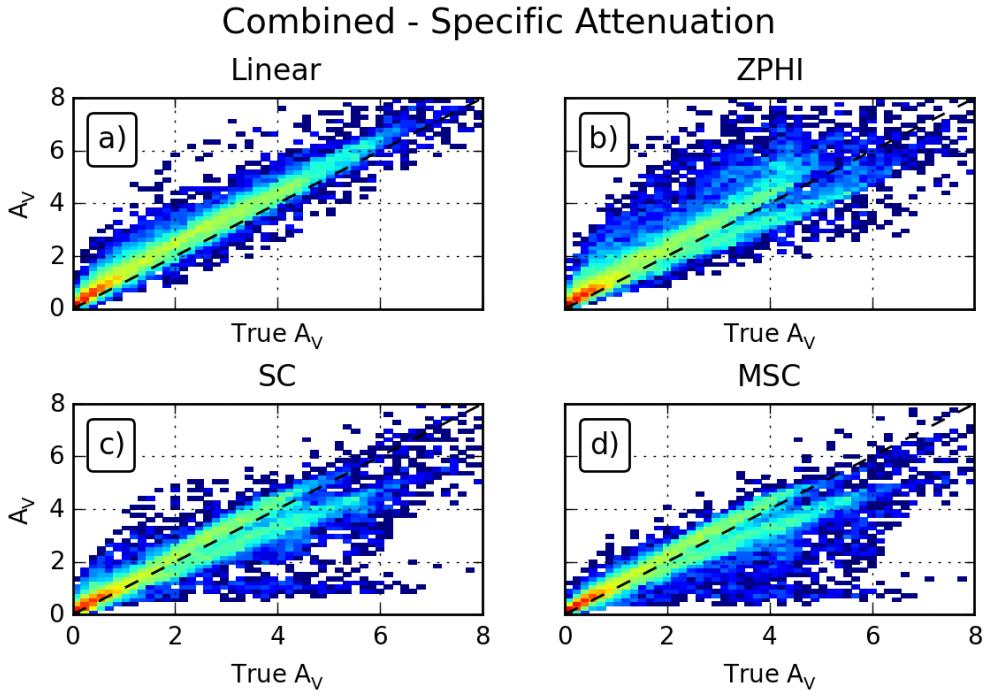

Figure 4.108: As in Figure 4.107, but for vertical polarization.

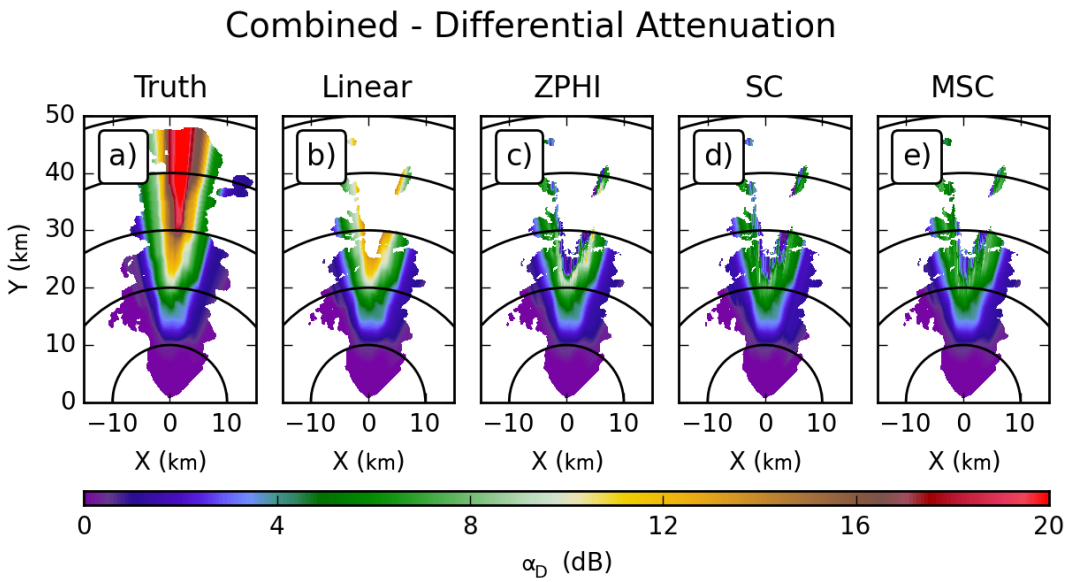

Figure 4.109: As in Figure 4.103, but for differential attenuation.

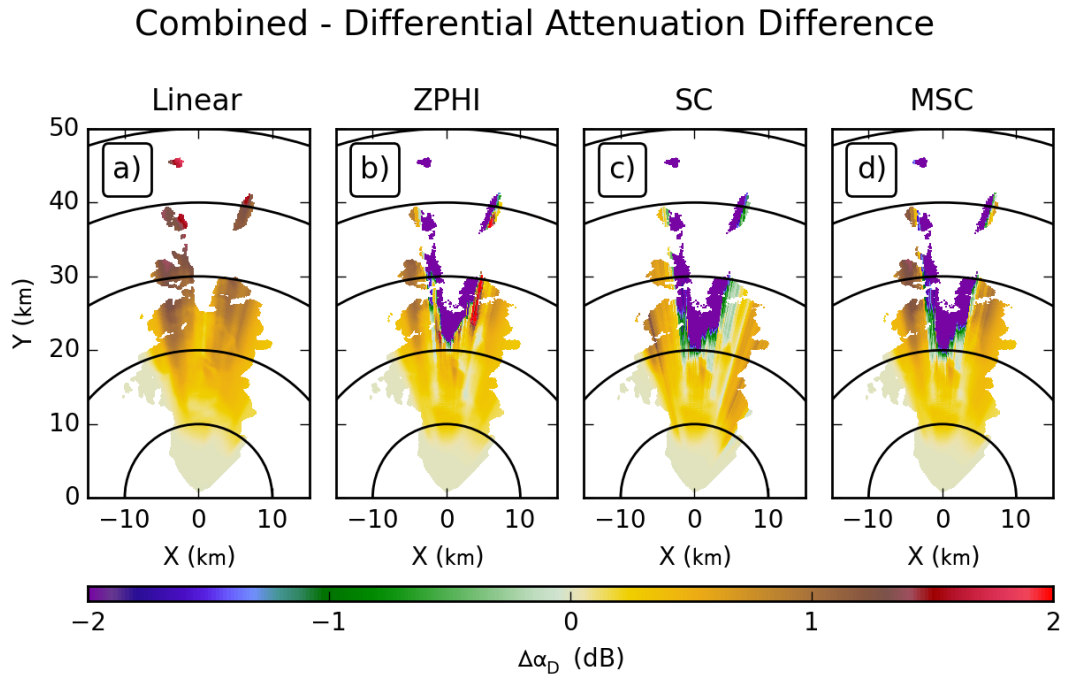

Figure 4.110: As in Figure 4.104, but for differential attenuation.

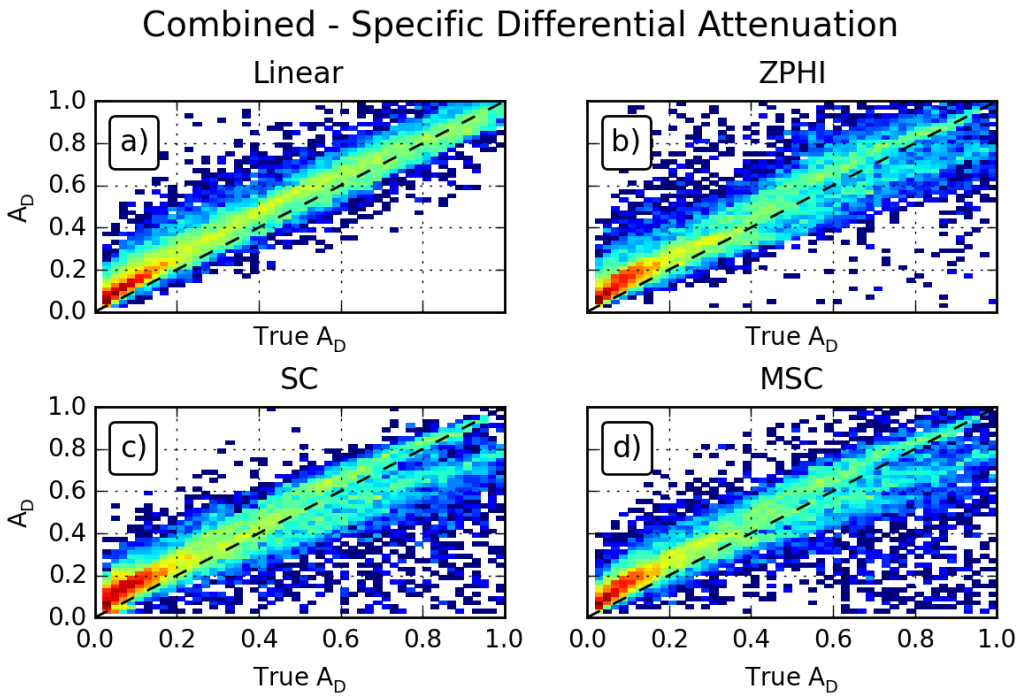

Figure 4.111: As in Figure 4.107, but for specific differential attenuation.

experiment. Linear shows errors up to 1.5 dB, though it should be noted that the other algorithms do not produce usable data in these regions. The histograms of specific differential attenuation, given in Figure 4.111, show pronounced shifts in the bands for the Linear and ZPHI algorithms, which correspond to the increases in positive bias of the estimates. The SC and MSC algorithms do not show such pronounced shifts, though they do appear to have increased numbers of points above the one-to-one line.

4.7 Conclusion

This chapter examines the results of running several attenuation correction techniques, Linear, ZPHI, Self-Consistent, and Modified Self-Consistent using simulated radar data. The focus here is on the impacts of the assumptions made in developing these

Algorithm	Bias (dB/km)	MSE (dB^2/km^2)	r^2
Horizontal			
Linear	0.3420	0.2691	0.9653
ZPHI	0.2355	0.4268	0.8988
SC	-0.0041	0.4510	0.8867
MSC	-0.0144	0.4748	0.8811
Vertical			
Linear	0.3115	0.2088	0.9659
ZPHI	0.2453	0.3956	0.8777
SC	0.0033	0.2802	0.8933
MSC	-0.0330	0.3185	0.8815
Differential			
Linear	0.0499	0.0082	0.9565
ZPHI	0.0419	0.0287	0.7810
SC	-0.0011	0.0298	0.7549
MSC	0.0081	0.0296	0.7458

Table 4.14: As in Table 4.4, but for the Combined experiment.

techniques and how the violation of these assumptions impacts algorithm performance. The baseline of performance is established using the Control experiment, where all assumptions made in obtaining the coefficients used in the algorithms are matched in the simulation procedure. At C-Band, Self-Consistent and Modified Self-Consistent prove most successful, thought Linear and ZPHI algorithms yielded useful results provided small biases are acceptable for a given application. At X-band, the Linear algorithm actually shows the least error, though the rest of the algorithms produced results that were only slightly worse. Overall, the algorithms all worked quite well in the Control experiment.

In the other experiments, when these assumptions were systematically violated, the Linear and ZPHI techniques, because they rely upon fixed coefficients, yielded much higher errors than the Self-Consistent and Modified Self-Consistent algorithms, at both X- and C-band. In almost all cases these latter algorithms were able to deliver reasonable results. While the biases for individual polarizations from these algorithms could still be in the range of $1\,\mathrm{dB}$ to $2\,\mathrm{dB}$, this was much more usable than the errors for the Linear and ZPHI algorithms in most cases.

Differential attenuation proved challenging for the algorithms in most cases, which is attributed to a collection of causes. Primarily, the challenge for correcting differential attenuation is that Z_{DR} is smaller, and thus its acceptable bias is an order of magnitude less than that for horizontal (or vertical) reflectivity. The other problem is that while the algorithms demonstrate very good results for calculating attenuation for individual polarizations, using the difference between the results exacerbates any errors.

In terms of sensitivity to assumptions, changing any one of them (canting, shape model, temperature, or wavelength), yielded pronounced changes, both in terms of the resulting attenuation field and in the results of the algorithms. This implies that successful use of these techniques depends upon carefully making assumptions that match nature. For physical processes (i.e., canting and shape model), this implies the need for good data and parameterizations of the microphysical processes involved. For something like temperature, which varies greatly, this implies a greater challenge. For fixed coefficient techniques, though, the biases introduced are significant, so making use of any temperature data available could yield significant gains in reducing the bias in reflectivity due to under- or over-correction for attenuation.

Most important of all effects, was the sensitivity to wavelength within the band. Changing the wavelength by only $10\,\%$ introduced at least $5\,$dB of error in the attenuation estimates by the Linear and ZPHI algorithms; this runs counter to the common wisdom that one can use coefficients for these algorithms that are appropriate to a given band. It is possible, then, to gain algorithm performance by simply tuning coefficients to the true operating wavelength of a given radar system. While the Self-Consistent algorithms were able to largely compensate for all of the violated assumptions, including wavelength, the best algorithm performance occurred for the Control experiment. Therefore, It is important to all algorithms to take care in making accurate assumptions; using the true wavelength of the radar, rather than some general waveband, is one of the simplest ways to eliminate errors.

Chapter 5

Sampling Errors in Attenuation Correction

Whereas the previous chapter focuses on the assumptions underlying the physical model used for scattering calculations, here the focus is on the impact of radar operating parameters on attenuation correction, specifically those parameters that impact the spatial sampling of the data. This includes hardware effects, such as the beamwidth or antenna sidelobes, as well as the data spacing.

One source of error arising from spatial sampling is integration within the resolution volume. The regressions underlying the attenuation correction coefficients fit radar observables calculated from a single drop size distribution; however, radar resolution volumes can contain scatterers spread across many different distributions. How integration of these scattering processes transforms into the actual measured radar data has profound implications for the performance of attenuation correction techniques. Another potential impact of spatial sampling is non-uniform beam-filling (NBF). NBF specifically refers to the idea that gradients in precipitation amount and/or type across the radar beam can cause artifacts in data, especially Φ_{DP}. Since Φ_{DP} is a critical variable in the process of correcting for attenuation, NBF poses a significant problem for robust attenuation correction.

As in the previous chapter, the impacts of spatial sampling are tested here with simulated data created using the previously described simulation procedure. Sets of data are generated, for both C- and X-band, using radar and scanning configurations that

explore different aspects of radar spatial sampling. The results of the different attenuation correction algorithms (Linear, ZPHI, SC, and MSC) are compared to the truth field, calculated using the same spatial sampling, to see how algorithm performance changes.

The base radar and simulation configuration is given in Table 5.1. The parameters here match closely those used previously, with the exception that the antenna is rotating more quickly at $20\,^\circ\,\mathrm{s}^{-1}$; this value was chosen to more naturally achieve the larger radial spacing used here without modifying the PRT. The parameters of the scattering model (canting width, wavelength, temperature, and shape model) are selected to match those used to generate the regression coefficients used in the correction algorithms, as was done in the Control experiment in the modeling chapter. This gives a best case scenario for algorithm performance and helps to ensure that any resulting errors are attributable to spatial sampling.

The individual experiments are listed in Table 5.2. The Control experiment here establishes baseline performance with a common radar configuration, 1° beamwidth with matched radial sampling. The other experiments systematically modify this configuration to explore the effects of sidelobes, increased beamwidth, radial sampling interval, and range resolution. Radial spacing is controlled by modifying the number of pulses used to create a radial of data; 75 and 150 pulses are used to create 1° and 2° radials, respectively. Also, pulse width is matched to gate width, such that a $0.8\,\mu\mathrm{s}$ pulse is used with the $125\,\mathrm{m}$ gate spacing and a $1.6\,\mu\mathrm{s}$ pulse is used with the $250\,\mathrm{m}$ gate spacing.

Antenna gain	45.5 dB
Peak power	250 kW
First range gate	500 m
Noise power	−113 dBm
Elevation	0.5°
PRT	0.667 ms
Canting Width	10
Wavelength	5.5 cm, 3.21 cm
Temperature	283 K
Shape Model	Brandes
Rotation Rate	$20\,^{\circ}\,\mathrm{s}^{-1}$

Table 5.1: Radar and scanning parameters common to the simulations

Experiment	Radial Spacing	Beamwidth	Antenna Limits	Gate Width
Control	1°	1°	Main-lobe only	125 m
Sidelobe	1°	1°	1 Side-lobe	125 m
Beamwidth	1°	2°	Main-lobe only	125 m
Radial Width	2°	2°	Main-lobe only	125 m
Range Resolution	1°	1°	Main-lobe only	250 m

Table 5.2: Parameters differing between different experiments

5.1 Control

The Control experiment establishes the reference point for the other experiments, with a scanning strategy that yields $1.0°$ radial spacing, matched to the $3\,$dB beamwidth. This differs from the Control experiment in the previous chapter by using both larger gates ($125\,$m versus $100\,$m), as well as larger beamwidth and radial spacing ($1.0°$ versus $0.25°$). These parameters are selected to form a baseline around a more reasonable (in comparison with standard real-world operations) spatial sampling than that of the modeling study, which is configured specifically to minimize the effects of spatial sampling.

5.1.1 C band

At C-band, the PPIs of horizontal attenuation for the Control experiment, shown in Figure 5.1, show that the Linear and ZPHI algorithms produce the highest estimates for horizontal attenuation, higher than the intrinsic values. The SC and MSC algorithms are much closer to the intrinsic values, though they each are slightly higher and lower, respectively, than the intrinsic values. When the intrinsic attenuation values are subtracted from the algorithm results, in Figure 5.2, the positive bias for the Linear and ZPHI algorithms exhibits maxima in the core of the reflectivity, with a value around $2\,$dB. The SC algorithm overall seems to be unbiased, but individual rays appear to have errors of approximately $0.5\,$dB of either sign. The MSC algorithm, on the other hand, does well to smooth out these errors and produces a field that seems to be unbiased and has only small errors. Histograms of horizontal specific attenuation, in Figure 5.5, show how these errors stack up on a gate-by-gate basis. Both the ZPHI and

Linear algorithms show that the bands of the highest numbers of points are slightly above the one-to-one line, which causes the observed positive bias. Conversely, both the SC and MSC algorithms have their bands of the greatest numbers of points right along the one-to-one line. The results for MSC also show a tighter clustering of points, which is why the algorithm exhibits less errors than the SC algorithm.

At vertical polarization, the results are similar. The PPIs of vertical attenuation in Figure 5.3 show that Linear and ZPHI again have the highest values, though visually they appear much closer to the intrinsic values. The MSC and SC algorithms are, at least visually, difficult to distinguish from the intrinsic results. The differences from the intrinsic values, shown in Figure 5.94, show that indeed the differences for Linear and ZPHI are less; only a positive bias of up to $1\,$dB is observed here. SC, on the other hand, appears to have developed a slight negative bias; while errors still change from radial to radial, the magnitude of negative errors (approaching $1\,$dB) are greater than the positive errors (less than $0.5\,$dB). MSC, again, smooths out these errors and produces a field with no apparent bias and small errors. The histograms of vertical specific attenuation, in Figure 5.6, explain the sources for these behaviors. For the Linear and ZPHI algorithms, the bands of most points sits just above the one-to-one line, yielding a small positive bias. For the SC algorithm, while the main band of points is along the one-to-one line, there are still significant numbers of points below this line, yielding the small negative bias. The MSC algorithm, on the other hand, has a tighter grouping of points and thus does not have the significant area of points below the line. This observed behavior yields the best bias and MSE values (Table 5.3) while still giving an r^2 value that is comparable to that of the Linear algorithm.

For the PPIs of results, at both polarizations neither the raw results nor the differences from the intrinsic values display any significant deviation from the Control experiment in the modeling study. While the change in resolution is clearly visible, the structure of the errors is unchanged between the two experiments. However, the histograms of specific attenuation do show an interesting change between the experiments. In the modeling study, which had a higher resolution, the results for all of the ZPHI-based algorithms showed a pronounced structure with two bands along which most points lay; one band was situated above the one-to-one line and one below. In this Control experiment, with 1.0 degree radial spacing, the two bands have collapsed to a single band that follows the one-to-one line. Also, all algorithms show tighter clustering of points in the lower-resolution data. This effect extends to the computed r^2 values, which have increased for all of the ZPHI algorithms versus the values for the modeling study.

For differential attenuation, the PPIs of the base values, in Figure 5.97, show that both Linear and ZPHI have values that are much larger, while SC and MSC appear to be closer, but too large and too small, respectively. The PPIs of the differences from intrinsic values, in Figure 5.7, show that the Linear algorithm has the most error, with a bias approaching 1.25 dB. ZPHI has a slightly smaller positive bias, only approaching 1.0 dB. SC shows errors fluctuating significantly from radial to radial, with errors of 0.5 dB in either direction. While the MSC algorithm smooths out this behavior, this smoothing yields a significant negative bias in the middle of the field, with a magnitude approaching 0.5 dB; this is a change from the behavior for the individual polarizations. Histograms of the specific differential attenuation values (Figure 5.9) show that both Linear and ZPHI's points are shifted above the one-to-one line, causing the observed

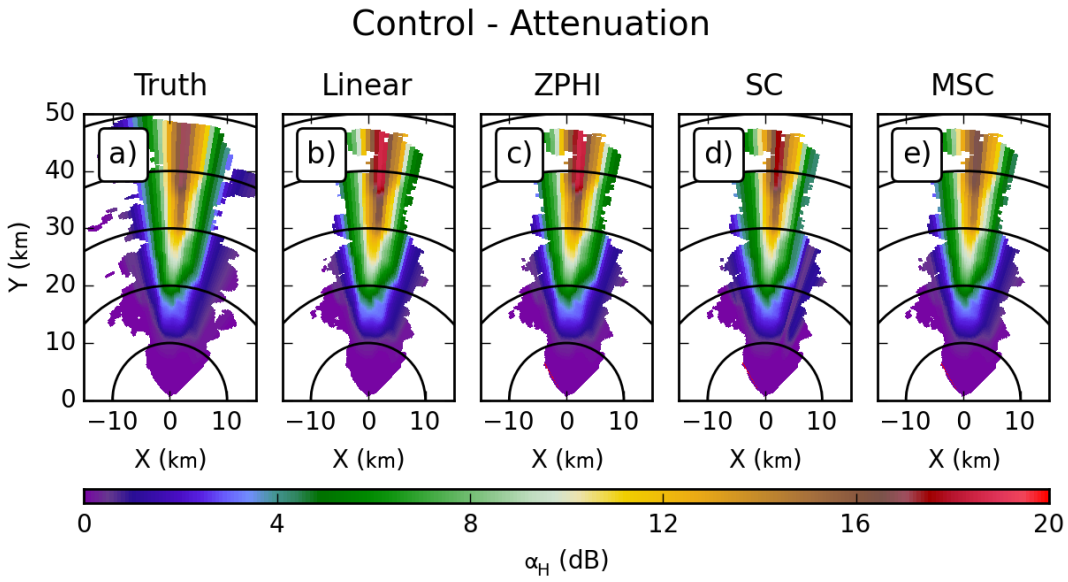

Figure 5.1: Plan Position Indicators (PPIs) of attenuation for horizontal attenuation at C-band for the Control experiment from various sources: (a) True field calculated from model (b) Linear algorithm (c) ZPHI algorithm (d) Self-Consistent algorithm (e) Modified Self-Consistent algorithm. Range rings are plotted every 10 km from the radar.

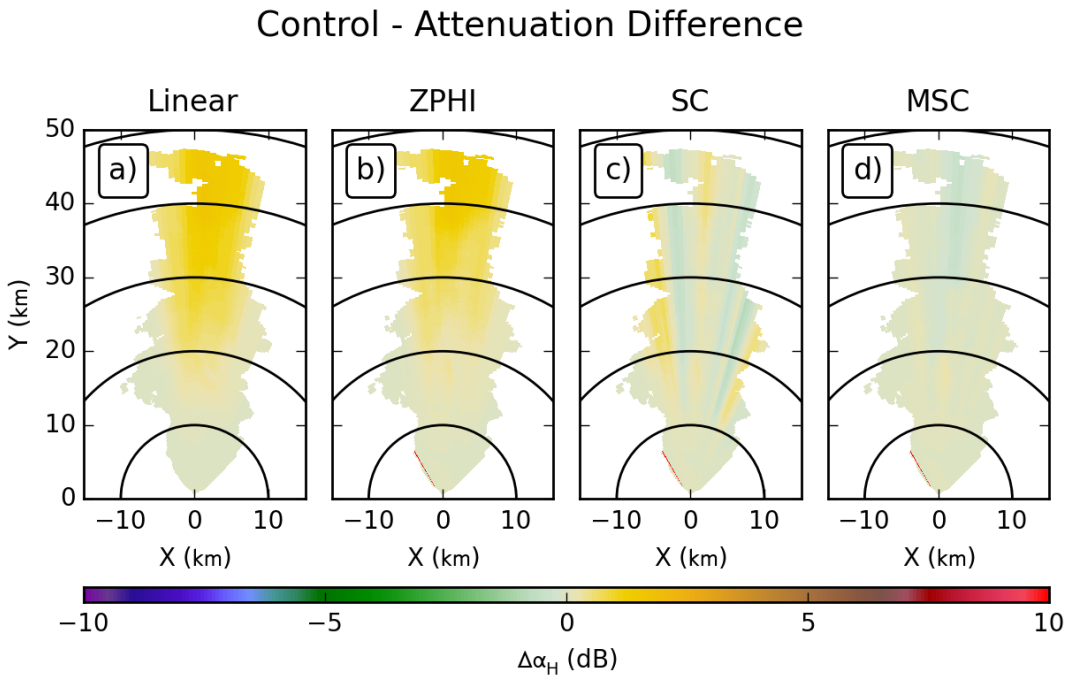

Figure 5.2: Plan Position Indicators (PPIs) for the Control experiment of the difference between the true horizontal attenuation values (from the model) at C-band and those calculated by algorithms: (a) Linear algorithm (b) ZPHI algorithm (c) Self-Consistent algorithm (d) Modified Self-Consistent algorithm. Range rings are plotted every 10 km from the radar.

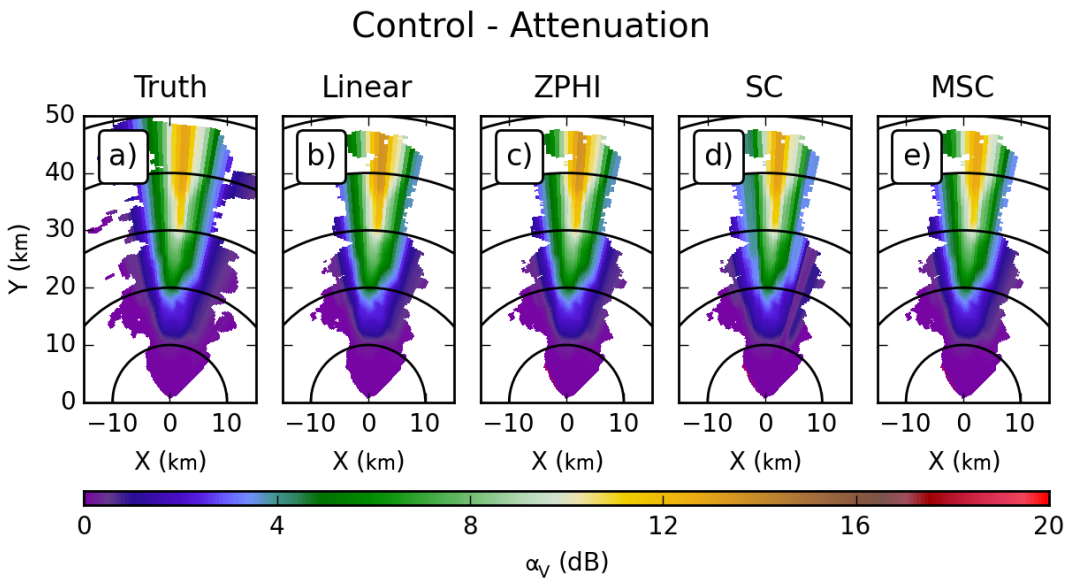

Figure 5.3: As in Figure 5.1, but for vertical polarization.

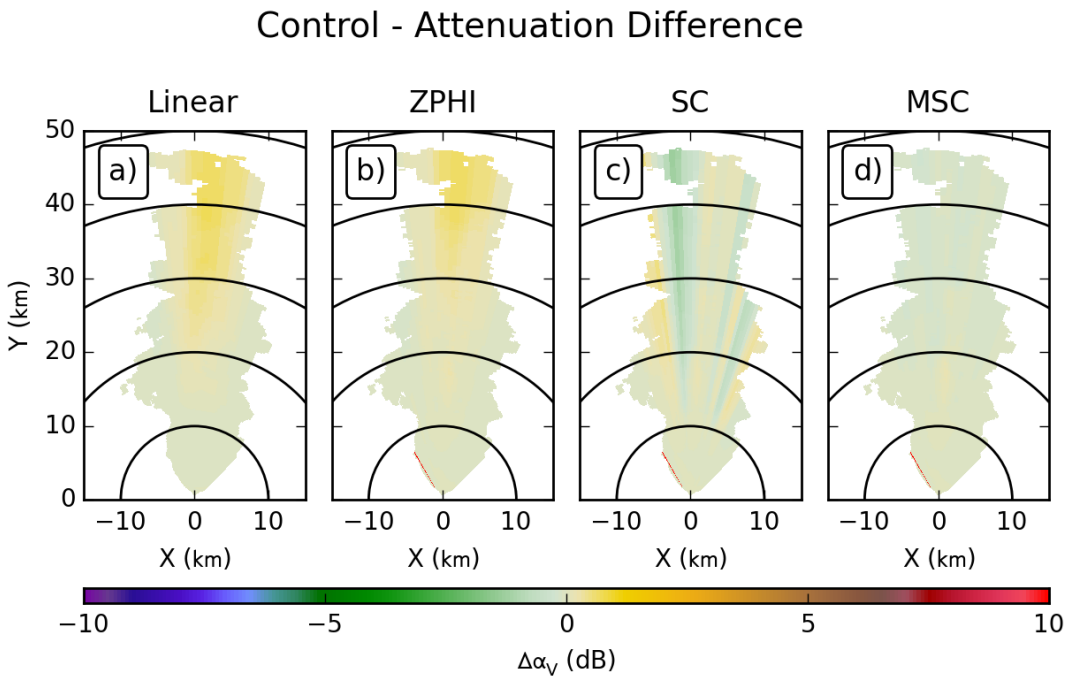

Figure 5.4: As in Figure 5.2, but for vertical polarization.

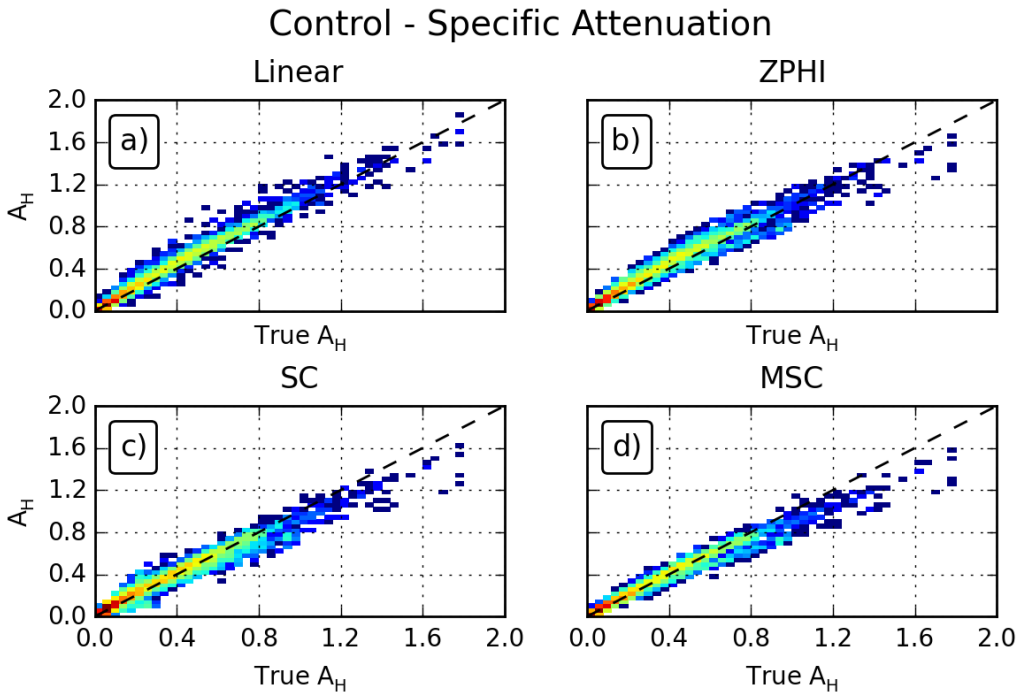

Figure 5.5: 2D histograms for the C-band Control experiment of true specific horizontal attenuation (x-axis) and calculated specific horizontal attenuation (y-axis) for: (a) Linear algorithm (b) ZPHI algorithm (c) Self-Consistent algorithm (d) Modified Self-Consistent algorithm.

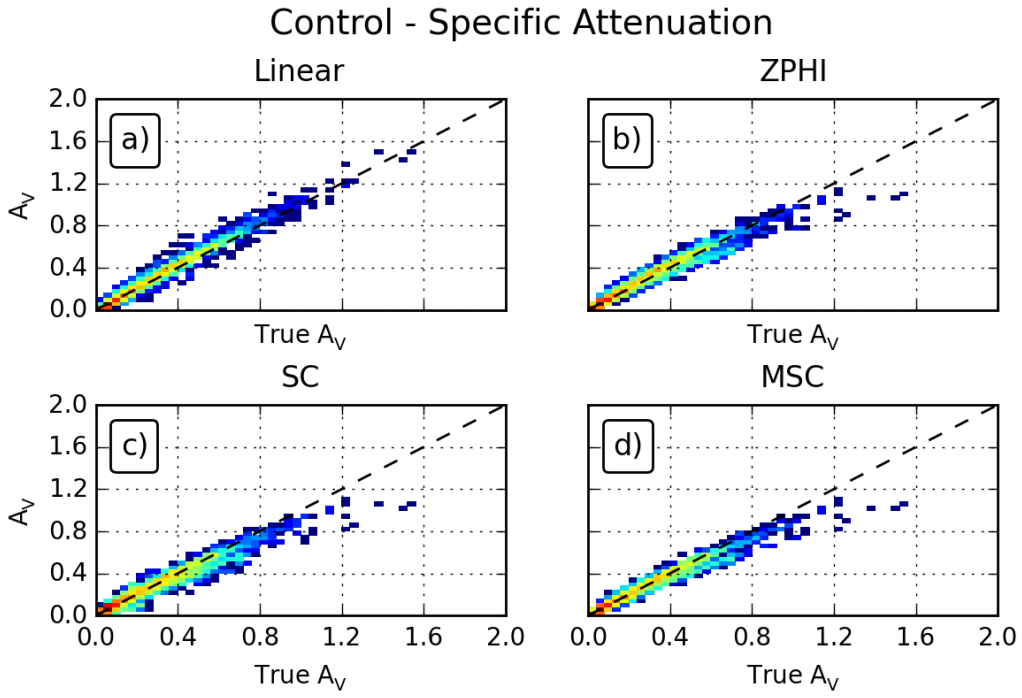

Figure 5.6: As in Figure 5.5, but for vertical polarization.

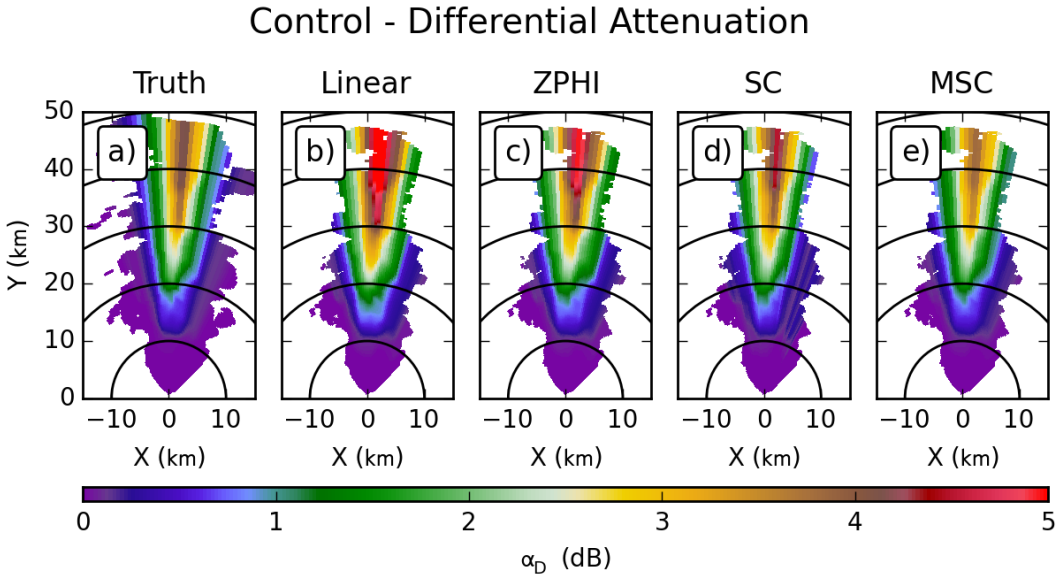

Figure 5.7: As in Figure 5.1, but for differential attenuation.

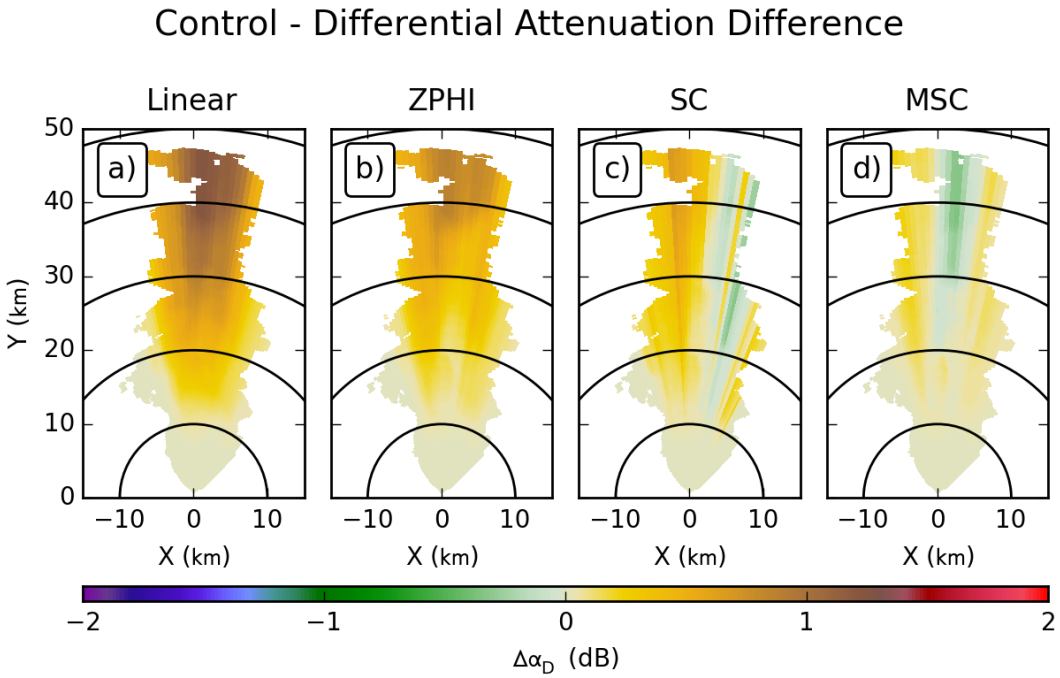

Figure 5.8: As in Figure 5.2, but for differential attenuation.

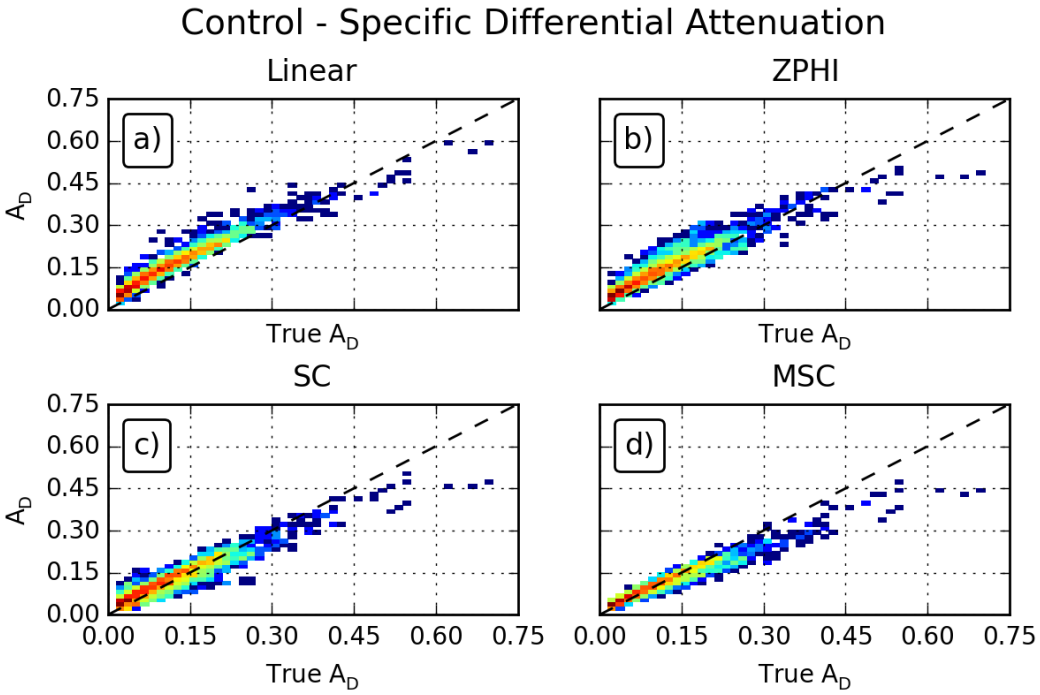

Figure 5.9: As in Figure 5.5, but for specific differential attenuation.

positive biases. The core band of points for the SC algorithm lies along the one-to-one line, though having significant spread. The MSC algorithm, conversely, has tilted away from the one-to-one line at higher attenuation values, causing the negative bias in the core of the reflectivity structure. This agrees with the computed bias values in Table 5.3, which show that SC and MSC have the lowest values, as well as the lowest values for MSE. For the first time, the MSC has the best values of r^2; the spatial smoothing removes artifacts that had caused MSC's variance to increase, and hence decrease the r^2 value.

Algorithm	Bias (dB/km)	MSE (dB^2/km^2)	r^2
Horizontal			
Linear	0.0314	0.0030	0.9789
ZPHI	0.0286	0.0036	0.9629
SC	0.0059	0.0035	0.9573
MSC	-0.0025	0.0026	0.9705
Vertical			
Linear	0.0101	0.0011	0.9820
ZPHI	0.0079	0.0014	0.9665
SC	-0.0031	0.0021	0.9493
MSC	-0.0055	0.0014	0.9686
Differential			
Linear	0.0407	0.0020	0.9380
ZPHI	0.0285	0.0014	0.8904
SC	0.0079	0.0007	0.8911
MSC	-0.0014	0.0005	0.9453

Table 5.3: Bias, mean squared-error, and r^2 for the specific attenuation results for the Control experiment at C-band.

5.1.2 X band

At X-band, due to the extinguished signal in the core of the reflectivity, it is more difficult to evaluate the performance of the algorithms using the PPIs of horizontal attenuation in Figure 5.10. The differences from the intrinsic values shown in Figure 5.11 show that all of the algorithms have similar performance, with positive biases (ignoring the regions of low-signal for the ZPHI algorithms) around $2\,\mathrm{dB}$. ZPHI appears to be slightly better than the rest, while MSC slightly worse. The histograms of specific attenuation, in Figure 5.14, show some very subtle results behind these biases. For the Linear and ZPHI algorithms, the main bands of points lie along the one-to-one line. However, the spread of points is uneven, with more points above the one-to-one line. For the ZPHI and SC algorithms, the spread is more even, but at lower attenuation values, the core of very many points lies above the line, causing the small bias. While these may seem like small effects, it is important to keep in mind that the observed biases are a few dB on top of calculated values on order $60\,\mathrm{dB}$. A small bias in specific attenuation values in the range of $1\,\mathrm{dB/km}$ is easily sufficient to yield the observed biases.

The results for vertical polarization are similar, with PPIs of the base attenuation values shown in Figure 5.12. The differences from the intrinsic values, shown in Figure 5.13, show that all algorithms have an overall positive bias. Here, ZPHI performs best, with the errors having a magnitude around $2\,\mathrm{dB}$. The other algorithms have larger errors that approach $4\,\mathrm{dB}$. Looking at the histograms of vertical specific attenuation in Figure 5.15, the cause of the differences is subtle. The ZPHI algorithm exhibits slightly less spread in the points, lessening the overall positive bias.

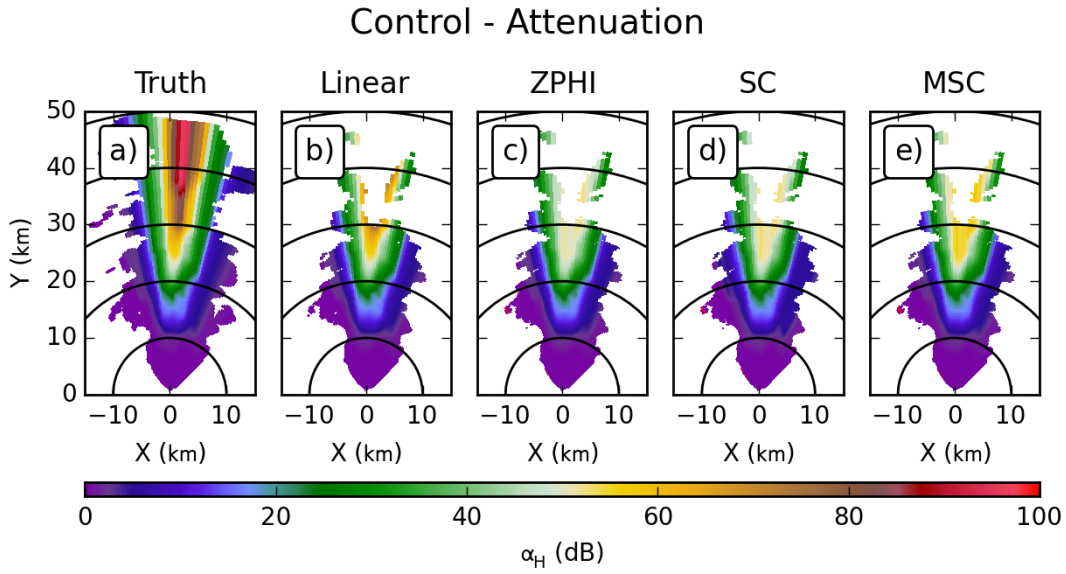

Figure 5.10: As in Figure 5.1, but for X-band.

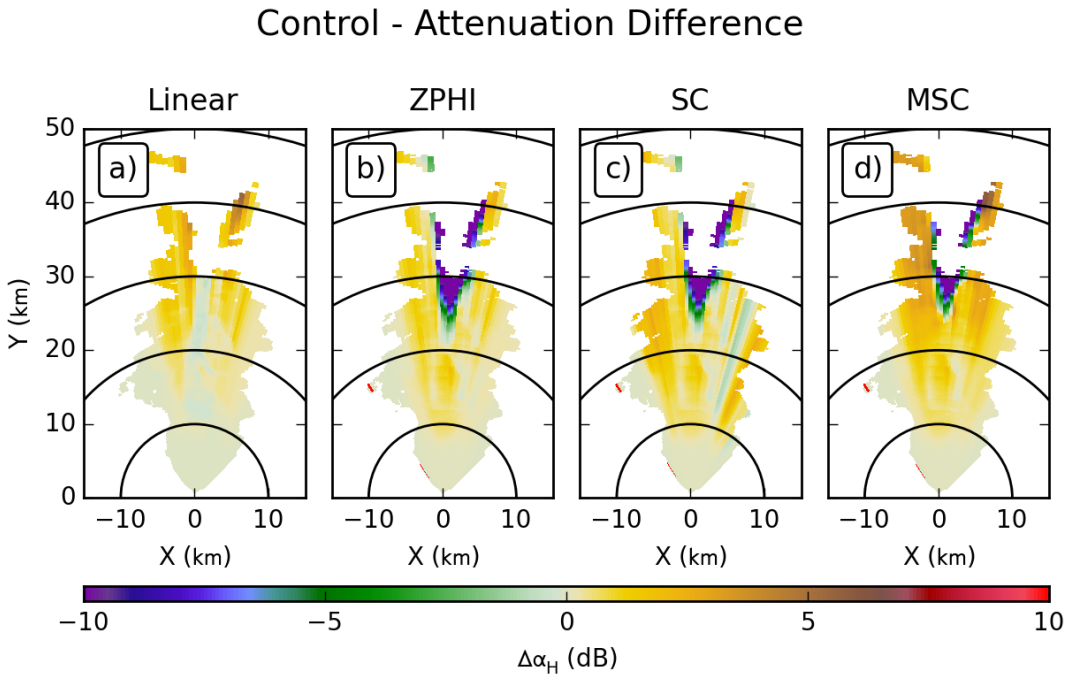

Figure 5.11: As in Figure 5.2, but for X-band.

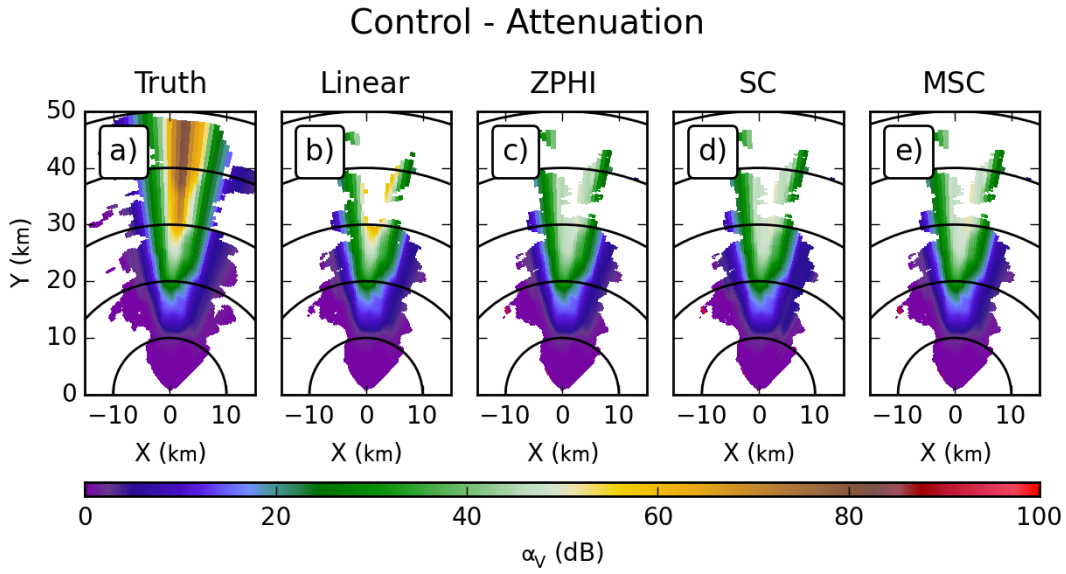

Figure 5.12: As in Figure 5.10, but for vertical polarization.

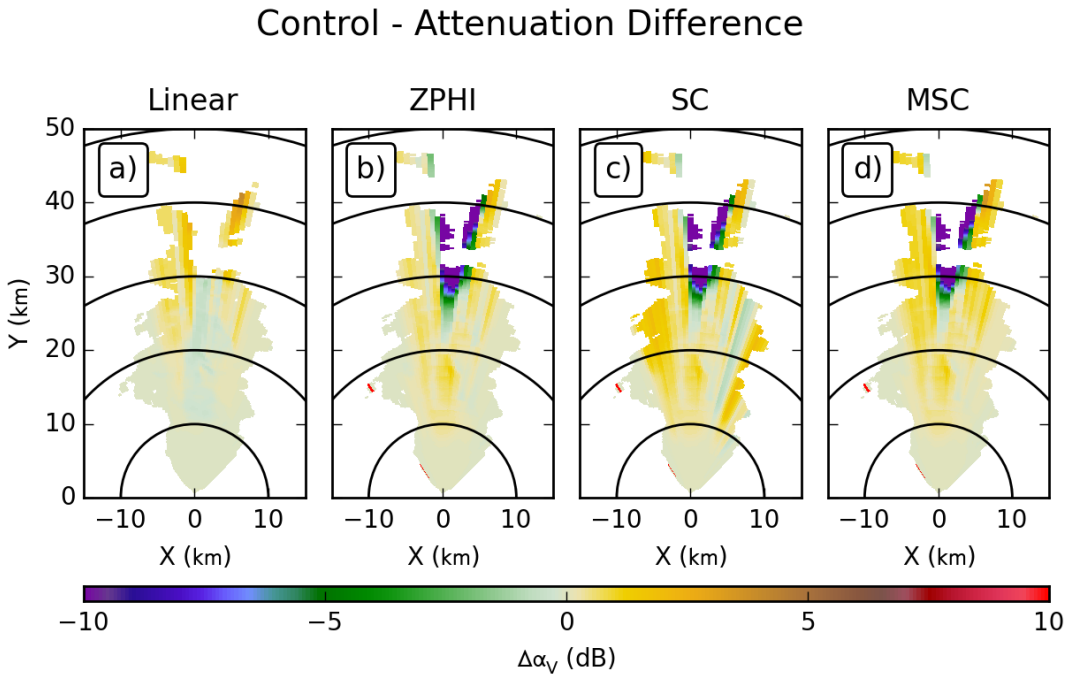

Figure 5.13: As in Figure 5.11, but for vertical polarization.

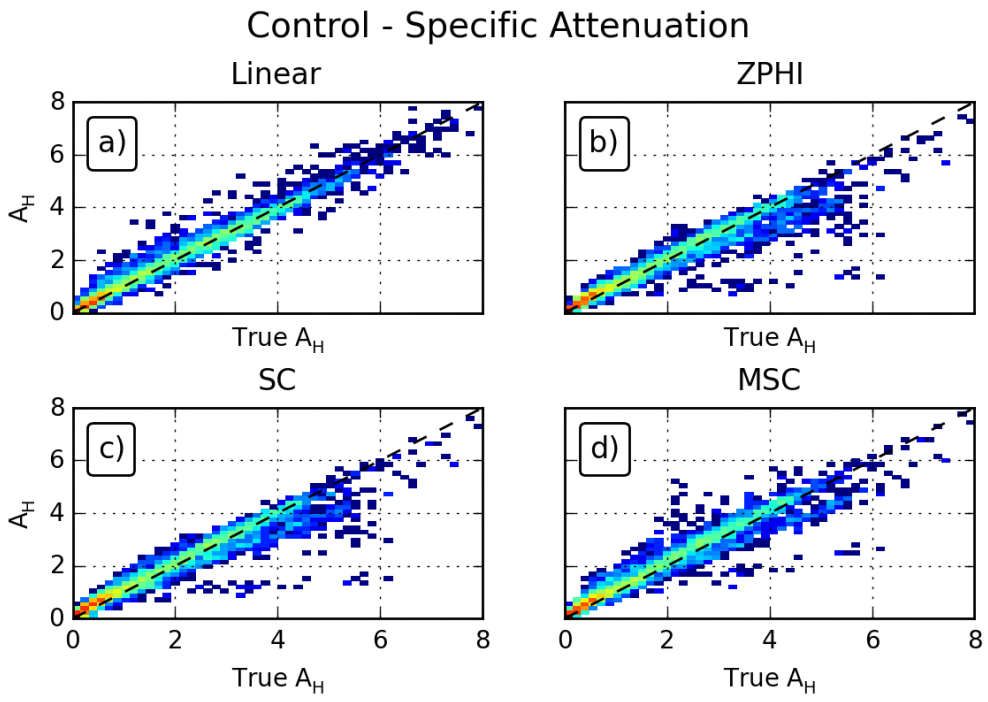

Figure 5.14: As in Figure 5.5, but for X-band.

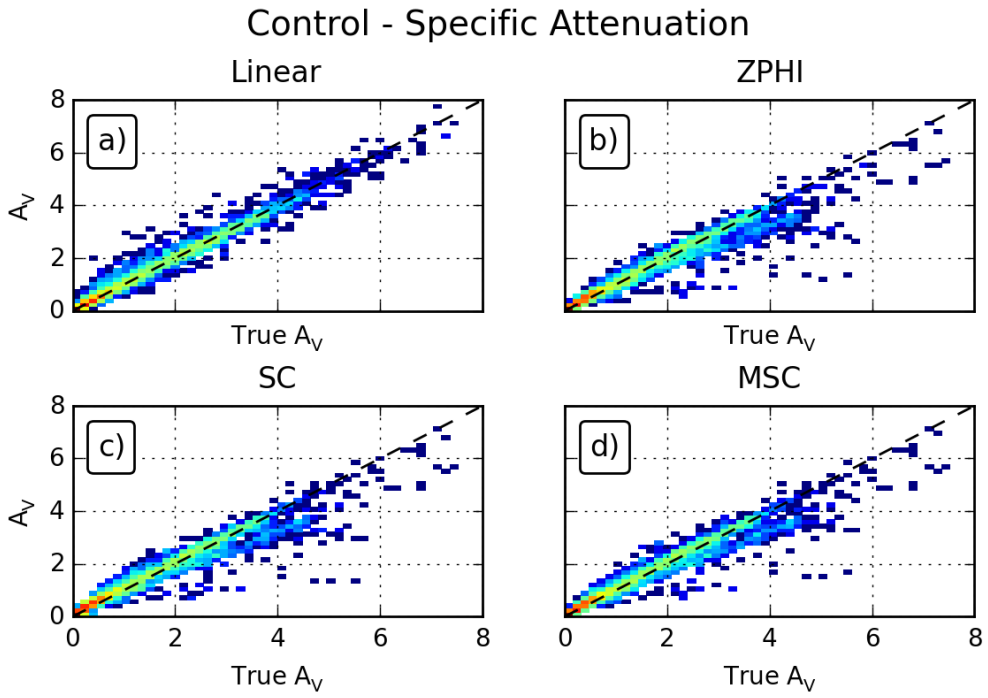

Figure 5.15: As in Figure 5.14, but for vertical polarization.

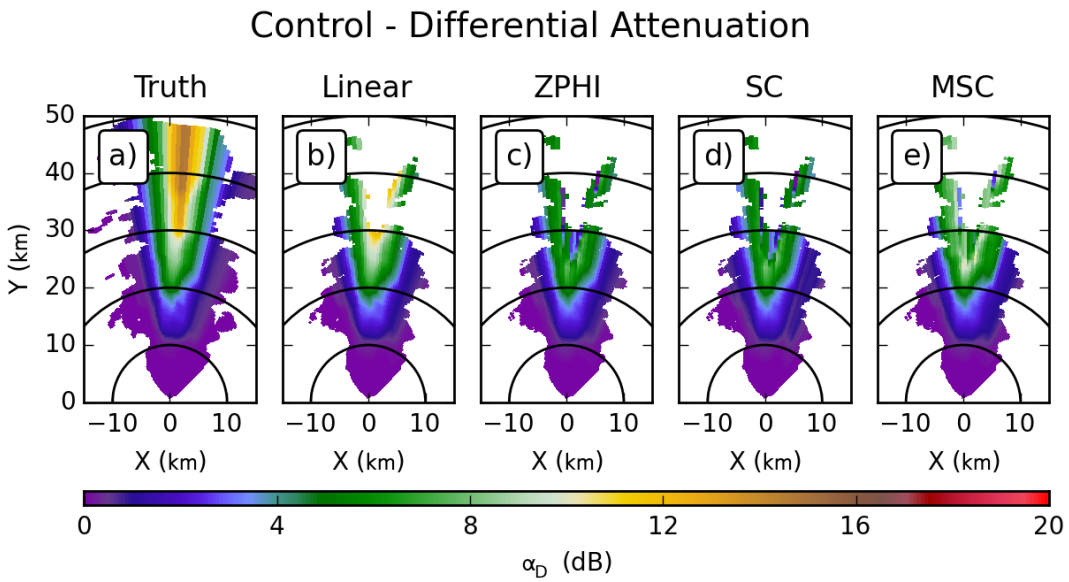

Figure 5.16: As in Figure 5.10, but for differential attenuation.

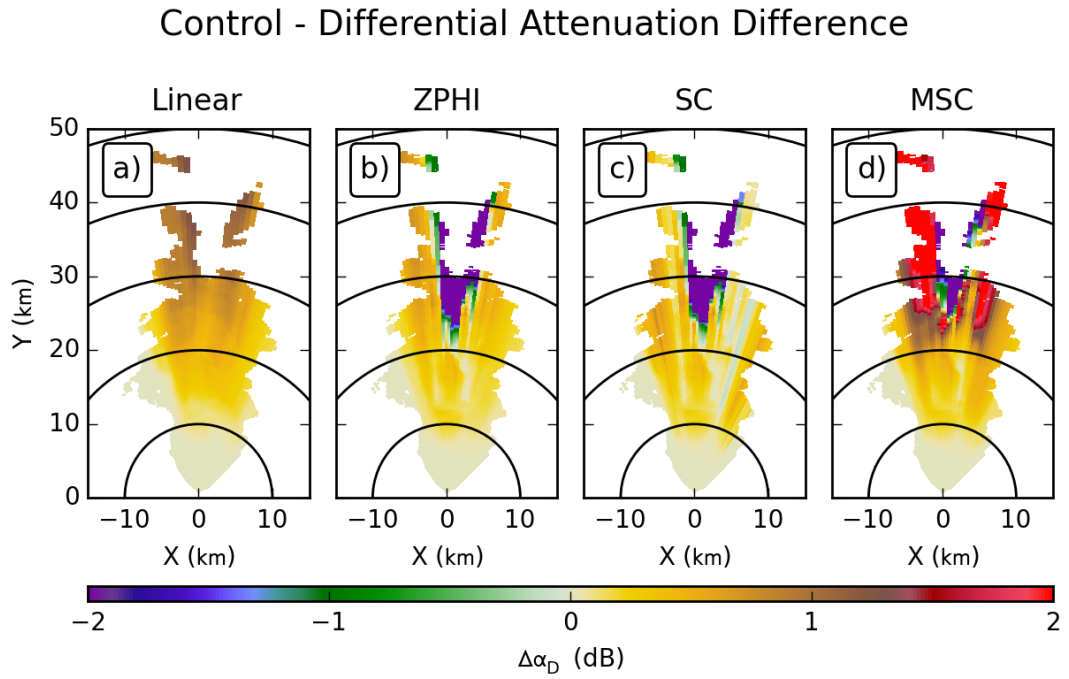

Figure 5.17: As in Figure 5.11, but for differential attenuation.

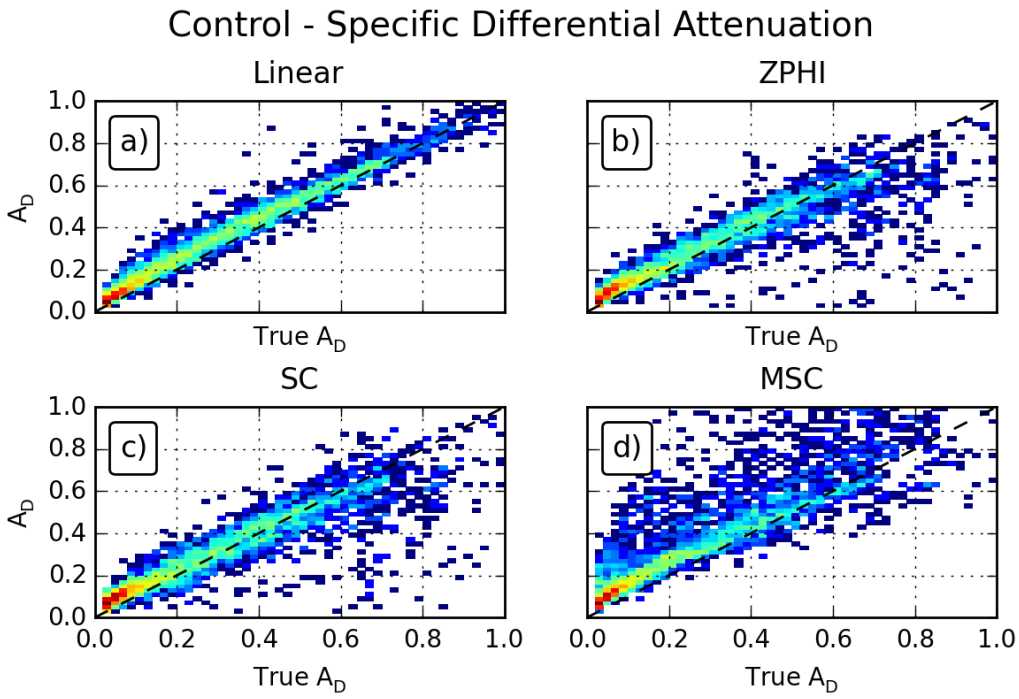

Figure 5.18: As in Figure 5.14, but for specific differential attenuation.

For differential attenuation, it is challenging to evaluate algorithm performance from the base PPIs in Figure 5.16. The differences from the intrinsic values, in Figure 5.17, make the picture clear that ZPHI and SC perform the best of all here. Both algorithms have biases less than 1 dB which, while significant, are much better than the 1.25 dB positive bias for the Linear algorithm. MSC, on the other hand, demonstrates a breakdown in performance, with errors over 2 dB. Such performance is unexpected given the performance of SC and ZPHI and is likely due to a poor choice in "smoothed" coefficient. The histograms of specific differential attenuation in Figure 5.18 show clear shifts for all of the algorithms, which yield the observed biases. Here, the MSC algorithm also shows a large spread of points above the line, which creates the exceptionally bad algorithm performance. This is reflected in the computed

bias values for MSC (Table 5.4), which are the highest for the horizontal polarization and differential cases.

Unlike at C-band, the X-band Control experiment here at a azimuthal spacing of 1.0° displays some interesting differences from the Control experiment of the modeling study at 0.25° azimuthal spacing. The histograms display similar changes as at C-band, with the bands of points clustering more tightly and the multiple bands for the ZPHI-based algorithms collapsing down to a single band. However, the attenuation results for the individual polarizations all show larger errors here than for the higher resolution data. It is interesting to note that the increase in errors is not reflected in the differential attenuation results, with the exception of the anomalous performance of the MSC algorithm. That the change in errors with the change in spacing from 0.25° to 1.0° is only observed at X-band, and not C-band, is likely a consequence of the much higher attenuation values observed at X-band.

5.2 Sidelobe

The purpose of the Sidelobe experiment is to test the effects of antenna sidelobes on the accuracy of attenuation correction techniques. This is achieved by modifying the Control experiment to include the first antenna sidelobes, which have peaks around $25\,\mathrm{dB}$ below the mainlobe level. This experiment tests the impact of the smearing effect of sidelobes on the accuracy of the correction techniques without modifying the inherent azimuthal resolution of the radar antenna.

Algorithm	Bias (dB/km)	MSE (dB^2/km^2)	r^2
Horizontal			
Linear	0.0530	0.0501	0.9789
ZPHI	-0.0034	0.1266	0.9453
SC	0.0365	0.1244	0.9468
MSC	0.0991	0.1105	0.9526
Vertical			
Linear	0.0254	0.0335	0.9793
ZPHI	-0.0131	0.0789	0.9518
SC	0.0260	0.0774	0.9529
MSC	0.0152	0.0670	0.9580
Differential			
Linear	0.0394	0.0031	0.9752
ZPHI	0.0098	0.0087	0.8600
SC	0.0098	0.0085	0.8637
MSC	0.1006	0.0364	0.7057

Table 5.4: Bias, mean squared-error, and r^2 for the specific attenuation results for the Control experiment at X-band.

5.2.1 C band

At C-band, the PPIs of horizontal attenuation in Figure 5.19 show minimal differences from those in the Control experiment. The only observable differences are a couple of anomalous rays in the ZPHI algorithms and a slight increase in the estimated attenuation for the MSC algorithm. The PPIs with the intrinsic values subtracted, shown in Figure 5.20, demonstrate that the change for MSC is very minor, on the order of 0.1 dB. At vertical polarization, the PPIs of the attenuation values (in Figure 5.21) show no visual differences from Control. Even the differences from the intrinsic values in Figure 5.22 show no discernable difference from the Control experiment, outside of the extra spurious ray in the ZPHI-based algorithms.

Consequently, the histograms of specific attenuation for both polarizations, in Figures 5.23 and 5.24, show almost no change between the Control and Sidelobe experiment. The exception is that the MSC algorithm, for horizontal specific attenuation, shows a slight upward shift for the Sidelobe experiment, bringing its core band of values into better alignment with the one-to-one line. This corresponds to a slight change in the bias computed for horizontal polarization (Table 5.5), from -0.0025 dB/km to 0.0015 dB/km. This change is a consequence of a better-matching coefficient being selected as the median, possibly a consequence of the bad rays. This highlights that despite goals to the contrary, the selection of the coefficient in the MSC algorithm can be sensitive to the data being processed. As opposed to in the modeling study, this sensitivity is likely more pronounced here because of the decreased number of radials of data.

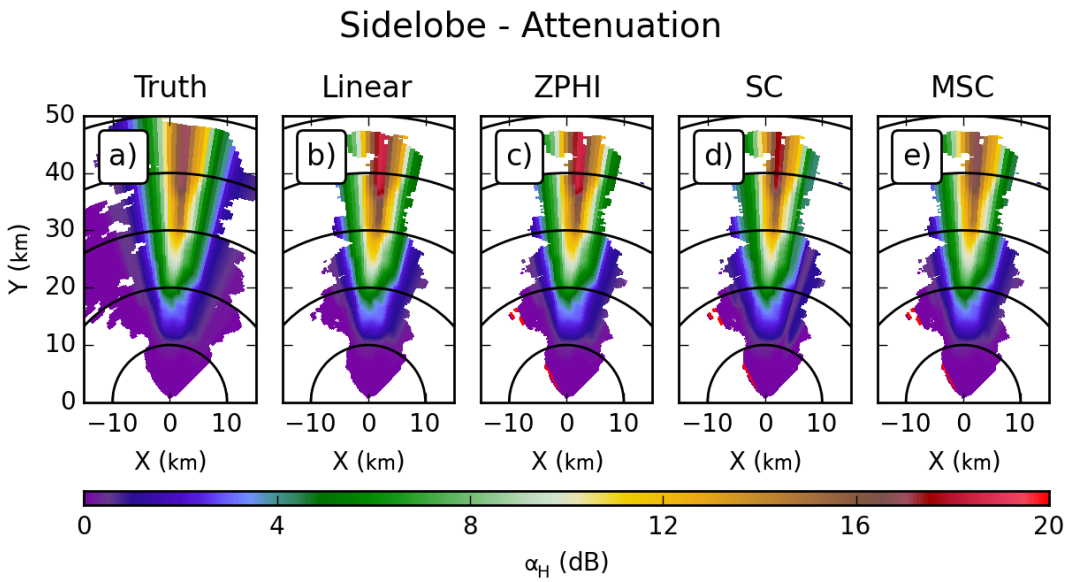

Figure 5.19: As in Figure 5.1, but for the Sidelobe experiment.

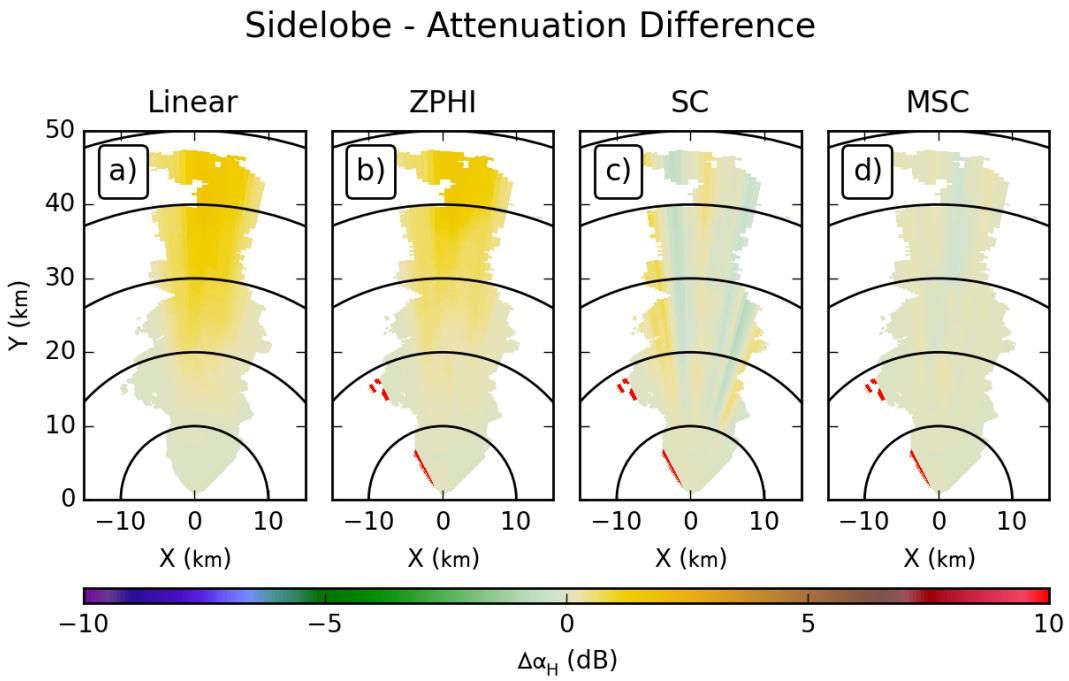

Figure 5.20: As in Figure 5.2, but for the Sidelobe experiment.

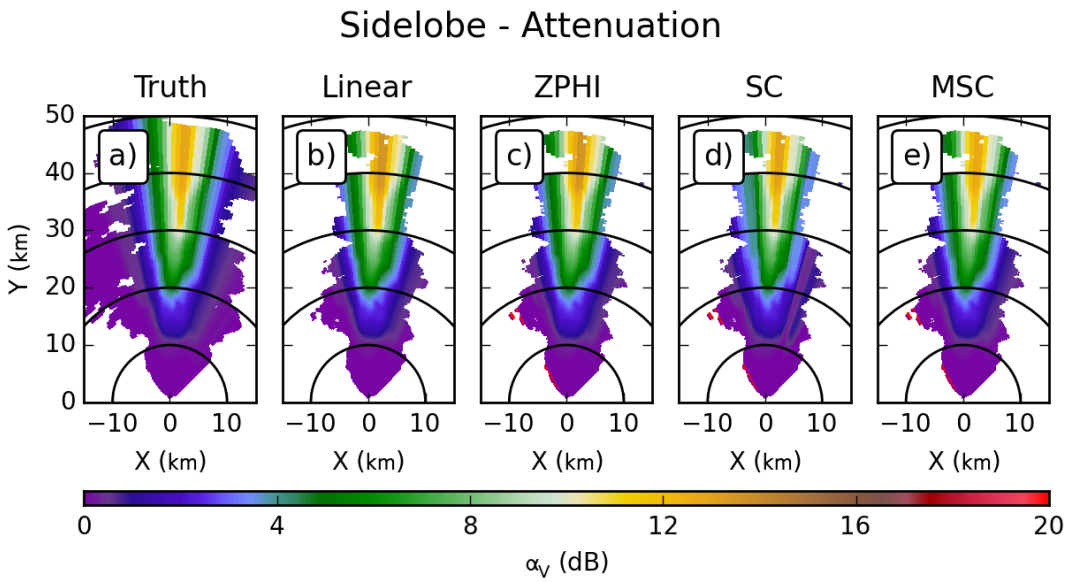

Figure 5.21: As in Figure 5.19, but for vertical polarization.

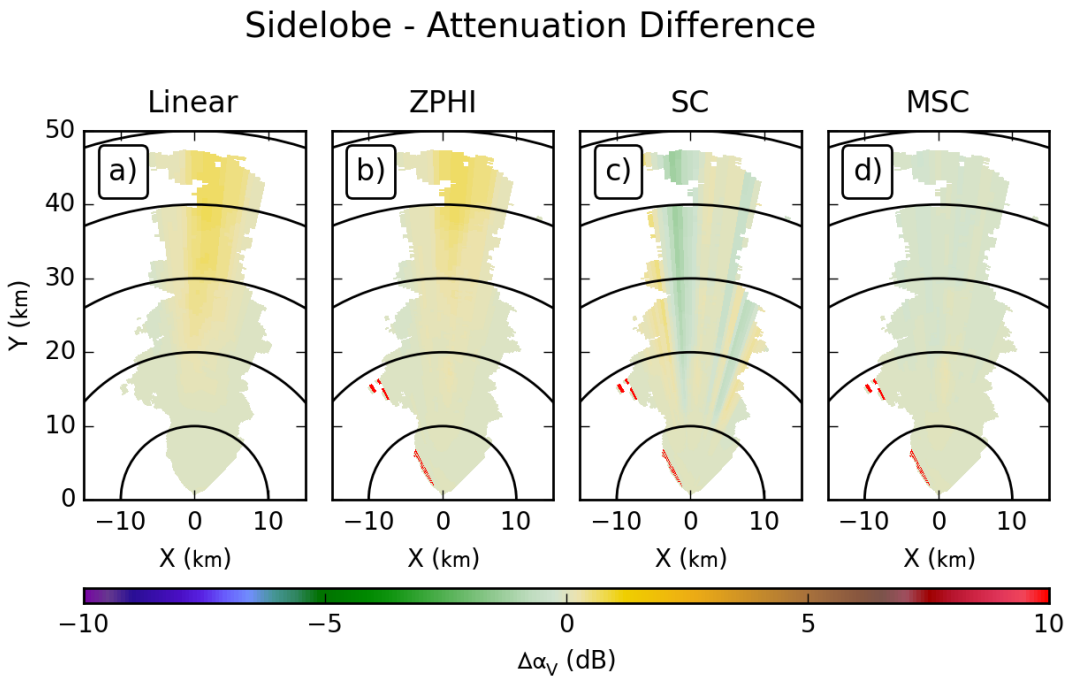

Figure 5.22: As in Figure 5.20, but for vertical polarization.

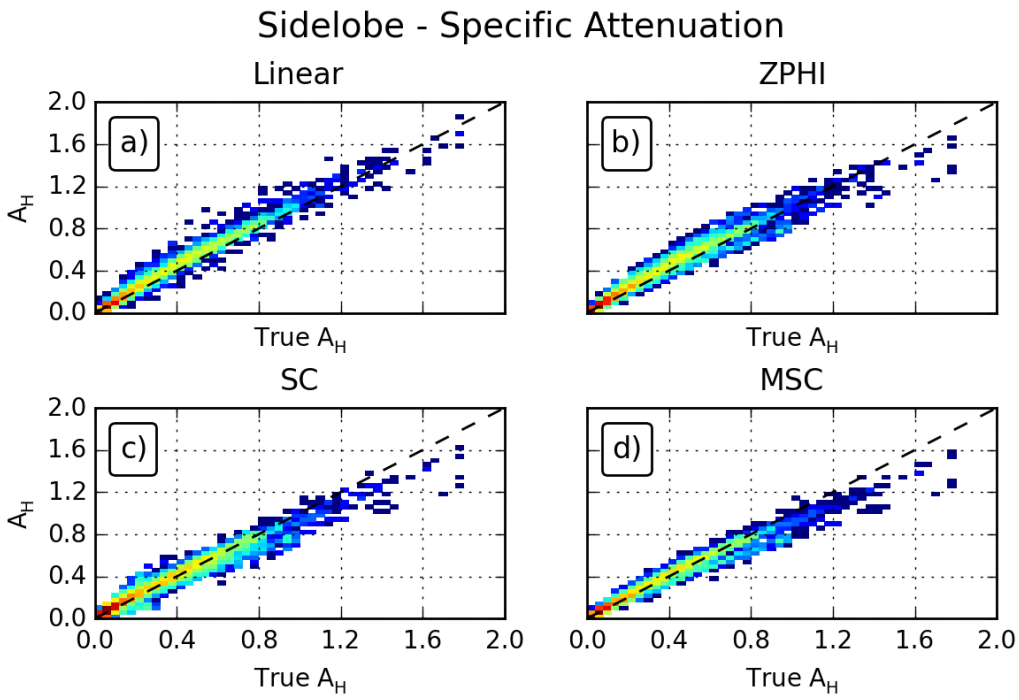

Figure 5.23: As in Figure 5.5, but for the Sidelobe experiment.

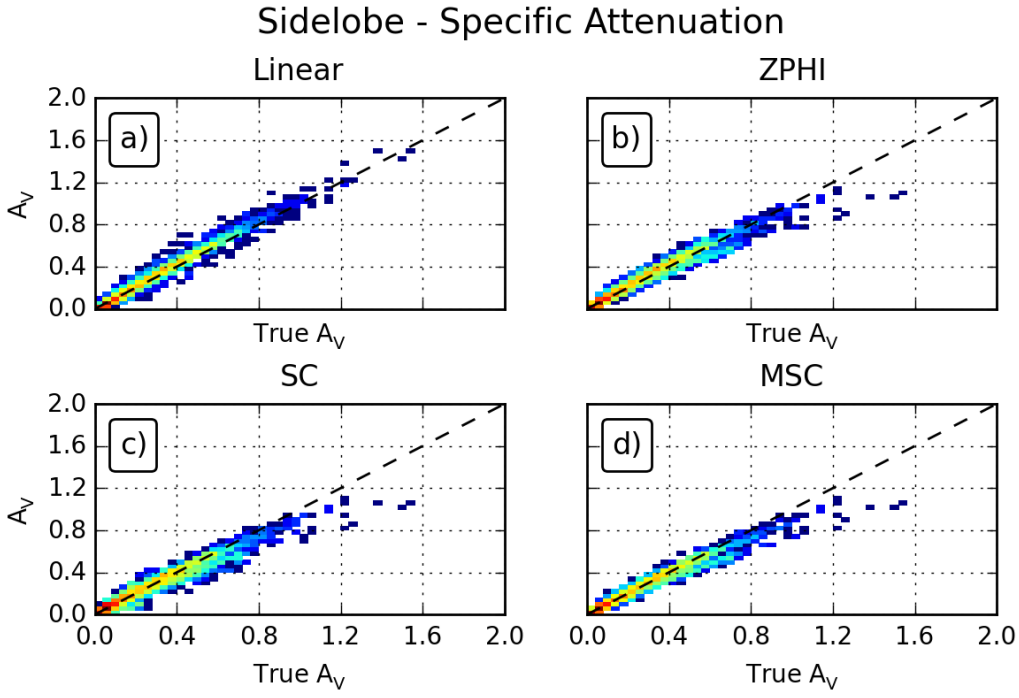

Figure 5.24: As in Figure 5.23, but for vertical polarization.

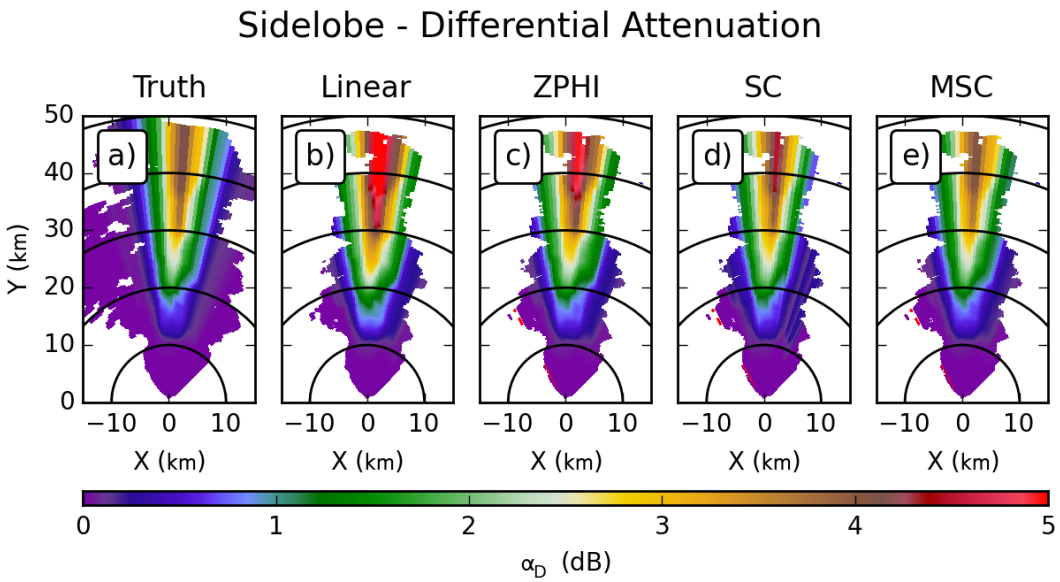

Figure 5.25: As in Figure 5.19, but for differential attenuation.

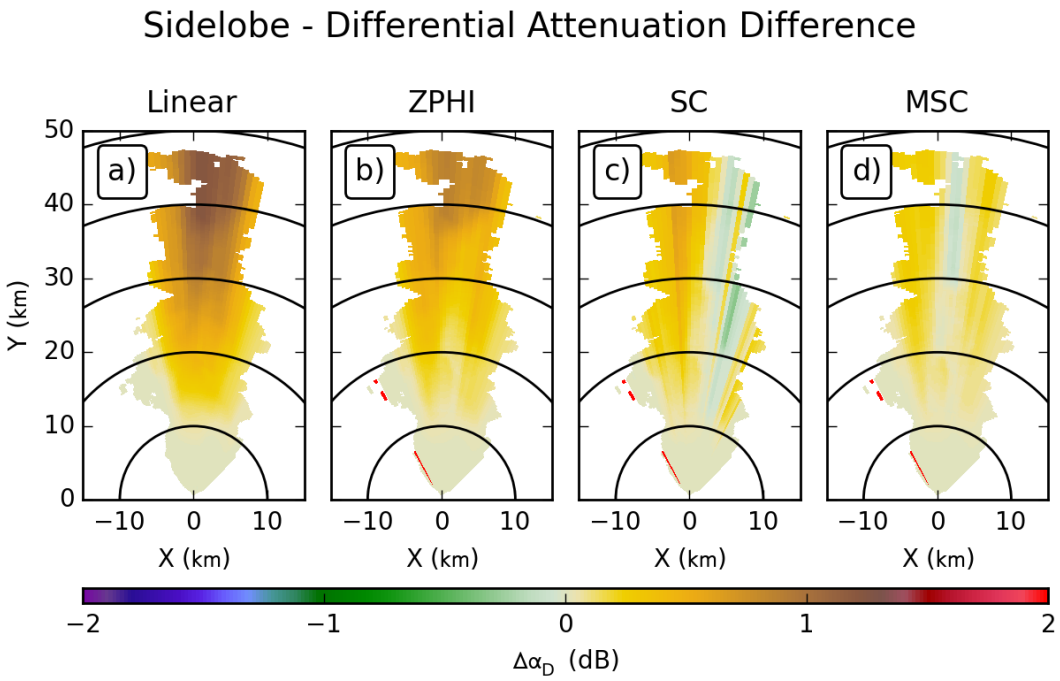

Figure 5.26: As in Figure 5.20, but for differential attenuation.

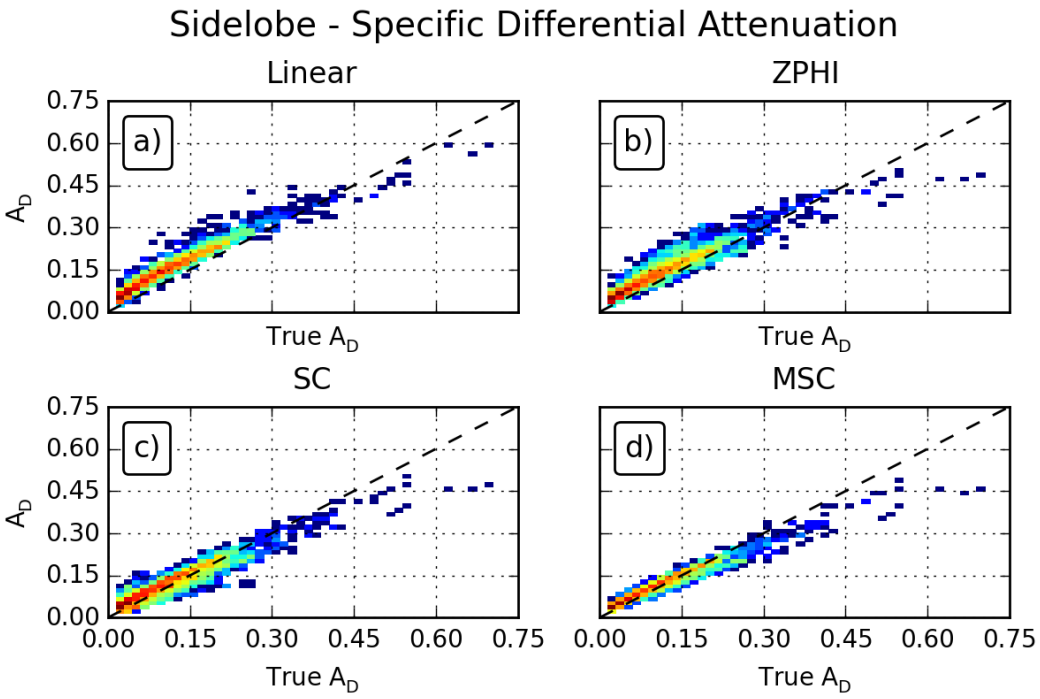

Figure 5.27: As in Figure 5.23, but for differential attenuation.

Given the lack of changes for the individual polarizations, it is unsurprising that PPIs of both the base differential attenuation fields and the differences from the intrinsic values, shown in Figures 5.25 and 5.26, respectively, exhibit no significant changes. The only exception is the MSC algorithm, which shows a decrease in its bias in estimating differential attenuation, a consequence of the change observed at horizontal polarization. This is reflected in the histograms of specific differential attenuation in Figure 5.27, which only change for MSC, showing the same shift to better agreement with the one-to-one line.

Algorithm	Bias (dB/km)	MSE (dB^2/km^2)	r^2
Horizontal			
Linear	0.0314	0.0030	0.9789
ZPHI	0.0286	0.0036	0.9630
SC	0.0059	0.0035	0.9573
MSC	0.0015	0.0025	0.9706
Vertical			
Linear	0.0101	0.0011	0.9820
ZPHI	0.0079	0.0014	0.9665
SC	-0.0032	0.0021	0.9493
MSC	-0.0055	0.0014	0.9687
Differential			
Linear	0.0407	0.0020	0.9380
ZPHI	0.0285	0.0014	0.8903
SC	0.0080	0.0007	0.8910
MSC	0.0053	0.0005	0.9530

Table 5.5: As in Table 4.3, but for the Sidelobe experiment.

5.2.2 X band

At X-band, the changes from the Control experiment are still minimal, though greater than at C-band. The PPIs of the base results for both horizontal and vertical polarizations, shown in Figures 5.28 and 5.30, respectively, exhibit no qualitative changes. For the Linear algorithm, the results look completely identical. The differences from the intrinsic values of horizontal attenuation, in Figure 5.29, show some small fluctuations, likely due to small changes in the data near the low-signal region. The MSC algorithm shows some slightly larger changes, due to the aforementioned sensitivity. The PPIs of differences for vertical polarization, in Figure 5.31, show some small changes as well, but much fewer than observed at horizontal polarization. The histograms of specific attenuation for both horizontal and vertical polarizations, in Figures 5.32 and 5.33, respectively, show that the only meaningful change from the Control experiment is for the MSC algorithm; here, the values shift closer to the one-to-one line, in agreement with the observed decrease in bias in the difference PPI.

For differential attenuation, the results reflect the lack of change for the individual polarizations. The PPIs of differential attenuation in Figure 5.34 show no qualitative changes for the Linear, ZPHI, and SC algorithms. However, the MSC algorithm does show a noticeable increase in value, a consequence of its increase in calculated horizontal attenuation for the Sidelobe experiment. These changes do help to resolve the anomalously high differences from intrinsic values that were observed for the MSC algorithm in the Control experiment, yielding much improved computed values for the bias in Table 5.6. Figure 5.35 shows that these differences have decreased from

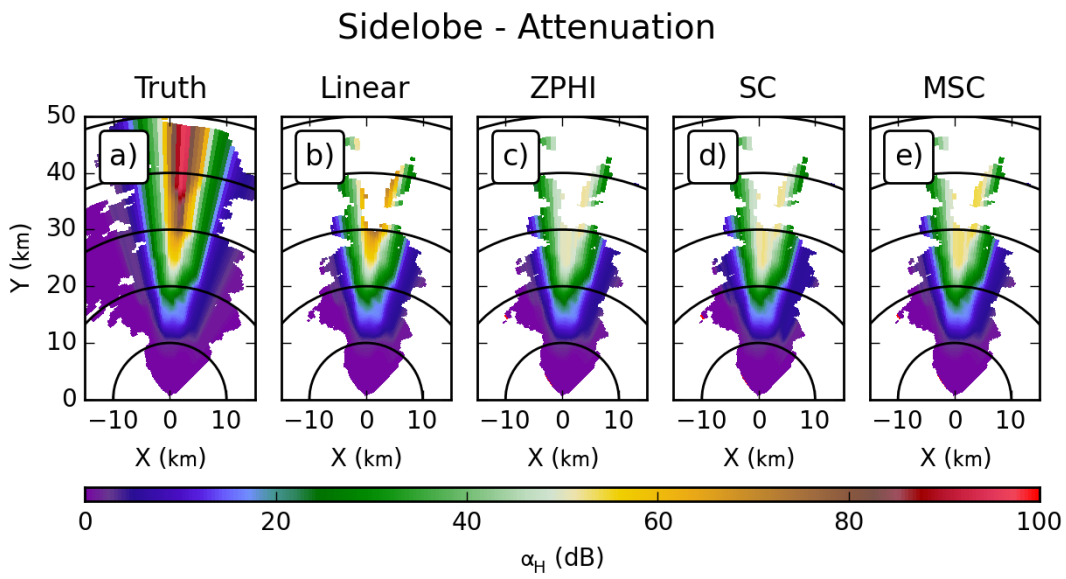

Figure 5.28: As in Figure 5.19, but for X-band.

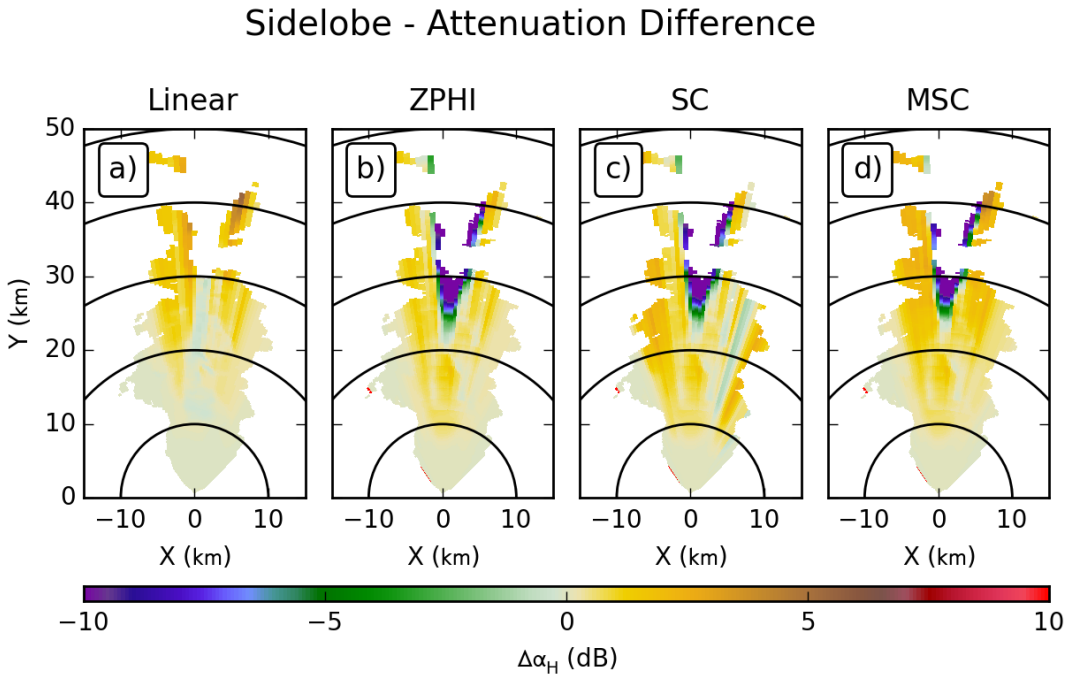

Figure 5.29: As in Figure 5.20, but for X-band.

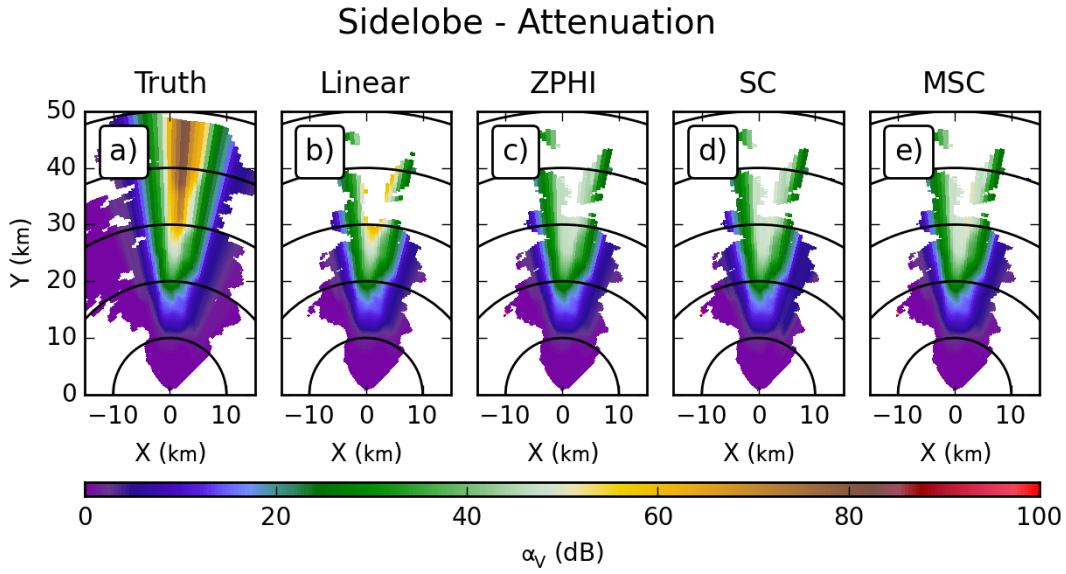

Figure 5.30: As in Figure 5.28, but for vertical polarization.

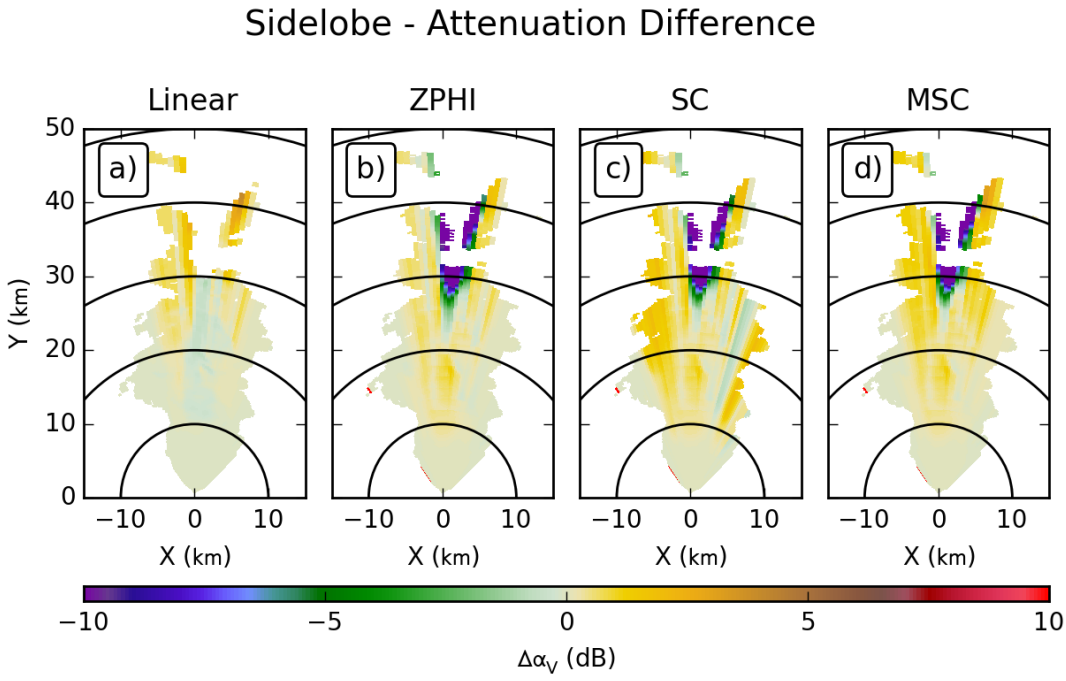

Figure 5.31: As in Figure 5.29, but for vertical polarization.

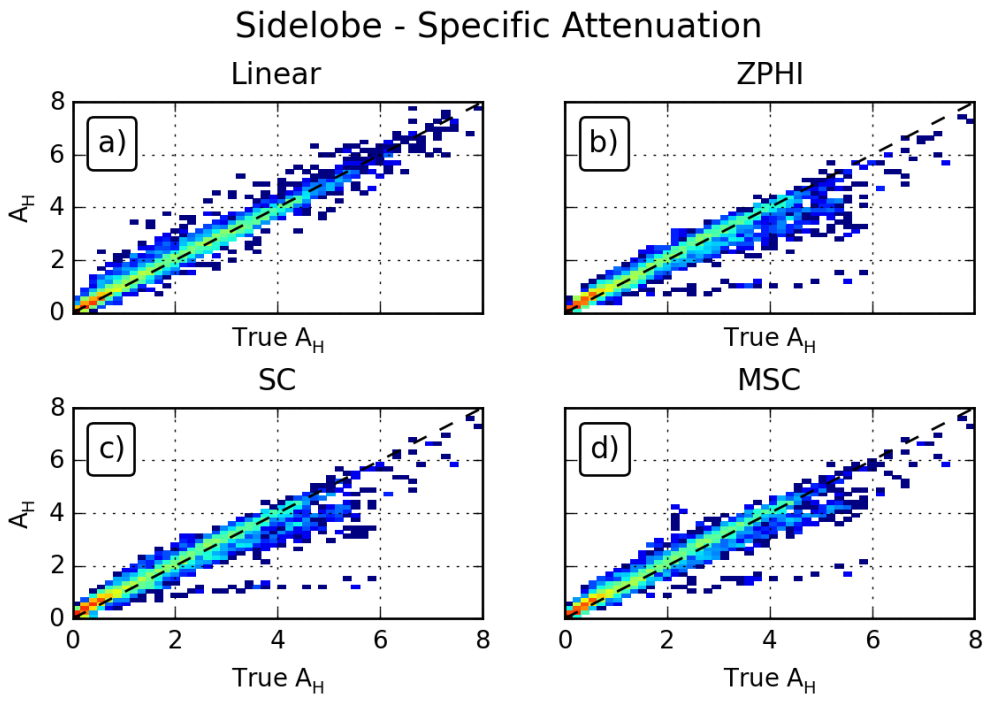

Figure 5.32: As in Figure 5.23, but for X-band.

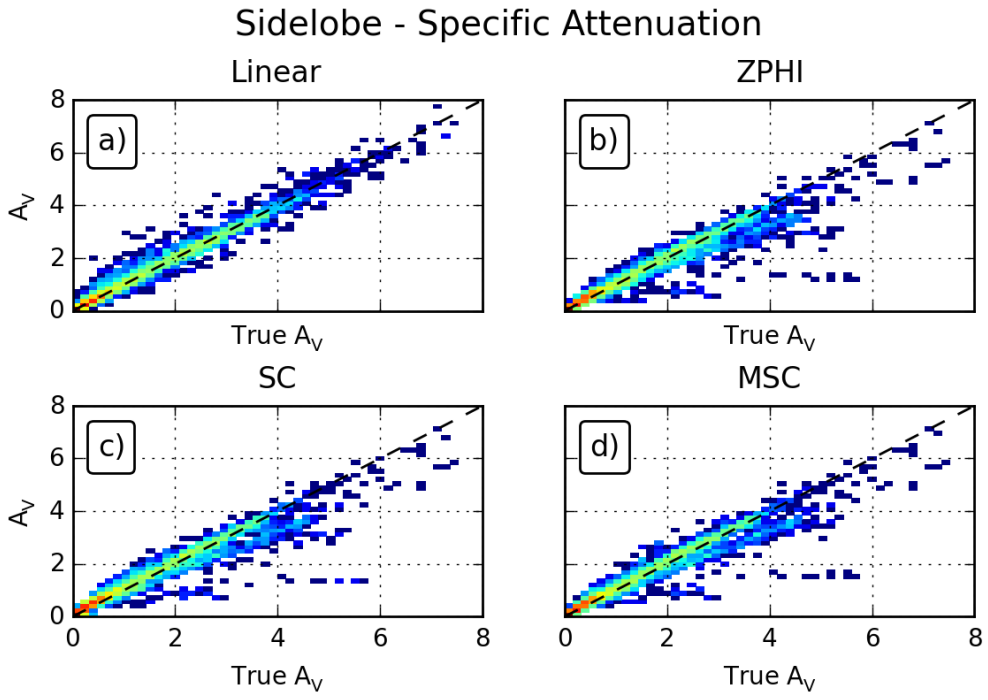

Figure 5.33: As in Figure 5.32, but for vertical polarization.

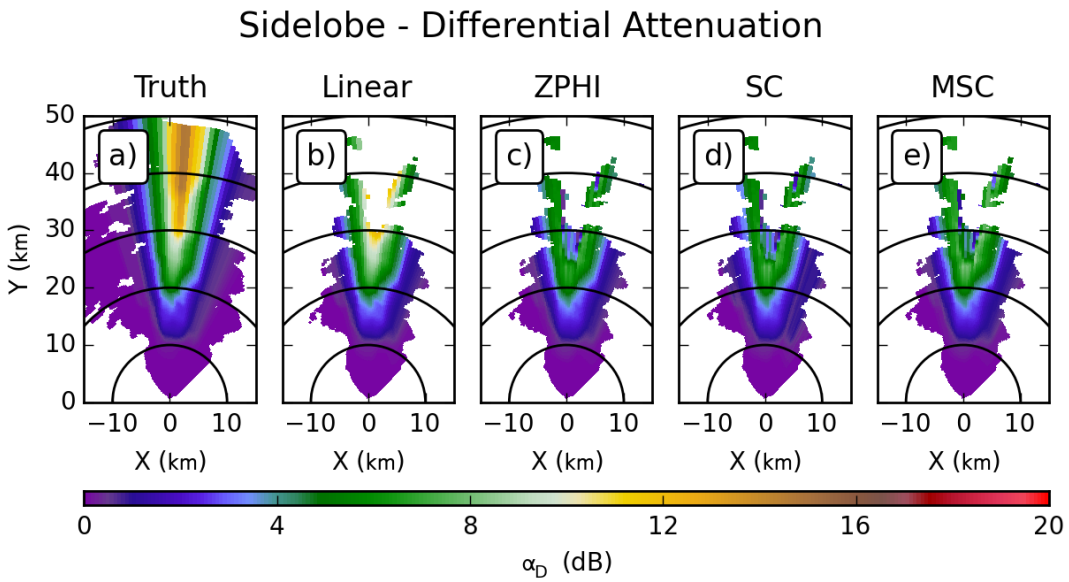

Figure 5.34: As in Figure 5.28, but for differential attenuation.

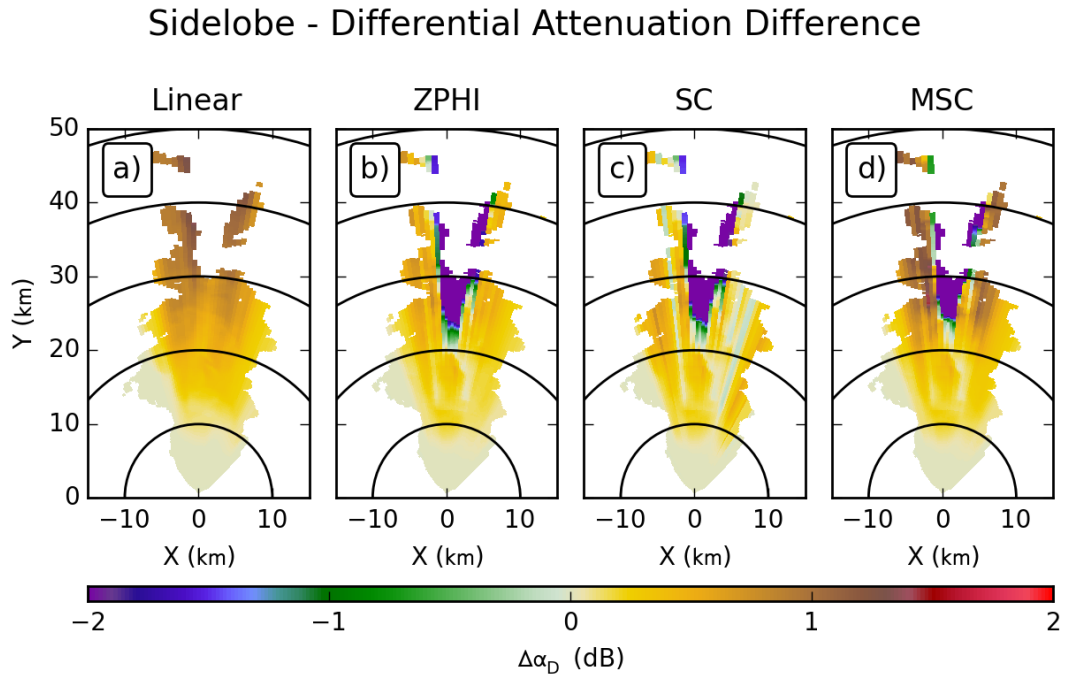

Figure 5.35: As in Figure 5.29, but for differential attenuation.

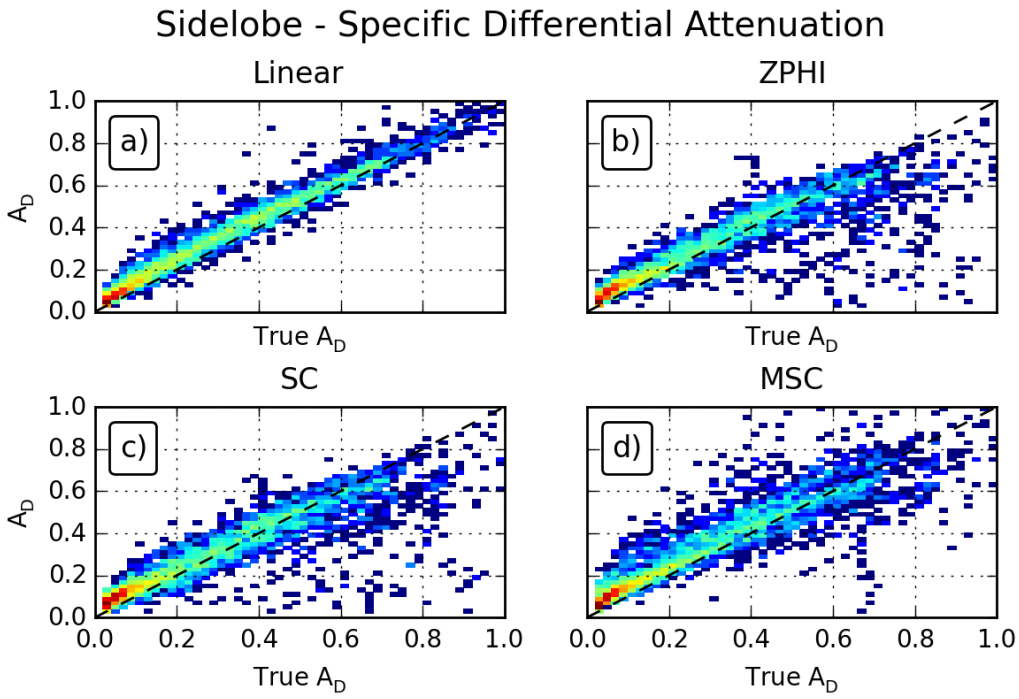

Figure 5.36: As in Figure 5.32, but for specific differential attenuation.

over 2 dB to around 1.25 dB. The histograms of specific differential attenuation in Figure 5.36 show that the values for MSC are now much more tightly clustered around the one-to-one line, in agreement with the observed improvement in performance.

5.3 Beamwidth

The Beamwidth experiment examines the impact of the antenna's 3 dB beamwidth, and hence azimuthal resolution, on the accuracy of attenuation corrections. Here, the azimuthal spacing is kept at 1.0°, so the data sampling interval is no longer matched to the resolution. This experiment, combined with the Radial Width experiment, helps to separate the two effects at play when determining azimuthal smearing in data.

Algorithm	Bias (dB/km)	MSE (dB^2/km^2)	r^2
Horizontal			
Linear	0.0531	0.0501	0.9789
ZPHI	-0.0029	0.1206	0.9482
SC	0.0372	0.1187	0.9495
MSC	0.0545	0.0986	0.9562
Vertical			
Linear	0.0254	0.0336	0.9793
ZPHI	-0.0162	0.0898	0.9444
SC	0.0230	0.0884	0.9452
MSC	0.0167	0.0760	0.9516
Differential			
Linear	0.0394	0.0031	0.9752
ZPHI	0.0067	0.0103	0.8333
SC	0.0060	0.0100	0.8412
MSC	0.0388	0.0102	0.8509

Table 5.6: As in Table 4.4, but for the Sidelobe experiment.

5.3.1 C band

In the Beamwidth experiment, the results for horizontal attenuation, in Figure 5.37, show only minor differences from those in the Control experiment. Based on the PPIs of the difference from intrinsic values, in Figure 5.38, the only substantive change at horizontal polarization is that for the MSC algorithm the negative bias in the core of the reflectivity is gone; however, this has been replaced by positive differences of a similar magnitude on either side. Overall this likely represents a shift in the optimized coefficient obtained by the algorithm. The histograms of horizontal specific attenuation in Figure 5.41 show no significant changes, other than a slight shift upward for the band of points for the MSC algorithm. This brings the points into slightly better alignment with the one-to-one line, reflecting the shift in bias from -0.0025 dB/km to 0.0065 dB/km (Table 5.7).

At vertical polarization, there is even less change, compared to the Control results, with no visible differences in the PPIs shown in Figure 5.39. The differences from the intrinsic values, in Figure 5.40, do not show much change either; the exception is that the pronounced negatively biased rays in the results for the SC algorithm show reduced errors. The histograms of vertical specific attenuation (Figure 5.42) do not show any qualitative changes from the results in the Control experiment; the reduction in errors for the few rays of the SC algorithm's results is too small to be clear in the histogram.

For differential attenuation, the PPIs in Figure 5.43 show that the only change is a substantial increase in the differential attenuation calculated using the MSC algorithm, a direct consequence of the increase in its estimated horizontal attenuation. The PPIs of the difference from the intrinsic values, in Figure 5.44, show that this increase has turned a pronounced negative bias within the core of the reflectivity structure into an

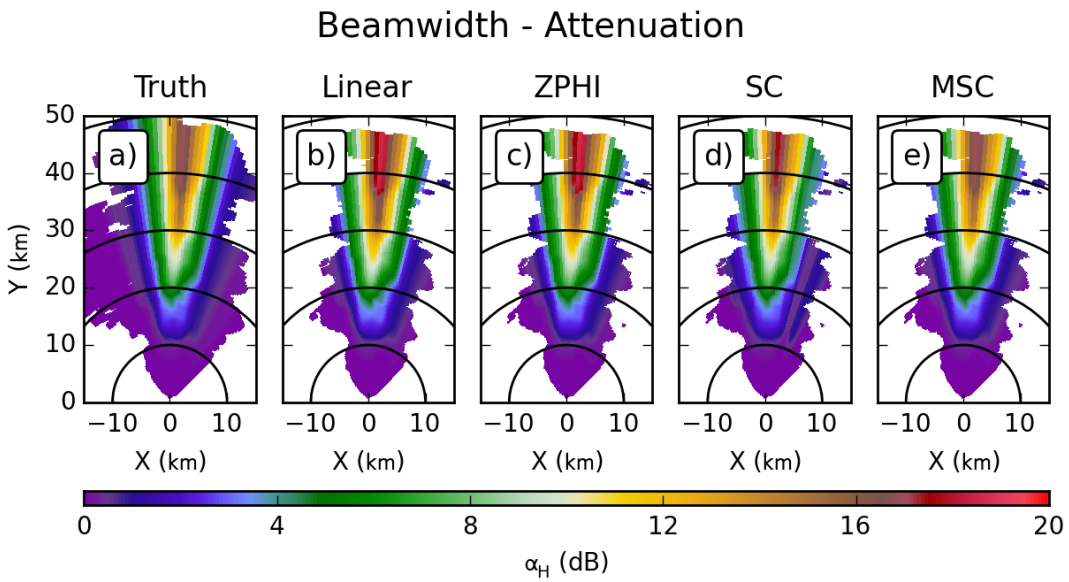

Figure 5.37: As in Figure 5.1, but for the Beamwidth experiment.

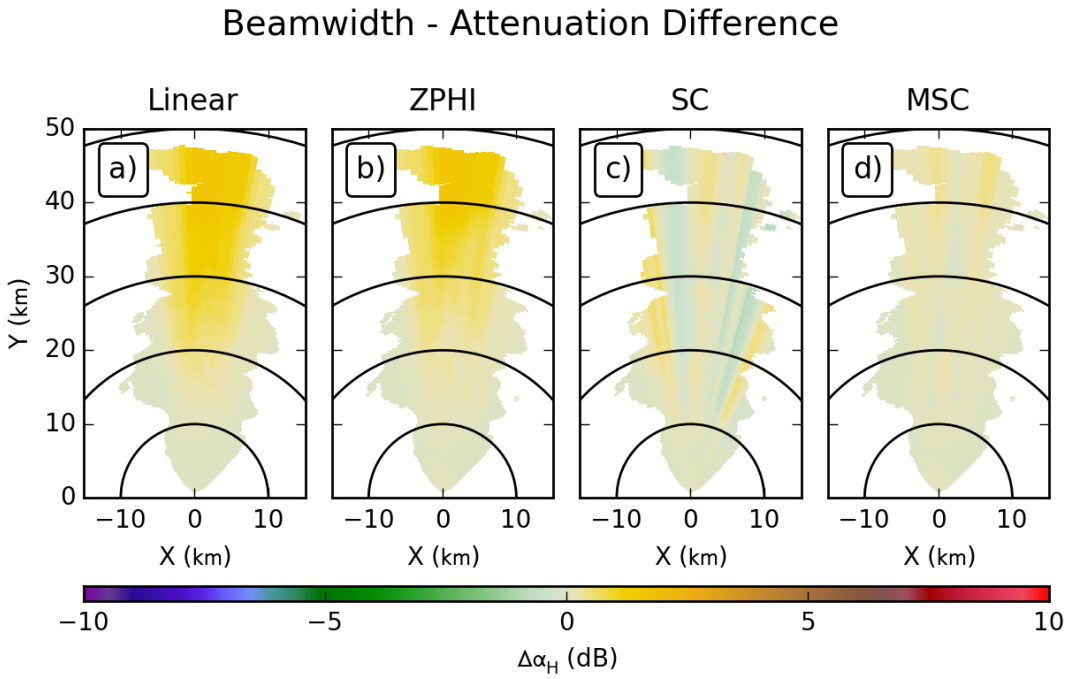

Figure 5.38: As in Figure 5.2, but for the Beamwidth experiment.

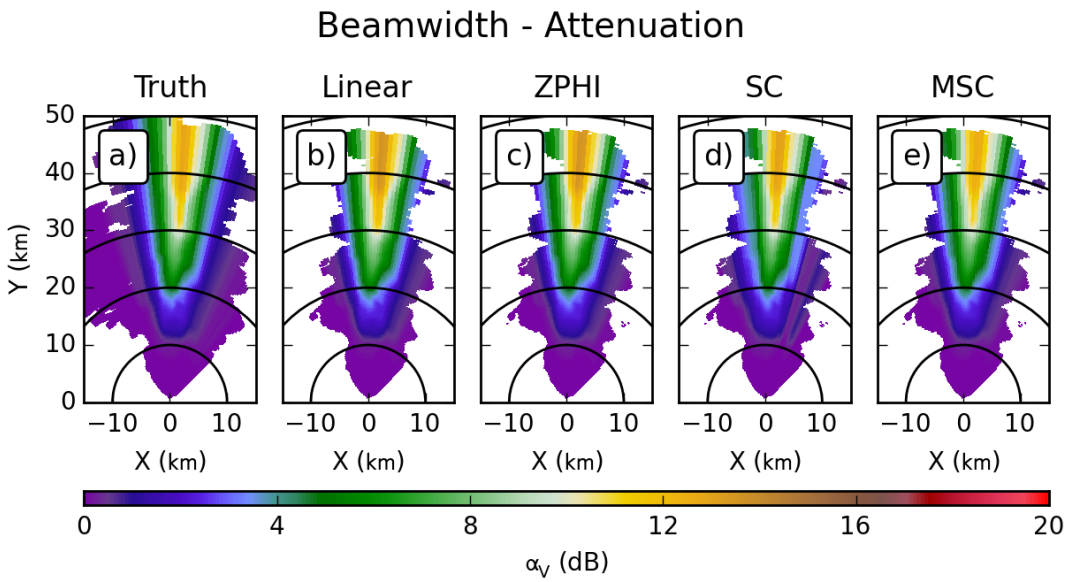

Figure 5.39: As in Figure 5.37, but for vertical polarization.

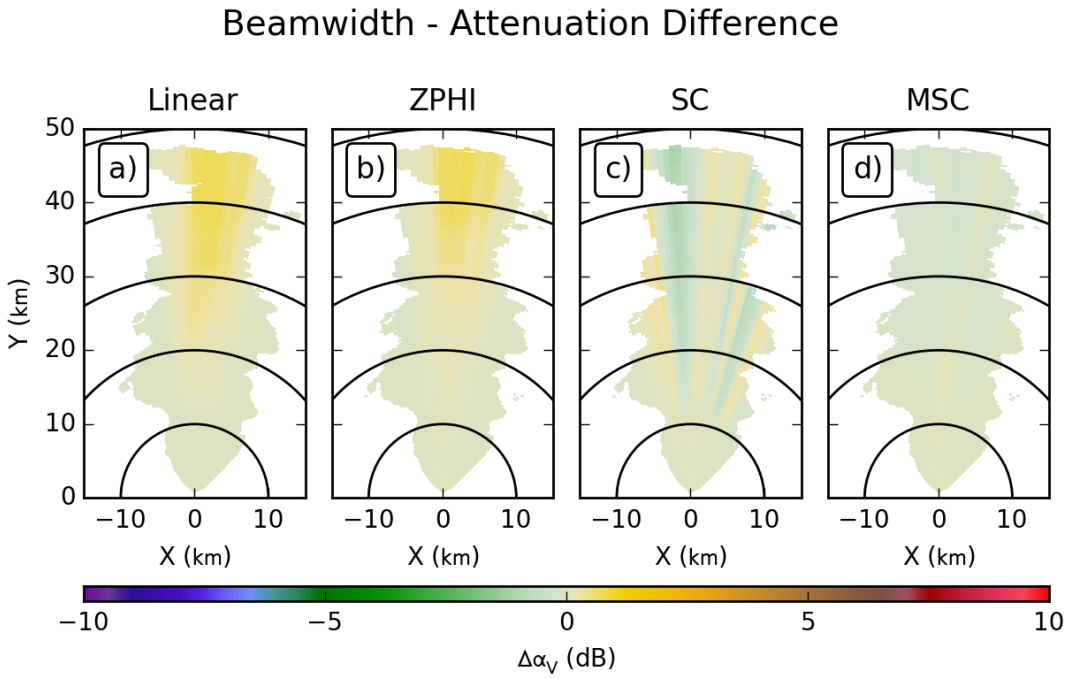

Figure 5.40: As in Figure 5.38, but for vertical polarization.

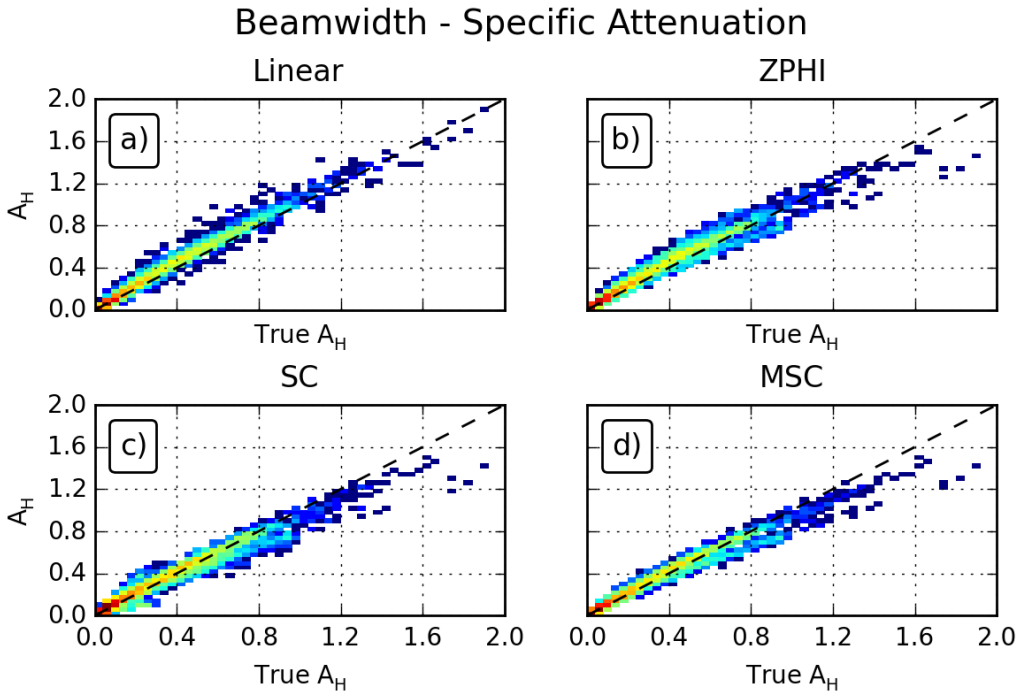

Figure 5.41: As in Figure 5.5, but for the Beamwidth experiment.

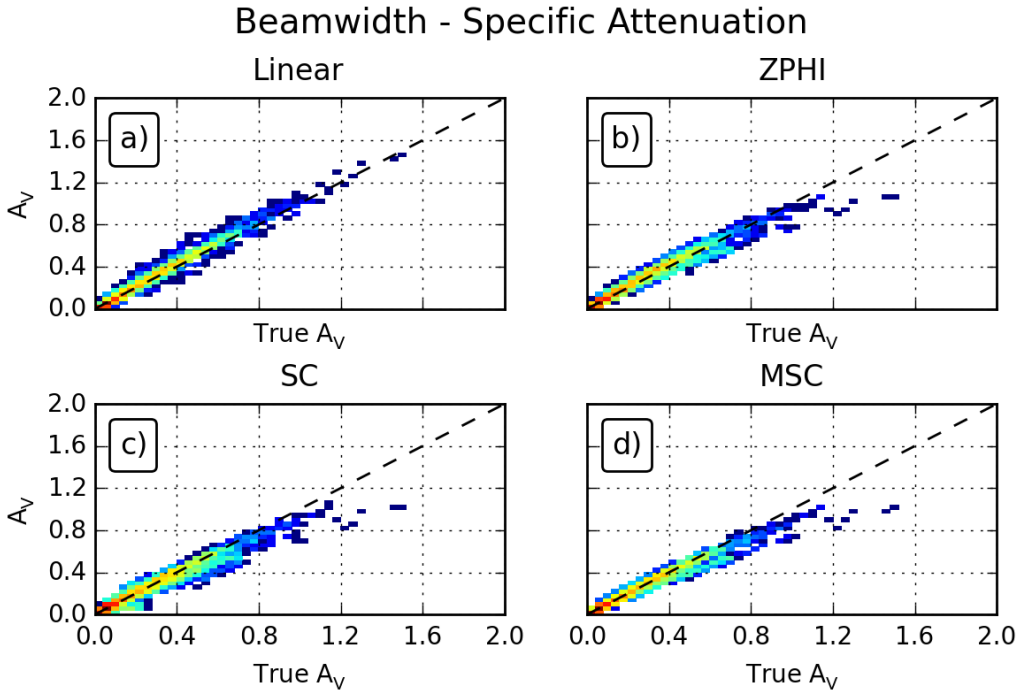

Figure 5.42: As in Figure 5.41, but for vertical polarization.

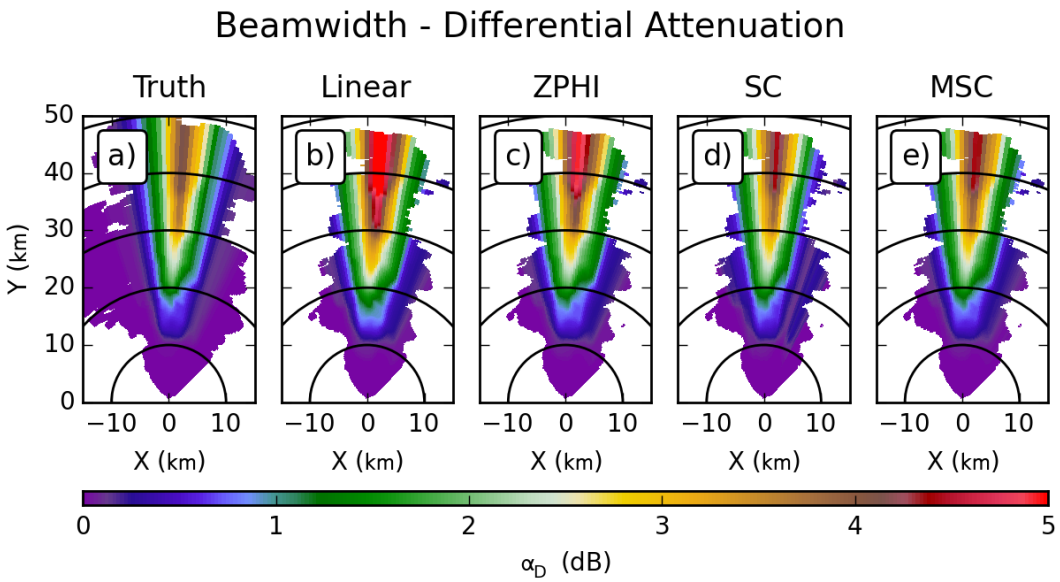

Figure 5.43: As in Figure 5.37, but for differential attenuation.

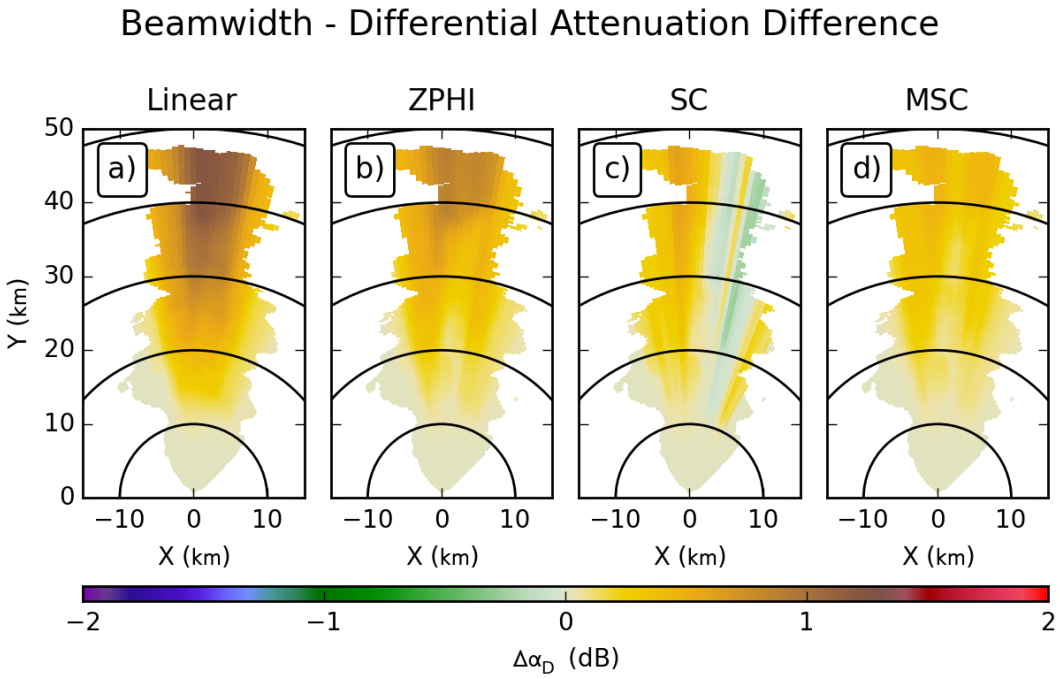

Figure 5.44: As in Figure 5.38, but for differential attenuation.

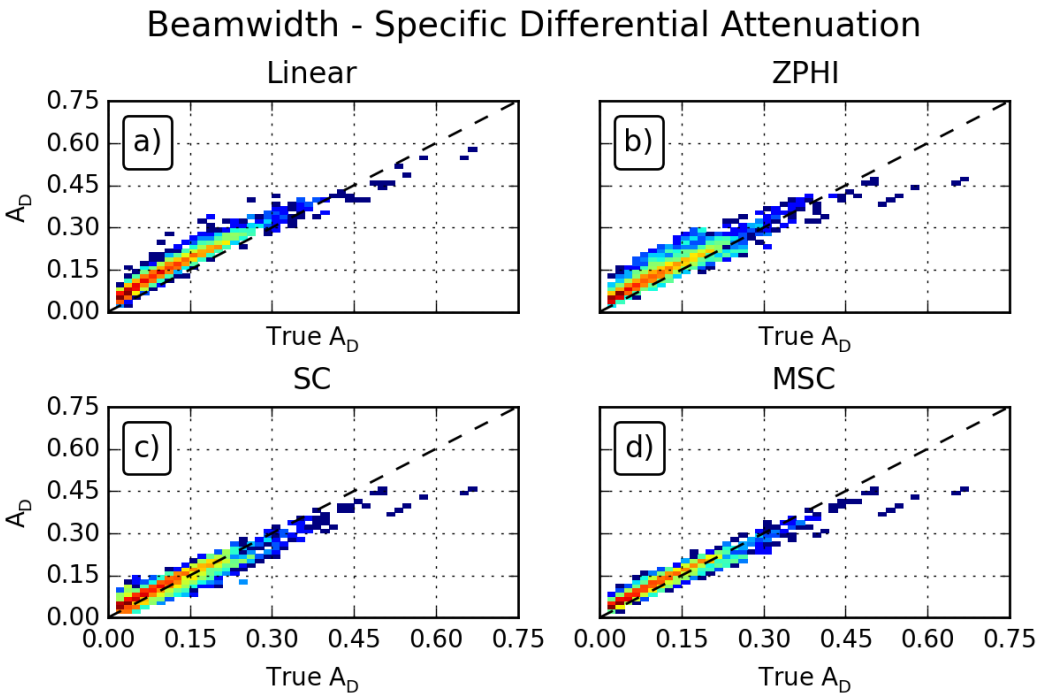

Figure 5.45: As in Figure 5.41, but for specific differential attenuation.

overall positive bias around 0.5 dB; this positive bias is still less than that of the ZPHI algorithm. The histograms of specific differential attenuation in Figure 5.45 show that only MSC shows a substantive change, with an upward shift in its band of points; this is in agreement with the increase in bias shown in Table 5.7.

Algorithm	Bias (dB/km)	MSE (dB^2/km^2)	r^2
Horizontal			
Linear	0.0322	0.0029	0.9808
ZPHI	0.0293	0.0035	0.9631
SC	0.0049	0.0032	0.9582
MSC	0.0065	0.0022	0.9712
Vertical			
Linear	0.0115	0.0011	0.9829
ZPHI	0.0091	0.0013	0.9668
SC	-0.0037	0.0020	0.9514
MSC	-0.0063	0.0013	0.9694
Differential			
Linear	0.0403	0.0019	0.9456
ZPHI	0.0278	0.0014	0.8880
SC	0.0072	0.0007	0.8975
MSC	0.0148	0.0006	0.9478

Table 5.7: As in Table 4.3, but for the Beamwidth experiment.

5.3.2 X band

At X-band, the effect of changing beamwidth is much more pronounced, evidenced by the PPIs of horizontal attenuation shown in Figure 5.46. Here, all the ZPHI-based algorithms show increases in the amount of calculated attenuation, versus their results from the Control experiment. Similar increases are observed for vertical polarization, shown in Figure 5.48. Taking the differences from the intrinsic attenuation, shown in Figures 5.47 and 5.49, it is clear that all of the algorithms, including Linear, have increased positive biases in their calculated attenuation fields at both polarizations. The histograms of specific attenuation for horizontal and vertical polarization, shown in Figures 5.50 and 5.51, respectively, show that these increases in bias are not due to any shift in the main bands of points. Rather, it is due to an increase in the spread of points above the one-to-one ratio line. These are reflected by increases in not only the computed biases, but in the MSE values as well (Table 5.8).

For differential attenuation, the changes are more minor. The PPIs of differential attenuation, in Figure 5.52, show that the most significant changes come from filling in area around the low-signal area. All of the ZPHI-based algorithms show significant changes here, especially the MSC algorithm; outside this region, the Beamwidth experiment results for differential attenuation are consistent with those for the Control experiment. The differences from the intrinsic values, shown in Figure 5.53, confirm these observations. Outside of the areas that were discussed, the only other changes observed here are that a few radials from the output of the SC algorithm changed their relative bias. Their proximity to the low signal region makes such data suspect. The histograms for specific differential attenuation, in Figure 5.54, show that there are no major changes to the character of the results for differential attenuation in the

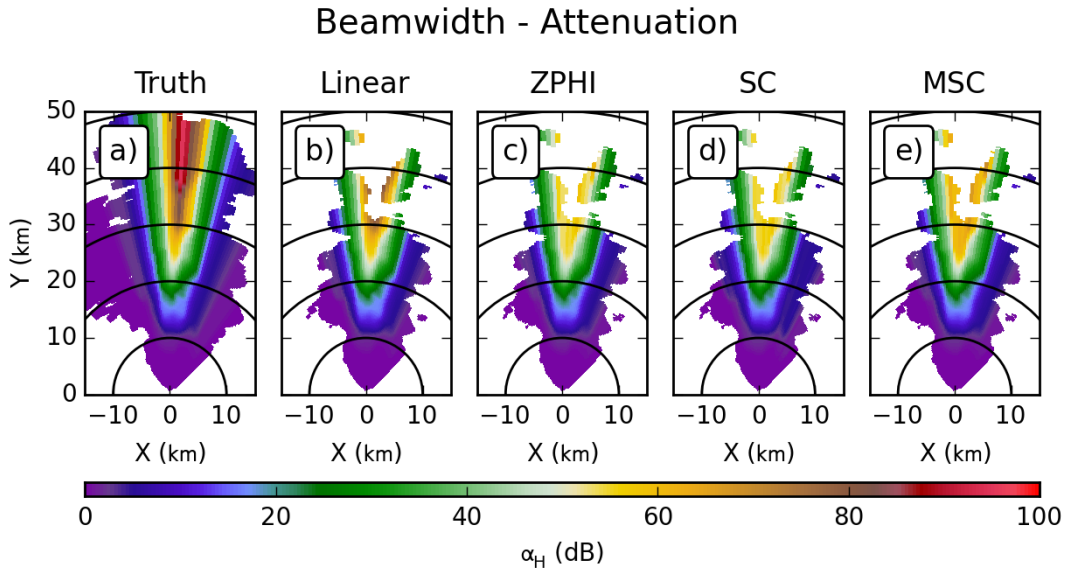

Figure 5.46: As in Figure 5.37, but for X-band.

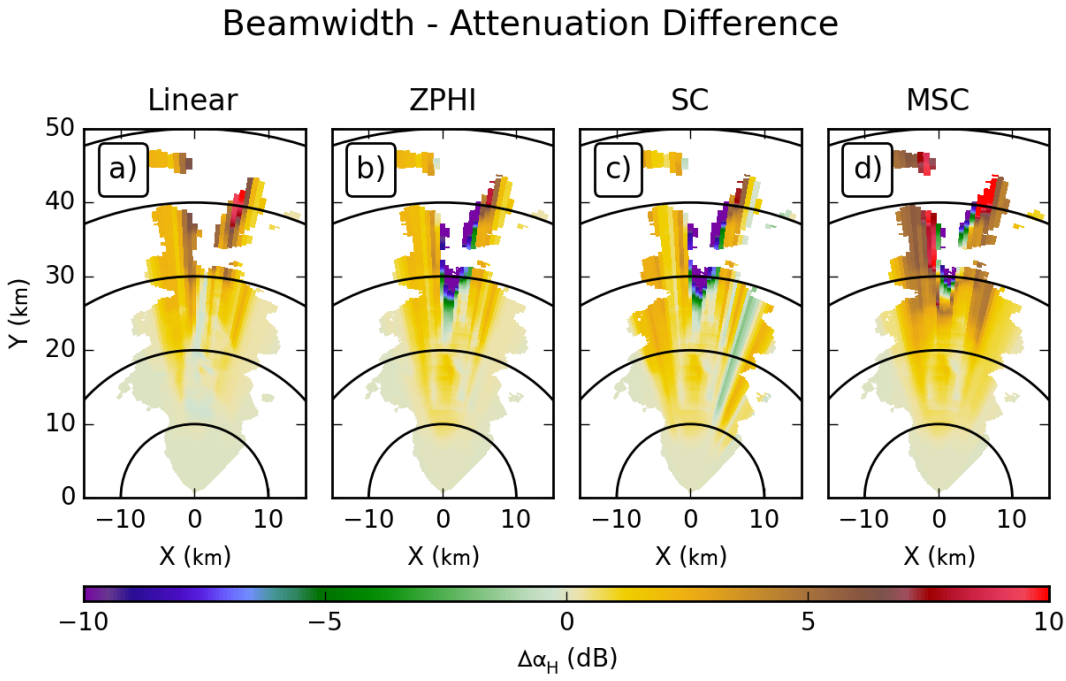

Figure 5.47: As in Figure 5.38, but for X-band.

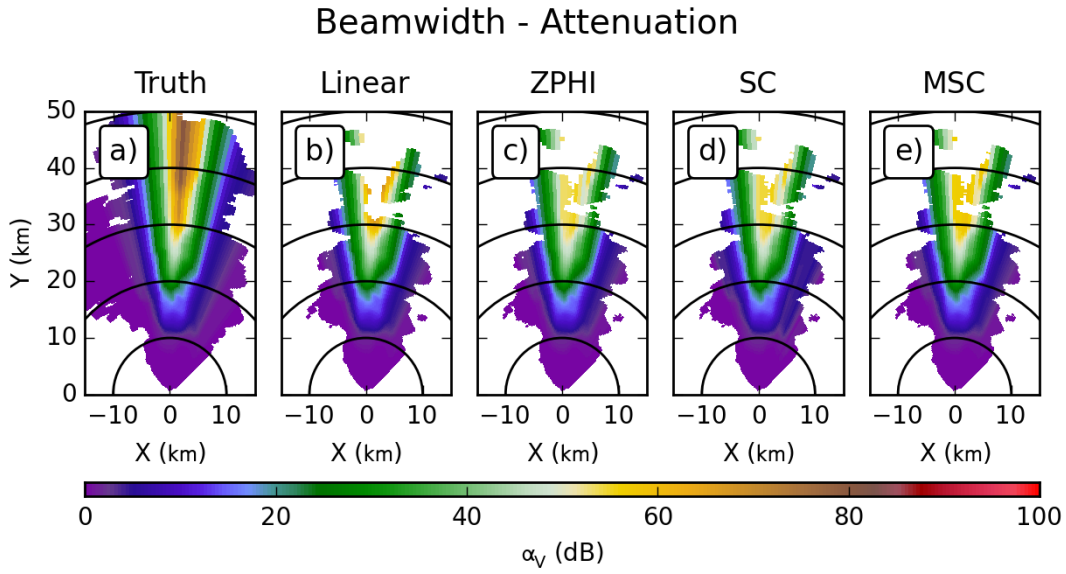

Figure 5.48: As in Figure 5.46, but for vertical polarization.

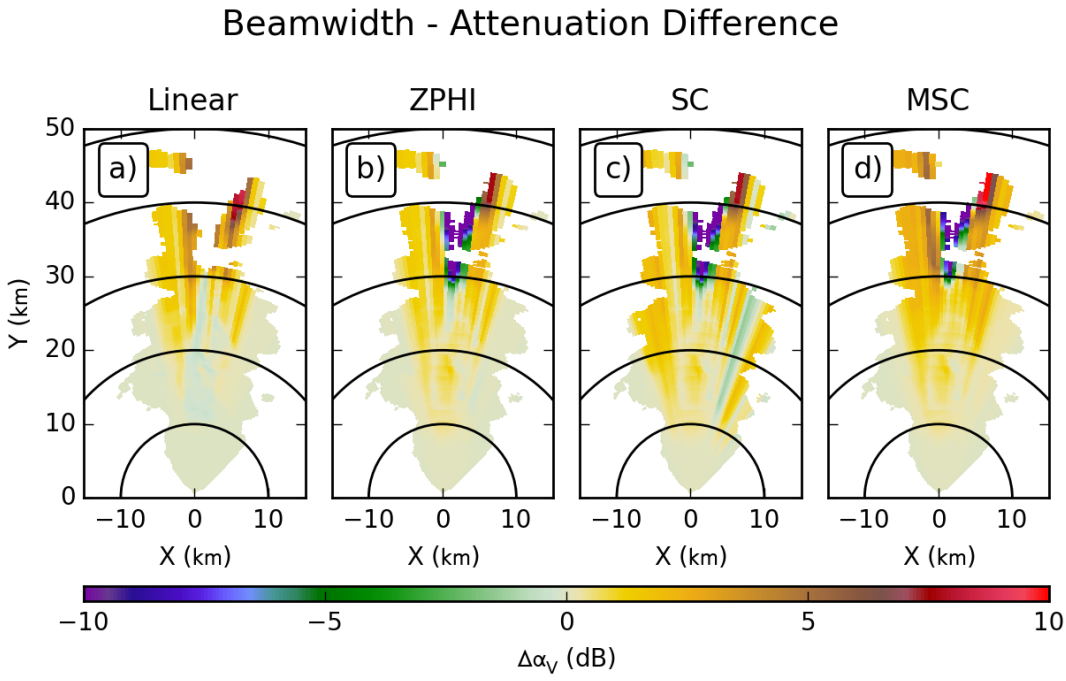

Figure 5.49: As in Figure 5.47, but for vertical polarization.

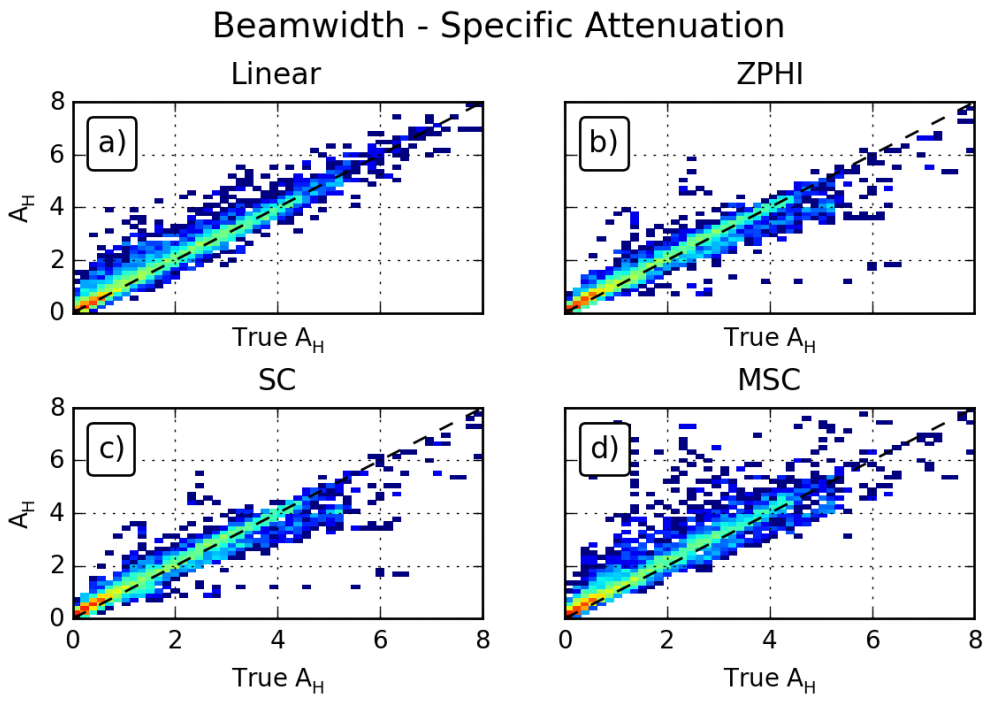

Figure 5.50: As in Figure 5.41, but for X-band.

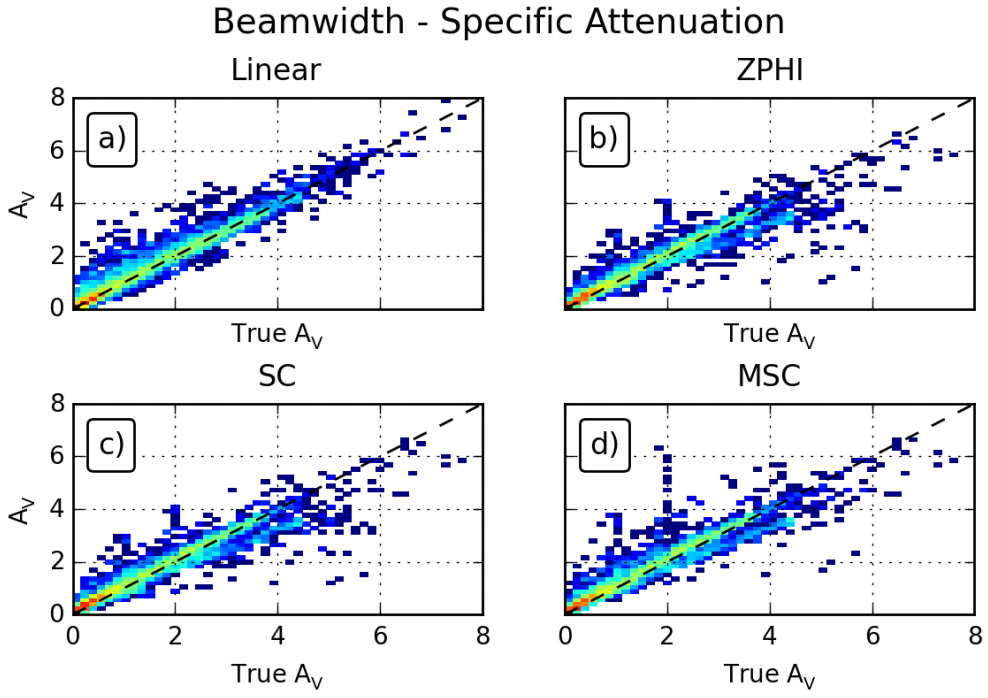

Figure 5.51: As in Figure 5.50, but for vertical polarization.

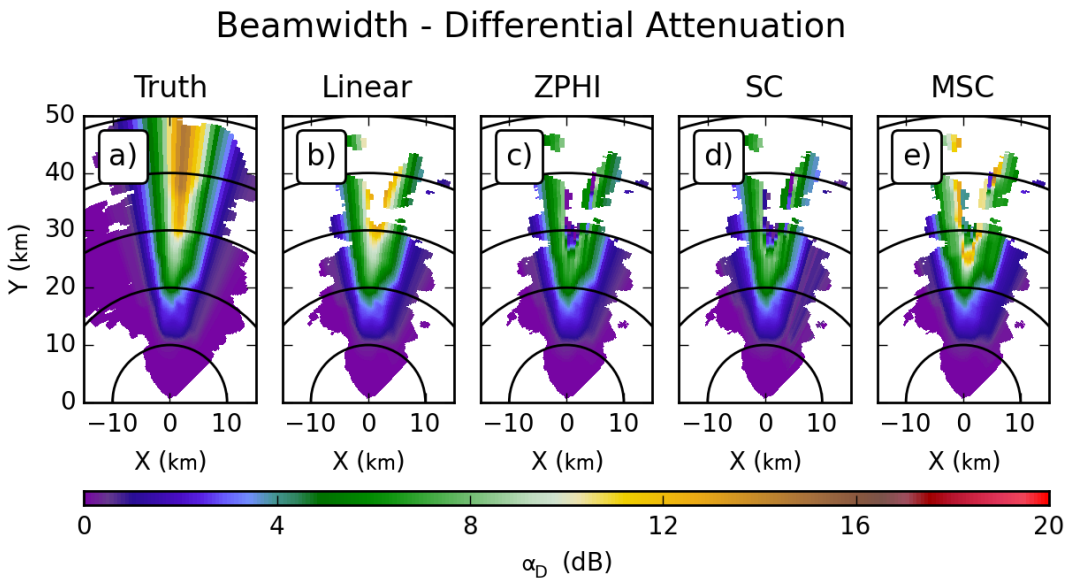

Figure 5.52: As in Figure 5.46, but for differential attenuation.

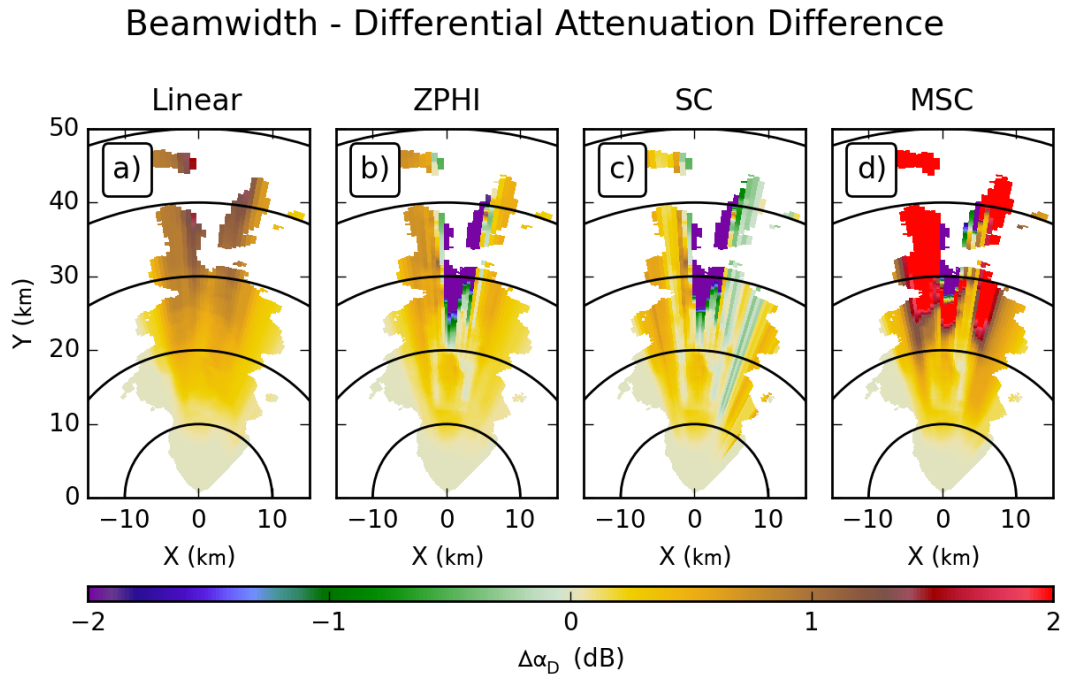

Figure 5.53: As in Figure 5.47, but for differential attenuation.

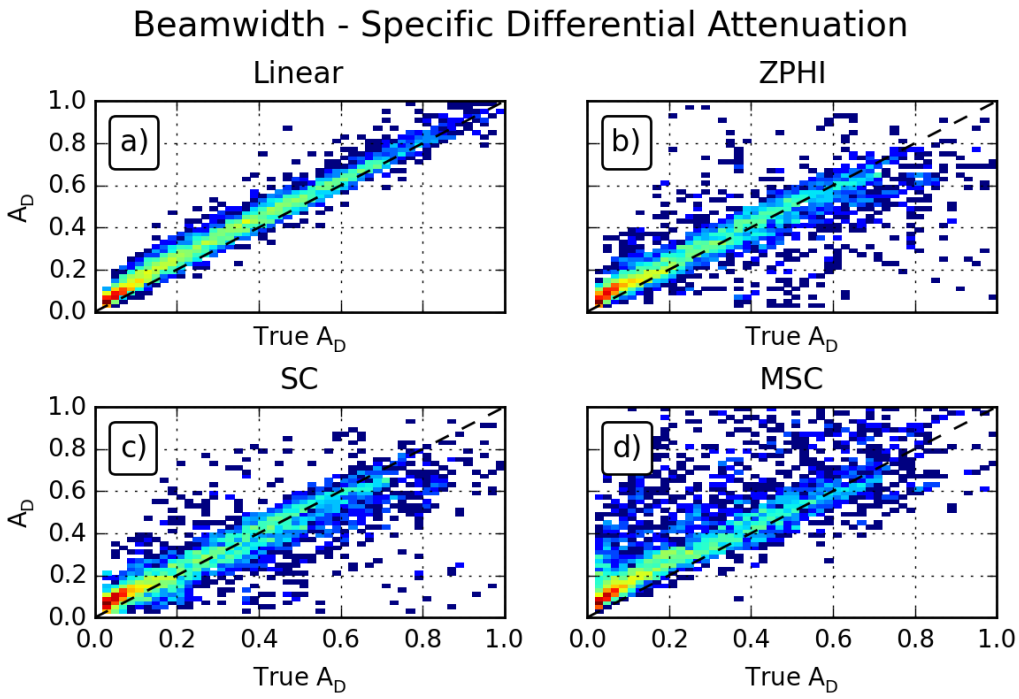

Figure 5.54: As in Figure 5.50, but for specific differential attenuation.

Beamwidth experiment. None of the main bands of points show any shift; there are changes in outlier points, but these are not systematic. The fact that the individual polarizations show significant changes, while differential attenuation remains relatively unchanged between the two experiments, indicates that the changes experienced by the two polarizations are very consistent.

5.4 Radial Width

The Radial Width experiment is the counterpart to the previous Beamwidth experiment. The beamwidth from the previous experiment is maintained at $2.0°$, while the radial spacing is increased to match. Effectively, two radials from the Beamwidth experiment will be combined into one in the Radial Width experiment. Comparisons

Algorithm	Bias (dB/km)	MSE (dB^2/km^2)	r^2
Horizontal			
Linear	0.1009	0.0974	0.9596
ZPHI	0.0454	0.1231	0.9415
SC	0.0687	0.1277	0.9413
MSC	0.2072	0.3123	0.8805
Vertical			
Linear	0.0730	0.0762	0.9537
ZPHI	0.0303	0.0921	0.9389
SC	0.0574	0.0974	0.9371
MSC	0.0909	0.1060	0.9334
Differential			
Linear	0.0407	0.0030	0.9776
ZPHI	0.0129	0.0135	0.7606
SC	0.0075	0.0115	0.7927
MSC	0.1524	0.1543	0.3618

Table 5.8: As in Table 4.4, but for the Beamwidth experiment.

between the two will reflect the impacts of this averaging on the correction techniques. Also, comparing against the Control baseline, which has sampling matched between beamwidth and radial spacing at $1.0°$, will explore how the overall change in resolution volume impacts the corrections.

5.4.1 C band

For the Radial Width experiment, the PPIs of attenuation at horizontal and vertical polarizations, in Figures 5.55 and 5.57, respectively, show no significant changes in comparison with the results of the Beamwidth experiment, in regards to the amount of attenuation; clearly different is the coarseness of the data, which is expected based on the change to the radial spacing. The PPIs of the difference between the algorithm calculation and the intrinsic values, in Figures 5.56 and 5.58, confirm the lack of significant differences. The MSC algorithm does show some small changes from small negative errors to small positive errors, but no significant changes to the magnitude of errors. This is likely another reflection of the sensitivity of MSC. The histograms of specific attenuation, in Figures 5.59 and 5.60, show no significant changes from the results in the Beamwidth experiment (other than an expected decrease in the total number of points). This is also reflected in the lack of significant changes to the bias and MSE values in Table 5.9.

For differential attenuation, the results are similar. The PPIs of the base attenuation fields in Figure 5.61 show no significant changes, except that the MSC algorithm appears to have produced less total differential attenuation. This is confirmed in Figure 5.62, which shows that the differences from the intrinsic values of differential attenuation have changed from an overall, small positive bias to a negative bias, around

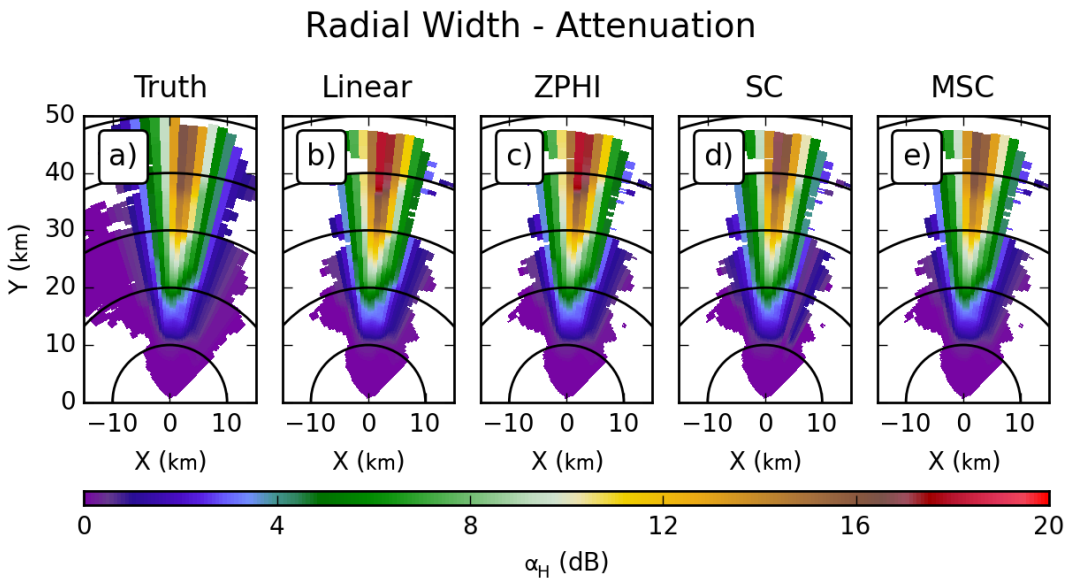

Figure 5.55: As in Figure 5.1, but for the Radial Width experiment.

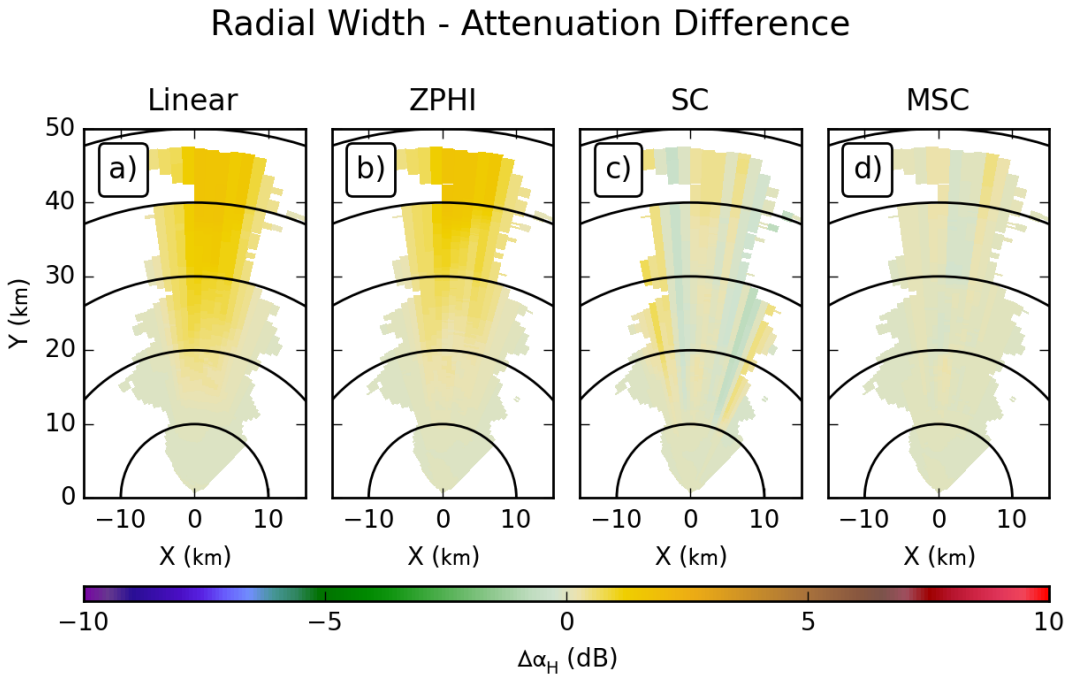

Figure 5.56: As in Figure 5.2, but for the Radial Width experiment.

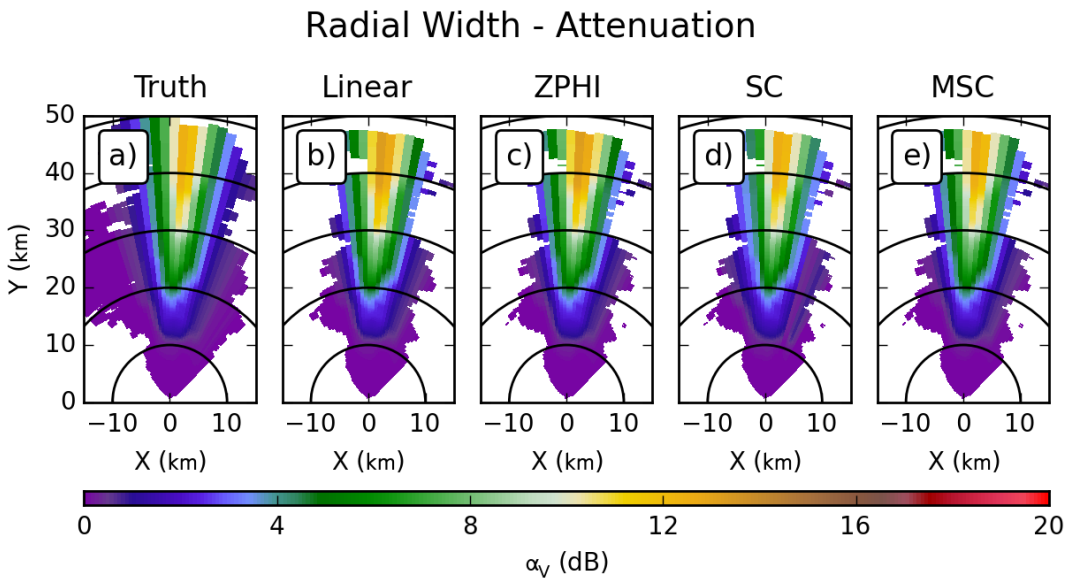

Figure 5.57: As in Figure 5.55, but for vertical polarization.

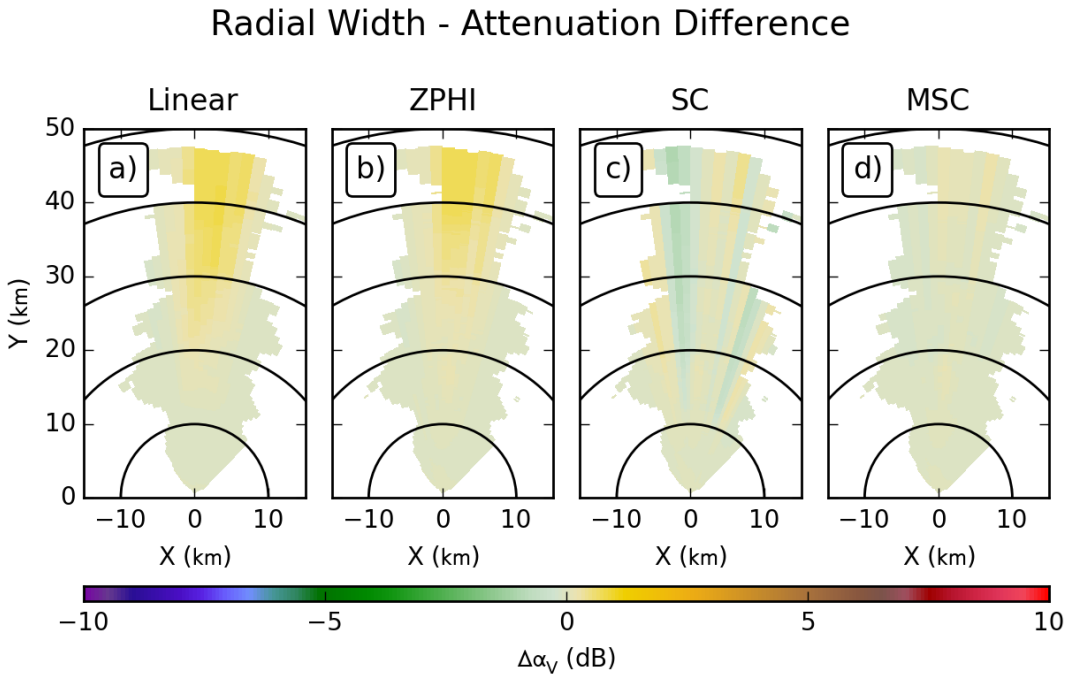

Figure 5.58: As in Figure 5.56, but for vertical polarization.

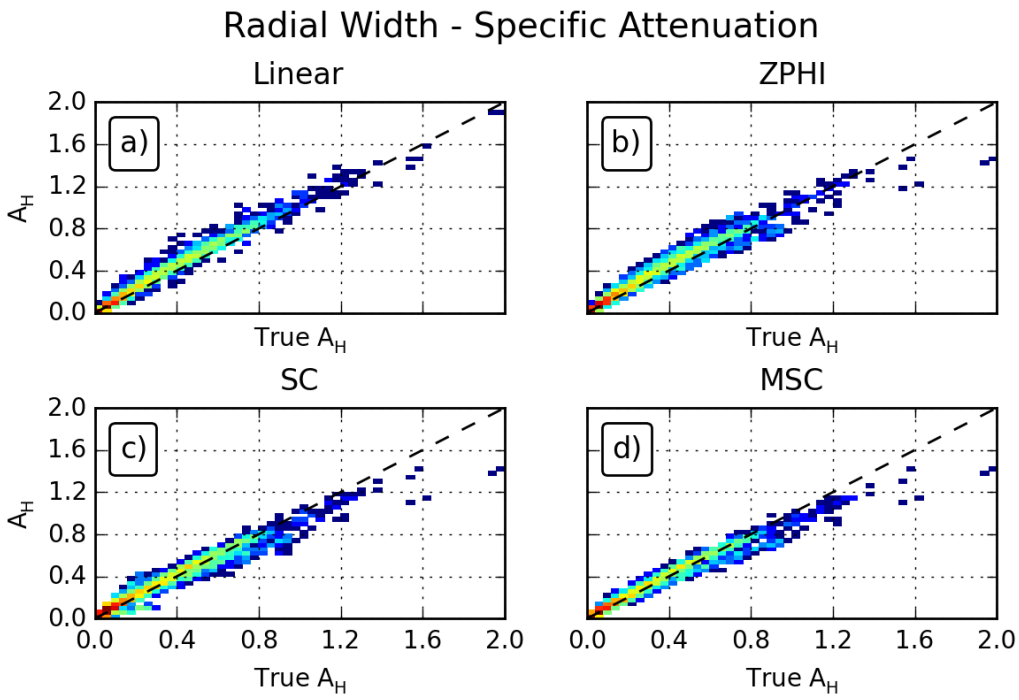

Figure 5.59: As in Figure 5.5, but for the Radial Width experiment.

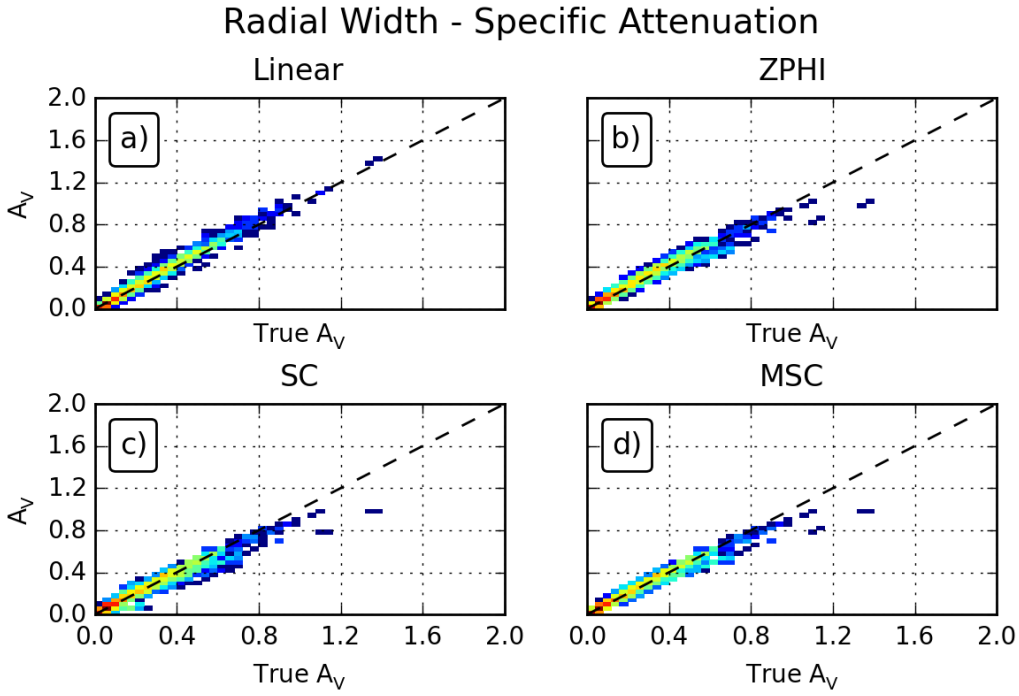

Figure 5.60: As in Figure 5.59, but for vertical polarization.

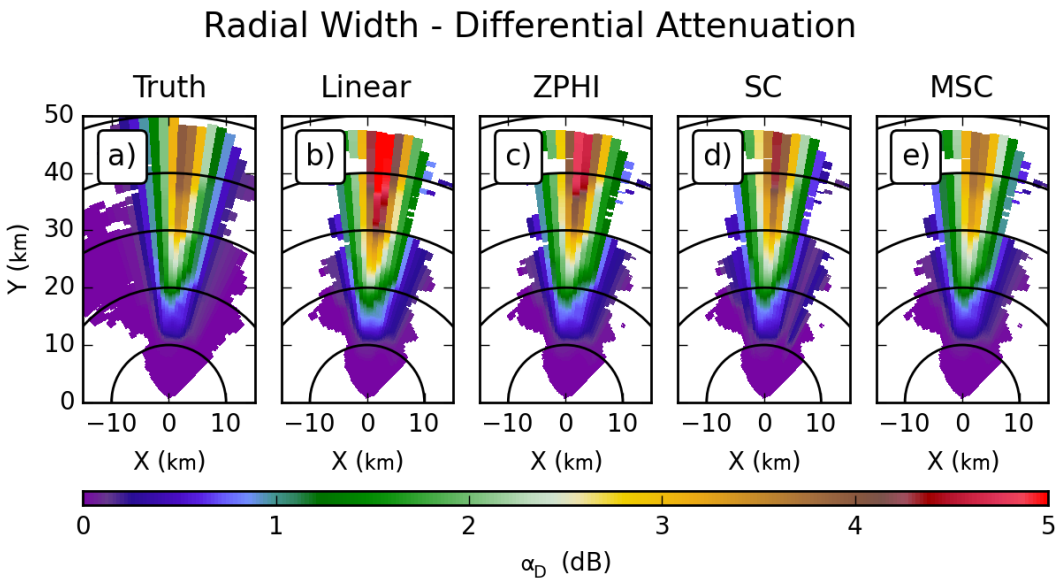

Figure 5.61: As in Figure 5.55, but for differential attenuation.

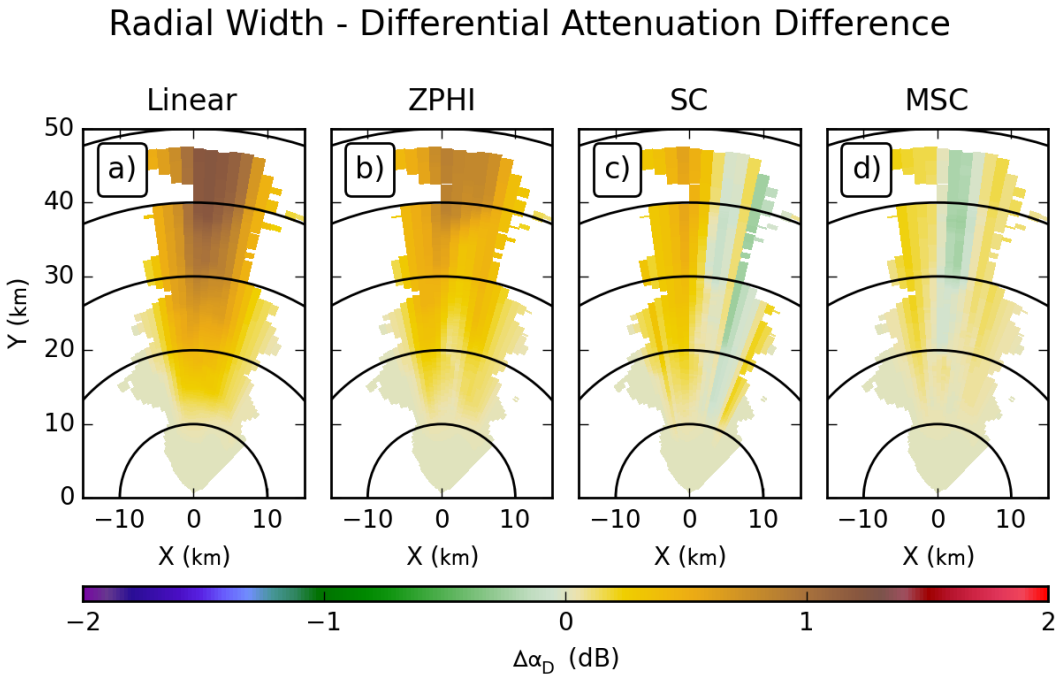

Figure 5.62: As in Figure 5.56, but for differential attenuation.

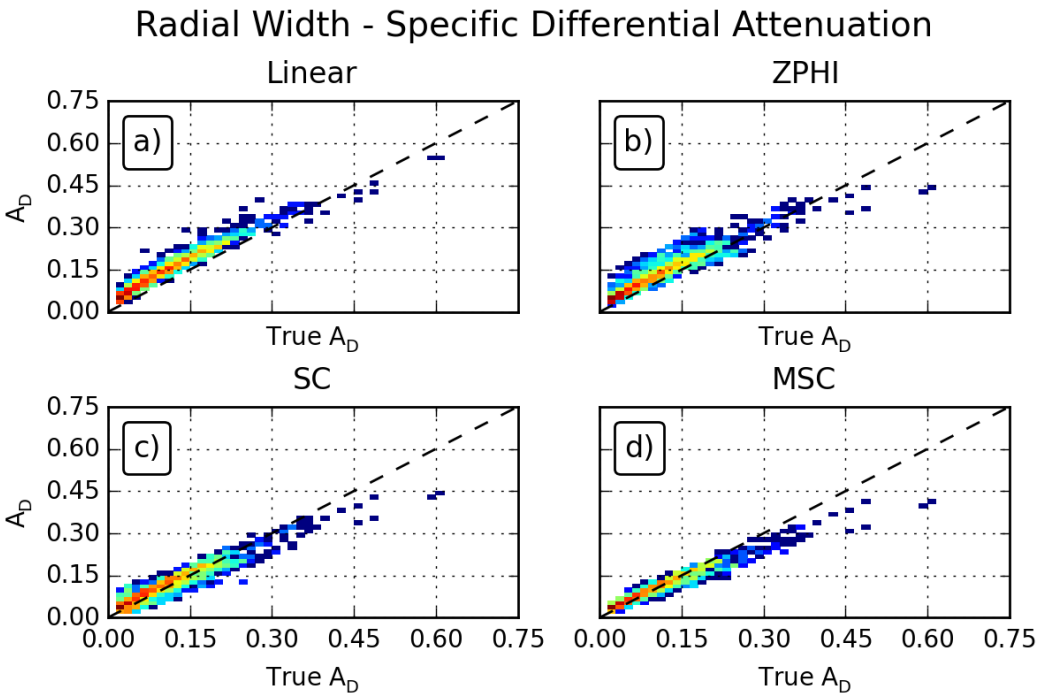

Figure 5.63: As in Figure 5.59, but for specific differential attenuation.

0.25 dB in the core of the reflectivity structure, as well as small positive biases on either side. The errors for the other algorithms show no significant changes with respect to the Beamwidth experiment. The histograms of specific differential attenuation, in Figure 5.63, show that the core band of points for the MSC algorithm has shifted down, putting the band of points along the one-to-one line for small values; for higher values, the band now curves below the one-to-one line. This yields the observed lessened bias for smaller attenuation along the edge of the reflectivity structure and pronounced negative bias for the higher values of attenuation in the middle of the structure. Overall, this value dependent bias reflects a failure of the algorithm to effectively capture the relationship between radar observables and attenuation.

Algorithm	Bias (dB/km)	MSE (dB^2/km^2)	r^2
Horizontal			
Linear	0.0334	0.0030	0.9806
ZPHI	0.0306	0.0036	0.9622
SC	0.0071	0.0031	0.9584
MSC	0.0035	0.0022	0.9716
Vertical			
Linear	0.0121	0.0011	0.9832
ZPHI	0.0099	0.0013	0.9665
SC	-0.0019	0.0018	0.9527
MSC	-0.0007	0.0012	0.9693
Differential			
Linear	0.0398	0.0019	0.9479
ZPHI	0.0274	0.0014	0.8851
SC	0.0069	0.0006	0.8937
MSC	0.0002	0.0004	0.9461

Table 5.9: As in Table 4.3, but for the Radial Width experiment.

5.4.2 X band

At X-band, the PPIs of horizontal and vertical attenuation, in Figures 5.64 and 5.66, respectively, show no observable changes in magnitude between the Beamwidth and Radial Width experiments. The differences from the intrinsic values, shown in Figures 5.65 and 5.67, confirm that there are no significant changes in the structure of the errors of the algorithms. The histograms of specific attenuation, in Figures 5.68 and 5.69, also exhibit no shifts or tilts that would indicate a change in performance. It is worth noting that the histograms for the Radial Width experiment show significantly fewer points at the higher values of specific attenuation; this is a reflection of how the larger azimuthal spacing smooths the data and reduces peaks. Also, at both polarizations, the ZPHI algorithms develop a collection of outlier points around a value of true specific attenuation of 1.5 dB/km; these points contribute to an increase in the bias and MSE (Table 5.10) but are otherwise insignificant compared to the core band of points.

For differential attenuation, the results are similarly stable between the Beamwidth and Radial Width experiments. The PPIs of the base fields, in Figure 5.70, show no significant changes in the algorithms, outside of the low-signal region which is expected to be dependent on the sensitivity of the radar. The differences from the intrinsic values, in Figure 5.71, show that the errors have not changed outside of the low-signal region. The anomalous regions in the MSC algorithm have had the magnitude of errors greatly reduced, though the values are still anomalously high. The histograms of the points, in Figure 5.72, also show no significant changes to the core bands of points. For the ZPHI-based algorithms, many of the outlier points are better clustered around the one-to-one line, especially for the MSC algorithm. This is another consequence of the smoothing effect of the larger radial spacing.

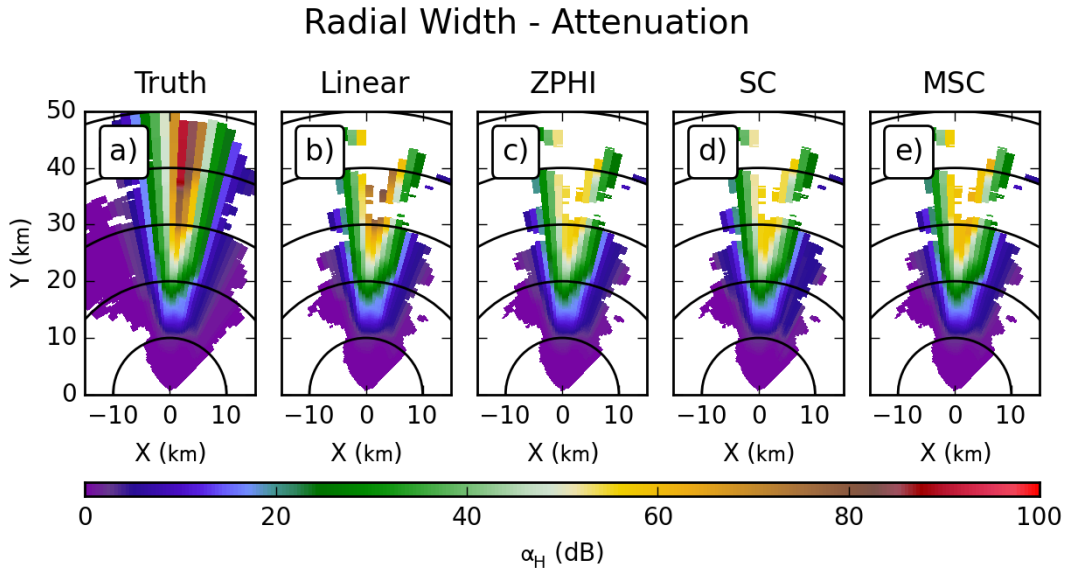

Figure 5.64: As in Figure 5.55, but for X-band.

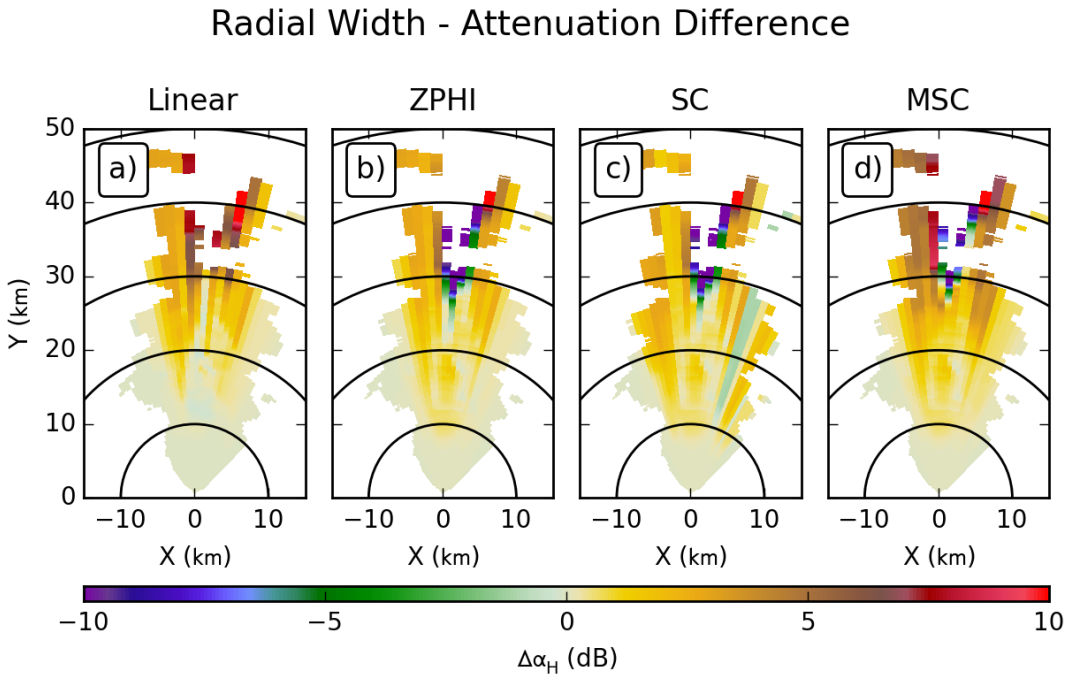

Figure 5.65: As in Figure 5.56, but for X-band.

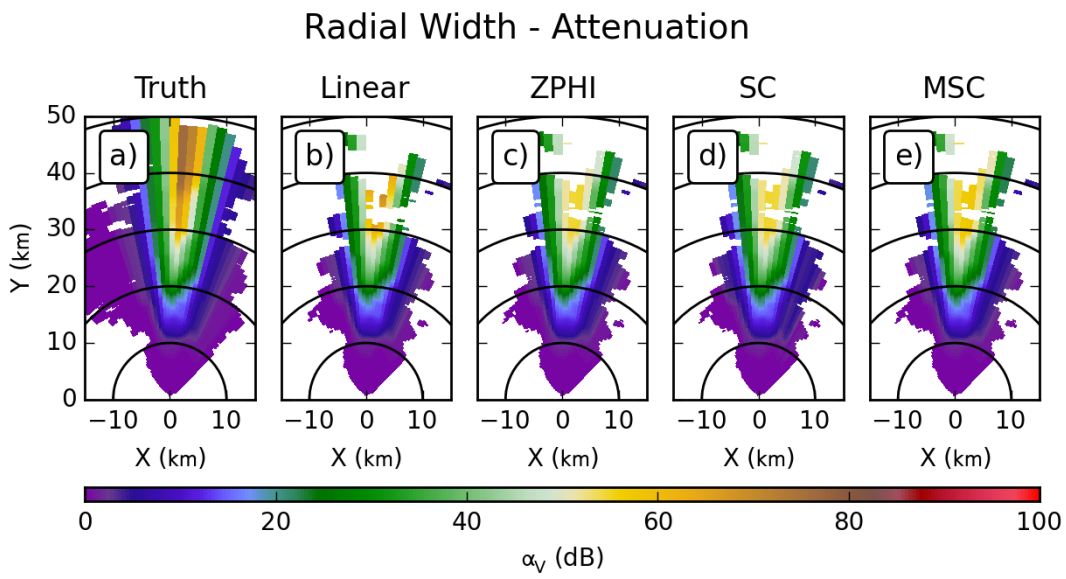

Figure 5.66: As in Figure 5.64, but for vertical polarization.

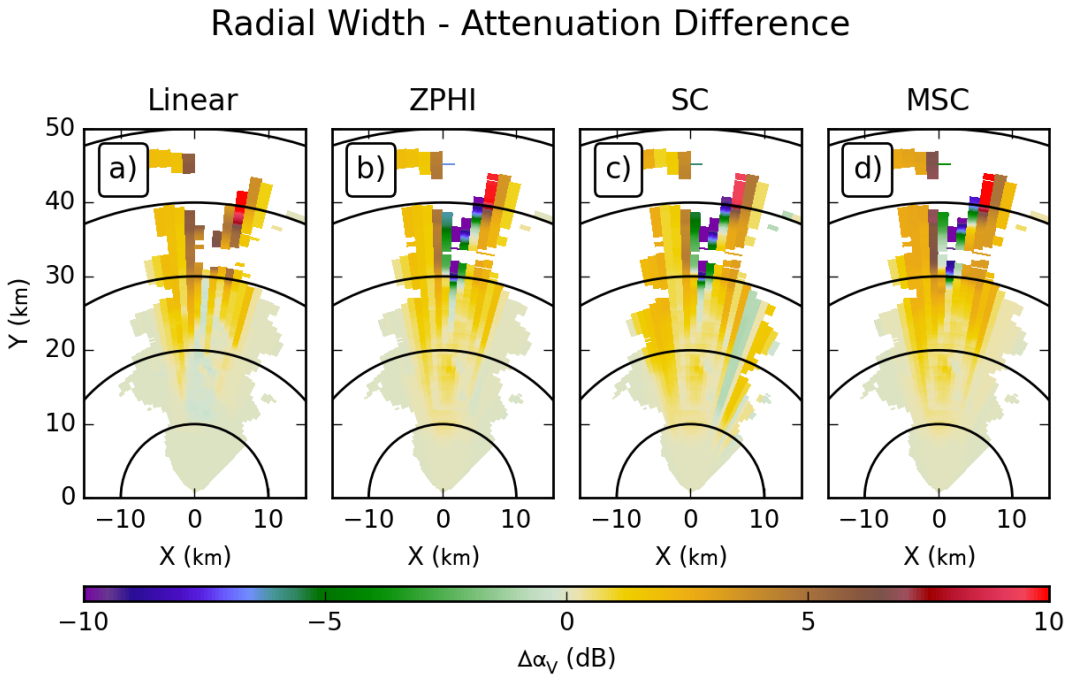

Figure 5.67: As in Figure 5.65, but for vertical polarization.

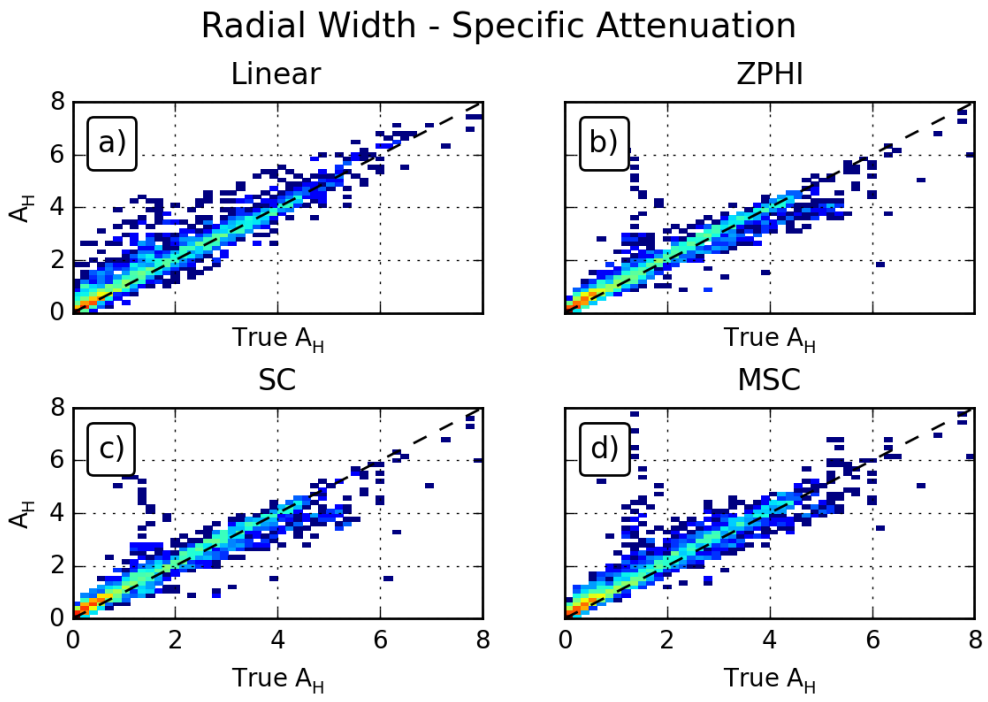

Figure 5.68: As in Figure 5.59, but for X-band.

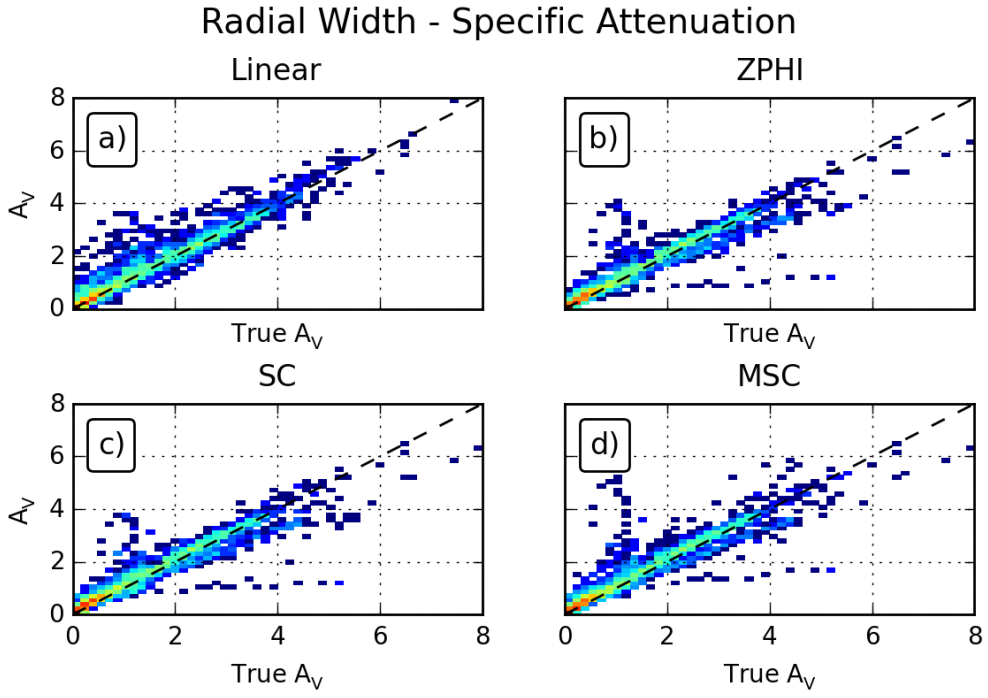

Figure 5.69: As in Figure 5.68, but for vertical polarization.

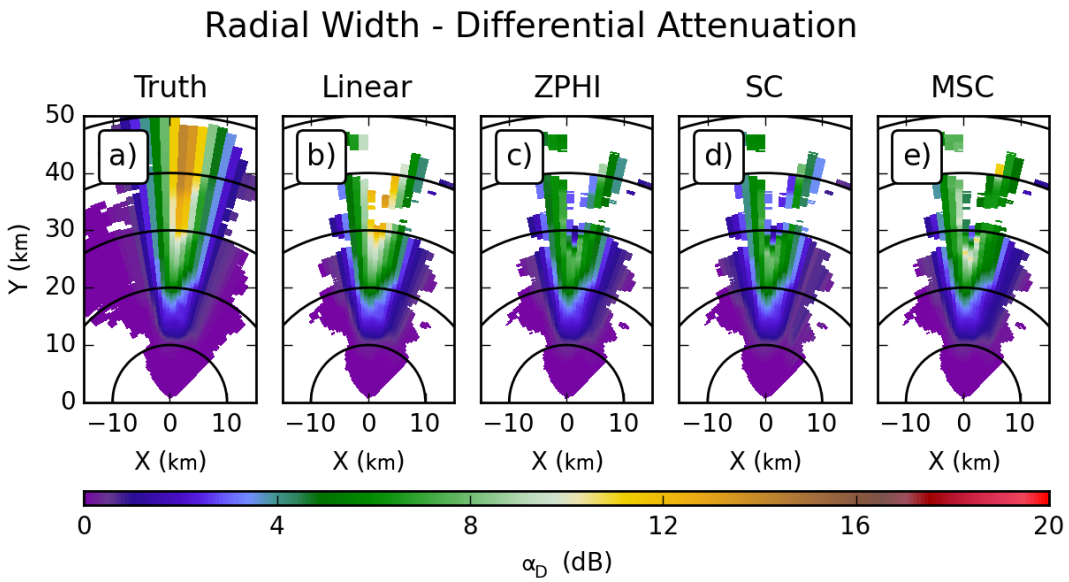

Figure 5.70: As in Figure 5.64, but for differential attenuation.

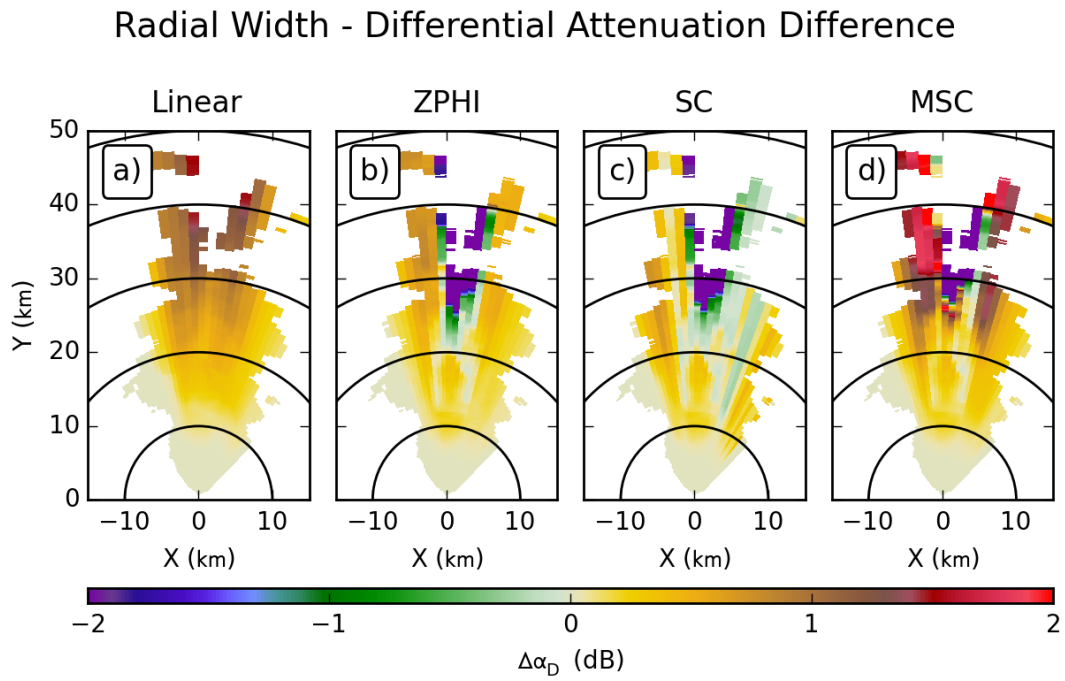

Figure 5.71: As in Figure 5.65, but for differential attenuation.

Algorithm	Bias (dB/km)	MSE (dB^2/km^2)	r^2
Horizontal			
Linear	0.1331	0.1477	0.9379
ZPHI	0.0743	0.1567	0.9216
SC	0.0910	0.1521	0.9264
MSC	0.1697	0.2799	0.8775
Vertical			
Linear	0.0969	0.1074	0.9340
ZPHI	0.0514	0.1131	0.9215
SC	0.0750	0.1187	0.9199
MSC	0.1016	0.1394	0.9095
Differential			
Linear	0.0416	0.0030	0.9782
ZPHI	0.0127	0.0169	0.6911
SC	0.0046	0.0106	0.7978
MSC	0.0779	0.0694	0.4196

Table 5.10: As in Table 4.4, but for the Radial Width experiment.

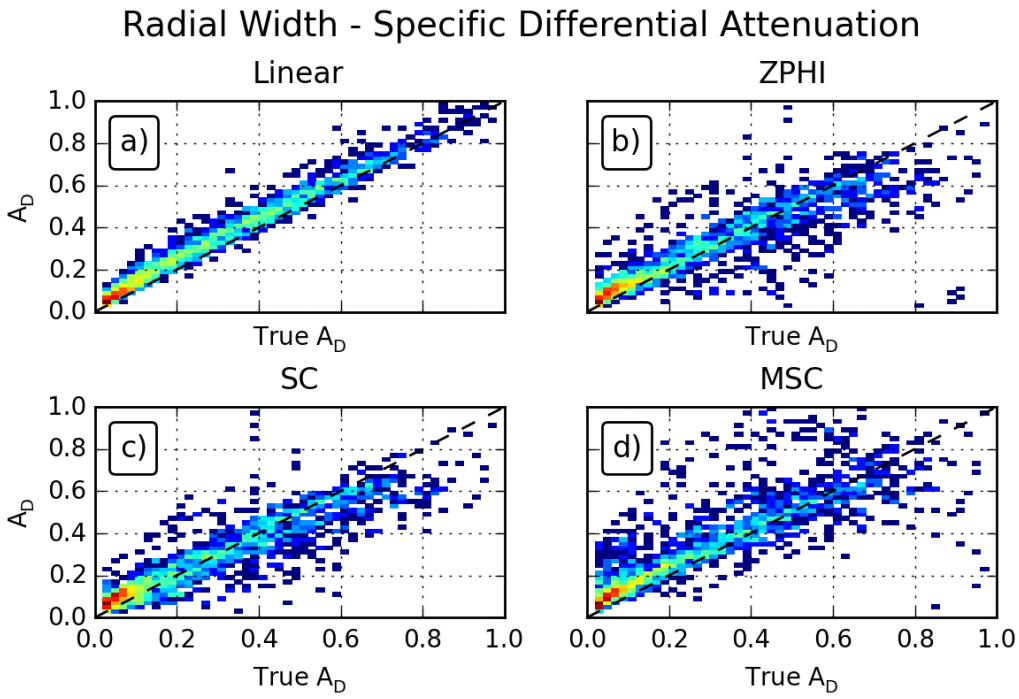

Figure 5.72: As in Figure 5.68, but for specific differential attenuation.

5.5 Range Resolution

While all previous experiments explored aspects of azimuthal sampling, the Range Resolution experiment looks at how the resolution in the alternate direction, along the range, impacts the attenuation corrections. Given that all of the algorithms rely on range integrals of various forms, range resolution and spacing is a very relevant consideration for the operation of attenuation correction techniques.

5.5.1 C band

The PPIs of the base attenuation fields for the Range Resolution experiment are given in Figures 5.73 and 5.75, for horizontal and vertical polarizations, respectively. These fields exhibit no significant differences from the results for the Control experiment.

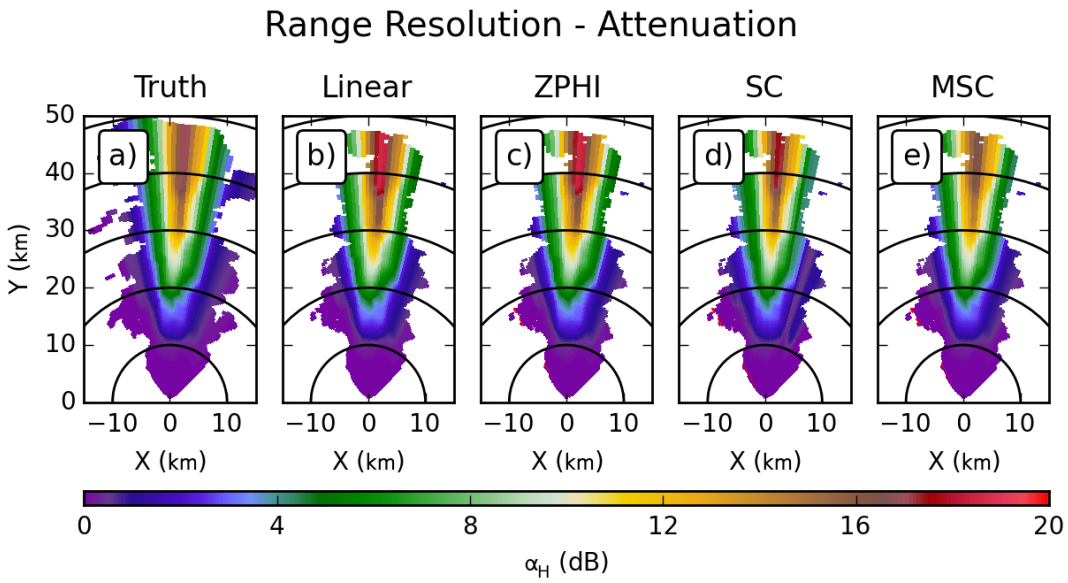

Figure 5.73: As in Figure 5.1, but for the Range Resolution experiment.

This consistency with the Control experiment also extends to the differences from the intrinsic values, shown in Figures 5.74 and 5.76. This lack of change is reflected in the histograms for specific attenuation, shown in Figures 5.77 and 5.78, for horizontal and polarizations, respectively. The only significant change is that all algorithms show fewer points with high values of specific attenuation, a consequence of the smoothing due to the larger pulse and gate spacing. However, the histograms have no observable changes with regards to the accuracy of the correction algorithms. This is reflected in the computed biases and MSE values as well (Table 5.11) which show only minor changes from the values for the Control experiment.

For differential attenuation, the results largely follow those for the individual polarizations. The PPIs of the base differential attenuation results, in Figure 5.79, show that the MSC algorithm is the only one that changes magnitude versus the results from the Control experiment. The differences from the intrinsic values, in Figure 5.80, show

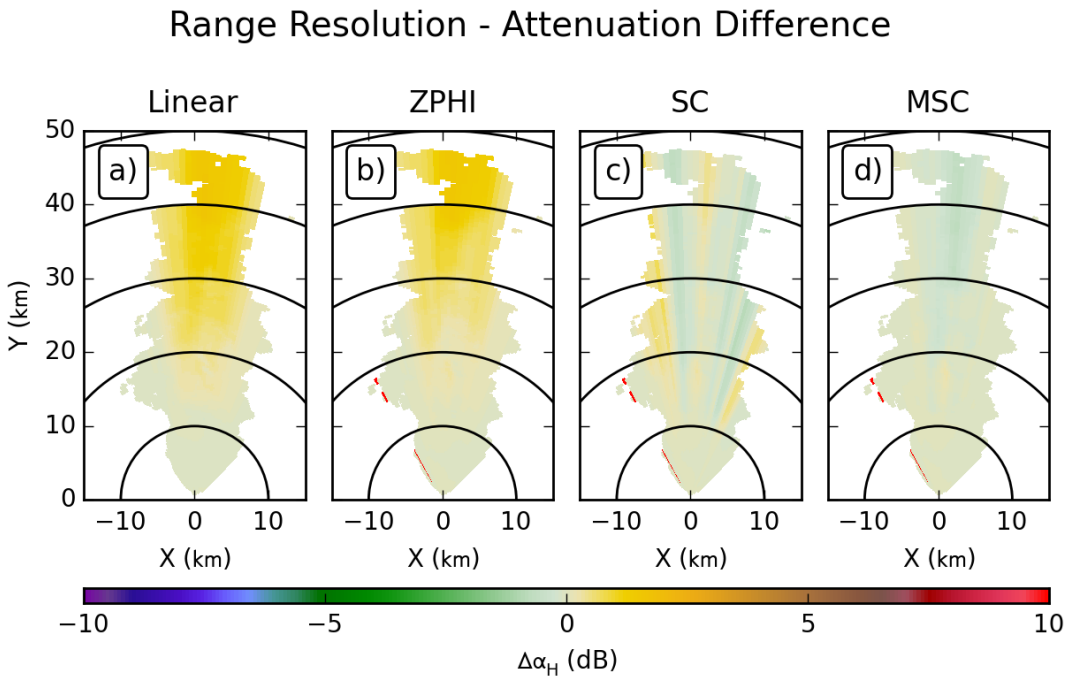

Figure 5.74: As in Figure 5.2, but for the Range Resolution experiment.

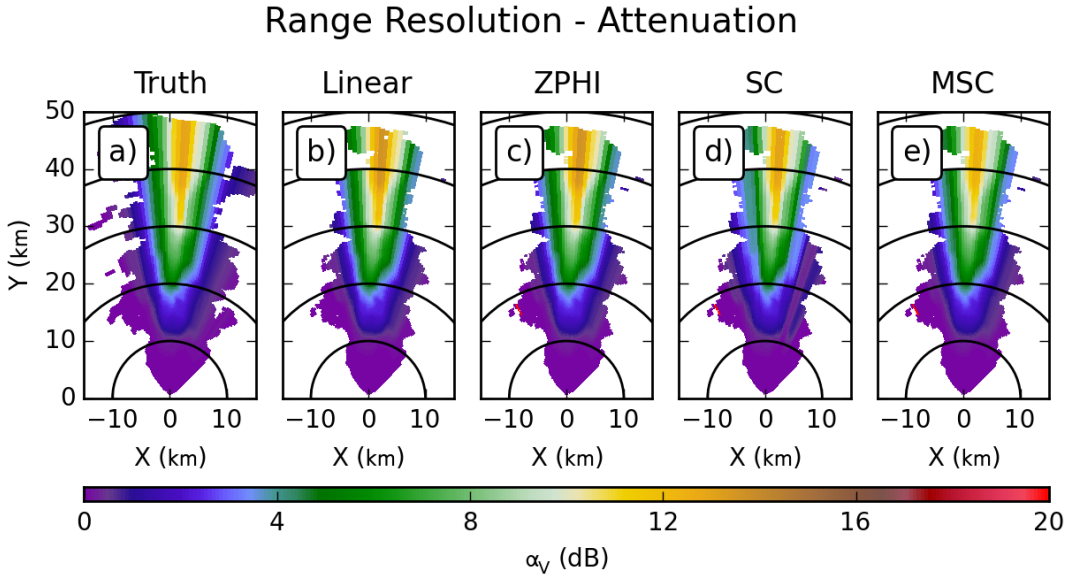

Figure 5.75: As in Figure 5.73, but for vertical polarization.

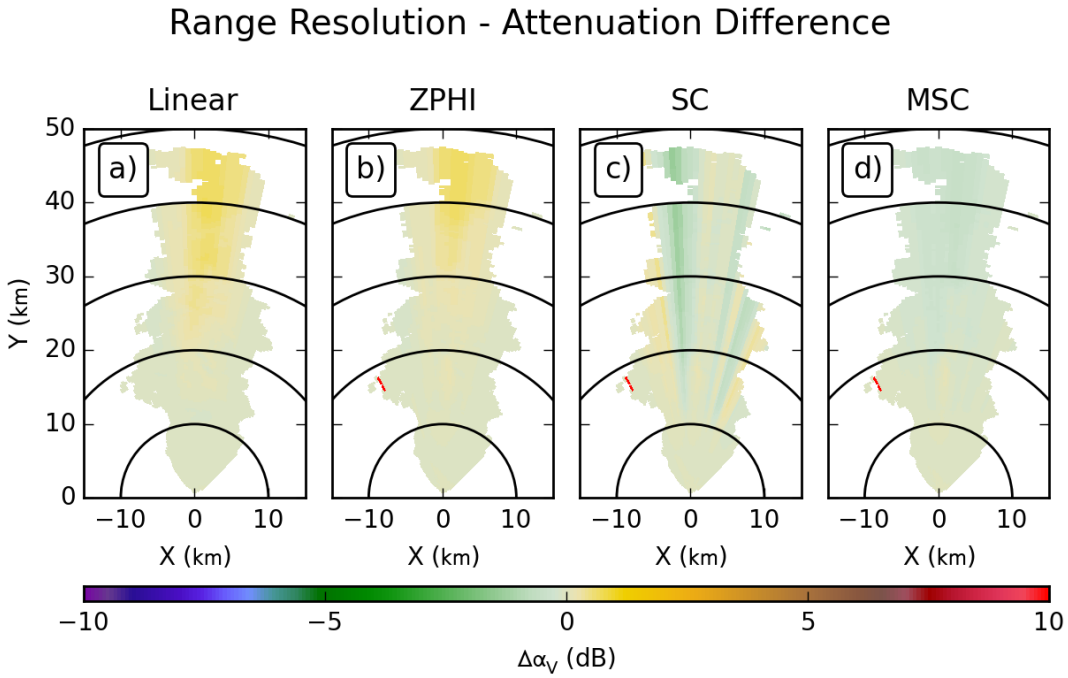

Figure 5.76: As in Figure 5.74, but for vertical polarization.

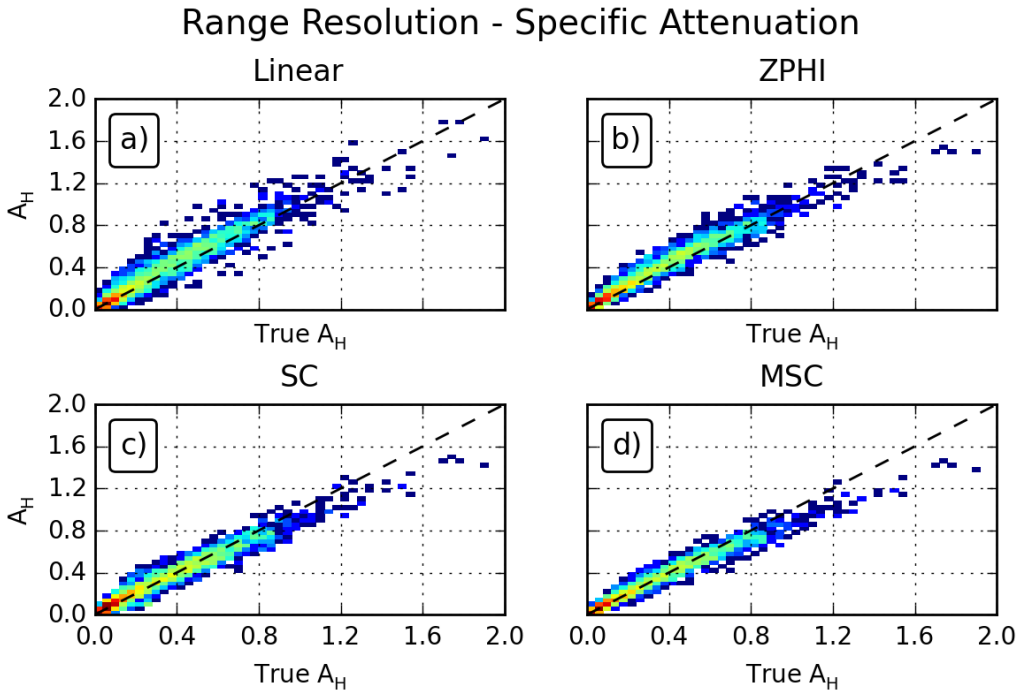

Figure 5.77: As in Figure 5.5, but for the Range Resolution experiment.

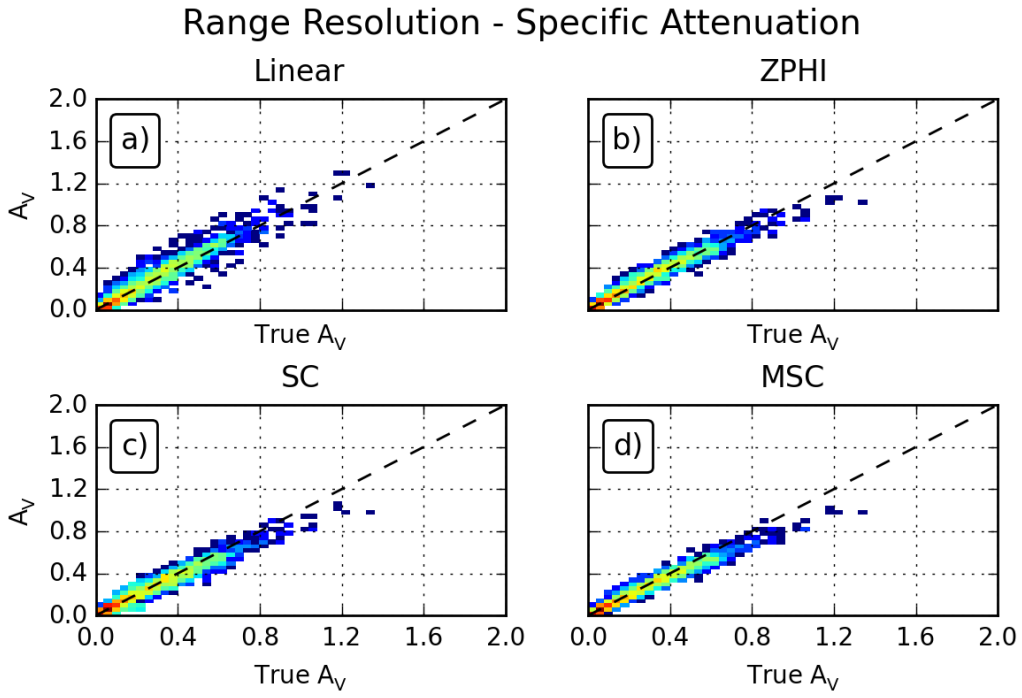

Figure 5.78: As in Figure 5.77, but for vertical polarization.

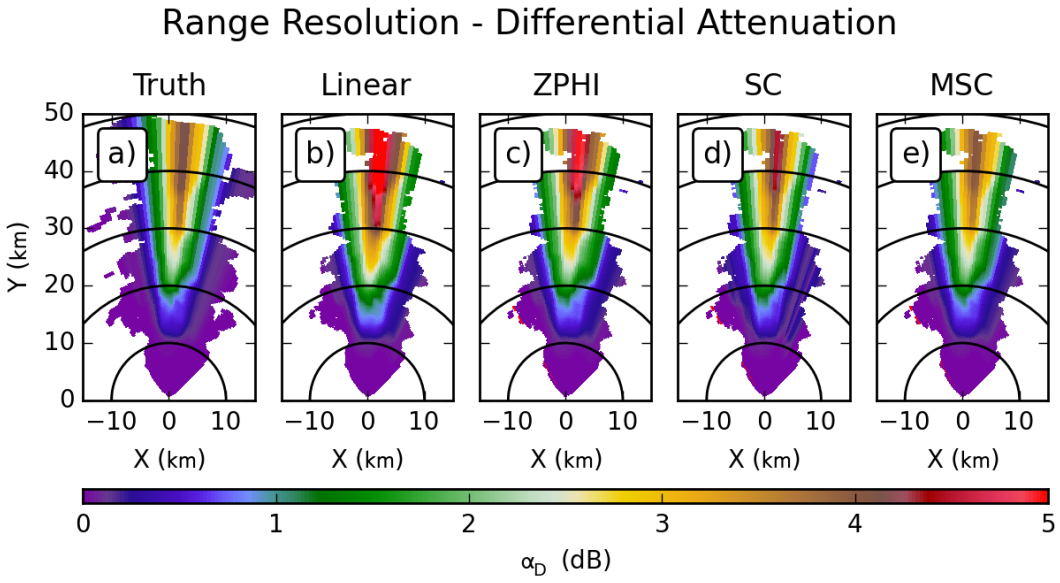

Figure 5.79: As in Figure 5.73, but for differential attenuation.

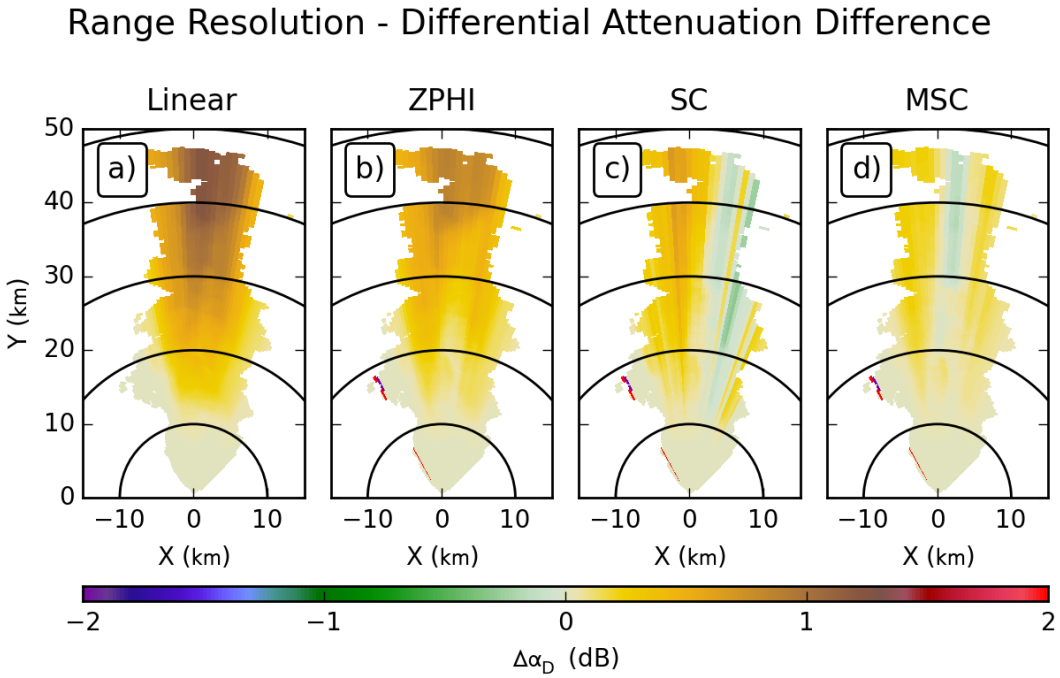

Figure 5.80: As in Figure 5.74, but for differential attenuation.

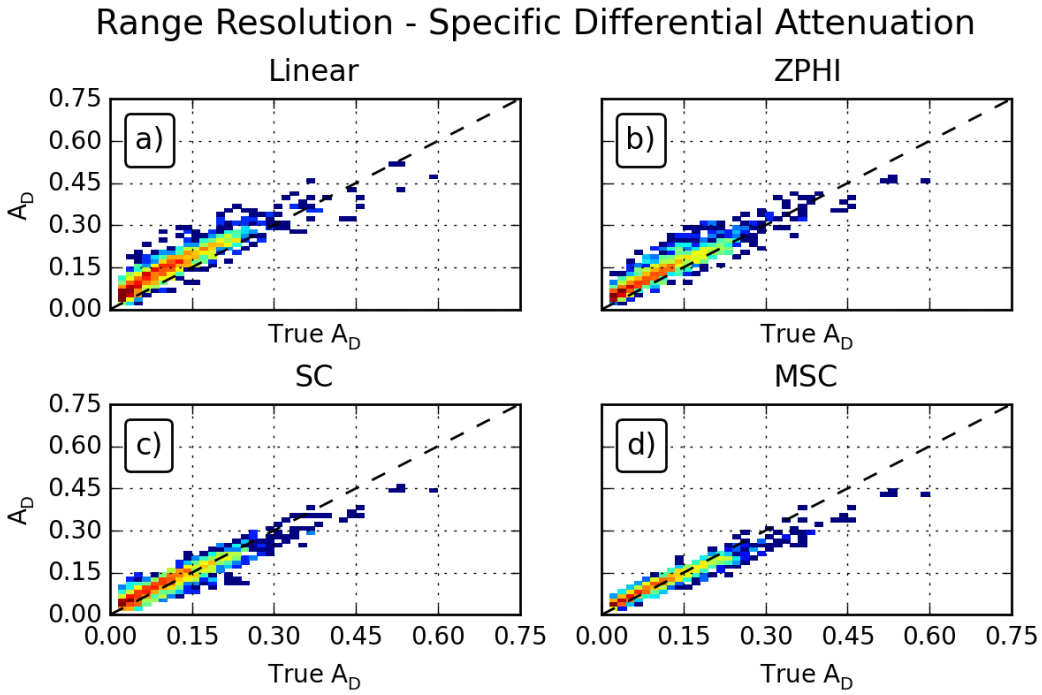

Figure 5.81: As in Figure 5.77, but for specific differential attenuation.

that the effect of this change is to reduce the negative bias in the core of the reflectivity structure from 0.5 dB to 0.25 dB. The remainder of the algorithms show no change in the structure of their errors versus the Control experiment. The histograms of specific differential attenuation, in Figure 5.81, show that the change in the results for the MSC algorithm result from a band at higher values being pulled into the main cluster rather than extending below the one-to-one line. The other algorithms show only a reduction of high values, similar to that observed for the individual polarizations.

Algorithm	Bias (dB/km)	MSE (dB^2/km^2)	r^2
Horizontal			
Linear	0.0313	0.0063	0.9356
ZPHI	0.0284	0.0038	0.9590
SC	0.0021	0.0035	0.9548
MSC	-0.0054	0.0027	0.9690
Vertical			
Linear	0.0101	0.0029	0.9368
ZPHI	0.0078	0.0014	0.9642
SC	-0.0065	0.0022	0.9467
MSC	-0.0114	0.0016	0.9677
Differential			
Linear	0.0392	0.0023	0.8609
ZPHI	0.0280	0.0015	0.8741
SC	0.0073	0.0007	0.8822
MSC	0.0034	0.0005	0.9445

Table 5.11: As in Table 4.3, but for the Range Resolution experiment.

5.5.2 X band

The horizontal attenuation results for X-band in the Range Resolution experiment, in Figure 5.82, show larger attenuation values for all of the ZPHI-based algorithms. The differences from the intrinsic values, shown in Figure 5.83, show that these increases are constrained, at least for ZPHI and SC, to the region of low-signal. The areas that are expected to be more stable show no changes versus the Control experiment. The MSC algorithm is the lone exception and shows an overall decrease in its positive bias, from 5 dB to around 3 dB. Given that this change is not reflected by the ZPHI and SC algorithms, it is a consequence of a different coefficient being obtained by the optimization process of the algorithm. The Linear algorithm exhibits the development of an area with negative bias near the radar, with values moving from near 0 dB to around 1 dB. The histograms for horizontal specific attenuation, in Figure 5.86, show no significant changes from the Control experiment, at least in regards to biases. The MSE value for the Linear algorithm (Table 5.12) do reflect a large increase over the results of the Control experiment and are likely related to the increase in errors observed earlier; none of the other algorithms exhibit this increase. All of the algorithms do reflect a shrinking of the overall range of values, a reflection of the smoothing process due to the increases in pulse width and gate size in the Range Resolution experiment.

For vertical polarization, the results are similar. The base fields of attenuation in Figure 5.84 show increases in estimated attenuation in the region of low-signal. Outside of these areas, the only significant changes to the structure of the errors shown in Figure 5.85 are for the Linear algorithm near the radar, where a small negative bias around 1 dB develops. The histograms of vertical specific attenuation in Figure 5.87

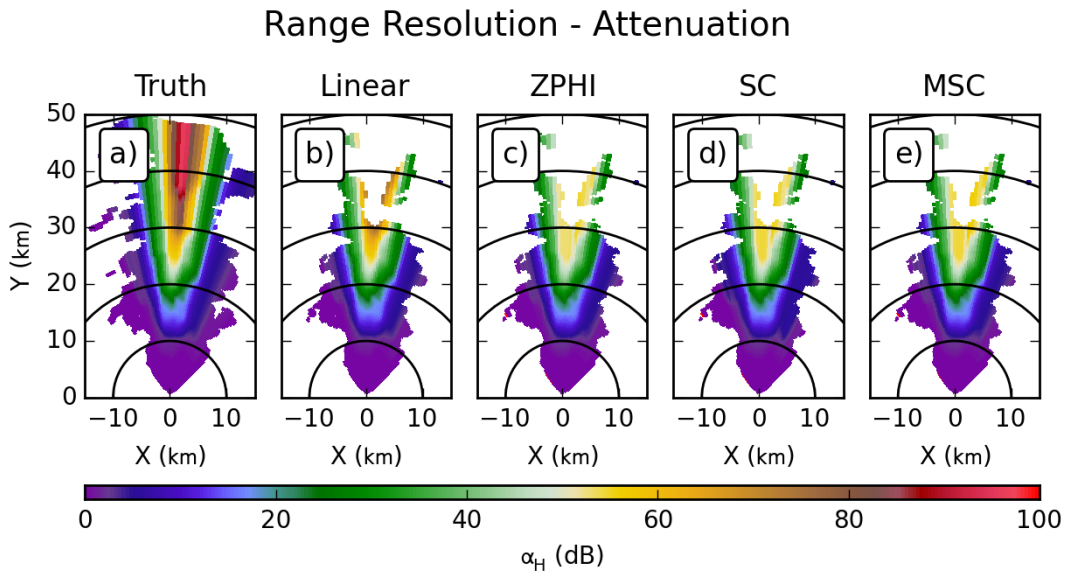

Figure 5.82: As in Figure 5.73, but for X-band.

show no significant changes other than the loss of points at higher values of specific attenuation.

For differential attenuation, the results are largely the same as at the individual polarizations. The base field of differential attenuation, in Figure 5.88, shows no significant changes in magnitude, and this is also reflected by no significant changes in the errors from intrinsic values, shown in Figure 5.89. The one exception to the lack of changes is that the modifications to the range resolution has helped improve the results for MSC around the area of low signal; this is likely just a consequence of the technique's sensitivity. The histograms of specific differential attenuation, in Figure 5.90, show some notable differences. For the ZPHI-based algorithms, the points are better clustered in the Range Resolution experiment, versus the Control experiment; the MSC algorithms points have especially lost some spread, an outcome that

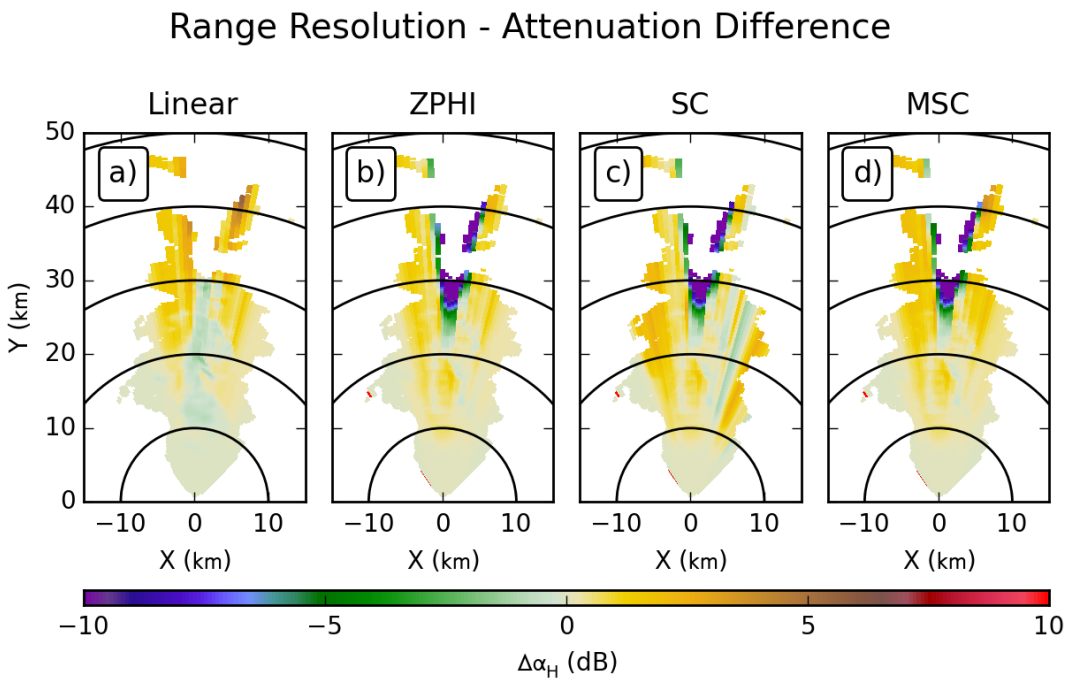

Figure 5.83: As in Figure 5.74, but for X-band.

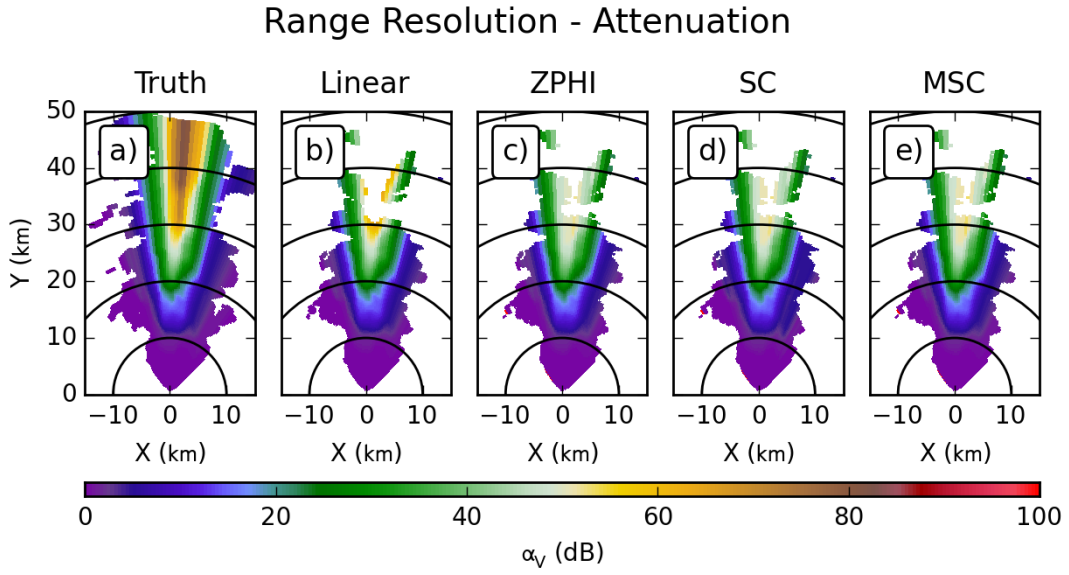

Figure 5.84: As in Figure 5.82, but for vertical polarization.

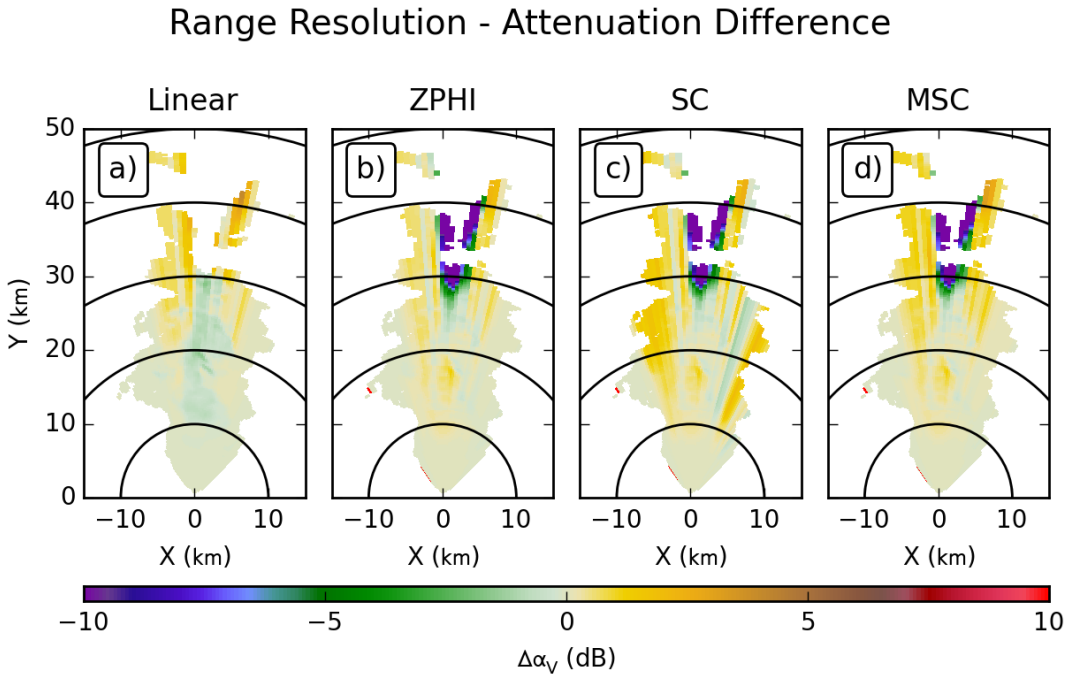

Figure 5.85: As in Figure 5.83, but for vertical polarization.

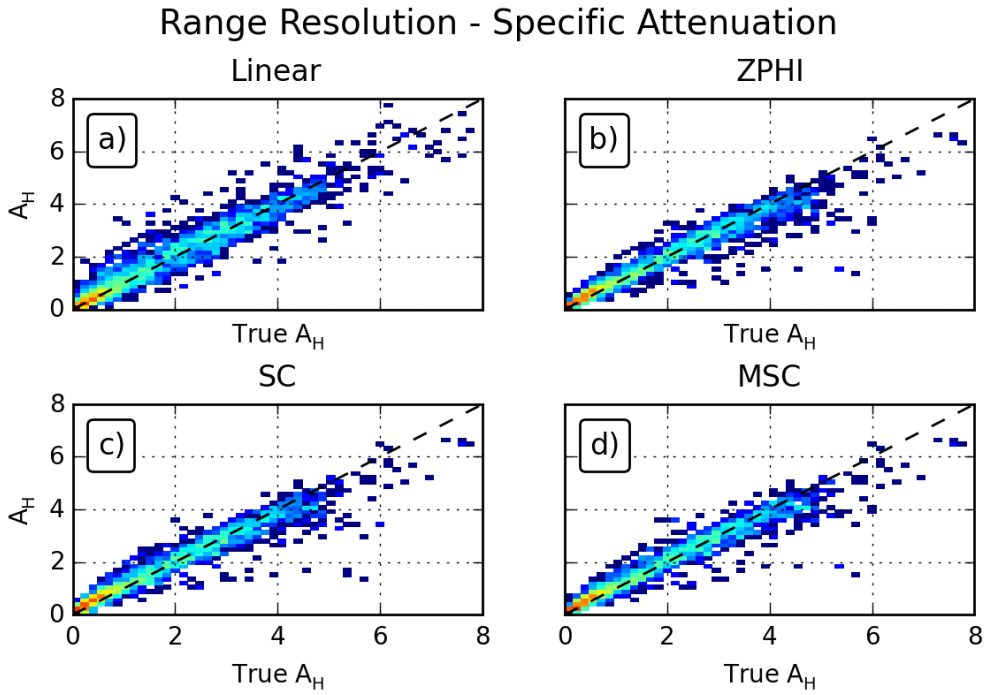

Figure 5.86: As in Figure 5.77, but for X-band.

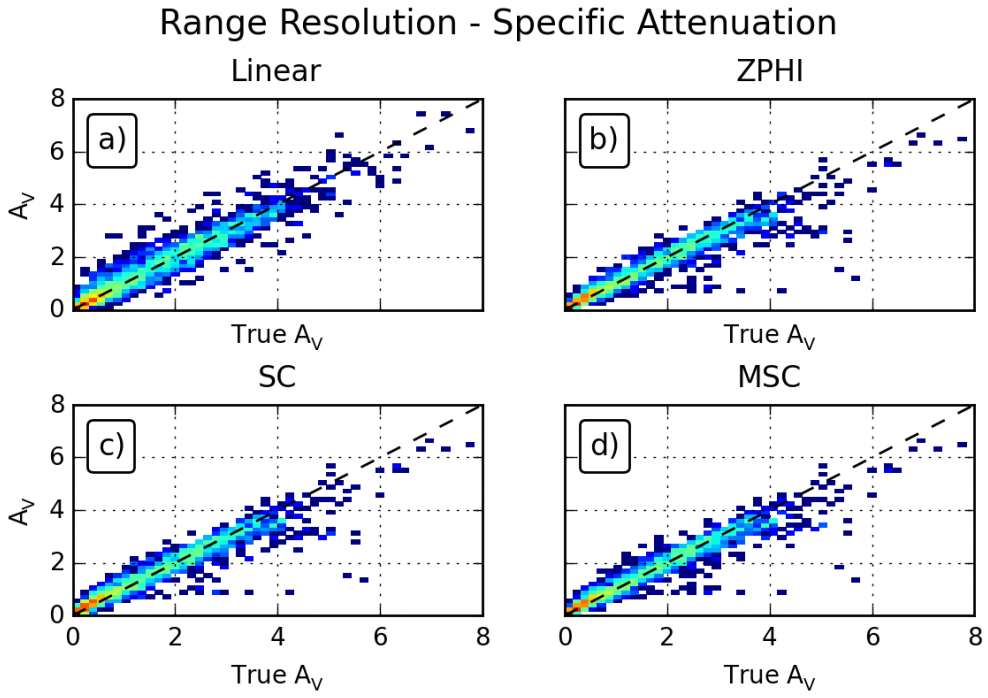

Figure 5.87: As in Figure 5.86, but for vertical polarization.

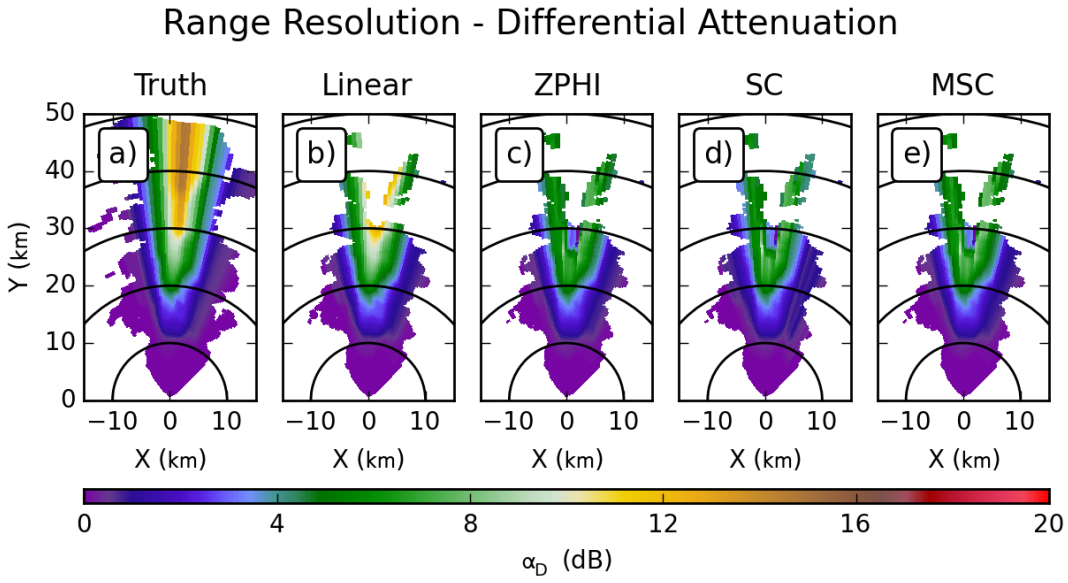

Figure 5.88: As in Figure 5.82, but for differential attenuation.

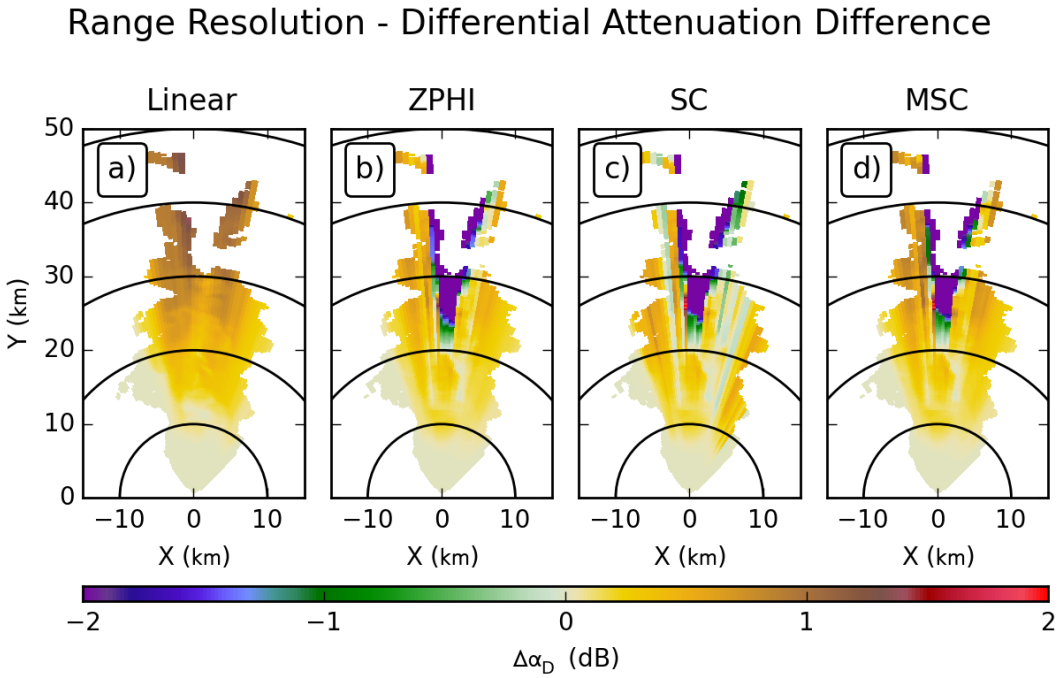

Figure 5.89: As in Figure 5.65, but for differential attenuation.

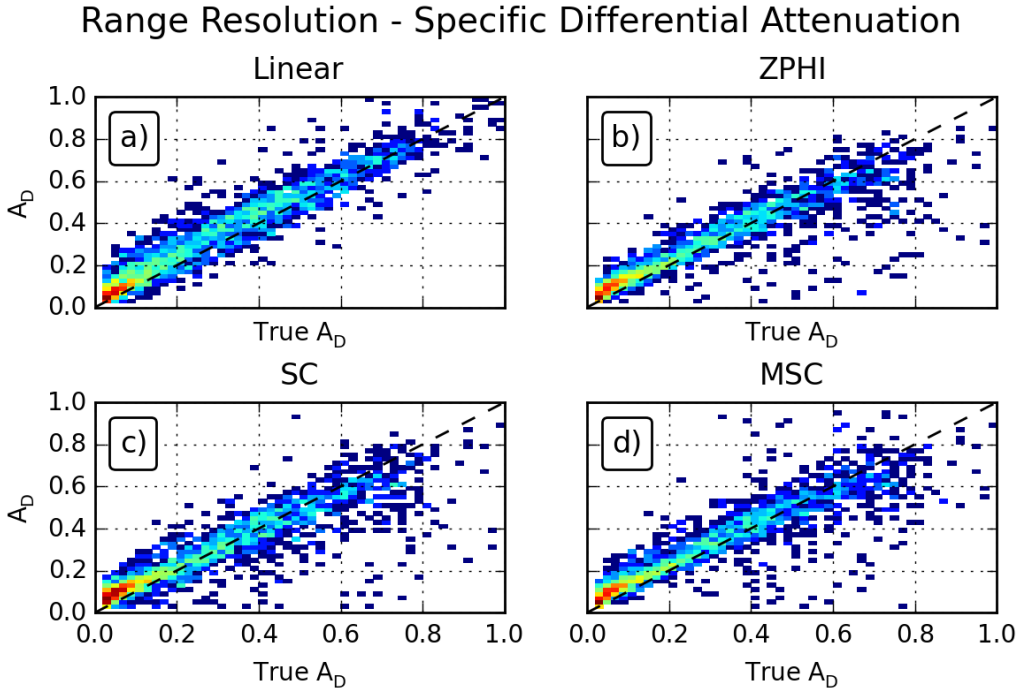

Figure 5.90: As in Figure 5.86, but for specific differential attenuation.

drives the observed improvement to the previously anomalous results. The Linear algorithm shows a greater spread in points.

5.6 Combined

The Combined experiment is separate from the others, as it does not involve exploring sampling directly. Instead, this experiment, like in the previous modeling study, looks at the impact of the violation of assumptions made about scattering. Here the radar simulation is performed with the baseline sampling parameters (1.0° beamwidth and radial spacing, 125 m gate spacing) so that sampling effects are also included. For the violated assumptions, this case is designed to be reasonable and representative, so only the shape model and temperature assumptions are violated; this uses the Pruppacher and Beard (1970) shape model (as opposed to Brandes et al. (2002)) and the model simulation temperatures (approximately 295 K as opposed to 283 K). These aspects are chosen because they are both important and challenging to address (from the standpoint of natural variability) when obtaining coefficients for the algorithms. Overall, this experiment is designed to reflect a real-world set of sampling intervals along with a reasonable set of modeling errors.

Algorithm	Bias (dB/km)	MSE (dB^2/km^2)	r^2
Horizontal			
Linear	0.0507	0.1286	0.9425
ZPHI	-0.0048	0.1114	0.9504
SC	0.0258	0.1136	0.9500
MSC	0.0264	0.0966	0.9560
Vertical			
Linear	0.0237	0.0900	0.9424
ZPHI	-0.0190	0.0859	0.9455
SC	0.0114	0.0869	0.9448
MSC	0.0037	0.0751	0.9513
Differential			
Linear	0.0378	0.0056	0.9295
ZPHI	0.0085	0.0092	0.8442
SC	0.0051	0.0105	0.8192
MSC	0.0187	0.0099	0.8321

Table 5.12: As in Table 4.4, but for the Range Resolution experiment.

5.6.1 C band

The base attenuation fields for the Combined experiment at C-band are presented in Figures 5.91 and Figure 5.93, for horizontal and vertical polarizations, respectively; these PPIs show the impact of the modifications to the scattering model. The intrinsic attenuation has decreased for both polarizations, and this decrease is matched fairly well by the SC and MSC algorithms. The Linear and ZPHI algorithms, however, show a significant increase between the Control and Combined experiments. With the intrinsic values subtracted, the PPIs in Figures 5.92 and 5.94 show that this change greatly increases the biases for the Linear and ZPHI algorithms, though Linear has a larger area of peak errors. At horizontal polarization, this changes the errors from around $2\,$dB to $10\,$dB; for vertical the change is slightly smaller, from $1\,$dB to almost $8\,$dB. Conversely, the SC and MSC algorithms only exhibit minors changes in the structure of their errors between the experiments. The histograms of specific attenuation for horizontal, Figure 5.95, and for vertical, Figure 5.96, polarizations show very large upward shifts in the points for both the Linear and ZPHI algorithms, causing the positive bias. These correspond to greater than an order of magnitude increase in the computed values of bias and MSE (Table 5.13). An additional problem for the ZPHI algorithm is that the distribution of points changes from being tightly clustered around the one-to-one line to being very spread out; this poor fit represents a very poor match of ZPHI's internal scattering model to the data. The points from the SC and MSC algorithms, conversely, show no significant shifts between the Control and Combined experiments. While the computed bias values increase a little, the MSE values stay the same; more importantly, the bias values for SC and MSC are an order of magnitude smaller than those of the Linear and ZPHI algorithms (Table 5.13). This is evidence

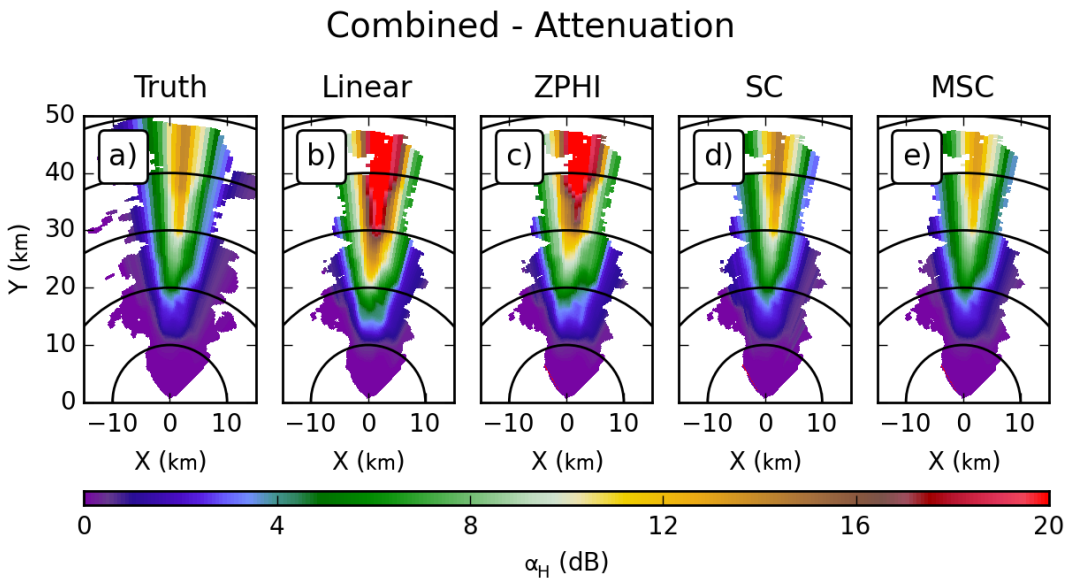

Figure 5.91: As in Figure 5.1, but for the Combined experiment.

that the optimization of a single coefficient is sufficient to correct the problems observed by ZPHI.

For differential attenuation, the PPIs in Figure 5.97 show that the Linear and ZPHI algorithms have the most trouble with the changes between the Control and Combined experiments. The differences from the intrinsic values, in Figure 5.98, show that for these two algorithms, their positive biases have increased from around 1 dB to well over 2 dB. As in the individual polarizations, the histograms of the points, in Figure 5.99, show that the Linear and ZPHI algorithms experience large shifts in the points between the Control and Combined experiments. The SC and MSC algorithms experience no such shift.

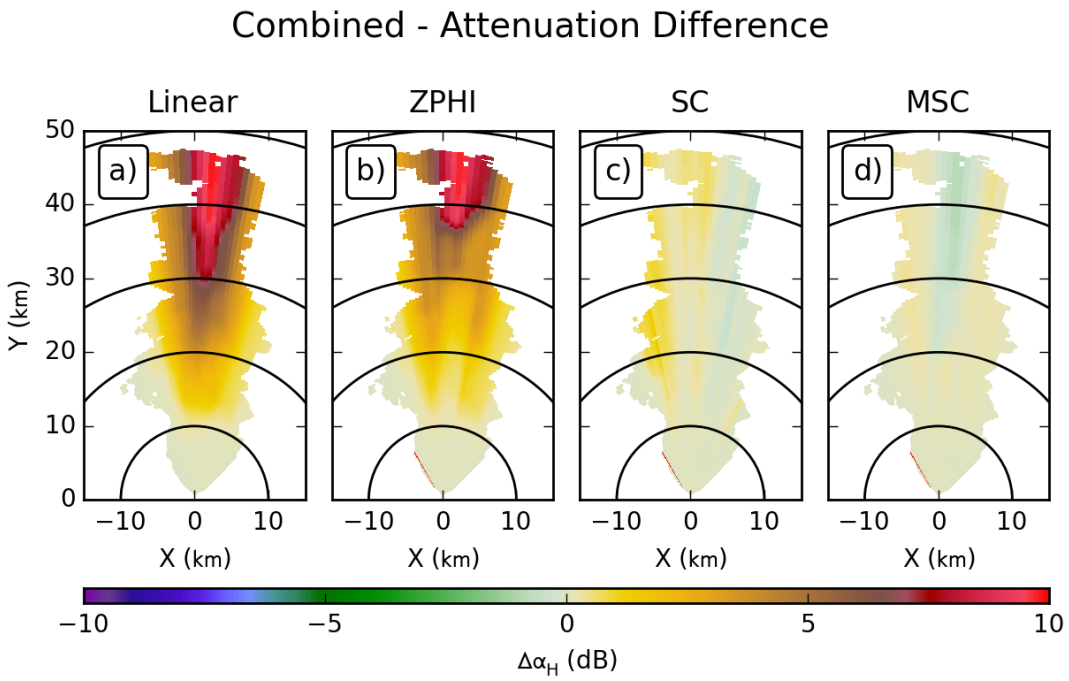

Figure 5.92: As in Figure 5.2, but for the Combined experiment.

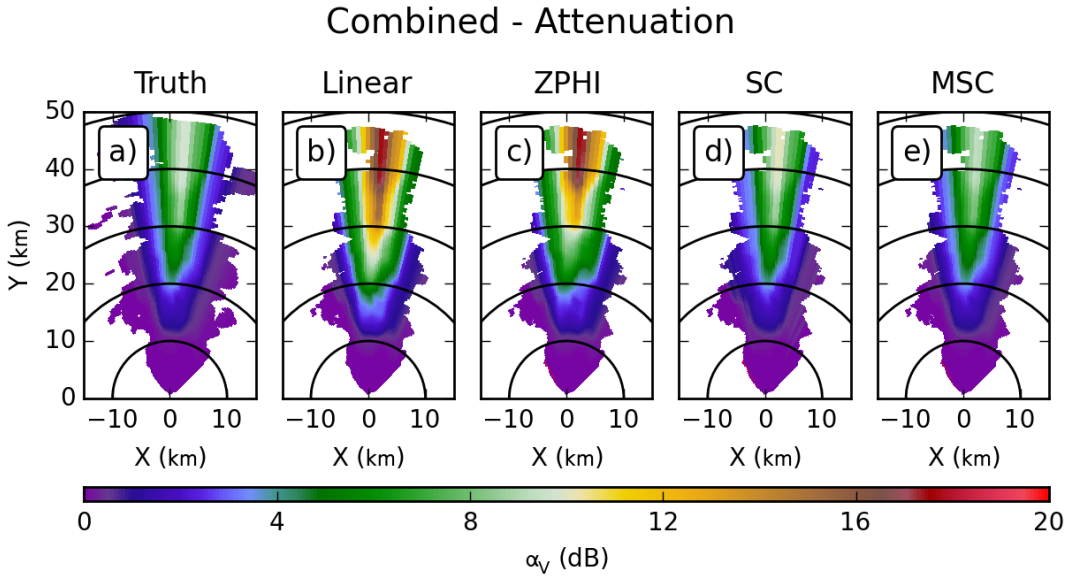

Figure 5.93: As in Figure 5.91, but for vertical polarization.

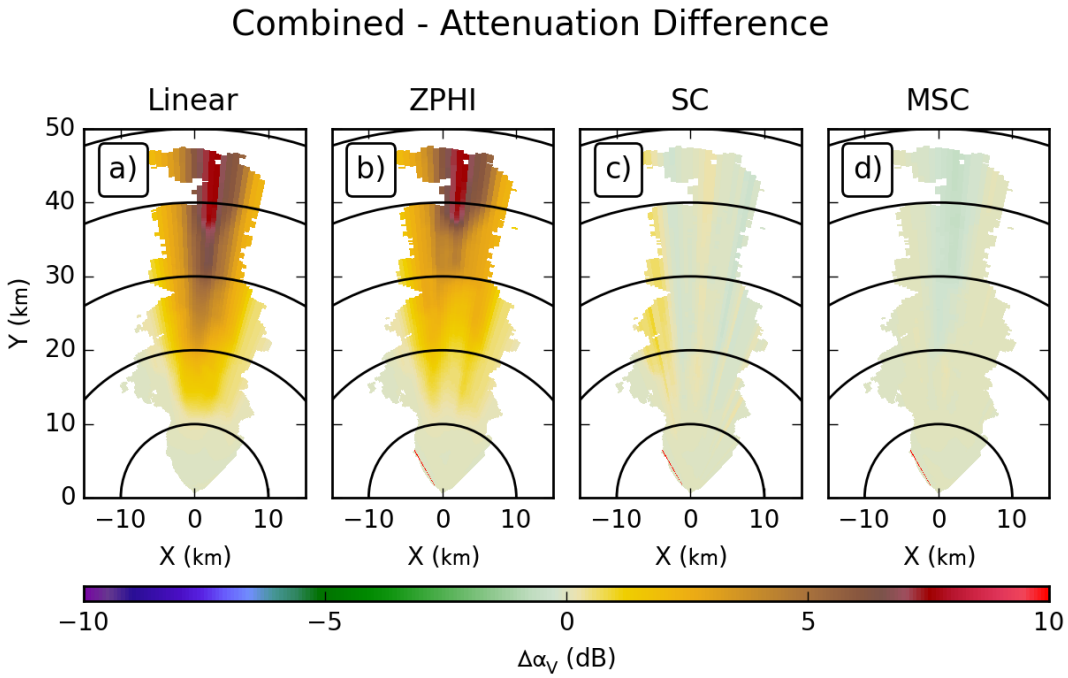

Figure 5.94: As in Figure 5.92, but for vertical polarization.

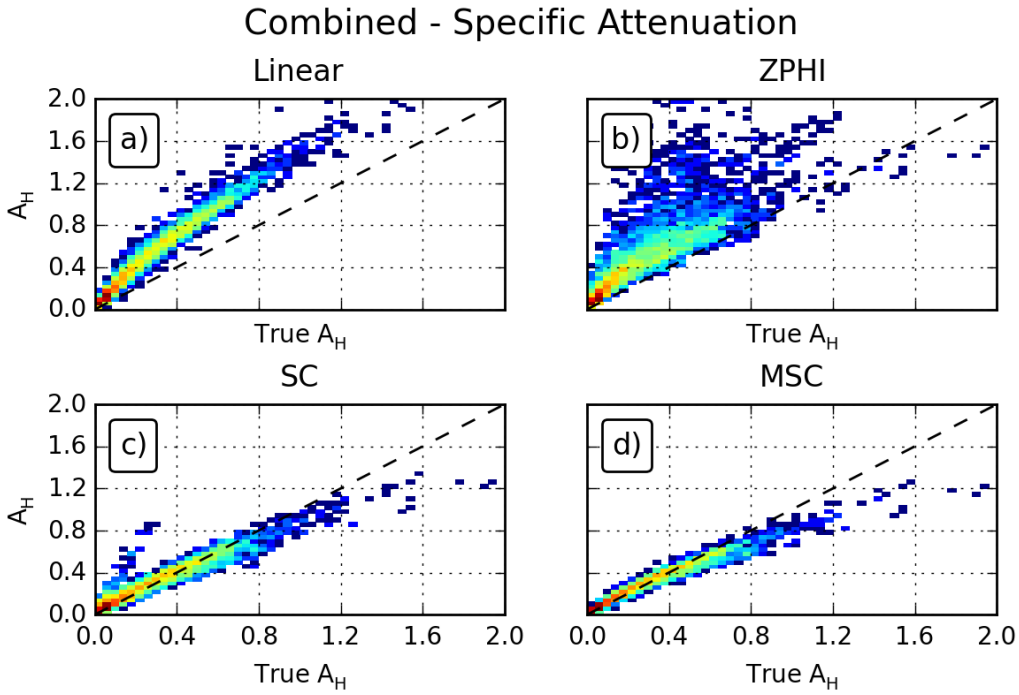

Figure 5.95: As in Figure 5.5, but for the Combined experiment.

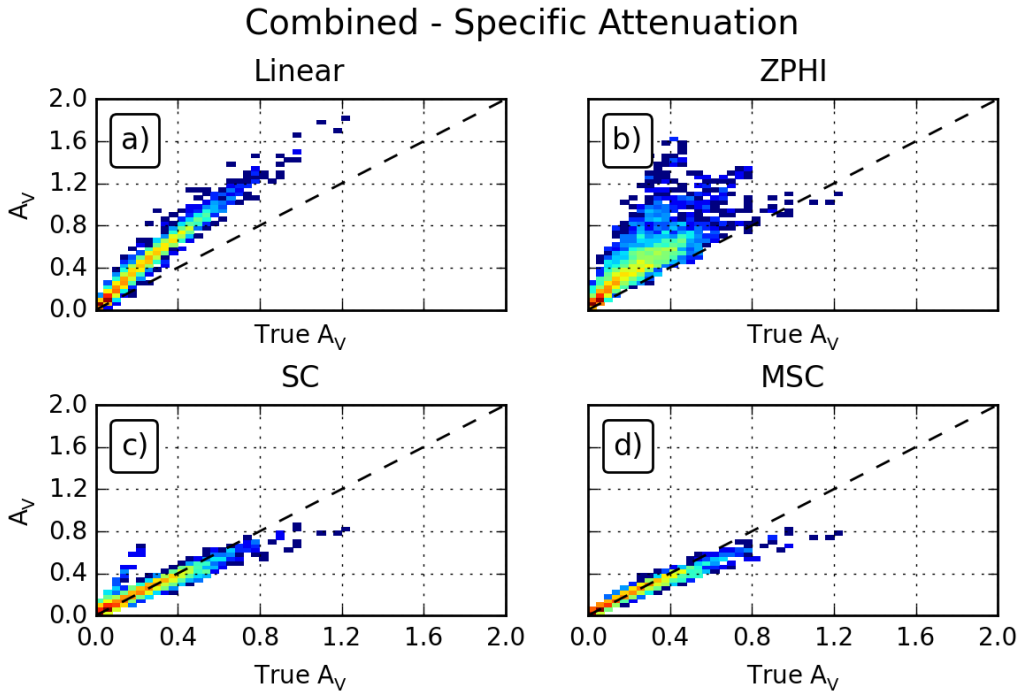

Figure 5.96: As in Figure 5.95, but for vertical polarization.

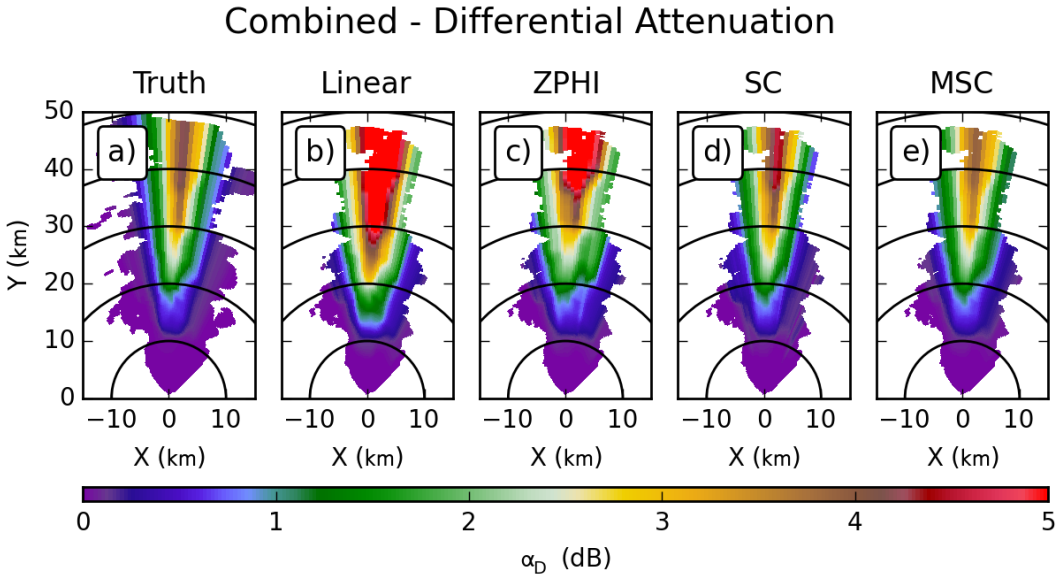

Figure 5.97: As in Figure 4.94, but for differential attenuation.

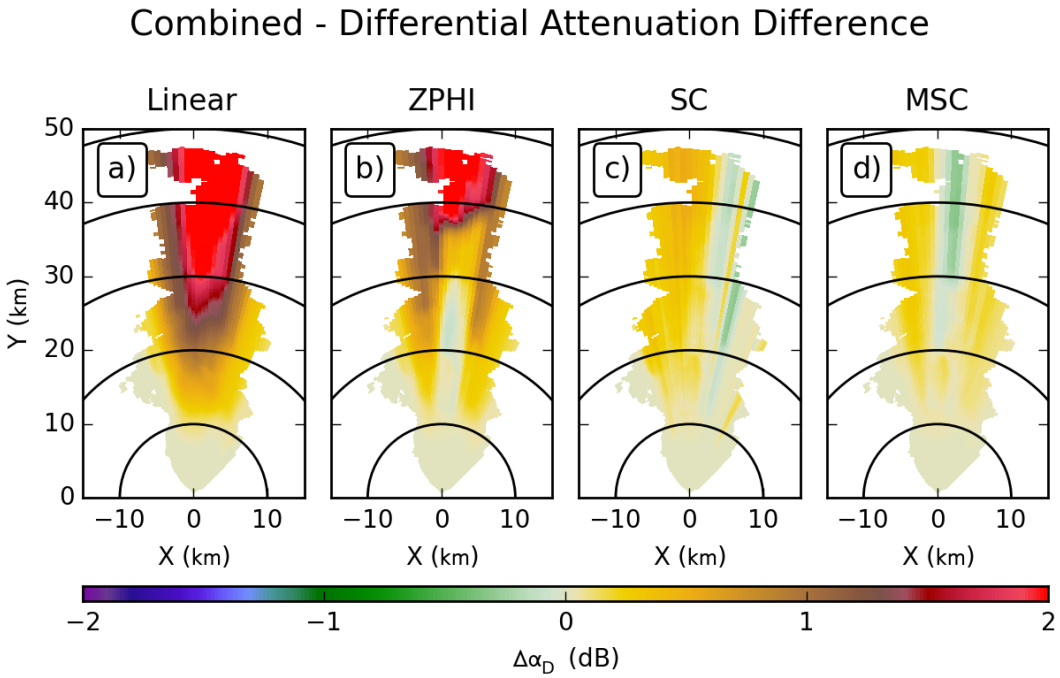

Figure 5.98: As in Figure 5.92, but for differential attenuation.

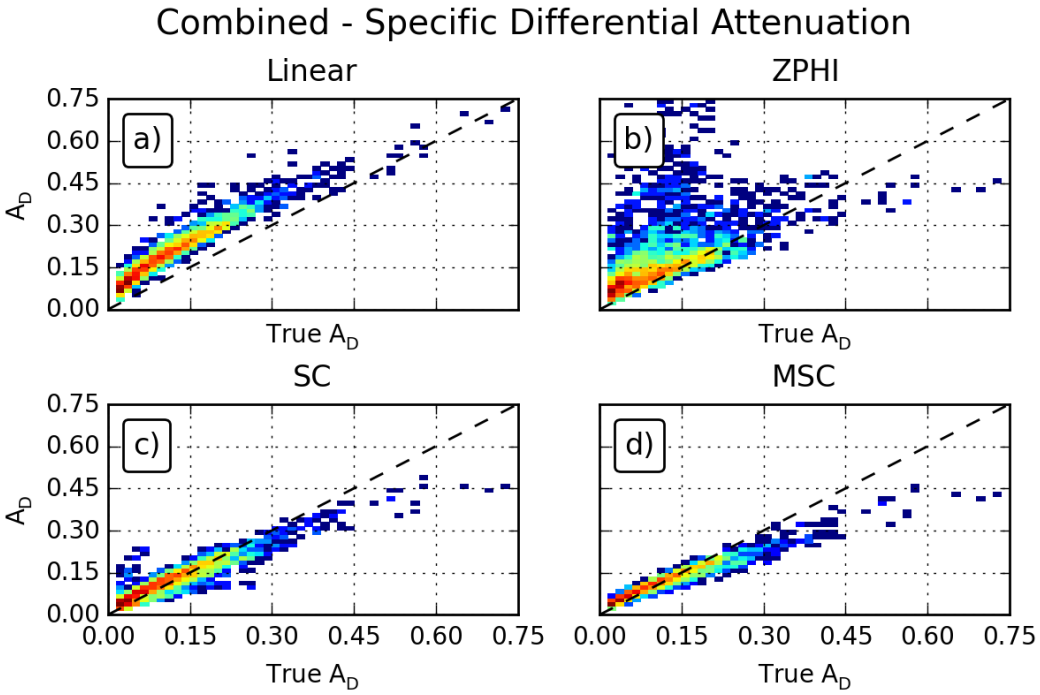

Figure 5.99: As in Figure 5.95, but for specific differential attenuation.

Algorithm	Bias (dB/km)	MSE (dB^2/km^2)	r^2
Horizontal			
Linear	0.1911	0.0564	0.9661
ZPHI	0.1877	0.0823	0.7022
SC	0.0172	0.0043	0.9294
MSC	0.0035	0.0028	0.9629
Vertical			
Linear	0.1445	0.0339	0.9759
ZPHI	0.1419	0.0416	0.7687
SC	0.0079	0.0019	0.9240
MSC	-0.0028	0.0012	0.9644
Differential			
Linear	0.0843	0.0079	0.9179
ZPHI	0.0653	0.0141	0.2917
SC	0.0062	0.0009	0.8761
MSC	0.0022	0.0007	0.9411

Table 5.13: As in Table 4.3, but for the Combined experiment.

5.6.2 X band

At X-band, the PPIs of horizontal and vertical attenuation, in Figures 5.100 and 5.102, show that the effect of the Combined experiment is to increase the intrinsic attenuation. Unlike C-band, the SC and MSC algorithms appear to decrease, while the Linear and ZPHI algorithms increase. The differences from intrinsic values, in Figures 5.101 and 5.103, show that the net result is to increase errors across the board. The SC and MSC algorithms have smaller changes, increases on the order of 1 dB. For the Linear and ZPHI algorithms, this change is from 1 dB to well-over 10 dB at both polarizations. This is reflected in the histograms of specific attenuation, shown in Figures 5.104 and 5.105, which show large shifts for both the Linear and ZPHI algorithms. The Linear algorithm exhibits a shift of its entire band of points above the one-to-one ratio line, which results in the extremely large positive bias, approaching 0.5 dB/km (Table 5.14). The effect on ZPHI is slightly smaller, in that the shift only occurs for smaller attenuation values; the larger values still lie along the one-to-one line. This still results in much larger computed values for bias and MSE, with the bias approaching 0.4 dB/km. For ZPHI, the spread of points also changes, from having a few outliers below the one-to-one line, to having many more outliers, almost all of which are above that line.

For differential attenuation, the PPIs in Figure 5.106 show increases across the board, both for the intrinsic values and the algorithms. The differences from the intrinsic values, in Figure 5.107, show that Linear and ZPHI have the largest increases in errors, as was the case for the individual polarizations. The Linear algorithm's positive bias increases from approximately 1 dB to over 2 dB. The ZPHI algorithm, outside of the low-signal region, has its positive bias increase from around 0.5 dB to over 1 dB. Conversely, the SC algorithm exhibits no significant changes in errors between the

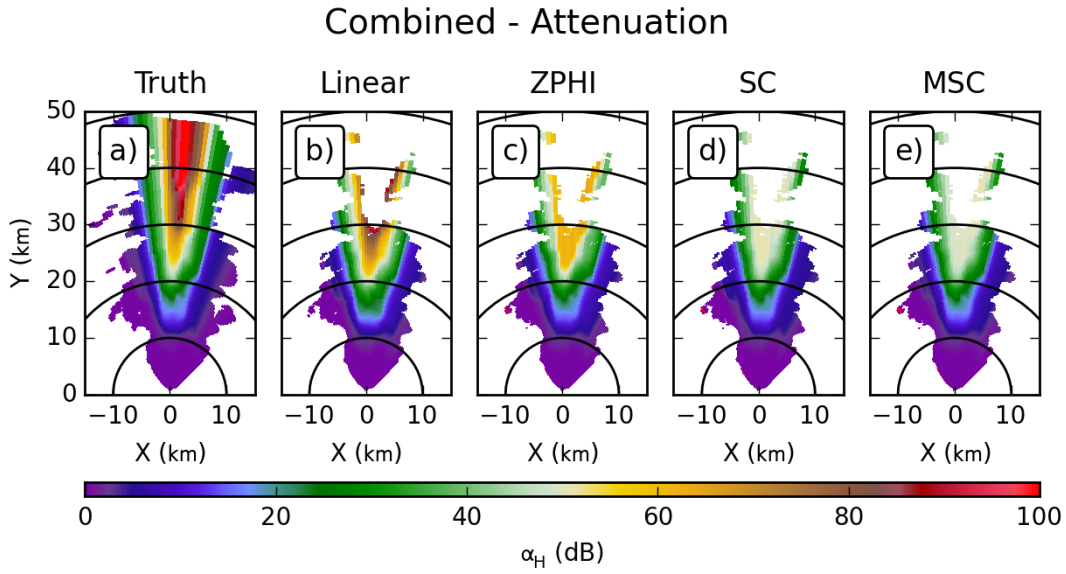

Figure 5.100: As in Figure 5.91, but for X-band.

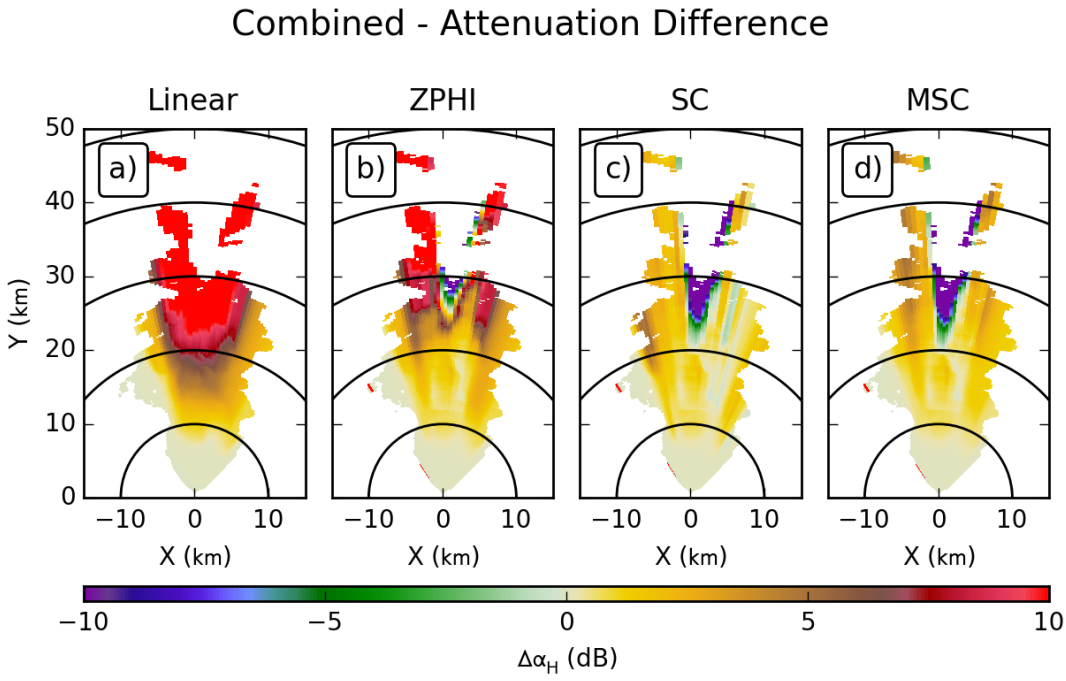

Figure 5.101: As in Figure 5.92, but for X-band.

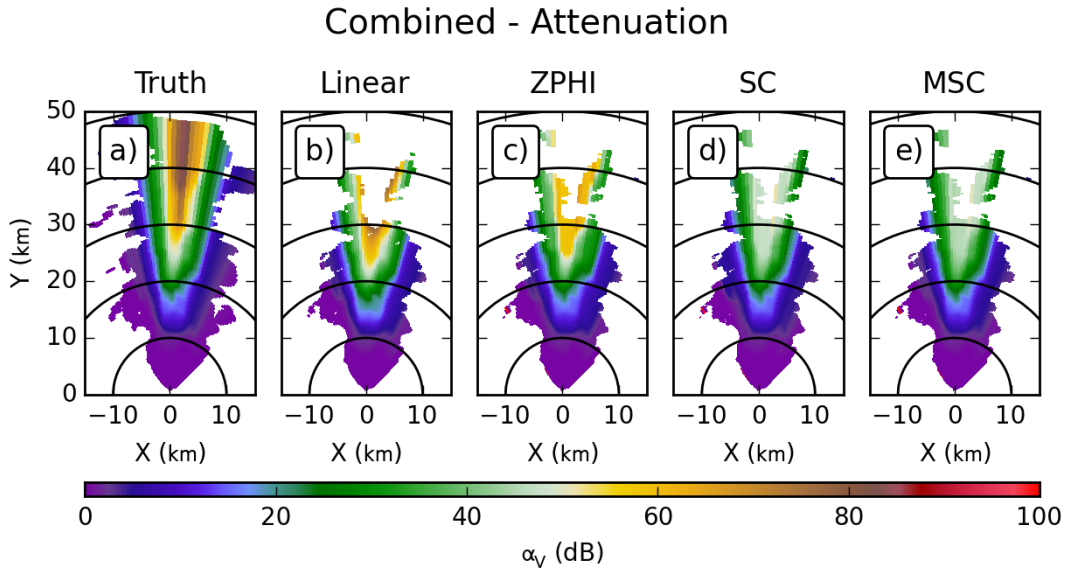

Figure 5.102: As in Figure 5.100, but for vertical polarization.

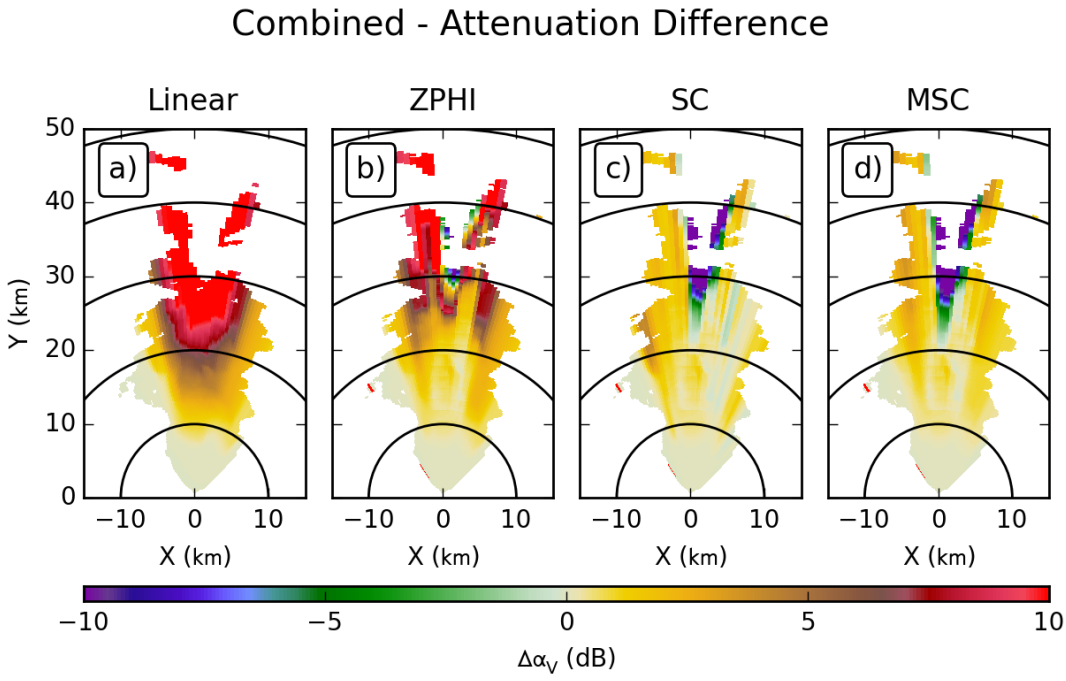

Figure 5.103: As in Figure 5.101, but for vertical polarization.

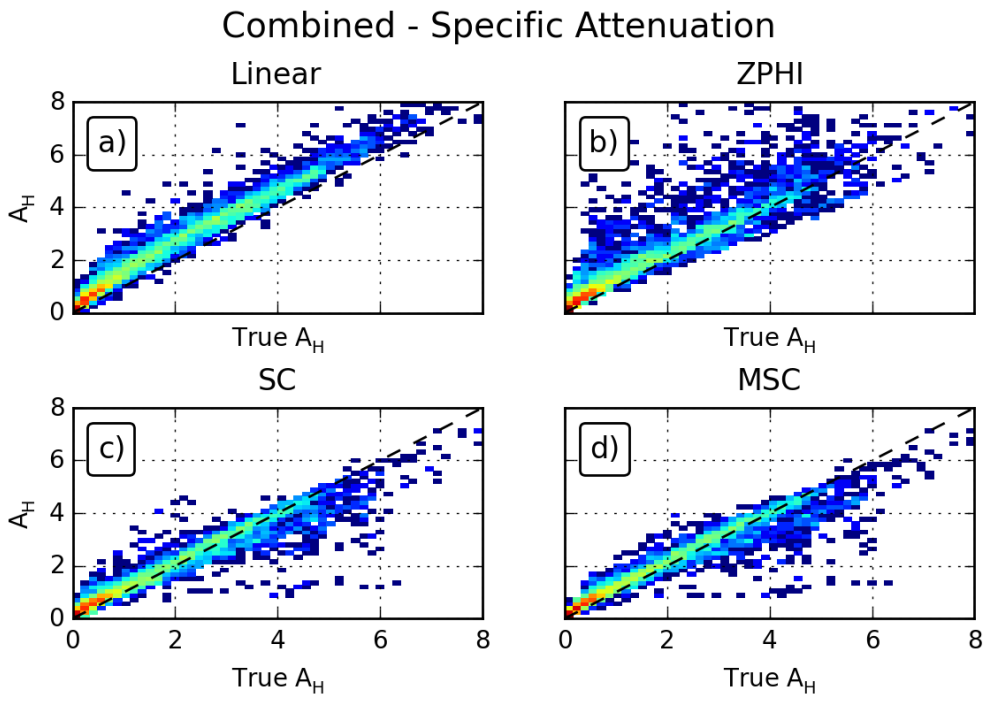

Figure 5.104: As in Figure 5.95, but for X-band.

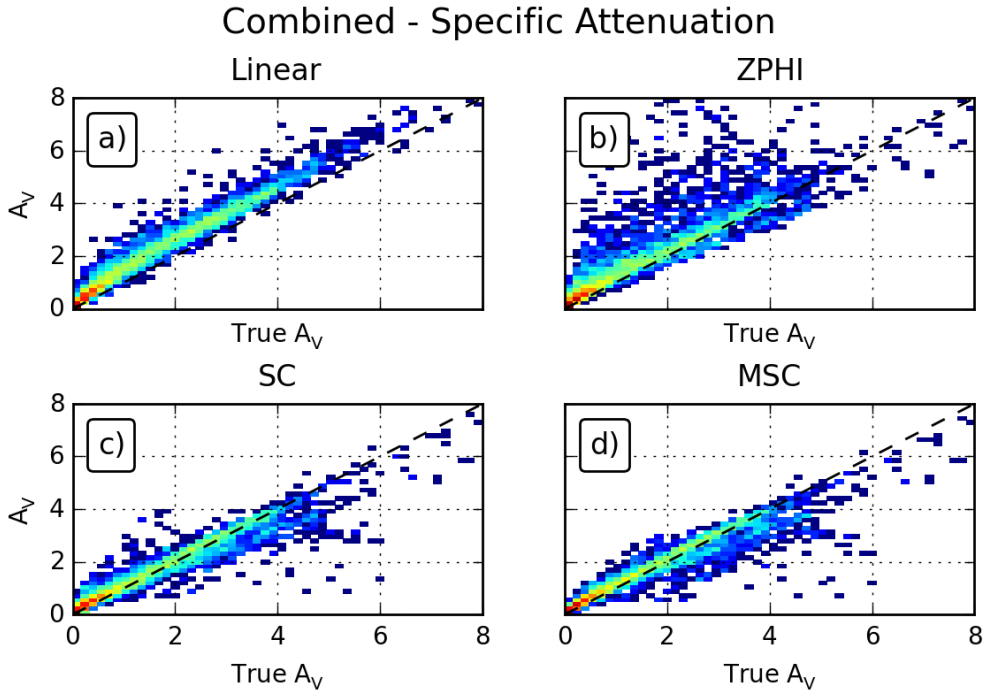

Figure 5.105: As in Figure 5.104, but for vertical polarization.

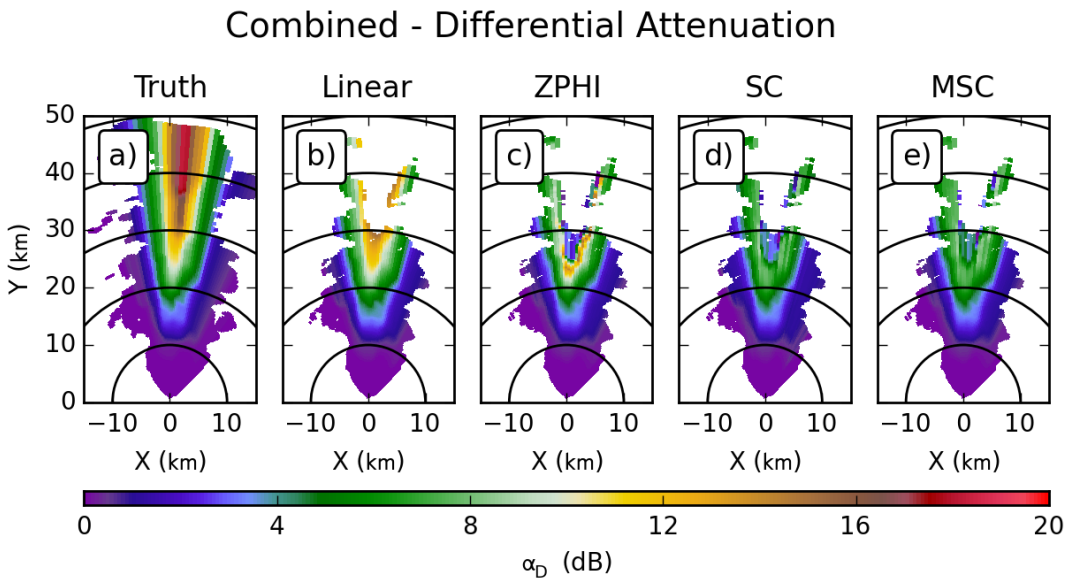

Figure 5.106: As in Figure 5.100, but for differential attenuation.

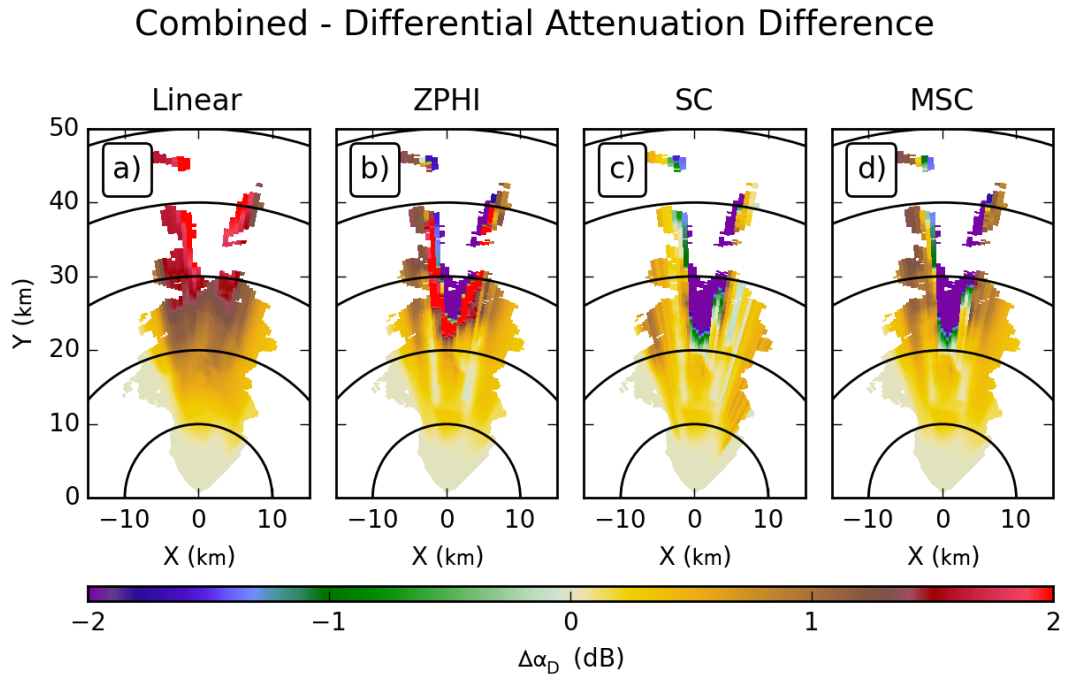

Figure 5.107: As in Figure 5.101, but for differential attenuation.

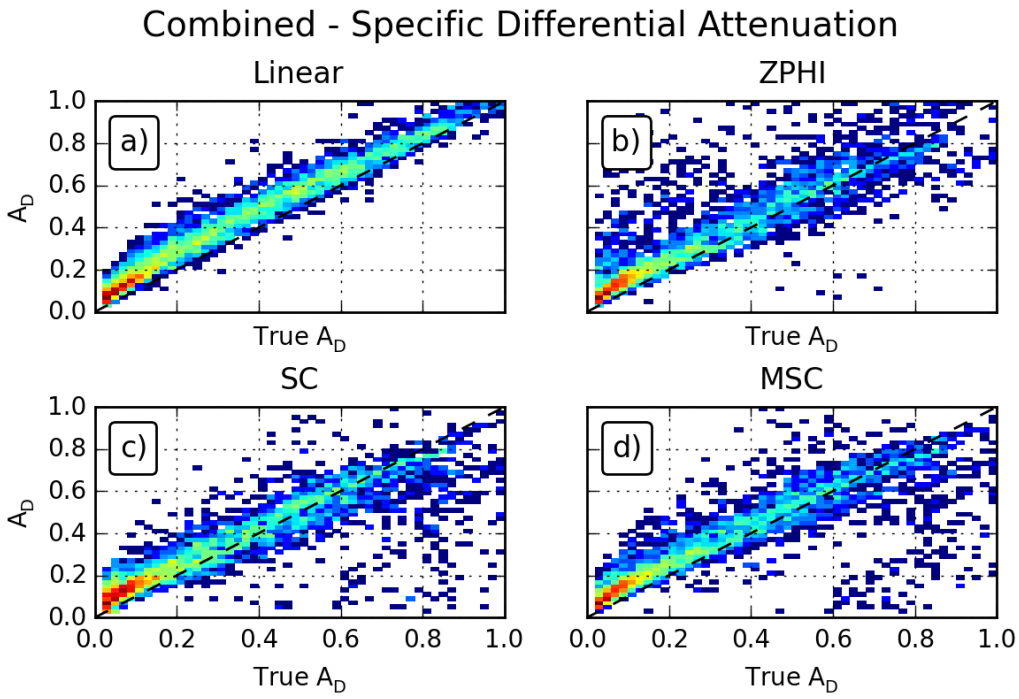

Figure 5.108: As in Figure 5.104, but for specific differential attenuation.

Control and Combined experiments, while the MSC algorithm reduces its errors, as some of its anomalously bad results are corrected. These changes are reflected by the histograms of specific attenuation, in Figure 5.108, which show a large shift for the results of the Linear algorithm above the one-to-one ratio line. The ZPHI algorithm shows an increase in the spread of its points, with the spread being biased above the one-to-one line.

Algorithm	Bias (dB/km)	MSE (dB^2/km^2)	r^2
Horizontal			
Linear	0.4650	0.3601	0.9675
ZPHI	0.3973	0.7653	0.8163
SC	0.0551	0.1962	0.9300
MSC	0.0690	0.1902	0.9322
Vertical			
Linear	0.4151	0.2852	0.9677
ZPHI	0.3743	0.8375	0.7451
SC	0.0455	0.1177	0.9376
MSC	0.0374	0.1245	0.9343
Differential			
Linear	0.0705	0.0076	0.9709
ZPHI	0.1441	0.2471	0.3742
SC	0.0129	0.0170	0.8062
MSC	0.0252	0.0195	0.7740

Table 5.14: As in Table 4.4, but for the Combined experiment.

5.7 Conclusion

This chapter examined the effects of running several different attenuation correction algorithms, Linear, ZPHI, Self-Consistent, and Modified Self-Consistent on radar data with different spatial sampling characteristics. These configurations explored azimuthal effects, including sidelobes, mainlobe beamwidth, and radial spacing, as well as the range resolution effect of changing pulse width and gate spacing. Remarkably, the algorithms overall showed very little sensitivity to these changes. The initial Control experiment, which started with matched beamwidth and radial spacing of 1.0° showed no significant differences from the modeling study. The lack of sensitivity to sampling continued through the remainder of the experiments that only tested aspects of spatial sampling.

One effect revealed by this study is that the Modified Self-Consistent algorithm can be sensitive to the data. By virtue of its single optimized value, any spuriously obtained coefficient can bias all of the results. The method of choosing the median value originally was chosen to try to smooth the results from the Self-Consistent algorithm in a way that is less sensitive to outliers. However, these results reveal that when few radials of data are available, as occurred when moving from the 0.25° spacing of the modeling study to the 1.0° (or even 2.0°) used here, the ranking of coefficients can be sensitive to bad radials, degrading algorithm performance. When the algorithm performs well, the results are indeed azimuthally more smooth and more robust than Self-Consistent itself; this lends credence to the concept of smoothing coefficients from the Self-Consistent algorithm. However, the choice of median is not sufficiently robust for operational applications.

The Combined experiment, which used both a 1.0° spacing as well as violating the assumed temperature and drop shape model, demonstrates the sensitivity of the fixed-coefficient algorithms (Linear and ZPHI) to the validity of the assumed scattering model for standard resolution data (lower than that of the modeling study); these methods had up to 10 dB of errors with the multiple violated assumptions. This highlights the need to use more sophisticated methods, like Self-Consistent, that can automatically tune coefficients to yield the best results for the data at hand. In the results shown here, these algorithms (SC and MSC) resulted in an order of magnitude less bias in estimates of specific attenuation at the individual polarizations.

Chapter 6

Conclusion

This work examines the practical aspects of performing correction for rain-induced attenuation in dual-polarization radar data. Given the large biases in reflectivity data that are caused by attenuation at C- and X-band, correction for this effect is important for many radar applications, including QPE.

6.1 Simulator

This study of attenuation is conducted through the use of simulated radar data. The simulation procedure builds on the work of May et al. (2007), and extends it to produce dual-polarization time series data. The dual-polarization aspect of the simulation is accomplished by the inclusion of full T-matrix based scattering calculations (Mishchenko 1993), as well as supporting the use of the output from two-moment model microphysics schemes (Ziegler 1985). These calculations form the foundation for calculating radar intrinsic variables, like reflectivity factor, specific attenuation, and specific differential phase shift. By feeding these starting variables into the path integration procedure of May et al. (2007), the path-integrated attenuation and differential phase are properly simulated, including differential effects across the radar antenna. The time-series simulation is based upon a combination of the work of Muschinski

et al. (1999) and Galati (1995); together, these form the basis of using the radar scattering parameters to generate stochastic time series data. This stochastic data allows the simulation to accurately capture the errors in the radar data due to both intrinsic variability and the procedure of moment estimation; this ensures that errors identified using simulated data represent those experienced by real-world radar systems.

The use of simulated data is vital to this study. Previous studies of the accuracy of radar attenuation algorithms, such as Carey et al. (2000) and Gorgucci et al. (1998), rely upon indirect comparisons, either to rain gauge data (to examine changes to biases in QPE) or to data from a separate, non-attenuated, radar system. The benefit of using simulated data is that the true, non-attenuated reflectivity fields are known and can serve as a direct truth field in any analysis.

6.2 Algorithms

The attenuation correction techniques examined consist of two broad families: Linear (Bringi et al. 1990) and ZPHI (Testud et al. 2000). The ZPHI family, in addition to the ZPHI algorithm itself, also includes the Self-Consistent algorithm (Bringi et al. 2001). This work also tests a proposed Modified Self- Consistent technique, which attempts to address shortcomings in the robustness of the standard Self-Consistent algorithm.

All of the aforementioned techniques require empirically determined coefficients that represent the relations between radar observables and attenuation. To maximize the potential algorithm performance and because different algorithms used differing assumptions for coefficients, this work calculates its own set of "optimal" coefficients.

This ensures the coefficients accurately reflect the known assumptions used in the simulation of data, as well as reflect the drop size distribution used in the underlying numerical weather simulation.

6.3 Modeling Errors

The first study conducted examined the sensitivity of the algorithms to assumptions made in calculating the coefficients, such as wavelength, temperature, shape model, etc. The baseline of performance is established using a Control experiment, where the radar data are simulated using a set of assumptions that match those used to obtain the coefficients for the algorithms. Overall, all algorithms worked well at both C- and X-bands in the Control experiment.

In the other experiments, when these assumptions were systematically violated, the Linear and ZPHI techniques, because they rely upon fixed coefficients, yielded much higher errors than the Self-Consistent and Modified Self-Consistent algorithms, at both X- and C-band. In almost all cases these latter algorithms were able to deliver reasonable results. While the biases for individual polarizations from these algorithms could still be in the range of $1\,\mathrm{dB}$ to $2\,\mathrm{dB}$, this was much more usable than the errors for the Linear and ZPHI algorithms in most cases.

In terms of sensitivity to assumptions, changing any one of them (canting, shape model, temperature, or wavelength), yielded pronounced changes, both in terms of the resulting attenuation field and in the results of the algorithms. This implies that successful use of these techniques depends upon carefully making assumptions that match nature. For physical processes (i.e., canting and shape model), this implies the

need for good data and parameterizations of the microphysical processes involved. For something like temperature, which varies greatly, this implies a greater challenge. For fixed coefficient techniques, though, the biases introduced are significant, so making use of any temperature data available could yield significant gains in reducing the bias in reflectivity due to under- or over-correction for attenuation.

Most important of all effects was the sensitivity to wavelength within the band. Changing the wavelength by only $10\,\%$ introduced at least $5\,$dB of error in the attenuation estimates by the Linear and ZPHI algorithms; this runs counter to the common wisdom that one can use coefficients for these algorithms that are appropriate to a given band. It is possible, therefore to gain algorithm performance by simply tuning coefficients to the true operating wavelength of a given radar system. While the Self-Consistent algorithms were able to largely compensate for all of the violated assumptions, including wavelength, the best algorithm performance occurred for the Control experiment. Therefore, It is important to all algorithms to take care in making accurate assumptions; using the true wavelength of the radar, rather than some general waveband, is one of the simplest ways to eliminate errors.

6.4 Spatial Errors

The second study examined the effects of the spatial sampling characteristics of the radar data on algorithm performance. This includes azimuthal effects (sidelobes, mainlobe beamwidth, and radial spacing), as well as the range resolution effect of changing pulse width and gate spacing. Remarkably, the algorithms overall showed very little sensitivity to these changes. The initial Control experiment, which started with

matched beamwidth and radial spacing of 1.0° showed no significant differences from the modeling study. The lack of sensitivity to sampling continued through the remainder of the experiments that only tested aspects of spatial sampling.

One effect that was revealed by this study is that the Modified Self-Consistent algorithm can be sensitive to the data. By virtue of its single optimized value, any spuriously obtained coefficient can bias all of the results. While the Modified Self-Consistent technique does at times show improved, smoother results, the sensitivity is a problem to its robustness. Further work is necessary to adjust the technique and find a method that better smooths its coefficients to produce results that are consistently better than the regular Self-Consistent technique.

The spatial study also performed an experiment that combined standard spatial sampling (1.0° azimuthal spacing) with violating the assumed temperature and drop shape model. This experiment demonstrates the sensitivity of the fixed-coefficient algorithms (Linear and ZPHI) to the validity of the assumed scattering model for standard resolution data (lower than that of the modeling study); these methods had up to 10 dB of errors with the multiple violated assumptions. This highlights the need to use more sophisticated methods, like Self-Consistent, that can automatically tune coefficients to yield the best results for the data at hand; these algorithms, in the cases studied here, result in an order of magnitude less bias in estimates of specific attenuation.

Bibliography

Anagnostou, E. N., M. N. Anagnostou, W. F. Krajewski, A. Kruger, and B. J. Miriovsky, 2004: High-Resolution Rainfall Estimation from X-Band Polarimetric Radar Measurements. *Journal of Hydrometeorology*, **5 (1)**, 110–128.

Anagnostou, E. N., M. Grecu, and M. N. Anagnostou, 2006a: X-band Polarimetric Radar Rainfall Measurements in Keys Area Microphysics Project. *Journal of the Atmospheric Sciences*, **63 (1)**, 187–203.

Anagnostou, M. N., E. N. Anagnostou, and J. Vivekanandan, 2006b: Correction for Rain Path Specific and Differential Attenuation of X-Band Dual-Polarization Observations. *IEEE Transactions on Geoscience and Remote Sensing*, **44 (9)**, 2470–2480.

Atlas, D., 2002: Radar calibration-Some simple approaches. *Bulletin of the American Meteorological Society*, **83 (9)**, 1313–1316.

Aydin, K., Z. Yang, and T. A. Seliga, 1989: Rain-induced attenuation effects on C-band dual-polarization meteorological radars. *IEEE Transactions on Geoscience and Remote Sensing*, **27 (1)**, 57–66.

Bean, B. R. and E. J. Dutton, 1966: *Radio Meteorology. National Bureau of Standards Monograph., No. 92*. U.S. Government Printing Office, 435 pp.

Berne, A. and R. Uijlenhoet, 2005: A stochastic model of range profiles of raindrop size distributions: Application to radar attenuation correction. *Geophysical Research Letters*, **32 (10)**, 2–5.

Borowska, L., A. V. Ryzhkov, D. S. Zrnić, C. Simmer, and R. Palmer, 2011: Attenuation and Differential Attenuation of 5-cm-Wavelength Radiation in Melting Hail. *Journal of Applied Meteorology and Climatology*, **50 (1)**, 59–76.

Brandes, E. A., G. Zhang, and J. Vivekanandan, 2002: Experiments in Rainfall Estimation with a Polarimetric Radar in a Subtropical Environment. *Journal of Applied Meteorology*, **41 (6)**, 674–685.

Brandes, E. A., G. Zhang, and J. Vivekanandan, 2004: Comparison of Polarimetric Radar Drop Size Distribution Retrieval Algorithms. *Journal of Atmospheric and Oceanic Technology*, **21 (4)**, 584–598.

Bringi, V. N. and V. Chandrasekar, 2001: *Polarimetric Doppler Weather Radar: Principles and Applications*. Cambridge University Press, Cambridge, 636 pp.

Bringi, V. N., V. Chandrasekar, N. Balakrishnan, and D. S. Zrnić, 1990: An Examination of Propagation Effects in Rainfall on Radar Measurements at Microwave Frequencies. *Journal of Atmospheric and Oceanic Technology*, **7 (6)**, 829–840.

Bringi, V. N., T. D. Keenan, and V. Chandrasekar, 2001: Correcting C-band radar reflectivity and differential reflectivity data for rain attenuation: a self-consistent method with constraints. *IEEE Transactions on Geoscience and Remote Sensing*, **39 (9)**, 1906–1915.

Capsoni, C., M. D'Amico, and R. Nebuloni, 2001: A Multiparameter Polarimetric Radar Simulator. *Journal of Atmospheric and Oceanic Technology*, **18 (11)**, 1799–1809.

Capsoni, C. and M. DAmico, 1998: A Physically Based Radar Simulator. *Journal of Atmospheric and Oceanic Technology*, **15 (2)**, 593–598.

Carey, L. D., S. A. Rutledge, D. A. Ahijevych, and T. D. Keenan, 2000: Correcting Propagation Effects in C-Band Polarimetric Radar Observations of Tropical Convection Using Differential Propagation Phase. *Journal of Applied Meteorology*, **39 (9)**, 1405–1433.

Chandrasekar, V. and V. N. Bringi, 1987: Simulation of Radar Reflectivity and Surface Measurements of Rainfall. *Journal of Atmospheric and Oceanic Technology*, **4 (3)**, 464–478.

Cheong, B. L., R. D. Palmer, and M. Xue, 2008: A Time Series Weather Radar Simulator Based on High-Resolution Atmospheric Models. *Journal of Atmospheric and Oceanic Technology*, **25 (2)**, 230–243.

Crum, T. D. and R. L. Alberty, 1993: The WSR-88D and the WSR-88D Operational Support Facility. *Bulletin of the American Meteorological Society*, **74 (9)**, 1669–1688.

Doviak, R. J., V. N. Bringi, A. V. Ryzhkov, A. Zahrai, and D. S. Zrnić, 2000: Considerations for Polarimetric Upgrades to Operational WSR-88D Radars. *Journal of Atmospheric and Oceanic Technology*, **17 (3)**, 257–278.

Doviak, R. J. and D. S. Zrnić, 1993: *Doppler Radar and Weather Observations*. 2d ed., Academic Press, 562 pp.

Galati, G., 1995: Computer simulation of weather radar signals. *Simulation Practice and Theory*, **3 (1)**, 17–44.

Giuli, D., M. Gherardelli, A. Freni, T. A. Seliga, and K. Aydin, 1991: Rainfall and Clutter Discrimination by Means of Dual-linear Polarization Radar Measurements. *Journal of Atmospheric and Oceanic Technology*, **8 (6)**, 777–789.

Gorgucci, E. and L. Baldini, 2007: Attenuation and Differential Attenuation Correction of C-Band Radar Observations Using a Fully Self-Consistent Methodology. *IEEE Geoscience and Remote Sensing Letters*, **4 (2)**, 326–330.

Gorgucci, E., V. Chandrasekar, and L. Baldini, 2006: Rainfall estimation from X-band dual polarization radar using reflectivity and differential reflectivity. *Atmospheric Research*, **82 (1-2)**, 164–172.

Gorgucci, E., G. Scarchilli, and V. Chandrasekar, 1996: Error structure of radar rainfall measurement at C -band frequencies with dual polarization algorithm for attenuation correction. *Journal of Geophysical Research*, **101 (D21)**, 26 461–26 471.

Gorgucci, E., G. Scarchilli, and V. Chandrasekar, 2000: Practical Aspects of Radar Rainfall Estimation Using Specific Differential Propagation Phase. *Journal of Applied Meteorology*, **39 (6)**, 945–955.

Gorgucci, E., G. Scarchilli, V. Chandrasekar, P. F. Meischner, and M. Hagen, 1998: Intercomparison of Techniques to Correct for Attenuation of C-Band Weather Radar Signals. *Journal of Applied Meteorology*, **37 (8)**, 845–853.

Gosset, M., 2004: Effect of Nonuniform Beam Filling on the Propagation of Radar Signals at X-Band Frequencies. Part II: Examination of Differential Phase Shift. *Journal of Atmospheric and Oceanic Technology*, **21 (2)**, 358–367.

Gourley, J. J., P. Tabary, and J. Parent du Châtelet, 2007: Empirical Estimation of Attenuation from Differential Propagation Phase Measurements at C Band. *Journal of Applied Meteorology and Climatology*, **46 (3)**, 306–317.

Gu, J.-Y., A. V. Ryzhkov, P. Zhang, P. Neilley, M. Knight, B. Wolf, and D.-I. Lee, 2011: Polarimetric attenuation correction in heavy rain at C band. *Journal of Applied Meteorology and Climatology*, 39–58.

Harris, F. J., 1978: On the Use of Windows for Harmonic Analysis. *Proceedings of the IEEE*, **66 (1)**, 51–83.

Hildebrand, P. H., 1978: Iterative Correction for Attenuation of 5 cm Radar in Rain. *Journal of Applied Meteorology*, **17 (4)**, 508–514.

Hitschfeld, W. and J. Bordan, 1954: Errors Inherent in the Radar Measurement of Rainfall at Attenuating Wavelengths. *Journal of the Atmospheric Sciences*, **11 (1)**, 58–67.

Hubbert, J. C., V. Chandrasekar, V. N. Bringi, and P. F. Meischner, 1993: Processing and Interpretation of Coherent Dual-Polarized Radar Measurements. *Journal of Atmospheric and Oceanic Technology*, **10 (2)**, 155.

Ishimaru, A., 1991: *Wave Propagation and Scattering in Random Media*. IEEE Press, 600 pp.

Jameson, A. R., 1983: Microphysical Interpretation of Multi-Parameter Radar Measurements in Rain. Part I: Interpretation of Polarization Measurements and Estimation of Raindrop Shapes. *Journal of the Atmospheric Sciences*, **40 (7)**, 1792–1802.

Jung, Y., M. Xue, and G. Zhang, 2010: Simulations of Polarimetric Radar Signatures of a Supercell Storm Using a Two-Moment Bulk Microphysics Scheme. *Journal of Applied Meteorology and Climatology*, **49 (1)**, 146–163.

Klazura, G. E. and D. A. Imy, 1993: A Description of the Initial Set of Analysis Products Available from the NEXRAD WSR-88D System. *Bulletin of the American Meteorological Society*, **74 (7)**, 1293–1312.

Krajewski, W. F., R. Raghavan, and V. Chandrasekar, 1993: Physically Based Simulation of Radar Rainfall Data Using a Space-Time Rainfall Model. *Journal of Applied Meteorology*, **32 (2)**, 268–283.

Lewellen, W. S., D. C. Lewellen, and R. I. Sykes, 1997: Large-Eddy Simulation of a Tornados Interaction with the Surface. *Journal of the Atmospheric Sciences*, **54 (5)**, 581–605.

Liu, Y., V. N. Bringi, and M. Maki, 2006: Improved Rain Attenuation Correction Algorithms for Radar Reflectivity and Differential Reflectivity with Adaptation to Drop Shape Model Variation. *2006 IEEE International Symposium on Geoscience and Remote Sensing*, 1910–1913.

Magarvey, R. H. and B. W. Taylor, 1956: Free Fall Breakup of Large Drops. *Journal of Applied Physics*, **27 (10)**, 1129–1135.

Mardia, K. V., 1972: *Statistics of directional data*. Probability and mathematical statistics, Academic Press.

Marshall, J. S., R. C. Langillel, and W. M. Palmer, 1947: Measurement of Rainfall by Radar. *Journal of the Atmospheric Sciences*, **4 (6)**, 186–192.

Marshall, J. S. and W. M. Palmer, 1948: The Distribution of Raindrops with Size. *Journal of the Atmospheric Sciences*, **5 (4)**, 165–166.

Matrosov, S. Y., K. a. Clark, B. E. Martner, and A. Tokay, 2002: X-Band Polarimetric Radar Measurements of Rainfall. *Journal of Applied Meteorology*, **41 (9)**, 941–952.

Matsumoto, M. and T. Nishimura, 1998: Mersenne twister: a 623-dimensionally equidistributed uniform pseudo-random number generator. *ACM Transactions on Modeling and Computer Simulation*, **8 (1)**, 3–30.

Matzler, C., 2002: Matlab functions for Mie scattering and absorption – version 2. *Research Report no. 2002-11*, 19.

May, R. M., M. I. Biggerstaff, and M. Xue, 2007: A Doppler Radar Emulator with an Application to the Detectability of Tornadic Signatures. *Journal of Atmospheric and Oceanic Technology*, **24 (12)**, 1973–1996.

Mie, G., 1908: Beitrge zur Optik trber Medien, speziell kolloidaler Metallsungen. *Annalen der Physik*, **330 (3)**, 377–445.

Mishchenko, M. I., 1993: Light scattering by size-shape distributions of randomly oriented axially symmetric particles of a size comparable to a wavelength. *Applied Optics*, **32 (24)**, 4652–4666.

Mishchenko, M. I., L. D. Travis, and D. W. Mackowski, 1996: T-matrix computations of light scattering by nonspherical particles: A review. *Journal of Quantitative Spectroscopy and Radiative Transfer*, **55 (5)**, 535–575.

Muschinski, A., P. P. Sullivan, D. B. Wuertz, R. J. Hill, S. A. Cohn, D. H. Lenschow, and R. J. Doviak, 1999: First synthesis of wind-profiler signals on the basis of large-eddy simulation data. *Radio Science*, **34 (6)**, 1437–1459.

Park, S.-G., V. N. Bringi, V. Chandrasekar, M. Maki, and K. Iwanami, 2005a: Correction of Radar Reflectivity and Differential Reflectivity for Rain Attenuation at X Band. Part I: Theoretical and Empirical Basis. *Journal of Atmospheric and Oceanic Technology*, **22 (11)**, 1621–1632.

Park, S.-G., M. Maki, K. Iwanami, V. N. Bringi, and V. Chandrasekar, 2005b: Correction of Radar Reflectivity and Differential Reflectivity for Rain Attenuation at X Band. Part II: Evaluation and Application. *Journal of Atmospheric and Oceanic Technology*, **22 (11)**, 1633–1655.

Pruppacher, H. R. and K. V. Beard, 1970: A wind tunnel investigation of the internal circulation and shape of water drops falling at terminal velocity in air. *Quarterly Journal of the Royal Meteorological Society*, **96 (408)**, 247–256.

Ray, P. S., 1972: Broadband Complex Refractive Indices of Ice and Water. *Applied Optics*, **11 (8)**, 1836–1844.

Ryzhkov, A. V., S. E. Giangrande, V. M. Melnikov, and T. J. Schuur, 2005a: Calibration issues of dual-polarization radar measurements. *Journal of Atmospheric and Oceanic Technology*, **22 (8)**, 1138–1155.

Ryzhkov, A. V., S. E. Giangrande, and T. J. Schuur, 2005b: Rainfall Estimation with a Polarimetric Prototype of WSR-88D. *Journal of Applied Meteorology*, **44 (4)**, 502–515.

Ryzhkov, A. V., T. J. Schuur, D. W. Burgess, P. L. Heinselman, S. E. Giangrande, and D. S. Zrnić, 2005c: The Joint Polarization Experiment: Polarimetric Rainfall Measurements and Hydrometeor Classification. *Bulletin of the American Meteorological Society*, **86 (6)**, 809–824.

Ryzhkov, A. V. and D. S. Zrnić, 1995: Precipitation and Attenuation Measurements at a 10-cm Wavelength. *Journal of Applied Meteorology*, **34 (10)**, 2121–2134.

Scarchilli, G., E. Gorgucci, V. Chandrasekar, and T. A. Seliga, 1993: Rainfall Estimation Using Polarimetric Techniques at C-Band Frequencies. *Journal of Applied Meteorology*, **32 (6)**, 1150–1160.

Smyth, T. J. and A. J. Illingworth, 1998: Correction for attenuation of radar reflectivity using polarization data. *Quarterly Journal of the Royal Meteorological Society*, **124 (551)**, 2393–2415.

Snyder, J. C., H. B. Bluestein, G. Zhang, and S. J. Frasier, 2010: Attenuation Correction and Hydrometeor Classification of High-Resolution, X-band, Dual-Polarized Mobile Radar Measurements in Severe Convective Storms. *Journal of Atmospheric and Oceanic Technology*, **27 (12)**, 1979–2001.

Stout, G. E. and E. A. Mueller, 1968: Survey of Relationships Between Rainfall Rate and Radar Reflectivity in the Measurement of Precipitation. *Journal of Applied Meteorology*, **7 (3)**, 465–474.

Straka, J. M., D. S. Zrnić, and A. V. Ryzhkov, 2000: Bulk Hydrometeor Classification and Quantification Using Polarimetric Radar Data: Synthesis of Relations. *Journal of Applied Meteorology*, **39 (8)**, 1341–1372.

Tabary, P., G. Vulpiani, J. J. Gourley, A. J. Illingworth, R. J. Thompson, and O. Bousquet, 2009: Unusually High Differential Attenuation at C Band: Results from a Two-Year Analysis of the French Trappes Polarimetric Radar Data. *Journal of Applied Meteorology and Climatology*, **48 (10)**, 2037–2053.

Testud, J., E. Le Bouar, E. Obligis, and M. Ali-Mehenni, 2000: The Rain Profiling Algorithm Applied to Polarimetric Weather Radar. *Journal of Atmospheric and Oceanic Technology*, **17 (3)**, 332–356.

Testud, J., S. Oury, R. a. Black, P. Amayenc, and X. Dou, 2001: The Concept of Normalized Distribution to Describe Raindrop Spectra: A Tool for Cloud Physics and Cloud Remote Sensing. *Journal of Applied Meteorology*, **40 (6)**, 1118–1140.

Torres, S. M. and D. S. Zrnić, 2003: Whitening of Signals in Range to Improve Estimates of Polarimetric Variables. *Journal of Atmospheric and Oceanic Technology*, **20 (12)**, 1776–1789.

Ulbrich, C. W., 1983: Natural Variations in the Analytical Form of the Raindrop Size Distribution. *Journal of Applied Meteorology*, **22 (10)**, 1764–1775.

Vulpiani, G., F. S. Marzano, and V. Chandrasekar, 2005: Constrained iterative technique with embedded neural network for dual-polarization radar correction of rain path attenuation. *IEEE Transactions on Geoscience and Remote Sensing*, **43 (10)**, 2305–2314.

Vulpiani, G., P. Tabary, J. Parent du Châtelet, and F. S. Marzano, 2008: Comparison of Advanced Radar Polarimetric Techniques for Operational Attenuation Correction at C Band. *Journal of Atmospheric and Oceanic Technology*, **25 (7)**, 1118–1135.

Waterman, P. C., 1971: Symmetry, Unitarity, and Geometry in Electromagnetic Scattering. *Physical Review D*, **3 (4)**, 825–839.

Wicker, L. J. and R. B. Wilhelmson, 1995: Simulation and Analysis of Tornado Development and Decay within a Three-Dimensional Supercell Thunderstorm. *Journal of the Atmospheric Sciences*, **52 (15)**, 2675–2704.

Wood, V. T. and R. A. Brown, 1997: Effects of Radar Sampling on Single-Doppler Velocity Signatures of Mesocyclones and Tornadoes. *Weather and Forecasting*, **12 (4)**, 928–938.

Zahiri, E.-P., M. Gosset, J.-P. Lafore, and V. Gouget, 2008: Use of a Radar Simulator on the Output Fields from a Numerical Mesoscale Model to Analyze X-Band Rain Estimators. *Journal of Atmospheric and Oceanic Technology*, **25 (3)**, 341–367.

Zhang, G., J. Vivekanandan, and E. A. Brandes, 2001: A method for estimating rain rate and drop size distribution from polarimetric radar measurements. *IEEE Transactions on Geoscience and Remote Sensing*, **39 (4)**, 830–841.

Ziegler, C. L., 1985: Retrieval of Thermal and Microphysical Variables in Observed Convective Storms. Part 1: Model Development and Preliminary Testing. *Journal of the Atmospheric Sciences*, **42 (14)**, 1487–1509.

Zrnić, D. S., 1975: Simulation of Weatherlike Doppler Spectra and Signals. *Journal of Applied Meteorology*, **14 (4)**, 619–620.